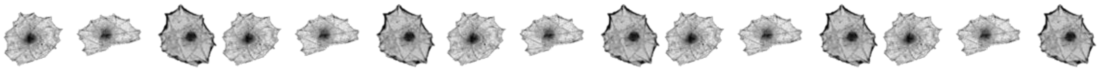

How Cells Sense the Matrix Geometry: a Novel Nanopatterning Approach

Stefania Di Ciò
2013-2017

School of Engineering and Material Science
Queen Mary University of London
Submitted for the Degree of Doctor of Philosophy

Declaration

I, Stefania Di Ciò, confirm that the research included within this thesis is my own work or that where it has been carried out in collaboration with, or supported by others, that this is duly acknowledged below and my contribution indicated. Previously published material is also acknowledged below.

I attest that I have exercised reasonable care to ensure that the work is original, and does not to the best of my knowledge break any UK law, infringe any third party's copyright or other Intellectual Property Right, or contain any confidential material.

I accept that the College has the right to use plagiarism detection software to check the electronic version of the thesis.

I confirm that this thesis has not been previously submitted for the award of a degree by this or any other university.

Signature:
Date:

Details of collaboration and publications:
Dr. Núria Gavara performed the actin cytoskeleton analysis for immunostained samples. The live movies were partially analysed using the MatLab code given from Dr. Núria Gavara.
Chapter 1 has been published (Di Cio and Gautrot, 2016).
Parts of Chapter 2 and 3 have been published (Di Cio et al., 2016).

Acknowledgment

I would like to thank my supervisor Dr. Julien Gautrot for his endless support during these years and the precious advices he gave me. Thanks to Dr. John Connelly for his support and for the possibility he gave me together with Julien to participate in this project and to Queen Mary University of London and the Institute of Bioengineering for founding it.

Thanks to the SEMS and NanoVision centre technicians, Mr Chris Mole, Mr Shafir Iqbal, Mr Douge Thomson, Dr Dongsheng Wu and Mr Russell Bailey for the patient help with the instruments and with the lab maintenance. Thanks to Dr. Geroge Nevill from the physic school for the gold coated glass slides. Thanks to Dr. Estelle Collin and Dr. Stephen Thorpe for their help whenever I was bothering them.

Thanks to Dr. Núria Gavara, for the image analysis of cell cytoskeleton and for kindly giving the MatLab code for the analysis of the actin movie.

A big thank to my family, especially my mum, dad and brother, for always supporting me and helping when needed.

Last but not least, I would like to thank my friends from home and all the amazing people I met at QM and outside here in London, for making these hard years a real crack!! In particular my lab friends Will, Dexu, Pei, Khai The President, Xi, Burcu, Mahentha, my “sister” Yaqi, Matt, Maria, Ed, Servann, Anuroopa and Gaston and my patient office colleagues Michalis and Sahand!

Abstract

Tissue engineering and regenerative medicine aim to develop materials that mimic some of the characteristics of the tissue they are replacing and control the growth and proliferation of cells. Despite exceptional advances in the range and quality of materials used, much remains to discover about the processes regulating interfaces between cells and their surroundings, or at cell-material interfaces. In order to study and control such interactions, scientists have produced engineered matrices aiming to mimic some of the feature of natural extra-cellular matrix (biochemistry, geometry/topography and mechanical properties).

In order to pattern 2D-nanofibers on relatively large areas and throughput, allowing comprehensive biological studies, we developed a nano-fabrication technique based on the deposition of sparse mats of electrospun fibres with different diameters. These mats are used as masks to grow cell resistant polymer brushes from exposed areas. After removal of the fibres, the remaining brushes define a quasi-2D fibrous pattern onto which ECM molecules such as fibronectin can be adsorbed. Chapter 2 includes details of the techniques used to produce and characterize the fibrous nanopattern. Chapter 3 is focused on cell phenotype observed on the different nanofibres sizes. Adhesion assays showed that cell spreading, shape and polarity are regulated by the size of fibres but also the density of the nanofibres, similarly to previous observations made on circular nanopatterns. We then focused on the study of focal adhesion formation and maturations on these nanofibres and the role of key proteins involved in the regulation of the adhesion plaque: integrins and vinculin. Cells expressing different integrins were found to sense the nanoscale geometry differently. Vinculin sensing is the topic of Chapter 4. Although vinculin recruitment dynamics was affected by the nanofibrous patterns and focal adhesions arrange differently on the nanofibres, this protein does not seem to mediate nanoscale sensing.

In Chapter 5, we finally focused on the role of the actin cytoskeleton as a direct sensor of nanoscale geometry. A gradual decrease in stress fibre formation was observed as the nanofibres dimensions decrease. Live imaging also demonstrated that the geometry of the extracellular environment strongly affects cytoskeleton rearrangement, stress fibres formation and disassembly. We identify the role of cytoskeleton contractility as an important sensor of the nanoscale geometry.

Our study provides a deeper insight in understanding cell adhesion to the extracellular environment and the role of the matrix geometry and topography on such phenomena, but also raises questions regarding the more detailed molecular sensory elements enabling the direct sensing of nanoscale geometry through the actin cytoskeleton.

Contents

Acknowledgment ii
Abstract iii
Abbreviations ix
List of figures xii
List of tables xxv
Chapter 1. Introduction 1
- 1.1 Nanoscale architecture and dynamics of the cytoskeleton and integrin-mediated adhesions 2
  - 1.1.1 Focal adhesion structure and dynamics 2
  - 1.1.2 Actin structure and dynamics 13
- 1.2 Design of nanostructured platforms controlling cell adhesion and cell phenotype 21
  - 1.2.1 Geometrically patterned surfaces 22
  - 1.2.2 Surface topography 28
- 1.3 Nanoscale sensing of the physical environment 32
  - 1.3.1 Geometrical control of integrin clustering 32
  - 1.3.2 Geometrical control of FA maturation 35
  - 1.3.3 Topography sensing 41
- 1.4 Conclusions 45
- 1.5 Aims and Objectives 47

Chapter 2. Electrospun Nanofibres Lithography- ENL 48
- 2.1 Introduction 48
  - 2.1.1 Electrospinning 51
  - 2.1.2 Etching 53
  - 2.1.3 Polymer brushes - ATRP 55

2.2 Nanofibres pattern fabrication: materials and methods 57

2.2.1 Materials and chemicals 57

2.2.2 Silanization 57

2.2.3 Electrospinning...58

2.2.4 Annealing 60

2.2.5 Wet etching 60

2.2.6 Polymer brushes growth - ATRP 62

2.2.7 Fibronectin deposition 64

2.2.8 Fibronectin immunostaining 64

2.2.9 Characterization 64

2.3 Nanofibres pattern fabrication: results and discussions 66

2.3.1 Electro-spinning of fibres...66

2.3.2 Thermal annealing 70

2.3.3 Wet etching 72

2.3.4 Polymer brush growth 76

2.3.5 Fibronectin deposition...84

2.4 Conclusions...86

Chapter 3 Cell sensing of the matrix nanoscale geometry 88

3.1 Introduction...88

3.2 Materials and methods 91

3.2.1 Materials and chemicals. 91

3.2.2 PLL-PEG functionalization of circular patches..91

3.2.3 Cell culture and seeding...92

3.2.4 Immunostaining. 92

3.2.5 Cell characterization..93

3.3 Results and discussions 95

3.3.1 Control of cell adhesion. 95

3.3.2 Impact of nanoscale geometry on cell spreading and shape. 98

3.3.3 Impact of integrin expression on nanoscale sensing of ECM geometry.105

3.4 Conclusion 111

Chapter 4 Vinculin sensing of the geometry 113

4.1 Introduction....................113

4.2 Materials and methods 114

4.2.1 Materials and chemicals. 114

4.2.2 Cell culture and seeding.....................115

4.2.3 GEβ3 transfection for FRAP experiments 115

4.2.4 MEFvin$^-$/$^-$ vinculin transfection....................116

4.2.5 Immuno-fluorescence microscopy and data analysis.....................116

4.2.6 Statistical analysis. 118

4.3 Results and discussions 118

4.3.1 How integrin expression affect focal adhesion formation 118

4.3.2 How is vinculin regulated at the nanoscale 123

4.4 Conclusions....................130

Chapter 5 Actin sensing of the geometry 132

5.1 Introduction....................132

5.2 Matherials and methods 133

5.2.1 Materials and chemicals 133

5.2.2 Cell culture and seeding....................134

5.2.3 Cytoskeleton inhibitors treatment....................134

5.2.4 Immunostaining for myosin II and α-actinin....................134

5.2.5 GEβ1 and GEβ3 transfection....................134

5.2.6 Immuno-fluorescence microscopy and data analysis....................135

5.2.7 Statistical analysis 137

5.3 Results and discussions 138

5.3.1 Actin cytoskeleton organisation on nanofibres 138

5.3.2 GEβ3 cells sensing of the topography is associated with an impaired cytoskeleton organization 152

5.4 Conclusions 169

Chapter 6. Summary of conclusions and future directions 171

Bibliography 175

Appendix 1 190

Appendix 2 193

Abbreviations

µCP - micro contact printing

AFM - atomic force microscopy

ALP - alkaline phosphatase

ARP - actin-related proteins

ATRP - atom transfer radical polymerisation

BSA – bovine serum albumin

CL - colloidal lithography

CRP - controlled radical polymerization

$CuBr_2$ - copper(II) bromide

CuCl - copper (I) cloride

$CuCl_2$ - copper(II) chloride

DAPI - 4,6-diamidino-2-phenylindole

DMF - N, N-Dimethylformamide

DMSO - dimethyl sulfoxide

DNA - deoxyribonucleic acid

DPN - dip-pen nanolithography

EBL – electron- beam lithography

ECM – extracellular matrix

EDS - energy dispersive spectroscopy

ENL – electrospun nanofiber lithography

ERK - extracellular-signal-regulated kinases

FA- focal adhesion

FAK - focal adhesion kinase

FBS – foetal bovine serum

FC – focal complex

FIB - Focused Ion Beam

FLIP - fluorescence loss in photobleaching

FN - fibronectin

FRAP - fluorescence-recovery after photobleaching

FRET - Förster resonance energy transfer

GTA - glutaraldehyde

HA - hyaluronic acid

hESC - human embryonic stem cell

HSQ - hydrogen silsesquioxane

HTS – high throughput screening

IJP - inkjet printing

ILK - integrin-linked kinase

MAPKs - Mitogen-activated protein kinases

MEF –mouse embryonic fibroblast

MSCs – mesenchymal stem cells

Mw – molecular weight

NaCl - sodium chloride

NEB - High resolution chemically amplified negative resist

NIL- nanoimprint lithography

NRVMs - neonatal rat ventricular myocytes

NSCs – neural stem cells

PAA - polyacrylic acid

PAAm - poly(acrylamide)

PALM - photo-activated localization microscopy

PAN - Polyacrylonitrile

PB - phosphate buffer

PCL - poly(3-caprolactone)

PDMS - poly(dimethyl siloxane)

PE - polyethylene

PEA - poly(ethyl acrylate)

PEG (or PEO) - Polyethylene glycol

PES - polyethersulfone

PET - poly(ethylene terephthalate)

PFA - paraformaldehyde

PLA - polylactic acid
PMA - poly(methyl acrylate)
PMEDSAH – poly-[2-(Methacryloyloxy)ethyl]dimethyl-(3-sulfopropyl)ammonium hydroxide
PMMA - poly(methyl methacrylate)
POEGMA – poly- Oligo(ethylene glycol methyl ether methacrylate)
POR - porin
PP – polypropylene
PS - Polystyrene
PVA - Poly(vinyl acetate)
PVC - poly(vinyl chloride)
PVP - polyvinylpyrrolidone
Rap1 - Ras-proximate-1
rBM - reconstituted basement membrane
RGD - arginylglycylaspartic acid
RhoA - Ras homolog gene family, member A
RIE – reactive ion etching
ROCK - rho-associated, coiled-coil-containing protein kinase
SDS - sodium dodecyl sulfate
SEM - scanning electron microscopy
SFM – serum free medium
STORM - stochastic optical reconstruction microscopy
TCPS - tissue-culture polystyrene
TEM- transmission electron microscopy
TIRF - total internal reflection fluorescence
VASP - vasodilator-stimulated phosphoprotein
VEGF - vascular endothelial growth factor
VNC – Vinculin
ZEP - high performance positive EB resists

List of figures

Figure 1.1 Focal adhesion architecture. There are three main layers identified in focal adhesion architecture: “integrin signalling layer” comprising FAK and paxillin (yellow); a “force transduction layer” comprising talin and vinculin (green) and a final “actin-regulatory layer” including zyxin, VASP and α-actinin (blue). The proteins represented are the main components of FA. Adapted by permission from Macmillan Publishers Ltd: Nature (Kanchanawong et al., 2010), copyright (2010). 6

Figure 1.2 Differential integrin signalling pathways. Integrin heterodimers $\alpha_5\beta_1$ and $\alpha_v\beta_3$ differentially regulate myosin II-based contractility in sensing the mechanics of the ECM. They cooperate synergistically with the α_v (green) having a structural role and the α_5 (orange) a force generation role. The arrows indicate the different pathways activated and the molecules involved: signalling proteins like Rac, RhoA, Rock, kindling and actin associated protein like mDia and Arp2/3 differently modulate the process. Adapted by permission from Macmillan Publishers Ltd: Nat Cell Bio (Schiller et al., 2013), copyright (2012)..9

Figure 1.3 Vinculin regulation of FA maturation. Experiments with cells presenting a full active vinculin or vinculin knock- out show that vinculin affects F-actin flow velocity and FA growth rate. The presence of this molecule decreases the F-actin flow. Reproduced from Thievessen et al. 2013 originally published in J. Cell Biol. doi: 10.1083/jcb.201303129 (Thievessen et al., 2013)..11

Figure 1.4 FA maturation. Schematic of adhesion assembly, turnover and maturation and their association with actin polymerization and myosin II activity. Nascent adhesions form in the lamellipodium, they move inward towards the lamella maturing and association with actin stress fibres, crosslinked by myosin II and α- actinin. In b a cell edge cross section is shown with the direction of the focal adhesion maturation velocity (v). X indicates the cell basal plane and point towards the cell centre. Adapted by permission from Macmillan Publishers Ltd: Nat Cell Bio (Choi et al., 2008), copyright (2008). 13

Figure 1.5 The F-actin cytoskeleton imaged via super-resolution microscopy. (a) Actin structure with vertical cross sections (b, c) along the dotted line and apparent thickness of the two layers (f) shown in b. Ventral and dorsal actin layer before (g, h) and after treatment with blebbistatin (i, j). Vertical cross section (k, l) of the dotted lines from i. Adapted by permission from Macmillan Publishers Ltd: Nature Methods (Xu et al., 2012), copyright (2012). 15

Figure 1.6 Patterning techniques. A: representation of the micelle nanolithography technique used to produce ordered and disordered gold nanosphere and their functionalization. Block co- polymer are used to tune the spacing between the micelles that contain the gold sphere. Micelles are then removed via plasma treatment and the gold nanoparticles left are functionalised with RGD peptide and the background is passivated with PEG. Adapted with permission from (Huang et al., 2009). Copyright (2009) American Chemical Society. B: colloidal lithography approach schematic (top) and SEM images of patterns with different sizes (bottom). Here colloids are deposited on a gold coated surface (1 and 2) and a layer of Si is then evaporated on top (3). Colloids are then removed leaving gold circles surrounded by Si (4). Adapted with permission from (Malmstrom et al., 2010). Copyright (2010) American Chemical Society 25

Figure 1.7 Effect of ordered and disordered nanopatterns on integrin clustering. Spacing RGDs further apart than 70 nm (b, d) prevents integrin clustering and FA maturation. Maturation is instead allowed on disordered patterns with similar spacing (a, c). Adapted with permission from (Huang et al., 2009). Copyright (2009) American Chemical Society. 34

Figure 1.8 Effect of nanopatterns on cell behaviour. Keratinocytes spreading on homogenous surfaces (Au) or on nano-patches with different diameters (3000, 600, 300 and 100 nm). Differentiation (left column, involucrin is a keratinocytes terminal differentiation marker), focal adhesion formation and keratinocytes spreading (central column, right column showing zooms of areas delimited by the doted boxes) are controlled by the nanoscale geometry of adhesions. Adapted with permission from (Gautrot et al., 2014). Copyright (2014) American Chemical Society............................38

Figure 1.9 Cells adhering and deforming elastic micropillar. SEM (A) and epifluorescent (B, fibronectin coated micropillars are in red and paxillin is in green) images of a cell adhering on elastic micropillars. C represents the inset in B with the sequential FA formation and micropillar displacement. D: schematic of the staining (fibronectin coated micropillars in red and paxillin in green) and force displacement. E: relationship between force measured and adhesion area over time. Reproduced from (Trichet et al., 2012)..39

Figure 1.10 Schematic of topography sensing through RhoA/ROCK signalling. Different signalling pathways are activated depending on the surface topography and myosin IIa is involved in the sensing and triggers differentiation depending on the force/ tension felt. On the curved surface there is a higher tension felt that ultimately results in higher levels of differentiation. Reprinted with permission from ref (Ozdemir et al., 2013). Copyright 2013 The Royal Society of Chemistry...42

Figure 2.1 Electrospun nanofibres lithography (ENL). Schematic of the two methods tested for the production of the fibrous pattern. Main steps are electrospinning, annealing and ATRP. 50

Figure 2.2 Schematic of electrospinning process (Ziabari et al., 2009). The polymer solution flows through a syringe that ends with a needle where the Taylor cone forms. This cone is the accelerated by electrostatic forces and forms a jet directed to the collector..51

Figure 2.3 Example of combination of dry and wet etching. A photoresist (PR) is deposited on a Nickel coated surface (Ni) and patterned via UV light (LIL). The pattern is then transferred to the surface below via subsequent wet and dry etching. (Lai and Cheng, 2014) 54

Figure 2.4 Strategies for polymer brush deposition. (A) Physical absorption of diblock copolymers. (B) Chemical absorption via adhesion of end-functionalized polymers with complementary functional groups. (C) Polymer brushes grown via surface-initiated polymerization methods (Barbey et al., 2009). 55

Figure 2.5 Schematic of a conventional ATRP (Matyjaszewski, 2012). 56

Figure 2.6 Experimental set-up for electrospinning. The polymer solution flows through a needle where an electric field is applied; this charges the solution so that the jet is formed. A plastic box of 1 X 1 m (grey square) protects the area where the Taylor cone is formed and the metal collector where the fibres are deposited. The metal collector is supported by a metal structure that is grounded. 59

Figure 2.7 Fibre dimensions (diameter) obtained using different PMMA concentrations (x axis) and with or without the use of an electrolyte (salt, NaCl 0.1% in weight). Bars are standard errors, n≥3, number of experiments. For statistical test: *, P < 0.05; **, P < 0.01; ***, P < 0.001; ****, P < 0.0001. 66

Figure 2.8 SEM images of electrospun fibres from different solution concentration. Small fibres (200 nm, top row) were produced from 3.5% PMMA solution; intermediate fibres (500 nm) from 5% PMMA solution; and biggest fibres (1000 nm) from 10% solutions. Images are taken at different magnifications (see label). 69

Figure 2.9 Percentile change of three sizes of fibre dimension (obtained from 3.5, 7 and 10% w/w PMMA solution concentration) at different annealing temperatures. Error bars are SD. 70

Figure 2.10. SEM images of fibres (200, 800 and 1000 nm diameters as spun) after thermal annealing at various temperatures. The first column represents the fibres as spun. 71

Figure 2.11. Gold etching on glass. Gold exposed areas were etched with solution (1). SEM images showing 700nm fibres (at different magnification) on glass etched with solution (1) without (A, B) and with (C) 0.1% SDS. 72

Figure 2.12 SEM images representing 800 nm (left) and 550nm (right) fibres on glass after 1min plasma treatment and etching with solution (1). 73

Figure 2.13. SEM images of about 600 nm diameter gold fibre on wafer (A, B) etched for 65 sec with solution (1) (A) and (2) (B). Solution (1) over etches the sample. 300 nm diameter fibres on glass after 70 s with solution (2) (C). 74

Figure 2.14. Effect of etching time for about 600 nm fibre diameter. Increasing the etching time decreases the fibre diameter. Error bars are SD. 75

Figure 2.15. AFM image (left) and height profile (right) of the gold nanofibres left after etching (fibres diameter around 600 nm). The height of the gold fibre left is about 15 nm. 75

Figure 2.16. SEM image of the nanofibres left after 65 s etching on wafer. Spectra are detected in points 1 and 2 on the image and a table with the detected elements and concentration (% in weight) is shown 76

Figure 2.17 POEGMA and PMEDSAH brushes structure grown via ATRP (Tan et al., 2013). Brushes grow perpendicular to the surface with the R group on the side of the chains. 77

Figure 2.18. Top. Fibres were electrospun, annealed and then removed with $CHCl_3$. The surface was then characterised via AFM (top left) showing a very thin layer of residual

PMMA left on the silicon (see height profile of the blue line, right). Scale bar 10 µm. Bottom. After polymer brushes growth and PMMA fibre removal, EDS analysis was performed to check the composition of the resulting pattern: some carbon is detected on the nanofibres even after removal of the PMMA fibres, suggesting there may be some PMMA left. 78

Figure 2.19. AFM imaging of nanopatterned substrates after polymer brush growth (POEGMA), prepared via the patterning via etching method. Left, topography image; right, height profile. The gold fibres left are higher (see profile) than the POEGMA functionalised background...79

Figure 2.20. POEGMA brushes produced following the patterning via ATRP method. SEM images (top row) of nanofibres with 250 nm (left) and 1000 nm (right) diameter. AFM (bottom row) of 1000 nm nanofibres with height profile. Scale bar is 2 µm........80

Figure 2.21. Patterns produced via ATRP method. Representative SEM (upper row, high density nanofibres and lower row low density) and AFM (high density nanofibres) images of the pattern after polymer brushes and mask removal. First column is 250 nm diameter nanofibres, second column is 600 nm nanofibres and last column is 1000 nm nanofibres (including a 3D AFM image). Scale bar in AFM images is 5 µm...................81

Figure 2.22 Evolution of fibre diameter over the patterning process following ATRP method: after electrospinning (green), annealing (grey) and polymer brushes functionalization (purple). Error bars are standard errors (n ≥ 3)................................82

Figure 2.23. Change in brush layer thickness (measured via ellipsometry after ATRP) before and after treatment with chloroform for removing PMMA fibres. Error bars are SE. No significant differences can be noticed. 82

Figure 2.24. Methodology used to assess fibre density and the gap area between the fibres. From a starting SEM image (A, 550 nm fibres and low density nanofibres. Scale bar is 30 μm) a threshold was applied to get a BW image (B and C inverted) from which the % of area covered from fibres (B) and the area of the gap in between fibres (C) was calculated. Average area of the gap between the fibres for 250, 550 and 800 nm diameter low density nanofibres (E). Error bars are standard deviation, n≥ 200, number of sampling. Comparisons are referred to the 250 nm. For statistical test: *, P < 0.05; **, P < 0.01; ***, P < 0.001; ****, P < 0.0001. Gap area distribution on different nanofibres diameters, 250 (green), 500 and 800 nm, at low density (F). Fractal

dimension of the pattern with low density fibres and diameters of 250, 550 and 1000 nm was also assessed using ImageJ (D). 83

Figure 2.25. PMEDSAH brushes grown via the patterning ATRP method. SEM of 300 nm diameter fibrous pattern (left) and AFM of 1000 nm fibrous pattern with height profile (right). Scale bar is 10 µm. 84

Figure 2.26. Images from epifluorescent microscopy showing nanofibres after fibronectin deposition and immunostaining. POEGMA and PMEDSAH brushes coating with different fibre size: 200, 600, 800 and 1000 nm for POEGMA and 200 and 800 nm for PMEDSAH. The inset shows the corresponding fibronectin intensity profile. Scale bar 50 µm. 85

Figure 2.27 Roughness analysis of 250 and 800 nm nanofibres (see representative AFM images for the two nanofibres size in the inset) with POEGMA brushes. Roughness was assessed before (wo FN) and after (w FN) FN deposition. Error bars are standard errors (n = 3). No significant differences are noticeable for these values (see tab. S3 for the details of statistical analysis)...86

Figure 3.1 A. HaCat cells spreading (for 24 hr) on nanofibres with different diameters. A. Confocal microscopy images of cells on 600 nm (top) and 800 nm (bottom) diameter nanofibres (passivated with POEGMA): colocalization can be noticed of vinculin (green) on fibronectin (red). Scale bar of the first images (normal size) is 10 µm, in the zoomed images the scale bar is 2 µm. B. Confocal images of immunostained samples for laminin (green) and FN/BSA (1/1, 594nm, red) of cells seeded on 600 nm and 1000 nm nanofibres (first two images) and laminin on 1000 nm nanofibres (last images on the right). Scale bar is 10 µm. C. Double staining for vinculin and fibronectin of cells seeded on circular patched (800 nm diameter). Scale bar is 10 µm in the first image and 2 µm in the zoomed images. 96

Figure 3.2 HaCat cells after 24 hr spreading. SEM images representing cells adhering on control homogenous surfaces, 800, 600 and 250 nm diameter fibres (different magnification). Scale bar is 5 µm. 98

Figure 3.3 . HaCat cells after 24 hr spreading. Data showing ell area (green) and relative area change (purple, relative to control surfaces) on low (A), medium (C) and high (E) density nanofibres with 250, 550, 800 and 1000 nm diameters (POEGMA patterns). Ctrl is the homogenous control surface. Cell morphology quantified via circularity (green) and aspect ratio (purple, longer cell axis divided by the smaller axis)

on low (B), medium (D) and high (F) density nanofibres. Error bars are SE, n ≥ 3, with n representing the number of experiments. For statistical test: *, P < 0.05; **, P < 0.01; ***, P < 0.001; ****, P < 0.0001. 100

Figure 3.4 Graph: HaCat cell density on low, medium and high density nanofibres, with fibres of different diameters. Ctrl is the homogenous control surface. Error bars are SE, n ≥ 3. No significant differences are noticeable from this data, across different densities and nanofibres dimensions. Bottom: representative epifluorescent microscope images of cells seeded on low density nanofibres with different fibre sizes (see picture). Scale bar is 100 µm. 101

Figure 3.5 A. Confocal images of HaCat cells spreading (24 hr) on different nanofibre diameter (POEGMA brushes): vinculin (green) and actin (red) staining of cell spreading on control homogenous surfaces (first column, Ctrl), 800 nm (second column), 550 nm (third column) and 250 nm (last column) nanofibres (low density). Scale bar is 10 µm. B. Confocal images of HaCat spreading on 1000 nm (average nanofibres density), 800 nm (average nanofibres density), 550 nm (high nanofibres density) and 250 nm (average nanofibres density). Green represents vinculin and the background is taken in reflection mode. Scale bar is 20 µm.. 103

Figure 3.6 HaCat cells seeded on nanofibres with PMEDSAH functionalised background (24 hr spreading). Here there is a mixture of intermediate and high densities. Cell area for cell seeded on different nanofibres size and at different density. Scale bar is 10 µm. 104

Figure 3.7 First row: SEM images of the circular patches (in order: 300, 500 and 800 nm diameter). Second row. HaCat cells spreading (24 hr) and relative area change (to control) on circular patches (A), cell shape descriptors (B) and cell density (C). Third row. Representative confocal images of cells spreading on the different size patches: vinculin (green) and actin (red). Scale bar is 10 µm. Error bars are SE, n ≥ 3, with n representing the number of experiments. For statistical test: *, P < 0.05; **, P < 0.01; ***, P < 0.001; ****, P < 0.0001. 105

Figure 3.8 Expression of β1 and αv integrins by GE cells spreading on control homogenous surfaces and 500 and 1000nm diameter nanofibres (as indicated in the figure). The anti- integrin antibodies are shown in green and the FN/ BSA (1/1) in red (confocal images). Scale bar is 10 µm. 106

Figure 3.9 GE cells after 24 hr spreading. Cell area (green) and relative area change of GE (A), GEβ1 (C) and GEβ3 (E) on fibrous patterns (see schematics of integrin expression on the side). Shape descriptor (circularity and aspect ratio), for GE (B), GE β1 (D) and GE β3 (F) cells on different nanofibres sizes. GE cell density on different nanofibres size (G).Ctrl is the homogenous control surface. Error bars are SE ($n \geq 6$, with n representing the number of experiments). For statistical test: **, $P < 0.01$; ***, $P < 0.001$; ****, $P < 0.0001$; *****$P < 0.00001$. 107

Figure 3.10 GE cells spreading on nanofibrous patterns (after 24 hr). Confocal images representing vinculin (green) and actin (red) staining of GE cells spreading on control homogenous (Ctrl) surfaces and 1000, 550 and 250 nm diameter fibres (from top to bottom). Scale bar 15 μm. 109

Figure 3.11 GEβ1 cells spreading on nanofibrous patterns (after 24 hr). Confocal images representing vinculin (green) and actin (red) staining of GE β1 cells spreading on control homogenous (Ctrl) surfaces and 1000, 550 and 250 nm diameter fibres (from top to bottom). Scale bar 20 μm..110

Figure 3.12 GEβ3 cells spreading on nanofibrous patterns (after 24 hr). Confocal images representing vinculin (green) and actin (red) staining of GE β3 cells spreading on control homogenous (Ctrl) surfaces and 1000, 550 and 250 nm diameter fibres (from top to bottom). Scale bar 20 μm..111

Figure 4.1 Focal adhesion distributions. A, B and C: focal adhesion size distribution for the GE, GEβ1 and GEβ3 cells (respectively) on the different nanofibres size. Focal adhesion sizes are divided in three ranges: from 0 to 1 μm^2 for focal complexes, from 1 to 5 μm^2 for mature focal adhesion and from 5 to 40 μm^2 for fibrillar adhesion. D: total number of FA per cell for each condition. Ctrl is the homogenous control surface. Error bars are SE, $n = 3$, with n representing the number of experiments. For statistical test: *, $P < 0.05$; **, $P < 0.01$; ***, $P < 0.001$; ****, $P < 0.0001$. 119

Figure 4.2 Focal adhesion shape descriptors distribution (for the three focal adhesion size ranges) of the GE, GEβ1 and GEβ3 cells on the different nanofibres size: circularity (left) and aspect ratio (AR, right). Ctrl is the homogenous control surface. Error bars are SE, $n = 3$, with n representing the number of experiments. For statistical test: *, $P < 0.05$; **, $P < 0.01$; ***, $P < 0.001$; ****, $P < 0.0001$. 121

Figure 4.3 Focal adhesion intensity distribution of the GE, GEβ1 and GEβ3 cells on the different nanofibres size. Ctrl is the homogenous control surface. Error bars are SE, n =

3, with n representing the number of experiments. For statistical test: *, P < 0.05; **, P < 0.01; ***, P < 0.001; ****, P < 0.0001. 122

Figure 4.4 FRAP analysis for vinculin dynamics. Focal adhesions were selected at the cell edge and bleached to about 50% of the initial intensity. Vinculin recovery rate (A-*k*, s^{-1}) and immobile fraction (B) for cells seeded on homogenous surfaces (Ctrl) and patterned surfaces (550 and 1000 nm fibre diameter). The graph (C) shows typical recovery curves in the three conditions. Kymographs (D) of a sample focal adhesion for each condition during FRAP are also presented. 124

Figure 4.5 MEFvin$^-$/$^-$ cells transfected or not with the specific plasmid (vinculin venus, T12 and 880). Cells were spreading on nanofibres (300, 500 and 1000 nm diameter) or on homogenous surfaces (Ctrl) for 24 hr. Cell area (A), circularity (B) and aspect ratio (C) data are shown in the graphs. Error bars are SE ($n \geq 3$, with n representing the number of experiments). For statistical test: **, P < 0.01; ***, P < 0.001; ****, P < 0.0001; *****P < 0.00001. (D). Representative epifluorescent images of non-transfected cells and cells expressing the three different plasmid and spreading on homogenous surfaces. Scale bar is 50 µm. 126

Figure 4.6 Epifluorescent images of MEFvin$^-$/$^-$ cells spreading on nanofibres at different diameters (300, 500 and 1000 nm) and on homogenous surfaces (Ctrl). Cells were transfected or not with the specific vinculin plasmid (green in the images, vinculin venus, T12 and 880) . The white arrows point at transfected cells. Scale bar is 50 µm. 128

Figure 4.7 Epifluorescent images of MEFvin$^-$/$^-$ cells spreading on nanofibres at different diameters (300, 500 and 1000 nm) and on homogenous surfaces (Ctrl) (lower magnification). Cells were transfected or not with the specific vinculin plasmid (green in the images, vinculin venus, T12 and 880). The white arrows point at transfected cells. Scale bar is 100 µm. 129

Figure 5.1 Example of cell with low/ high chirality and convexity. 137

Figure 5.2 GEβ3 cells. Confocal images of the actin cytoskeleton (grey scale image on the left, scale bar is 10 µm) of cells spreading on nanofibres (1000 nm diameter) and homogenous surfaces (Ctrl) were analysed with a MatLab code to extract actin fibres measurements. On the right there are examples of maps extracted from the code: intensity of the F-actin, actin fibres identified (intensity map) and fibre direction. Axis units for the maps are pixels: 1µm = 0.19 pixel. 139

Figure 5.3 Actin fibres characterization for GE, GEβ1 and GEβ3 cells seeded on control and nanofibres (250, 550 and 1000 nm diameter). From confocal images after 24 hr spreading. Apparent thickness, length, convexity and chirality were measured from confocal images. Error bars are SE, n = 3, with n representing the number of experiments. For statistical test: *, P < 0.05; **, P < 0.01; ***, P < 0.001; ****, P < 0.0001. Comparisons are with the control surface for each cell type, unless differently specified. 140

Figure 5.4 Directionality map of actin stress fibres. Examples of directionality maps of actin stress fibres for GE, GEβ1 and GEβ3 cells seeded on control and nanofibres (250, 550 and 1000 nm diameter). Maps were extracted from confocal images of actin staining after 24 hr cell spreading. For angular direction: dark blue indicates direction toward the left of the paper (0°C), red indicates the opposite direction, toward right (180 °C) and yellow green indicates the up-down direction (90 °C). 141

Figure 5.5 Confocal images of the actin cytoskeleton. GEβ1 and GEβ3 cells spreading on nanofibres (250, 550 and 1000 nm diameter) and homogenous surfaces (Ctrl) at different time points. Scale bar is 20 µm. 142

Figure 5.6 Cell cytoskeleton analysis from confocal images acquired over a period of 150 min (every 1 min). Cell area change (A and B), cell trajectories (C and D) and velocity (E and F) of GEβ3 (left) and GEβ1 (right) cells spreading on 250, 500 and 1000 nm nanofibres and homogenous substrates (Ctrl). Area change graph (arbitrary units), the error bar are SD. Velocity error bars are SE. 144

Figure 5.7 Cell protrusion dynamics. A. Example of protrusion dynamics for GEβ1 (right) and GEβ3 (left) cells seeded on homogenous and nanofibres (1000, 500 and 250 nm fibre diameter). Velocity is measured by following the movement over time of the cell edge at a certain angle respect to the cell centre of mass. B. Kymographs from confocal images showing the evolution over time(y axis) of cell edge at a certain angle with respect of the cell centre. Scale bar is 10 µm. C. Data for cell edge velocity. Average velocity (<v>), max velocity (Vmax) of the cell edge and total distance travelled by the cell edge (average of 5 cells) are represented in graph C. Total distance is measured summing all the distances travelled for each time point. 145

Figure 5.8 GEβ3 cells. Confocal images of actin cytoskeleton dynamics (at different time points) for cells spreading on homogenous (Ctrl) and nanofibres (1000, 500 and 250 nm fibre diameter). Red arrows show fibre assembly and disassembly and blue arrows point at actin foci noticeable on patterned surfaces. Numbers in the images represent time in minutes. Scale bar is 20 µm. 147

Figure 5.9 GEβ1 cells. Confocal images of actin cytoskeleton dynamics (at different time points) for cells spreading on homogenous (Ctrl) and nanofibres (1000, 500 and 250 nm fibre diameter). Red arrows show fibre assembly and disassembly and blue arrows point at actin foci noticeable on patterned surfaces. Numbers in the images represent time in minutes. Scale bar is 20 µm. 148

Figure 5.10 Confocal images of actin cytoskeleton dynamics. Sudden edge retraction of GEβ1 and GEβ3 cells spreading on 500 and 1000 nm nanofibres. Number is each tiles represent time in minutes. Scale bar is 20 µm. 149

Figure 5.11 Example of actin fibres evolution over time of GEβ1 and GEβ3 cells (for one cell) spreading on homogenous and nanofibres (1000, 500 and 250 nm fibre diameter). Actin fibres were analysed via a MatLab from confocal images taking during 2 hr period time. Parameters analysed were apparent fibre thickness and length, chirality and convexity. 151

Figure 5.12 Colocaliation experiments myosin II/ actin and α-actinin/actin. Representative confocal images for GEβ1 and GEβ3 cells seeded on 250, 550 and 1000 nm nanofibres and homogenous control surfaces for 24 hr and stained for actin (magenta) and either myosin II or α-actinin (green). Scale bar is 20 µm. 153

Figure 5.13 Colocalization analysis. Pearson's coefficient of α-actinin/ actin and myosin II/ actin colocalization measured for GEβ1 and GEβ3 cells seeded on 250, 550 and 1000 nm nanofibres and homogenous control surfaces. Error bars are SE (n = 10-15, where n is the number of cells analysed). 154

Figure 5.14 Cell area, density and shape (circularity and aspect ratio) of GEβ3 cells seeded on different nanofibres sizes (250, 550 and 1000 nm diameter) presenting two polymer brushes heights (10 and 30 nm). Error bars are SE, n = 3, with n representing the number of experiments. For statistical test: *, $P < 0.05$; **, $P < 0.01$; ***, $P < 0.001$; ****, $P < 0.0001$. Confocal representative images of GEβ3 cells spreading on the different nanofibres types (250, 550 and 1000 nm fibre diameter and 10 and 30 nm brush layer). Scale bar is 20 µm. 157

Figure 5.15 Geβ3 cells seeded on different nanofibres sizes (250, 550 and 1000 nm) and two brushes heights (10 and 30 nm) and treated or not with cytoskeleton inhibitors: Y-27632 (red) or Blebbistatin (light purple). Cells were allowed to spread for

24 hr and then treated with the proper inhibitor for 4 hr. Control samples were treated with DMSO (10 µM). Cell area, density and shape descriptors (circularity and aspect ratio) are shown in the graphs for the two inhibitors. Error bars are SE, n = 3, with n representing the number of experiments. For statistical test: *, $P < 0.05$; **, $P < 0.01$; ***, $P < 0.001$; ****, $P < 0.0001$. 159

Figure 5.16 Representative epifluorescent images for GEβ3 cells seeded on different nanofibres diameters (250, 550 and 1000 nm) and two brushes height (10 and 30 nm) and treated or not with cytoskeleton inhibitors: Y-27632 (second column) or Blebbistatin (third column). Scale bar is 100 µm. 161

Figure 5.17 Focal adhesion (vinculin staining)size distributions for the GEβ3 cells treated or not with the Y-27632 inhibitor and spreading on the different nanofibres diameters (250, 550 and 1000 nm) and brush height (10 or 30 nm). Ctrl is the homogenous control surface. Adhesion sizes were divided in three ranges: 0 to 1 µm^2, 1 to 5 and 5 to 40 µm^2. Error bars are SE, n = 3, with n representing the number of experiments. For statistical test: *, $P < 0.05$; **, $P < 0.01$; ***, $P < 0.001$; ****, $P < 0.0001$ 162

Figure 5.18 Focal adhesion size distributions for the GEβ3 cells treated or not with the Y-27632 inhibitor and spreading on the different nanofibres diameters (250, 550 and 1000 nm) and brush height (10 or 30 nm). Ctrl is the homogenous control surface. Adhesion sizes were divided in three ranges: 0 to 1 µm^2, 1 to 5 and 5 to 40 µm^2. Error bars are SE, n = 3, with n representing the number of experiments. For statistical test: *, $P < 0.05$; **, $P < 0.01$; ***, $P < 0.001$; ****, $P < 0.0001$. 163

Figure 5.19 Total number of FAs per cell for GEβ3 cells seeded on different nanofibres diameters (250, 550 and 1000 nm) and brush height (10 and 30 nm) and treated or not with the either Y-27632 or Blebbistatin. Ctrl is the homogenous control surface. Error bars are SE, n = 3, with n representing the number of experiments. For statistical test: *, $P < 0.05$; **, $P < 0.01$; ***, $P < 0.001$; ****, $P < 0.0001$. 164

Figure 5.20 Focal adhesion shape descriptor distributions of the GEβ3 cells on the different nanofibres diameters (250, 550 and 1000 nm) and brushes heights (10 and 30 nm) and treated with Y-27632: circularity (left) and aspect ratio (right). Ctrl is the homogenous control surface. Error bars are SE, n = 3, with n representing the number of experiments. For statistical test: *, $P < 0.05$; **, $P < 0.01$; ***, $P < 0.001$; ****, $P < 0.0001$ 166

Figure 5.21 Focal adhesion intensity distributions (vinculin marker) of the GEβ3 cells on the different nanofibres diameters (250, 550 and 1000 nm) and brushes height treated with either Y-27632 or Blebbistatin. Ctrl is the homogenous control surface. Error bars are SE, n = 3, with n representing the number of experiments. For statistical test: *, P < 0.05; **, P < 0.01; ***, P < 0.001; ****, P < 0.0001. 167

Figure 5.22 Confocal images of GEβ3 cells seeded on different nanofibre diameters (250, 550 and 1000 nm) and brush heights (10 and 30 nm) and treated or not with the cytoskeleton inhibitor Y- 27632 or Blebbistatin. Red is actin cytoskeleton and green is vinculin marker for FAs (for separate channel see Appendix 1). Scale bar is 20 µm. ..168

Figure A1.1 Focal adhesion shape descriptors distribution of the GEβ3 cells on the different nanofibres diameters (250, 550 and 1000 nm) and brushes height and treated with blebbistatin: circularity (left) and aspect ratio (right). Ctrl is the homogenous control surface. Error bars are SE, n = 3, with n representing the number of experiments. For statistical test: *, P < 0.05; **, P < 0.01; ***, P < 0.001; ****, P < 0.0001. For Chapter 5. 190

Figure A1.2 Confocal images of Geβ3 cells seeded on different nanofibres diamaters (250, 550 and 1000 nm) and brush heights (10 and 30 nm) and treated or not with the cytoskeleton inhibitor Y- 27632. Red is actin cytoskeleton and green is vinculin. Scale bar is 20 µm. For Chapter 5...191

Figure A1.3 Confocal images of Geβ3 cells seeded on different nanofibres diameters (250, 550 and 1000 nm) and brush heights (10 and 30 nm) and treated or not with the cytoskeleton inhibitor blebbistatin. Red is actin cytoskeleton and green is vinculin. Scale bar is 20 µm. For Chapter 5. 192

List of tables

Table 2.1 Conditions used for electrospinning of PMMA fibres and the corresponding fibre dimensions. In order in the table: PMMA concentration, molecular weight (Mw), ratio of CHCl3 to DMF, presence of salt, Humidity, Flow rate, Voltage, average fibre diameter (nm) and relative standard deviation. 68

Table 2.2 Annealing temperatures chosen for the fibre diameter of interest. 71

Table 2.3. Etching conditions tested on wafer and glass. W= gold coated silicon wafer (different fibre dimensions); G= 200/ 300 nm diameter fibres on gold coated glass slides. Etching via solution (1) – the more concentrated – led to over-etching for all the time tested; with solution (2) it was possible to obtain continuous nanofibres by optimizing the etching time. 74

Table A2.1 Statistical analysis for as spun fibre dimension starting from different PMMA concentration. For statistical test: *P < 0.05, **P < 0.01, ***P < 0.001, ****P < 0.0001 (corresponding to Fig. 2.7). 193

Table A2.2 Statistical analysis for gap area on 250, 550 and 800 nm nanofibres at low density. For statistical test: *P < 0.05, **P < 0.01, ***P < 0.001, ****P < 0.0001 (corresponding to Fig. 2.24). 193

Table A2.3 Statistical analysis for patterns roughness data before and after fibronectin deposition (Figure S6). For statistical test: *P < 0.05, **P < 0.01, ***P < 0.001, ****P < 0.0001. No differences can be noticed for this analysis (corresponding to Fig. 2.27). 193

Table A2.4 Statistical analysis for HaCaT cell area and relative ratio on low, medium and high density nanofibres. Ctrl is the homogenous surface. For statistical test: *P < 0.05, **P < 0.01, ***P < 0.001, ****P < 0.0001 (corresponding to Fig. 3.3). 194

Table A2.5 Statistical analysis for HaCaT cell shape descriptor (circularity and aspect ratio, AR) on low, medium and high density nanofibres. Ctrl is the homogenous surface. For statistical test: *P < 0.05, **P < 0.01, ***P < 0.001, ****P < 0.0001 (corresponding to Fig. 3.3). 194

Table A2.6 Statistical analysis for HaCaT cell density on different pattern type (circular or fibrous), size (250, 550 800 and 100 nm for fibrous, 300, 500 and 800 nm for circular) and density (low, medium and high). Ctrl is the homogenous surface. For statistical test: *P < 0.05, **P < 0.01, ***P < 0.001, ****P < 0.0001. No significant differences can be noticed for this analysis (corresponding to Fig. 3.4 and 3.7 C). 195

Table A2.7 Statistical analysis for HaCaT cell area and relative ratio on circular patterns. For statistical test: *P < 0.05, **P < 0.01, ***P < 0.001, ****P < 0.0001 (corresponding to Fig. 3.7 A). 196

Table A2.8 Statistical analysis for HaCaT cells shape descriptor seeded on circular patches (300, 500 and 800 nm diameter): circularity and aspect ratio. For statistical test: *P < 0.05, **P < 0.01, ***P < 0.001, ****P < 0.0001 (corresponding to Fig. 3.7 B). 196

Table A2.9 Statistical analysis for GE, GEβ1 and GEβ3 cell area and relative ratio on fibrous patterns with 250, 550 and 1000 nm diameters and control surfaces (Ctrl). For statistical test: *P < 0.05, **P < 0.01, ***P < 0.001, ****P < 0.0001 (corresponding to Fig. 3.9). 196

Table A2.10 Statistical analysis for GE cells shape descriptor (circularity and aspect ratio, AR) seeded on different nanofibres sizes (250, 550 and 1000nm fibre diameter) and control surfaces (Ctrl). For statistical test: *P < 0.05, **P < 0.01, ***P < 0.001, ****P < 0.0001 (corresponding to Fig. 3.9). 197

Table A2.11 . Statistical analysis for GE, GE β1 and GE β3 cells density on different fibrous pattern size (250, 550 and 1000 nm fibre diameter) and control surfaces (Ctrl). For statistical test: *P < 0.05, **P < 0.01, ***P < 0.001, ****P < 0.0001 (corresponding to Fig. 3.9 G). 197

Table A2.12 Statistical analysis for GE, GE β1 and GE β3 focal adhesion size distribution (for adhesion sizes between 1 to 5 μm^2) on fibrous patterns (250, 550 and 1000 nm) and homogenous surfaces (Ctrl). For statistical test: *P < 0.05, **P < 0.01, ***P < 0.001, ****P < 0.0001 (corresponding to Fig. 4.1). 197

Table A2.13 Statistical analysis for GE, GEβ1 and GEβ3 focal adhesion shape factors (circularity and aspect ratio, AR) distributions on fibrous patterns (250, 550 and 1000 nm) and homogenous surfaces (Ctrl) for adhesion sizes between 1 to 5 μm^2. For statistical test: *P < 0.05, **P < 0.01, ***P < 0.001, ****P < 0.0001 (corresponding to Fig. 4.2). 198

Table A2.14 Statistical analysis for GE, GEβ1 and GEβ3 focal adhesion mean grey value (binned depending on adhesion size, µm2) on fibrous patterns (250, 550 and 1000 nm) and homogenous surfaces (Ctrl). For statistical test: *P < 0.05, **P < 0.01, ***P < 0.001, ****P < 0.0001 (corresponding to Fig. 4.3). 198

Table A2.15 Statistical analysis for FRAP experiments on GEβ3 cells. Comparison of recovery rates (*k*, s^{-1}) and immobile fraction of cells seeded on 550 and 1000 nm nanofibres and homogenous surfaces (Ctrl). For statistical test: *P < 0.05, **P < 0.01, ***P < 0.001, ****P < 0.0001 (corresponding to Fig. 4.4). 198

Table A2.16 Statistical analysis for MEFvin^{-}/$^{-}$ cells spreading on homogenous surfaces (Ctrl) or different nanofibres size (300, 550 and 1000 nm) and being transfected (T) or not. Cell were transfected with vinculin venus, T12 and 880. For statistical test: *P < 0.05, **P < 0.01, ***P < 0.001, ****P < 0.0001 (corresponding to Fig. 4.5 A). 199

Table A2.17 Statistical analysis for MEFvin^{-}/$^{-}$ cells shape descriptor (circularity and aspect ratio – AR) on homogenous surfaces (Ctrl) or different nanofibres size (300, 550 and 1000 nm) and being transfected (T) or not. Cell were transfected with vinculin venus, T12 and 880. For statistical test: *P < 0.05, **P < 0.01, ***P < 0.001, ****P < 0.0001 (corresponding to Fig. 4.5 B). 200

Table A2.18 Statistical analysis for GE, GEβ1 and GEβ3 cells (and cross analysis between the different cell type) cytoskeleton parameters after immunostaining (apparent thickness and length, chirality and convexity). Cells were seeded on different nanofibres sizes and homogenous surfaces (Ctrl). For statistical test: *P < 0.05, **P < 0.01, ***P < 0.001, ****P < 0.0001 (corresponding to Fig. 5.3). 201

Table A2.19 Statistical analysis for GEβ1 and GEβ3 cells velocity on different nanofibres sizes (250, 500 and 1000 nm) and homogenous surfaces (Ctrl). For statistical test: *P < 0.05, **P < 0.01, ***P < 0.001, ****P < 0.0001 (corresponding to Fig. 5.6). 202

Table A2.20 Statistical analysis for GEβ3 cells spreading, density and shape descriptors (circularity and aspect ratio) on different nanofibres size (250, 550 and 1000 nm) and with brush height of either 10 or 30 nm. For statistical test: *P < 0.05, **P < 0.01, ***P < 0.001, ****P < 0.0001 (corresponding to Fig. 5.14). 202

Table A2.21 Statistical analysis for Geβ3 cells spreading on different nanofibres size (250, 550 or 1000 nm) and with brush height of either 10 or 30 nm and treated (+) or not (-) with either Y-27632 or Blebbistatin. For statistical test: *P < 0.05, **P < 0.01, ***P < 0.001, ****P < 0.0001 (corresponding to Fig. 5.15). 203

Table A2.22 Statistical analysis for Geβ3 cells density and shape descriptors (circularity and aspect ratio – AR) on different nanofibres size (250, 550 or 1000 nm) and with brush height of either 10 or 30 nm and treated (+) or not (-) with either Y-27632 or Blebbistatin. For statistical test: *P < 0.05, **P < 0.01, ***P < 0.001, ****P < 0.0001 (corresponding to Fig. 5.15). 204

Table A2.23 Statistical analysis for GE β3 focal adhesion size (0.2, 0.3 0.46 and 3.46 µm^2 adhesion sizes) distribution on different nanofibres size (250, 550 or 1000 nm) and with brush height of either 10 or 30 nm and treated (+) or not (-) with either Y-27632 or Blebbistatin. For statistical test: *P < 0.05, **P < 0.01, ***P < 0.001, ****P < 0.0001 (corresponding to Fig. 5.17 and 5.18). 205

Table A2.24 Statistical analysis for GE β3 total number of focal adhesion per cell seeded on different nanofibres size (250, 550 or 1000 nm) and with brush height of either 10 or 30 nm and treated (+) or not (-) with either Y-27632 or Blebbistatin. For statistical test: *P < 0.05, **P < 0.01, ***P < 0.001, ****P < 0.0001 (corresponding to Fig. 5.19). 206

Chapter 1.

Introduction

Cell adhesion to neighbours and to extracellular matrix (ECM, a complex network of proteins and polysaccharides secreted and assembled by cells) is essential to maintain tissue structure and mechanical integrity. These interactions are mediated by transmembrane cell-cell and cell-matrix adhesion molecules, providing a direct connection between neighbouring cells or ECM proteins and the cell cytoskeleton. Such molecular networks are not only fundamental to confer an architecture to cells and tissues (their shape, structure and mechanical strength), control the orientation and localisation of subcellular organelles and cell polarity, but also for signal transduction (Lutolf and Hubbell, 2005, Geiger et al., 2009, Vogel and Sheetz, 2006). The signals transduced from the exterior of the cell and the cytoplasm (as well as the nucleus) through a variety of pathways regulate cell behaviour and associated patterns of gene expression. In addition, an increasing number of reports provide evidence that physical properties of the cell micro-environment such as matrix rigidity, topography and geometry modulate biochemical cues mediated by these molecular networks. Understanding the detailed mechanism via which molecular interactions allow cells to sense such physical properties is essential to the design of artificial ECM and biomaterials for tissue engineering and regenerative medicine applications. This chapter will focus on our understanding of the mechanisms underlying the sensing of the physical cellular environment at the nanoscale, with an emphasis on integrin mediated processes. Molecular mechanisms controlling the formation of integrin-mediated adhesions and their anchorage to the cell cytoskeleton are presented as their understanding is essential to the study of cell response to nanoscale physical properties of matrices. The design and main fabrication strategies used to prepare important engineered matrices are then introduced. Understanding how nanoscale properties are controlled in such platforms is essential to discuss and identify mechanisms underlying cell sensing at this scale. Finally, the mechanisms that are known to regulate nanoscale sensing of matrix geometry, topography and mechanics, and how these parameters impact on cell phenotype are more specifically discussed.

1.1 Nanoscale architecture and dynamics of the cytoskeleton and integrin-mediated adhesions

The formation of cell adhesions, whether to natural extra-cellular matrix or to synthetic biomaterials, relies on the self-assembly of molecular complexes that are inherently structured at the nanoscale although often extending in size up to the microscale. These adhesions are often associated with nanoscale sensing of surface properties, although other mechanisms have also been highlighted. Hence understanding the molecular processes underlying cell adhesion, the architecture of relevant complexes and their dynamics is essential to understand the response of cells to nanoscale physico-chemical properties of biomaterials.

1.1.1 Focal adhesion structure and dynamics

The formation of focal adhesions and the nanoscale structure.

In many eukaryotic cells, adhesion to the ECM is occurring via transmembrane heterodimers of the integrin family, alongside binding of other cell membrane receptors such as members of the immunoglobulin superfamily, non-integrin collagen and laminin receptors, glycolipids, glycosaminoglycans and glycosylphosphatidylinositol-linked receptors (Alberts et al., 2002). The formation of integrin heterodimers results from the noncovalent association of two glycoprotein subunits α and β, which span the cell membrane and bind ECM molecules on the extra-cellular part of the integrin and other adhesion-associated proteins in the cytoplasmic part (Harburger and Calderwood, 2009). 18 α and 8 β subunits are known, which combine together creating 24 different types of integrins (Zent, 2010, Barczyk et al., 2010). The main types of ECM proteins include collagen, fibronectin and laminin which are selectively recognized by different integrin subunits. The α1β1, α2β1, α10β1 and α11β1 integrins are collagen receptors. The α3β1, α6β1, α6β4 and α7β1 integrins are specific for laminin; and α5β1, α8β1, αIIββ3 and the αvβ integrins are the major fibronectin receptors and bind to the RGD motif (Arg-Gly-Asp) (Zent, 2010). It is worth noting that the α subunit head predominantly defines ligand specificity, while the reorganization of sites on the β head allow for the formation of the heterodimer (Luo et al., 2007). Nonetheless, the specific α and β subunit pairing also defines the specificity of the ligand bound, and while some heterodimer have been found to recognize only one specific extracellular protein (like the α5β1 for fibronectin), others were found to recognize more than one ligand (like the αvβ3 for both fibronectin and vitronectin) (Charo et al., 1990, Wayner et al., 1991).

Integrins that bind to fibronectin, recognize a specific region of the protein that is the RGD motif. This is a short sequence containing only three amino acids (arginine-glycine-aspartic acid) and proteins containing it have proved to promote cell adhesion (Ruoslahti, 1996). However, RGD-binding integrins do not bind to all RGD-expressing ligands and this may be because the sequence is not readily available for integrin binding (Ruoslahti, 1996) or residues outside this sequence may provide more or less affinity and specificity (Takagi, 2004).

Integrins normally live in an inactive close conformation where the extracellular part (the head) is bent and close to the cell membrane (Zent, 2010). Once they adhere to the extracellular ligands, they are activated (the head separate from the cell membrane and the heterodimer “opens”) and cluster into nascent adhesions (Petit and Thiery, 2000). Integrins associate with a number of cytoplasmic proteins, which provide a structural link between the membrane receptors and the actin cytoskeleton and can act as signalling molecules. These complexes evolve at the plasma membrane as the number of molecules involved increases and the mechanical strength of the adhesion becomes stronger (Wolfenson H. et al., 2010, Roca-Cusachs et al., 2013). At early stages of this process, small (0.5-1 µm in diameter) transient "dot-like" contacts (the focal complexes) are formed (Bershadsky et al., 2006). These structures are localized at cell protrusions called lamellipodia resulting from the polymerisation of a dense actin gel, which arises at the front edge of migrating or spreading cells (Worth and Parsons, 2008). Some of these complexes evolve into mature, elongated structures known as focal contacts or focal adhesions (FAs, 3-10 µm) which couple with actin and sustain the assembly of actin filament bundles and associated molecules such as myosins (Choi et al., 2008, Zaidel-Bar et al., 2003). The early stages of these processes occur at two distinctly organized and dynamic structures, the lamella and lamellipodium. Lamellipodia are rapidly forming and retracting protrusions that probe the ECM (Ponti et al., 2004). Lamellae are connected to the actomyosin network (and associated forces) and adhesion sites and sustain the formation of more stable adhesions.

FAs not only provide a mechanical link between the ECM and the cytoskeleton, but also act as mechanosensors, at the top of signalling pathways regulating cell phenotype (Huang et al., 2009, Malmstrom et al., 2010, Biggs et al., 2009). At early stages of integrin clustering, a number of proteins are recruited at FAs, linking integrins and the cytoskeleton and falling into two distinct families: proteins that directly associate with integrins (talin, α-actinin and filamin) and those that bind indirectly (Zent, 2010). Amongst these proteins, those that also directly bind the cytoskeleton play an important role in the regulation of FA assembly, cell adhesion and migration. Proteins that indirectly bind to integrins, such as vinculin (which binds to talin) and other adaptor and regulatory proteins, as VASP (vasodilator-stimulated phosphoprotein), zyxin, paxillin, p130Cas, focal adhesion kinase (FAK) and integrin-linked kinase (ILK), sustain the formation and stability of actin stress fibres and regulate cross-talking and signalling with the aforementioned molecules (Petit and Thiery, 2000).

Given the complex collection of molecular processes involved in integrin-mediated cell adhesion, the nanoscale structure of adhesion sites and the dynamics of molecular processes involved are essential to understand cell adhesion and migration. Recently, advances in microscopy techniques such as super-resolution techniques photo-activated localization microscopy, PALM (Shroff et al., 2007, Kanchanawong et al., 2010), and stochastic optical reconstruction microscopy, STORM (Xu et al., 2012), Förster resonance energy transfer, FRET (Pasapera et al., 2010, Grashoff et al., 2010), total internal reflection fluorescence, TIRF (Berginski et al., 2011), transmission electron microscopy, TEM (Kim et al., 2010, Smith et al., 1997) and Electron Tomography (development of TEM where data are acquired at different angles to allow the reconstruction of a high resolution 3D image) (Patla et al., 2010), provided some insight into the nanoscale, molecular, structure of cell adhesions.

Combining fluorescent microscopy (and immuno-staining for FA-associated proteins such as paxillin) with cryo-electron tomography (an EM technique) enabled imaging of cell protrusions at higher resolution (Patla et al., 2010). An important disadvantage of electron microscopy techniques is the lack of specific information regarding the biochemical composition of the structures imaged. Hence correlated microscopy techniques are particularly attractive to combine the benefits of traditional fluorescence and confocal microscopy with higher resolution electron microscopy. Correlated cryo-electron tomography and fluorescent microscopy provided evidence for the different organisation and orientation of actin filaments in the core and periphery of FAs, with peripheral fibres being parallel to the long axis of the adhesion (Patla et al., 2010). Below actin bundles, at the cell membrane interface, small ring-shaped structures (20-30 nm diameter) were also observed, which generally aggregate into “islands” depending on the organization of interacting fibres. They are thought to contribute to the link between the cytoskeleton and the membrane because they also tightly associate with vinculin-rich regions.

Therefore, FAs display a multi-layered structure with nano-scale organization in the z-direction: the structure starts at the plasma membrane with integrins, followed by a layer of adapter proteins including vinculin (evidenced in this study using gold nanoparticles), followed by short fibres connected with the actin stress fibres. Using photoactivated localization microscopy (PALM) Shroff et al. (Shroff et al., 2007) provided strong evidence for the colocalization of proteins forming adhesions. α-actinin and vinculin partially overlap, with α-actinin being tightly associated to stress fibres while vinculin being apparently randomly distributed along adhesion sites. Paxillin and actin were not found to be spatially correlated, although some areas of clustering were observed. Overall, the architecture of FAs displays three layers (within 40 nm) separating the actin network from the cell membrane-associated plane at which the tails of integrin molecules are found (Figure 1.1) (Kanchanawong et al., 2010): a first “integrin signalling layer” comprising FAK and paxillin; a “force transduction layer” comprising talin and vinculin and a final “actin-regulatory layer” including zyxin, VASP and α-actinin. Such well-defined architecture possibly underlies how forces are transmitted from the ECM, through the cell membrane, up to the actin cytoskeleton.

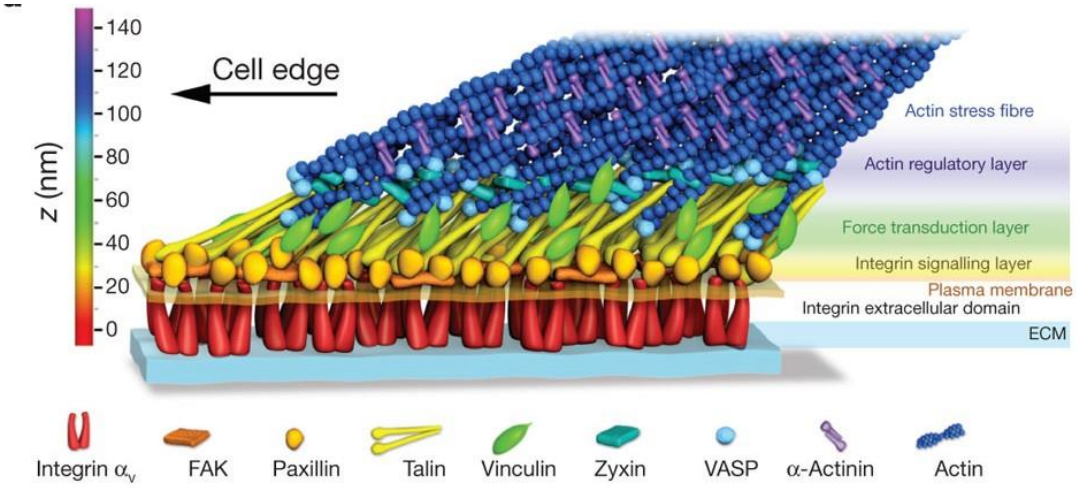

Figure 1.1 Focal adhesion architecture. There are three main layers identified in focal adhesion architecture: "integrin signalling layer" comprising FAK and paxillin (yellow); a "force transduction layer" comprising talin and vinculin (green) and a final "actin-regulatory layer" including zyxin, VASP and α-actinin (blue). The proteins represented are the main components of FA. Adapted by permission from Macmillan Publishers Ltd: Nature (Kanchanawong et al., 2010), copyright (2010).

Focal adhesion structure and dynamics (assembly, disassembly and turnover) is of fundamental importance for the reorganization of adhesive contacts and during cell migration. During these processes, new adhesions are formed at the front edge of the cell, mature and couple to the cytoskeleton and disassemble at the rear edge of the cell, associated with retraction fibres. The correct orchestration of the dynamics of these processes is essential to maintain cell spreading and control cell locomotion. Increasing evidence also identifies that FAs and their dynamics play essential roles in the sensing of nanoscale physical properties of the microenvironment.

Dynamics of focal adhesions

The structure of FAs must be tightly connected to the function that each molecule of the adhesome (the ensemble of molecules forming FAs) performs, in order to confer mechanical coupling. In addition, such structure and the localisation of associated proteins are inherently dynamic. Sensing of the extracellular environment, recruiting and release of molecules (turnover) and generation of the tension at the adhesion sites play important roles in controlling the mechanical coupling between the cell cytoskeleton and the ECM.

There are a number of adaptor proteins that do not function as a link with the cytoskeleton, but are signalling proteins: kinases (such as FAK, MAPKs, Fyn, Src and ILK) and GTPases (Rap1, Rho, Rac) which contribute to FA maturation and cell motility (Moore et al., 2010). Dissecting the function and dynamics of FAs and associated proteins is perhaps better understood by reconstructing the path of signals transduction, starting from ECM binding and integrin activation and moving upward through the architecture of FAs, the recruitment of key proteins and force generation.

Integrin activation and recruitment. Two main mechanisms have been proposed for integrin activation: outside-in by sensing and binding ECM molecules and inside-out by recruiting talin and other adapter proteins (Shattil et al., 2010). Integrins can be activated via the binding to ECM proteins when these have a fibrillar conformation with critic sites exposed (like RGD). On the other hand, integrins are required for fibrillogenesis as they “apply” mechanical tension to stretch ECM proteins and expose cryptic sites (Klotzsch et al., 2009). Via this bidirectional work, the disclosure of other binding sites on ECM proteins is possible and this promotes further integrin adhesion and enhance their function (Salmeron-Sanchez et al., 2011, Vanterpool et al., 2014).

Integrins themselves lack enzymatic activity (Zent, 2010), so they have to rely on other adaptor molecules and signalling proteins to achieve such function . In outside-in signalling, signals are transmitted through the integrin to the inner of the cell after integrin structure remodelling, due to ligand binding to the extracellular domain: this remodelling allows for integrin clustering and other molecules attachment which will then allow intracellular signalling (Giancotti and Ruoslahti, 1999).

As previously mentioned, integrins can also be activated from the inside of the cells (inside –out signalling). Many proteins regulate integrin activation, such as talins, kindlinds, filamins, migfilin, FAK and ILK. Talins and kindlins directly bind the β cytoplasmic tail and have been shown to be fundamental for the separation of the cytoplasmic tails, which are close to each other in the inactive state, leading to integrin activation (Luo et al., 2007). Talin disrupts the α - β cytoplasmic tails "bridge" destabilizing the electrostatic and hydrophobic interactions between them and so pulling them apart as well as the trans membrane segments, leading to integrin activation. Talin also plays a key role in inside-out integrin activation by binding integrin cytoplasmic tail to the actin cytoskeleton and it has binding sites for other proteins, such as vinculin, paxillin, α-actinin and tensin, that are recruited in order to strengthen that binding (Arnaout et al., 2007). Kindlins also bind the cytoplasmic tail, facilitating talin function.

When adhering to the ECM, integrins form clusters (proposed to be composed of 3-4 molecules), or nascent adhesions (Wiseman et al., 2004). Furthermore, these clusters are more stable in the central part of the cell while they are moving faster in areas of protrusion formation and retraction. FAs are also more dynamic in areas close to the leading edge where they probe the ECM and are coupled to membrane activity and actin retrograde flow (Schwingel and Bastmeyer, 2013, Shroff et al., 2008, Berginski et al., 2011, Gardel et al., 2008).

Different integrins were found to accomplish different adhesive roles (Roca-Cusachs et al., 2009). $\alpha_5\beta_1$ is required to strengthen adhesion to fibronectin, while mechanotransduction is controlled by $\alpha_v\beta_3$. Similarly, $\alpha_5\beta_1$ integrins are found in nascent adhesions at cell protrusions, independently of myosin-II activity, whilst α_v-class of integrins promote the formation of mature FAs mediating mechanosensing (Fig. 1.2) (Schiller et al., 2013). Furthermore, β_1 is stationary inside FAs (which could be connected to their role in strengthening the adhesion) while β_3 undergoes a rearward motion (Rossier et al., 2012). Hence, the association of these two classes of heterodimers to the actin cytoskeleton appears to be different. In contrast, in a separate study, β_3 integrins were found predominantly at the initiation of FA assembly, and β_1 was involved in mature adhesions (Roca-Cusachs et al., 2013). Hence the synergistic effects of these two integrins allows FA maturation, but the mechanism underlying such processes is not clear as both integrin heterodimers are able to bind a wide range of adapter proteins.

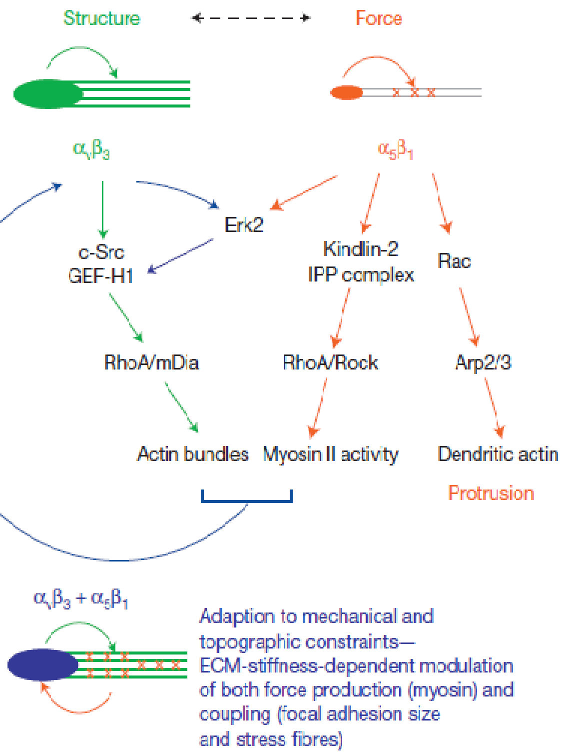

Figure 1.2 Differential integrin signalling pathways. Integrin heterodimers $\alpha_5\beta_1$ and $\alpha_v\beta_3$ differentially regulate myosin II-based contractility in sensing the mechanics of the ECM. They cooperate synergistically with the α_v (green) having a structural role and the α_5 (orange) a force generation role. The arrows indicate the different pathways activated and the molecules involved: signalling proteins like Rac, RhoA, Rock, kindling and actin associated protein like mDia and Arp2/3 differently modulate the process. Adapted by permission from Macmillan Publishers Ltd: Nat Cell Bio (Schiller et al., 2013), copyright (2012).

Recruitment of adapter proteins. Moving up along the structure connecting the ECM to the cell cytoskeleton, several adapter proteins directly or indirectly bind integrins. In this respect, α-actinin plays a dual role as adaptor protein, due to its direct binding to integrins, and as crosslinker molecule for actin (Roca-Cusachs et al., 2013). Furthermore α-actinin competes with talin in binding β_3 integrins (talin binds first and is then replaced by α -actinin to allow force transmission), while they cooperate in binding β_1 (Roca-Cusachs et al., 2013). Talin plays an important role in inside-out integrin activation by connecting the integrin cytoplasmic tail to the actin cytoskeleton and presenting binding sites for other proteins, such as vinculin, paxillin, α-actinin and tensin, which are recruited in order to strengthen that binding. Talin exists in a closed conformation and needs to be activated to enable vinculin binding (Lee et al., 2013b).

Its depletion is found not to influence initial cell spreading but to impair adhesion maturation and the generation of forces (Zhang et al., 2008).

Vinculin is a widely studied adapter protein, due to its role as a mechanotransducer. It is found in the cytoplasm but associates to FAs after opening of its conformation and activation (Bakolitsa et al., 2004). Vinculin couples to talin in a force dependent manner as mechanical stretching of talin exposes cryptic binding sites (del Rio et al., 2009). Mechanical forces generated via actomyosin contractility activate vinculin molecules (Dumbauld D.W. et al., 2013) and increase their binding to other adapter proteins such as talin or α-actinin. However, the relationship between vinculin recruitment, FA size and force generation is emerging as more complex. Not only is the recruitment of vinculin to FAs dependent on force transmission, but the stabilization of FAs is also reinforced when recruited vinculin molecules are under tension (Grashoff et al., 2010). Of critical importance is the understanding of vinculin activation and the role of the different domains of the molecule. For the formation of FAs, vinculin has to bind talin as well as the cytoskeleton, processes that are controlled by distinct domains. Vinculin molecules lacking the tail domain colocalize with integrins (β_1) (Humphries et al., 2007), controlling the number and distribution of integrin complexes (Dumbauld D.W. et al., 2013), and contribute to the formation of large FAs, colocalizing with talin and paxillin. The tail of vinculin forms a link with the actin network (Figure 1.3) (Thievessen et al., 2013) and does not colocalize with paxillin. Therefore, the head and tail domains of vinculin regulate distinct functions, where the head interacts with integrins and talin, and the tail sustains force transmission via linking to the actin cytoskeleton. The molecular interactions that these two domains regulate directly control the nanoscale spatial segregation of vinculin within FAs. In addition, a combination of superresolution microscopy and FRET biosensor highlighted that vinculin localisation shifts upwards, away from the cell membrane, during FA maturation. This reorganisation contributes to the mechanical strengthening of FAs (Case et al., 2015). In addition, vinculin was found to orchestrate the dynamics of other FA proteins, either directly (α-actinin, talin, VASP, vinexins, ponsin, Arp2/3, paxillin and actin) or indirectly (zyxin, FAK, p130Cas, ILK, parvin, tensin), through a force-mediated mechanism (Carisey et al., 2013).

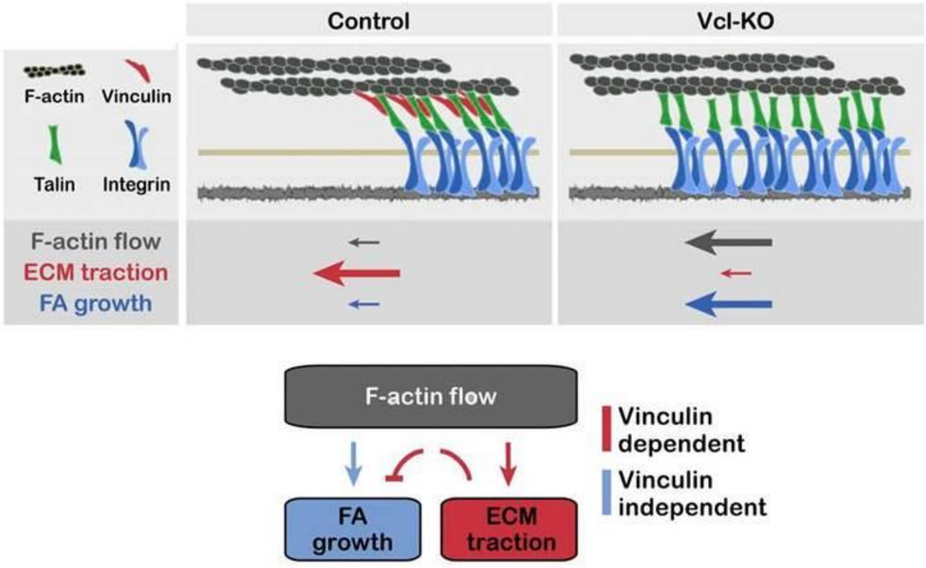

Figure 1.3 Vinculin regulation of FA maturation. Experiments with cells presenting a full active vinculin or vinculin knock- out show that vinculin affects F-actin flow velocity and FA growth rate. The presence of this molecule decreases the F-actin flow. Reproduced from Thievessen et al. 2013 originally published in J. Cell Biol. doi: 10.1083/jcb.201303129 (Thievessen et al., 2013).

Dynamics of FA-associated proteins. High resolution techniques such as TIRF and PALM have helped resolving the dynamics of FAs. Adhesions born at the cell edge normally present faster kinetics and play a role in probing the ECM (Figure 1.4). Adhesion complexes life cycle is generally constituted of different phases: formation, elongation, stabilization and merging with other adhesions, followed by disassembly at the rear of migrating cells or upon local disassembly of the actin network (Shroff et al., 2008). The study of paxillin flow in NIH 3T3 fibroblasts identified that adhesions arise in areas less than 5 µm from the cell edge and disassemble closer to the cell centre (Berginski et al., 2011). Adhesion complexes forming close to the cell edge were also spotted in Chinese hamster ovary (CHO). Paxillin turnover in these cells is around 60 s. Diffusion rates during disassembly are generally lower (0.02 ± 0.014 min^{-1}) than assembly (0.031 ± 0.023 min^{-1}). Similar rates were found for FAK dynamics although sizes of FAs observed were different for these two proteins (Berginski et al., 2011). α-Actinin is found in clusters with $\alpha_5\beta_1$ integrins and the two flow together during the life cycle of the adhesion, but during disassembly α-actinin follows actin retrograde flow dynamics (Wiseman et al., 2004), suggesting a distinct role during this phase of the adhesion life cycle. Disassembly rate of α_5 integrins was found to be 0.16 ± 0.02 min^{-1}: much faster than values found for paxillin. Similar turnover kinetics were also measured for other proteins in FAs (paxillin, vinculin, FAK and zyxin) (Choi et al., 2008).

The dynamics of proteins recruited at FAs was also reported to depend on adhesion size and stability (Le Devedec et al., 2012). Using simultaneous fluorescence loss in photobleaching (FLIP)-FRAP, the dynamics of recruitment of paxillin and FAK was quantified. FAK displayed a shorter residing time in FAs than paxillin, and size and strength of adhesions correlated with the recruitment dynamics of both proteins. With size increase, the rate of exchange of both proteins slows down while increasing adhesion strength gives rise to slower FAK turnover and the opposite happens for paxillin.

Hence, localization and recruitment of proteins is very dynamic and relies on several factors. This is also the case for force transmission. Using a tension sensor module based on fluorescence resonance energy transfer (FRET), forces exerted on vinculin molecules during FA assembly (when a maximum force is detected) and disassembly were studied (Grashoff et al., 2010). Forces were high at small adhesions forming at the leading edge and slightly decreased during size maturation. Finally, tension decreases rapidly during the retraction and disassembly stage. This highlights the dynamic nature of vinculin recruitment, and other FA-associated proteins, and force generation.

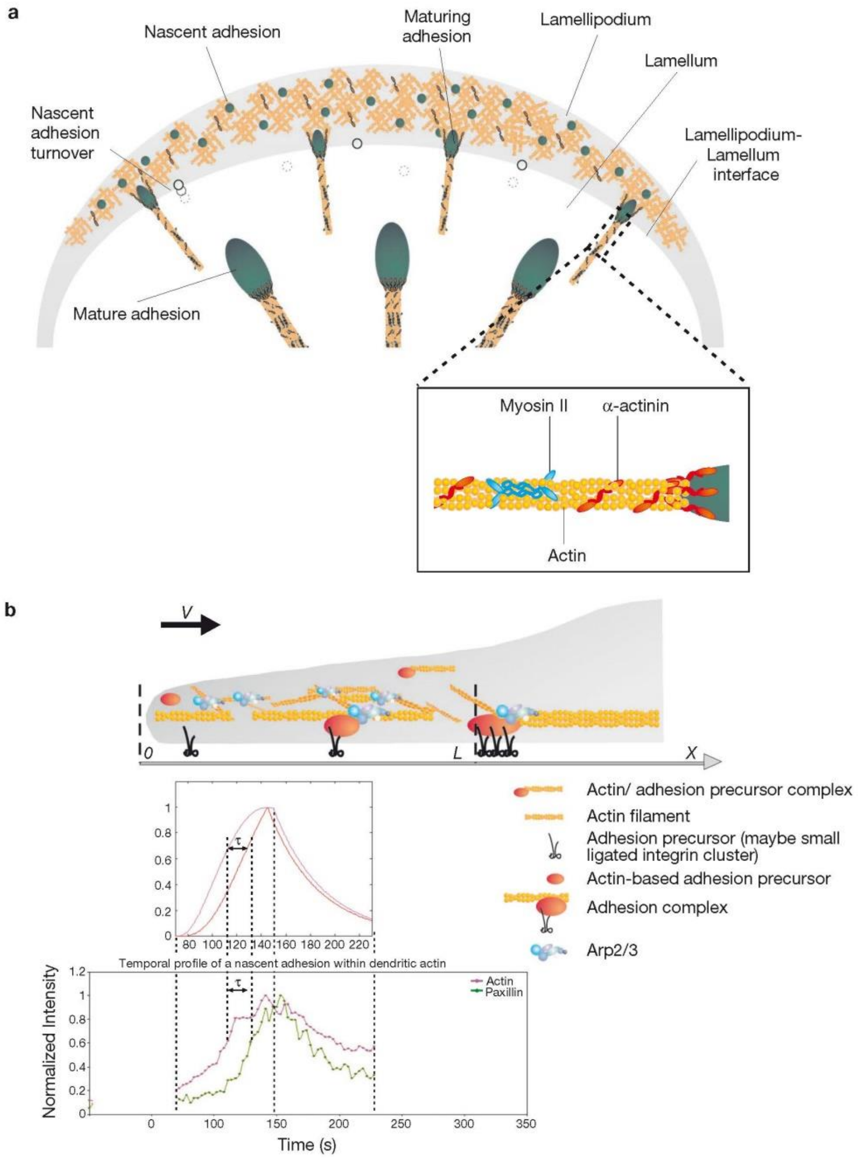

Figure 1.4 FA maturation. Schematic of adhesion assembly, turnover and maturation and their association with actin polymerization and myosin II activity. Nascent adhesions form in the lamellipodium, they move inward towards the lamella maturing and association with actin stress fibres, crosslinked by myosin II and α- actinin. In b a cell edge cross section is shown with the direction of the focal adhesion maturation velocity (v). X indicates the cell basal plane and point towards the cell centre. Adapted by permission from Macmillan Publishers Ltd: Nat Cell Bio (Choi et al., 2008), copyright (2008).

1.1.2 Actin structure and dynamics

Focal adhesion structure and dynamics are tightly connected to the cytoskeleton organization and its own dynamics. Following initial integrin activation and recruitment of proteins at the adhesion site, actin filaments couple to the nascent adhesion and allow the transmission of forces necessary for sustaining further membrane protrusion and adhesion maturation. During this phenomenon actin filaments are also assembled into thicker stress fibres, which in turn impact on cell structure and polarity.

Structure of the actin network

Considering the dimension of actin filaments (5-9 nm in diameter (Egelman, 1985)), super-resolution and electron microscopy techniques have proved particularly important to resolve the structure of the F-actin network. In cell protrusions, the cytoskeleton of fixed cells was found to be organized in two different layers, each 30-40 nm thick and separated by about 100 nm (Figure 1.5) (Xu et al., 2012). These two types of actin networks display distinct organisations of actin fibres, depending also on which type of adhesions they are coupled to. The dorsal layer looks more homogeneous with a mesh-like actin network organisation, whilst the ventral part also presents thick fibres originating from adhesion plaques. Disruption of myosin II activity perturbs the organization of the ventral actin bundles, resulting in a uniform mesh-like actin structure in both layers. In addition, the bundling of actin fibres enhances the mechanical properties of the network. Using optical tweezers, bundling forces in the range of 0.1 to 0.2 pN were measured, for the association of two filaments (Streichfuss et al., 2011). The bundling of several filaments generates relevant forces for the deformation of the cell membrane and, locally the ECM, sustained by myosin-based contractility (Grashoff et al., 2010). Forces near 1 pN were measured during actin polymerization of a small bundle of filaments (8), which is very close to the theoretical limit for a single actin filament growing (Footer et al., 2007). This could be explained considering that only the longest filament is actually interacting with the bead used in the optical trap assay of this study. Cells may also use other proteins/factors to generate higher forces and prevent actin from depolymerising. These forces are also similar to the measured average force across vinculin in stationary FAs (Grashoff et al., 2010). This highlights the importance of the geometry of force distribution on the ability of the actin cytoskeleton to sustain tension.

Bundles of 10- 30 actin filaments organise into so called stress fibres (Cramer et al., 1997, Pellegrin and Mellor, 2007, Naumanen et al., 2008), probably the most studied actin structure. Stress fibres have been divided into three main sub classes: ventral and dorsal stress fibres and transverse arcs. Ventral fibres are associated with focal adhesions on both ends and they are the major contractile machinery: they can also be found at cell protrusion (as described above (Xu et al., 2012)). Dorsal fibres are instead connected to FAs on one side only and grow up towards the upper cell end and they differ from other stress fibres because they do not contain myosin II and cannot thus contract (Tojkander et al., 2011). Dorsal arcs are parallel to the cell edge and do not contact with focal adhesions but dorsal stress fibres and move from the edge to the centre of the cell (Small et al., 1998, Hotulainen and Lappalainen, 2006).

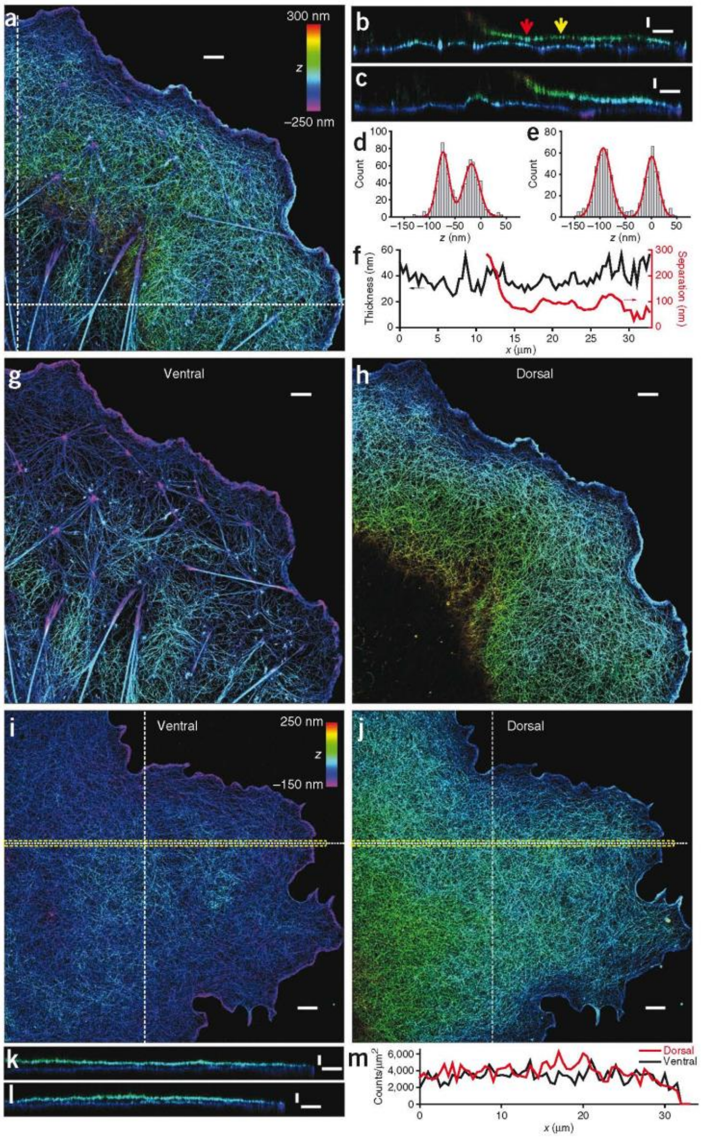

Figure 1.5 The F-actin cytoskeleton imaged via super-resolution microscopy. (a) Actin structure with vertical cross sections (b, c) along the dotted line and apparent thickness of the two layers (f) shown in b. Ventral and dorsal actin layer before (g, h) and after treatment with blebbistatin (i, j). Vertical cross section (k, l) of the dotted lines from i. Adapted by permission from Macmillan Publishers Ltd: Nature Methods (Xu et al., 2012), copyright (2012).

Dynamics of actin – binding proteins and myosin- based contractility

A number of proteins, such as formin, profilin, α-actinin, fascin and filamin, crosslink actin filaments, with associated effects on actin dynamics, controlling the rates of polymerization and depolymerisation, but also the structure and dimension of the networks of fibres formed. Actin dynamics is controlled by continuous actin polymerization regulated by a number of molecules such as formins, profilin or the Arp2/3 complex (Pollard et al., 2000). Other proteins such as cofilin increase the bending behaviour of actin filaments which in turns helps its disassembly (McCullough et al., 2008, Michelot et al., 2007). Furthermore the severing takes place at the boundaries of cofilin-decorated filament segments and depends on cofilin binding densities (Suarez C. et al., 2011). Proteins belonging to the formin family control actin dynamics (nucleation and elongation) upon association with profilin. Hence when tension is applied to anchored actin filaments, formin-controlled polymerization was slowed down in the absence of profilin, whilst an opposite trend was observed in its presence (Courtemanche et al., 2013). It was also demonstrated that formin enhances the elasticity of the actin network, above a certain concentration threshold, similarly to the impact of the bundling protein fascin, but in contrast to α-actinin and filamin (Esue et al., 2008).

A number of GTPases class proteins (Rho, rac and cdc42) regulates actin filaments formation and dynamics (Tojkander et al., 2012, Nobes and Hall, 1995, Hall, 1998, Tapon and Hall, 1997). The three different types of stress fibres introduced above were shown to have distinct formation pathways. Dorsal stress fibres are attached to one end to a focal adhesion and are generated through actin polymerization at this end. α-actinin 1, Rac1 and mDia1 formin were found to be required for their assembly (Kovac et al., 2013, Hotulainen and Lappalainen, 2006). Transverse arcs are instead generated from α- actinin crosslinked actin filaments nucleated by Arp2/3 complex and formin-nucleated myosin crosslinked actin filaments in the lamellipodium (Tojkander et al., 2012). They then connect with dorsal stress fibres and migrate towards the cell centre as cells move forward. Ventral stress fibres are instead formed by a combination of either two dorsal stress fibres that join together or dorsal stress fibres and transvers arcs. Actin polymerization and dynamics are dependent on force development and propagation and thus linked to actin contractility (Livne and Geiger, 2016).

Phosphorylation of the myosin light chain regulates actin stress fibres contractility and the Rho – ROCK (rho kinase) pathways are at the base of this regulation (Tojkander et al., 2012, Pellegrin and Mellor, 2007, Chrzanowska-Wodnicka and Burridge, 1996). Inhibiting myosin activity or the ROCK pathways would then prevent actin treadmilling leading to actin stress fibres dissociation and disassembly of focal adhesion (Endlich et al., 2007).

The crosslinking protein filamin connects the actin cytoskeleton and integrins, and was identified as an important adapter protein. It responds to the application of forces by increasing its binding affinity for the tail of β-integrin subunits (Ehrlicher et al., 2011). It is normally found in an autoinhibited state, as for the other adapter protein vinculin, and switches from a closed to an open conformation when under tension, thus increasing strongly its binding affinity (Rognoni et al., 2012).

Fascin is another actin-bundling protein, crosslinking actin filaments into parallel bundles at the end of stress fibres (Elkhatib et al., 2014), hindering the binding of myosin molecules. In fascin-depleted cells, focal adhesions are larger with thicker stress fibres. Moreover fascin unbinding was necessary for cofilin binding and severing for focal adhesion disassembly. Together with α-actinin, which also associates with stress fibres, fascin was also found to play a synergistic role in controlling actin biophysical properties (Tseng et al., 2005). Hence the mechanical response of actin filaments, after co-injection of the two proteins, was higher than that observed after injection of these two proteins independently. α-Actinin and fascin synergistically increase the stiffness of the cytoskeleton thus opposing to the rearward flow of actin at cell protrusions.

Protein dynamics within adhesions in the leading-edge lamella is strongly dependent on actin dynamics itself. Adhesion associated proteins (integrins, paxillin, zyxin and FAK) move slowly with a low coherency, integrins being the slowest, whilst actin binding protein (α-actinin, talin and vinculin) move faster and coherently (Hu et al., 2007). Differences between the dynamic behaviour of these proteins were highlighted and vinculin was found to be slower than talin but to move more coherently. In addition these proteins display a strong correlation with F-actin polymerisation, with α-actinin being the most tightly correlated protein. In contrast, zyxin, paxillin and FAK have little correlation with F-actin polymerisation. Together these results indicate that the dynamics of adhesion associated proteins is markedly different to that of actin-binding proteins in the lamella and highlight the potential role of such hierarchical organisation in force transmission.

Myosin is a molecular motor and interacts with F-actin to contract polymerized actin filaments by sliding two filaments in opposite directions. This protein itself can act as a powerful and direct force sensor (Laakso et al., 2008): it was evidenced, using an optical trap to manipulate single actin filaments, that even under very low load, myosin dramatically increased its binding affinity to actin, indicating an impressive sensitivity as mechanosensor. In addition, myosin can be recruited in FAs by activated Rac1 (Pasapera et al., 2015). Phosphorylation of one of the myosin IIA domains allows the maturation and turnover of FAs, enhancing cell migration.

Myosin II-based contractility influences adhesion assembly and dynamics, but its precise role is still debated. Adhesion formation, which occurs in the lamellipodium, is independent on myosin II activity, but is rather closely linked to actin polymerization and the speed of protrusion formation (Choi et al., 2008, Thievessen et al., 2013). Crosslinking of actin fibres mediated via myosin II and α-actinin, and associated contractility, promotes FA maturation: following α-actinin binding to elongating adhesions and coupling to the polymerised actin network, paxillin, talin, vinculin, tensin and myosin IIA are sequentially recruited. In this respect, α-actinin is a key protein responsible to couple actin fibre organization and FA development. In mouse embryonic fibroblasts adhering on fibronectin, engagement of β_1 integrin, talin and paxillin does not depend on myosin II contractility, whilst it does in the case of FAK, zyxin, vinculin and α-actinin (Pasapera et al., 2010). In addition, vinculin recruitment occurs via direct and indirect mechanisms as myosin II-dependent FAK activation in FAs enhanced the binding of vinculin, which in turn further increased vinculin binding to immature FAs.

Myosin II also influences the dissociation rate of proteins inside FAs (Wolfenson H. et al., 2010). Under myosin II inhibition, the rate of exchange of vinculin increased, whilst rates of paxillin and zyxin decreased. Considering first order kinetics for the molecular association/dissociation processes, the dissociation step is proposed to be the rate limiting step in focal adhesion turnover. A model accounting for such slow dissociation was proposed, involving the activation of new binding sites under mechanical tension, which would result in different kinetics for molecular association and dissociation, respectively, at least for a few important FA adapter proteins. Similarly, blocking myosin II contractility using the Rho-kinase inhibitor Y-27632 induced the release of proteins from FAs and a rapid disassembly (Lavelin et al., 2013). A few FA proteins were ranked in terms of their dissociation rate (measured via Fluorescence Recovery After Photobleaching, FRAP). VASP was found to be the fastest dissociating amongst the proteins tested, followed by zyxin, talin, paxillin, ILK, FAK, vinculin and kindlin. Models have been developed to explain how the asymmetry between association and dissociation, under mechanical control, is indeed connected to FA dynamics. Bruinsma et al presented a theoretical model capturing the impact of mechanical tension on the asymmetry between association and dissociation rates (Bruinsma, 2005). Their two state model describes the transition from initial adhesions, linked via a weak slip link to the cytoskeleton (passive state), to focal complexes (FC), which bear high forces and represent the active state. The switch from one state to the other is dependent on ECM mechanical properties. If the force applied for activating and reinforcing the adhesion site is lower than that required for its dissociation, a focal complex is formed. On the opposite, in the case of a soft substrate, the force applied to the adhesion is generally low and the adhesion will dissociate faster.

Not surprisingly, the influence of myosin on the regulation of the dynamics of FA-associated proteins and the actin network directly correlates with its role in mediating mechanical coupling to the ECM. Leea et al. demonstrated that actin binding switches from a catch type to a slip-like bond. Hence actin polymerisation displays a biphasic dependence in response to applied forces. The catch bond between actin repeat units and adhesions is strengthened by the application of mechanical forces, up to 20 pN, and decreases the lifetime of the slip region with further increase in tension (Lee et al., 2013a). Another important aspect of actin dynamics is the correlation between actin polymerisation, contractility of fibres formed and the generation of traction forces. F-actin polymerisation is correlated with the generation of traction forces according to a biphasic behaviour (Gardel et al., 2008). In small FAs in the lamellipodium small stresses correlate with fast F-actin polymerisation speeds. In the distal area, at the periphery of the lamella, and in the centre of large FAs, maximum traction stresses are generated and intermediate F-actin polymerisation speeds are measured. From central to proximal areas of large FAs slower polymerisation speeds and lower stresses are observed. Actin polymerisation speeds observed ranged from 0 to 30 nm/s with maximum stresses of 100 Pa. A switch between a strengthening and a weakening phase occurs at a threshold of actin polymerisation speed of 8-10 nm/s and is independent of protein density, stress quantity or stage of FA dynamics (Gardel et al., 2008, Han et al., 2015). Beyond the regulation of force generation, actin dynamics is also intrinsically directly regulating cell motility and linear correlations were identified between the rate of actin flow and the persistency of motile behaviour across multiple cell types (Maiuri et al., 2015).

Several numerical models have explored the very dynamic nature of the actin cytoskeleton and its relationship with FA formation. Loosli et al. (Loosli et al., 2010, Loosli et al., 2012) proposed a model connecting the growth of actin filaments and focal adhesion stabilization: the "length threshold maturation". This model is based on the observation of tangential and centripetal forces at the boundary between lamellum and lapellipodium. The actin bundles that form when adhesions are initiated grow perpendicular to the direction of the centripetal force applied. When a threshold in the actin bundle length is reached, adhesions mature into stable FAs and the forces are redirected tangentially, parallel to the lamellum- lamellipodium interface. By using micropatterns with different length of non-adhesive area, it was possible to determine an actin length threshold for different types of cells. Increasing the spacing on non-adhesive gaps from 2 to 6 µm leads to the formation of thick actin bundles between two separate adhesions and to their stabilization and maturation (Loosli et al., 2013). A computational model based on mechanical stressed applied to the actin network reproduces the behaviour of the dynamics of lamellipodia protrusion (Cardamone et al., 2011). In particular, the growth velocity of actin network was not found to depend on the external force applied, up to a "stalling" value, in agreement with experimental data (Shahapure et al., 2010, Prass et al., 2006, Parekh et al., 2005). In addition, the model predicted that reorientation of the filaments depends on the force exerted, within a range of 10^{-2} and 10^{-1} pN⁄nm.

Despite fantastic progress in the understanding of cell adhesion, the detailed temporal pattern according to which FA proteins are recruited and how this correlates with key activation steps and the establishment of actomyosin-based contractility, at the nanoscale remain elusive. The understanding of such processes clearly requires novel microscopy and molecular tools as well as engineered platforms.

1.2 Design of nanostructured platforms controlling cell adhesion and cell phenotype

The regulation of adhesion to the ECM is controlled by molecular processes that physically connect the matrix to the cell cytoskeleton via self-assembled protein complexes. In turn, cell adhesion to the ECM plays an important role in regulating important cell phenotypes such as proliferation, apoptosis, differentiation, endocytosis, motility, matrix degradation and remodelling. In addition, given the nature of the molecular events that translate matrix adhesion into biochemical signals, it is not surprising to find that processes controlling cellular sensing of the physical microenvironment rely on sensing of its nanoscale physical properties, such as nanoscale geometry, nano-topography and nanoscale mechanics. Importantly, it was demonstrated that these signals, although primarily determined by the biochemical context, depend on its geometry (Deeg et al., 2011, Rahmouni et al., 2013, Schvartzman et al., 2011), topography (Higgins et al., 2015, Pereza D.G. et al., 2015, Christopherson et al., 2009, Dalby et al., 2007) and mechanics (Engler et al., 2006, Trappmann et al., 2012, Wen et al., 2014). Engineered ECMs at the nanoscale have therefore attracted considerable attention recently, whether for the understanding of such nanoscale sensory events or for the design of scaffolds and cell culture platforms for regenerative medicine applications.

Thanks to advances in precise fabrication and engineering techniques such as electron-beam lithography, EBL (Kolodziej and Maynard, 2012), photolithography (Deeg et al., 2011, Rahmouni et al., 2013) and self- assembly (Salmeron-Sanchez et al., 2011, Yang et al., 2006)), it is now possible to create synthetic bio-interfaces with controlled physical properties at the nano- to micro-scale. These platforms aim to mimic some of the geometrical, topographical and mechanical properties of the cell micro-environment. These nano-structured substrates and matrices, functionalized with specific proteins or peptide sequences recognised by cell membrane receptors, have been utilised to control the phenotype of a wide range of cells, whether to study the underlying processes regulating such behaviours or for tissue engineering applications. In many cases, it has been established that such control of cell phenotype is mediated by the regulation of cell adhesion via processes such as integrin clustering, recruitment of associated proteins, maturation of nascent adhesions to FAs and their controlled disassembly. In turn, these processes result in the regulation of signalling pathways and cytoskeletal reorganisation directing cell phenotype.

To enable the development of such platforms, patterning methods have been widely used in the last few decades as they allow the fabrication of nano- to microstructured substrates with high accuracy, reproducibility and, in some cases, in large scale (Wood, 2007). These patterning processes allow the fabrication or reproduction (i.e. through a mask or master) of desired patterns on a substrate that can have 2D or 3D features. There are two main approaches to fabricate nanofeatures: in the top down approach, the bulk material is modified using processes controlled at the macroscopic level, whilst in the bottom up approach patterns are obtained by self-assembly of small building blocks. Depending on how the pattern is reproduced on the substrates, the patterning methods can also be divided into direct write, replicate and self-assembly. Here a brief introduction to the different techniques used to structure biomaterials at the nano-scale is presented, focusing on how their features allow the understanding or control of cell adhesion and associated phenotype (Nie and Kumacheva, 2008, Geissler and Xia, 2004, Yang et al., 2006, Gates et al., 2005, Zhang, 2003). A detailed discussion of the mechanisms via which cells sense these nano-scale properties will be the focused of the next section.

1.2.1 Geometrically patterned surfaces

The chemistry of the surface and how molecules are spaced and organized on a substrate affects cell behaviour. The functionalization of surfaces with patterning techniques has allowed the precise spacing at the molecular level of adhesion proteins and peptide sequences such as RGD (mimicking the adhesion properties of ECM proteins such as fibronectin), recognized by integrin heterodimers, and regulating cell adhesion and mechano-transduction. Thanks to these techniques it has been possible to understand at the molecular level some of the parameters controlling the very initial integrin recruitment steps in FA formation.

Self-assembly methods

Self- assembly techniques involve the organisation of small components (the building blocks) that interact to form larger, stable and potentially hierarchically organised objects (Geissler and Xia, 2004), this is thus a bottom- up approach. These structures can be used directly or as a mask in order to transfer the resulting pattern. One advantage of self-assembly techniques is that they allow the patterning of large area surfaces, suitable for biological studies that typically require high sample numbers.

Block copolymers are formed from at least two chemically distinct, and often immiscible, polymers covalently linked. The lack of miscibility of the two blocks is determined by their interaction parameters, according to Flory-Huggins theory and equations (Mai and Eisenberg, 2012). Unlike polymer blends that can fully demix into large, macro-scale phases, the covalent bond linking the two blocks frustrate their phase segregation and gives rise to a variety of nanoscale patterns or morphologies, depending on the chain length of the blocks, their chemistry and environmental conditions (temperature, solvent, pH) (Mai and Eisenberg, 2012, Klok and Lecommandoux, 2001, Bates, 1991, Steiner et al., 1994, Darling, 2007). In the biomedical field, block copolymers have been used as building blocks for micellar drug-delivery systems (Rosler et al., 2012), for the design of polymers for gene or drug delivery (Smart et al., 2008) and to functionalize surfaces for protein patterning and cell culture(Huang et al., 2009, Kumar and Hahm, 2005).

The work by Spatz and coworkers explored early stages of the integrin recruitment process using arrays of 5-10 nm gold clusters generated via block-copolymer micelle nanolithography (Figure 1.6 A) (Cavalcanti-Adam et al., 2006, Huang et al., 2009, Deeg et al., 2011). The dimension of each gold cluster adhesive site, functionalised with short peptide sequences such as RGDfK, allows the binding of only one cell membrane receptor (integrin). These adhesive sites are separated by a protein and cell resistant coating to ensure that membrane receptor binding is specific, with a controlled geometry. The spacing between adhesive sites, which can be tuned through the molecular design of the block-copolymer that formed the micellar array, can be defined readily, in the range of 20 to 250 nm. In addition, the level of order of the resulting array can also be adjusted, via the addition of free polymers of the same type as one of the block (e.g. polystyrene), resulting in the perturbation of the ordered lattice normally formed by the block copolymer micelles (Huang et al., 2009). This technique was further modified to obtain surfaces with simultaneous control of ligand spacing (local density) and global ligand density. This was achieved via micropatterning the nanopatterned surface to control the microscale geometry of adhesive sites independently of ligand spacing. To do so, the gold nanoclusters were removed selectively using photolithography (Deeg et al., 2011). To control simultaneously substrate mechanics and ligand spacing, PEG micropillar functionalised with gold cluster arrays were produced via microscope projection photolithography (Rahmouni et al., 2013). The nanocluster decorated pillars were generated using a layering approach in which the clusters, initially assembled on a slide are covalently bound to the hydrogel pillars during the photopatterning step and then simply transferred upon detachment of the substrate. Using this approach, the control of substrate stiffness and pillar geometry, each able to accommodate a mature FA, with a diameter of about 3.5 µm, was achieved.

Another self-assembly process that has been used to control cell adhesion and phenotype is the spontaneous assembly of fibronectin proteins into fibrillar nano-structures in contact with some polymer surfaces. Hence, whereas fibronectin molecules adsorb as relatively homogenous films onto poly(methyl acrylate) (PMA), presenting globular assemblies, fibronectin organised into nanofibrils (< 100 nm across) when interacting with poly(ethyl acrylate) (PEA) (Salmeron-Sanchez et al., 2011, Vanterpool et al., 2014, Gugutkov et al., 2009, Rico et al., 2009).

Similarly to the micellar self –assembly techniques, colloidal patterning consists of a solution of spheres that are deposited on a substrate to serve as mask or template for further processing (Figure 1.6 B). The solvent is then allowed to dewet or evaporate leaving spheres self-assembled into an array at the surface (Yang et al., 2006). The particles can either be tightly packed or more dispersed, depending on the starting colloidal concentration and deposition parameters. The resulting pattern can then be used directly or as a mask to protect areas of a substrate during subsequent steps. Hence in colloidal lithography (CL), the pattern resulting from the colloidal array is then transferred to the substrate via etching or physical vapour deposition.

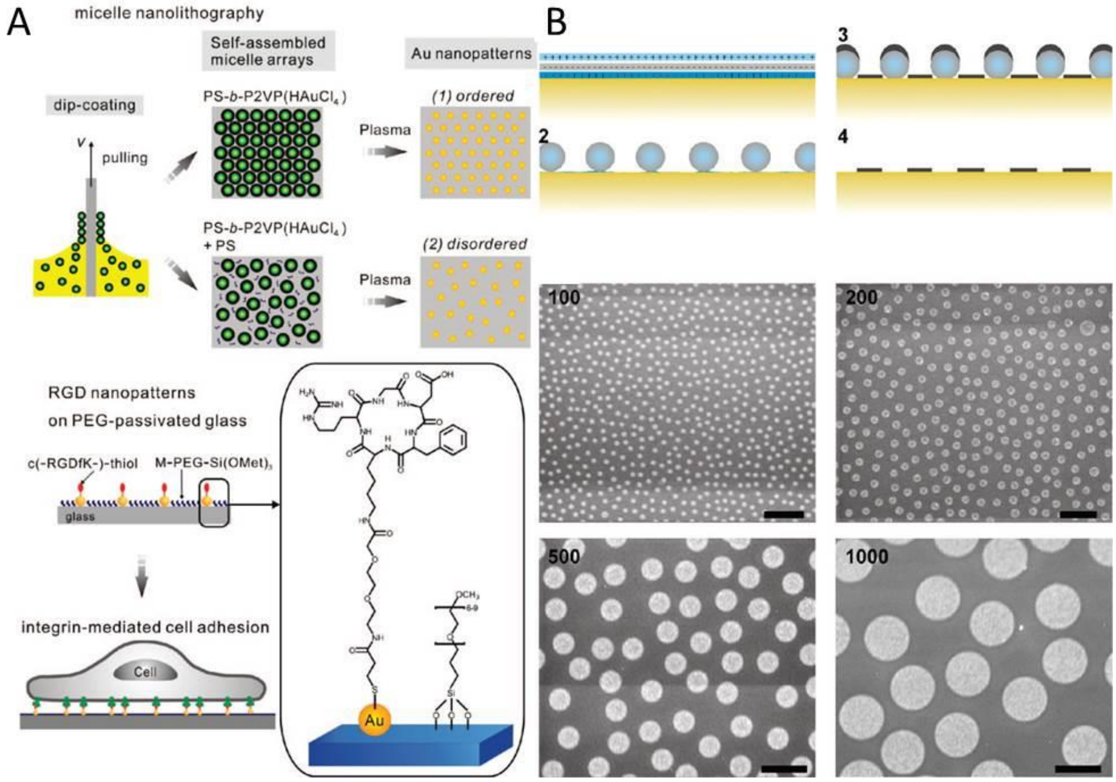

Figure 1.6 Patterning techniques. A: representation of the micelle nanolithography technique used to produce ordered and disordered gold nanosphere and their functionalization. Block co- polymer are used to tune the spacing between the micelles that contain the gold sphere. Micelles are then removed via plasma treatment and the gold nanoparticles left are functionalised with RGD peptide and the background is passivated with PEG. Adapted with permission from (Huang et al., 2009). Copyright (2009) American Chemical Society. B: colloidal lithography approach schematic (top) and SEM images of patterns with different sizes (bottom). Here colloids are deposited on a gold coated surface (1 and 2) and a layer of Si is then evaporated on top (3). Colloids are then removed leaving gold circles surrounded by Si (4). Adapted with permission from (Malmstrom et al., 2010). Copyright (2010) American Chemical Society

Using the CL approach, Sutherland and co-workers produced nanopatterned substrates presenting circular patches of gold surrounded by a SiO_2 or TiO_2 background. The patches display a short range order only and can be conveniently functionalized with fibronectin via simple incubation in a solution of this protein, after protection of the background with anti-adhesive poly(L-lysine)-graft-poly(ethylene glycol). The diameter of the patches generated using this approach ranged from 100 to 3000 nm (Malmstrom et al., 2010). The shape of the patterned objects that are obtained via CL is typically spherical, but other shapes, such as triangles, ellipsoids and hexagonal platelets have been successfully patterned too (Wood, 2007). Hence triangular and circular nanopatterns functionalized with fibronectin, with sizes ranging from 92 to 405 nm were generated via CL of polystyrene spheres (Slater et al., 2015). The spheres were removed after gold deposition. The patterns were also spaced from 177 nm to 1.534 µm, to allow the control of fibronectin density. The background was functionalised with a PEG silane to prevent uncontrolled cell attachment.

Replication methods

Replication methods include the use of a master (made through a direct writing method) which is used several times to reproduce the desired pattern (Geissler and Xia, 2004). The production of such masters is typically carried out via a lithography technique. The choice of the technique depends on the resolution and size of the features that are required. Photolithography is a commonly used replication technique to structure biomaterials. This process requires a mask, normally made of a transparent material (e.g. quartz), on which the desired pattern was previously designed. The target substrate is coated with a photoresist which contains a photosensitive element that is modified when irradiated (visible light, X-Ray or UV in the case of photolithography). When the substrate covered by the mask is exposed to those radiations, the photoresist generates either a positive or negative replica of the pattern above it. The modified or non-modified part of the photoresist is then removed and the pattern can in some cases be transferred to the substrate by either etching or deposition (del Campo and Arzt, 2008, Nie and Kumacheva, 2008). This technique has as main drawback the limitation of resolution by the wavelength used, in addition to other problems linked to photoresist and to the cost of the mask. Some people have implemented this method using immersion lithography in appropriate solutions to obtain up to 30 nm resolution features (Switkes and Rothschild, 2001).

Nanoimprint lithography (NIL), in conjunction with surface functionalization, was used to produce biomimetic arrays in which the position of single molecules or small clusters of molecules can be precisely controlled (Schvartzman et al., 2011, Cheng et al., 2013). Nanoimprint lithography is based on the use of a mould (normally produced by electron beam lithography, EBL) to imprint a thin polymer film. The resolution of the obtained patterns is determined by the feature size on the mask and the type of lithography used to generate such template (Hua et al., 2004). In Schvartzman et al. work the template, which was previously patterned via EBL, is reproduced on glass substrates by NIL on a PMMA film. The PMMA is then selectively removed from the surface via metal evaporation at an angle and etching of unprotected areas, leaving exposed areas onto which gold clusters can be deposited. The resulting gold clusters, with precise control of size and position on the substrate (determined at the EBL stage) are then functionalised with cyclic RGDfK and can only accommodate one integrin while the background is passivated to prevent cell adhesion.

Another technique belonging to replication methods is soft lithography. It relies on the use of a patterned elastomer (normally poly(dimethyl siloxane), PDMS), replicated from a master, to print small molecules or proteins onto a substrate (typically gold, silicon, glass or PDMS) (Geissler and Xia, 2004). The most widely employed of these techniques is micro contact printing (µCP), which normally uses PDMS stamps inked molecules to be transferred to the target substrate during conformal contact. Three main strategies have been developed to use µCP to control cell adhesion, with objects printed spanning four orders of magnitude, in the range of 100 nm (Coyer et al., 2007, Coyer et al., 2012) to 1000 µm. The first strategy relies on the direct printing of a protein/cell-resistant molecule. In the second approach an initiator molecule for surface initiated polymerisation is printed. Finally, the ECM protein itself can be printed before passivation of the background.

It is possible to directly deposit self-assembled monolayers of a protein and cell resistant molecules, which subsequently protect the printed areas from the adsorption of ECM molecules (Chen et al., 1998, Dike et al., 1999). Gallant et al. developed micropatterned self-assembled monolayers of thiols on gold, functionalized with adhesive and non-adhesive areas (Gallant et al., 2005). Microarrays of circular patches with diameters of 2, 5, 10, and 20 µm, spaced 75 µm, were produced to control cell adhesion and spreading depending on the adhesive area. Similarly, a technique based on µCP allowing the reproduction of a protein pattern at the nanoscale from a nanotemplate on an elastomeric surface was developed (Coyer et al., 2007). The method was used to generate adhesive nanoislands of fibronectin in a non-fouling background and study the dependence of FA assembly and force transmission. Nanoislands with controlled areas and density of ligand where prepared with this technique (Coyer et al., 2012). Alternatively, a second strategy consists in printing a monolayer of an initiator molecule from which polymer brushes can be generated via a controlled radical polymerisation process. The growth of ultra-protein resistant brushes, such as oligo(ethylene glycol) methacrylate and sulfobetain methacrylate brushes, allows the protection of patterned areas from protein adsorption, hence enabling the control of cell adhesion to well defined patterns, even during prolonged culture and in the presence of complex protein mixtures (Gautrot et al., 2010, Tan et al., 2013). Finally, it is possible to directly print the ECM protein before backfilling the non-printed areas with a protein and cell resistant molecule to prevent subsequent non-specific protein adsorption and uncontrolled cell adhesion (Théry et al., 2006).

Direct writing

Another approach for chemical patterning of 2D surfaces is the direct “writing” of patterns on a substrate (Nie and Kumacheva, 2008): in this case the pattern is literally "written" on the substrate by a lithographic tool in a serial process. This type of patterning can further be distinguished in direct writing with "ink" and without "ink". The former class includes techniques such as inkjet printing (IJP) and dip-pen nanolithography (DPN). The latter method uses an AFM tip to directly deliver chemical reagents on a specific area of the target substrate (Ginger et al., 2004) and has been very successful for patterning molecules and proteins for biological applications due to its high resolution. Arrays of protein patterns with features ranging from 100 to 350 nm and separated by an anti-fouling background were produced for cell adhesion assays (Lee et al., 2002a). Printing of collagen in 30-50 nm wide lines was also achieved with DPN: it was also possible to keep the structural organization of the biologically active molecule (Wilson et al., 2001). However, a drawback of these methods is their slow speed and throughput.

Methods not using inks are usually realized by rigid stylus, beam, electrical field and magnetic field (Geissler and Xia, 2004). A branch of these techniques realizes pattern using the tip of scanning probe microscopy (SPM) or atom force microscopy (AFM) to write patterns directly by scratching and indenting the surface (Pires et al., 2010).

1.2.2 Surface topography

Electrospinning

The control of cell behaviour simply via the design of the nano-topography of a surface is appealing as it avoids the requirement for chemical modification and has important implications for the design and processing of implants. Hence, a number of strategies to scaffolds with nano-scale features, displaying a range of sizes and morphologies, have been developed. Proteins in the extracellular matrix *in vivo* are often presented in the form of fibrils displaying defined diameters, but also a hierarchical structure, as in the case of collagen fibres. Collagen fibrils are naturally assembled into collagen fibres that ranges from about 20 to few hundreds nanometres (Woo et al., 2003). Electrospinning is an approach that has been widely exploited to reproduce a similar topography with polymeric materials, affording fibres with diameters ranging from a few tens of nanometres to a few microns (50 nm to 5 µm) (Shin et al., 2001). It has gained increasing attention thanks to the simplicity of the process and the accessibility of the equipment, the wide range of materials that can be “spun” and the dimensions obtained.

The electrospinning process is based on the application of an electric field to a flowing solution containing the polymer/material of interest. The electric field charges the liquid interface producing charge repulsion in the solution which competes with the surface tension resulting in a deformed “droplet” called the Taylor cone (Shin et al., 2001)**,** which shape depends on the equilibrium between electrostatic forces and surface tension. When the electrostatic repulsion overcomes the surface tension, a jet is generated from the Taylor cone which is then accelerated and "stretched" by the electrostatic forces, resulting in a decreased diameter (Teo and Ramakrishna, 2006)**.** The jet is then divided into multiple filaments with significantly smaller diameters, which stretch, bend and solidify into fibres. This behaviour is due to three instabilities that make the jet instable and start whipping (Shin et al., 2001): the Rayleigh instability due to surface tension changes, and two conductive instabilities, axisymmetric and whipping, regulated by electrostatic forces. During his journey to the collector, the jet stretches and bends and solidifies into fibres, thanks to the evaporation of the solvent, that deposit randomly onto the electrode.

This process is influenced by many factors, the effects of which are often difficult to isolate. Globally, the variables can be divided in solution properties (viscosity, conductivity and surface tension), processing conditions (flow rate, strength of the electric field and distance between the Taylor cone and the collector) and ambient parameters (temperature and humidity). These properties affect fibre shape and diameter (Deitzel et al., 2001, Fridrikh et al., 2003). Sizes obtained can go down to a few nanometers, with the smallest reported being close to 1 nm (Huang et al., 2006). Polymer concentration, and thus the viscosity of the solution, principally affects fibre diameter (Wnek et al., 2003, Sencadas et al., 2012). Increasing the conductivity of the solution, through the addition of salts, also allows the formation of smaller fibres: pyridine was used in formic acid to improve conductivity and it can conveniently be removed via evaporation (Huang et al., 2006). The flow rate also controls the diameter of fibres generated, resulting in narrower fibres at low flow rates (Fridrikh et al., 2003). A wide range of materials have been spun from polymers to metals to composites and hybrid materials (Greiner and Wendorff, 2007, Agarwal et al., 2009). A vast number of polymers have been used including natural (e.g. collagen, gelatin, cellulose, fibrinogen, silk and chitosan) and synthetic (PEO, PVA, PAA, PS, PET, PMMA, PVC, PE, PP) but also block copolymers (PLA-b-PEO, poly(lactide-*co*-glycolide)-*b*-PEO, PS-*b*-PP), metal (copper, iron, gold, and titanium), metal oxide and hybrid polymer/ metal oxide (zinc oxide, PEO/Au, PVP/Ag and PAN/Ag).

Lithographic and moulding approaches

Soft lithography has also been used to produce nanotopographic features. Nanogratings of 350 and 500 nm width and 350 nm depth were produced on poly(dimethylsiloxane) (PDMS) (Yim et al., 2010) via moulding from a nanoimprinted poly(methyl methacrylate) (PMMA)-coated Si master. Moulding allows the formation of patterns between the voids of a master substrate. Embossing is a related approach and recreates a relief on a substrate after application of mechanical stress (as well as softening of the materials for hot embossing) (Gadegaard et al., 2003, Dalby et al., 2004). Embossing was used to generate 500 nm features in materials such as tissue-culture polystyrene (TCPS), for example. Polymeric nanopillars with diameters ranging from 200 to 700 nm were fabricated using nanosphere lithography and nano-moulding (Kuo et al., 2014). Polystyrene nanospheres were used as a mask on silicon substrate to produce holes via etching. The patterned silicon is then used as a mask for a UV-curable polymer which is spin coated on top of the silicon, cured and peeled off to obtain an array of nanopillars with controlled diameters.

Fabrication of micro/sub-micro elastomeric pillars via moulding allows the production of systems with controlled topography (size and density of pillars) and mechanics: the apparent modulus of the materials is controlled by varying the diameter and height of the pillars (Yang et al., 2011). The pillars are obtained by producing a master via photolithographic methods and then using it as a mould to cast PDMS substrates (Trichet et al., 2012, Ghassemi et al., 2012, Fu et al., 2010). The top of the pillar is then selectively functionalised with a cell adhesive protein (typically fibronectin) to promote cell adhesion only at the top of the pillars. Spring constants obtained vary from 1 nN/µm to 1000 nN/µm.

Scanning Beam Lithography is another powerful fabrication method based on the "direct writing" of a programmed pattern into a substrate. The writing process is controlled by a focused beam of either electrons (Electron Beam Lithography - EBL) or ions (Focused Ion Beam - FIB) directed towards a resist (PMMA, ZEP, NEB31 and hydrogen silsesquioxane (HSQ)) (Gates et al., 2005). Normally the photoresist is exposed to the focused beam and the areas that were selectively exposed (or not exposed, depending on the type of resist) are removed by wet etching. This technique can generate patterns with resolution just below 10 nm, typically in the range of 10 nm to 1 mm for lateral dimensions (Kolodziej and Maynard, 2012). Biofunctional resist themselves can be used to generate the pattern directly (Kolodziej et al., 2012). However, the process is relatively slow and low throughput and the sample dimensions are restricted to small areas, typically below 1 cm^2. The resulting patterns can either directly be used as substrates for cell culture (Curtis et al., 2001, Christman et al., 2006) or as master for transfer of the patterns to a different material. Ion-beam and chemical etching have been used to create substrates with controlled texture at multiple scales. This technique was used to generate micropatterns on two semiconductor surfaces (Si and TiO_2) bearing areas with different nanoroughness (Pereza D.G. et al., 2015). The Si surfaces presented a pattern with 35 µm stripes and a root mean square roughness (R_{rms}) of 2.6 nm. The TiO_2 surface presented squares or stripes with 3 µm depth and R_{rms} of 1-4.5 nm, depending on the area.

1.3 Nanoscale sensing of the physical environment

The various techniques described in the previous section to control the nanoscale geometry, topography and mechanics of matrices have been applied to cell culture, for the control of cell phenotype. Cell adhesion plays an important part in mediating such cell-substrate interactions and sensing nanoscale physical properties of the matrix. Important questions that have been addressed by these studies to understand the role of such cues in directing cell phenotype will be discussed in this section. How do nanoscale physical properties control integrin clustering? How is the geometrical maturation of FAs and their ability to sustain tension coupled to nanoscale physical properties of the matrix? How is nano-scale topography sensed by cells, in a relatively homogenous biochemical context?

1.3.1 Geometrical control of integrin clustering

The control of integrin activation and clustering has attracted a noticeable interest from the research community, considering that this is the first step in the control of FA formation. The distance required for integrin heterodimers to cluster together and form nascent adhesions is an important parameter controlling the early stages of FA development. To control the clustering of cell membrane receptors, gold cluster arrays generated via block copolymer micelle nanolithography were used. Integrin clustering was controlled via the ligand density with a threshold of around 60 nm between two neighbouring ligands. Below this threshold, ligand densities allowed the formation of adhesions (Cavalcanti-Adam et al., 2006). On nanopatterns displaying greater inter-ligand distances, cells were unable to spread. This effect was not observed on disordered nanopatterns as the perturbed organisation of the clusters resulted in shorter inter-ligand distances locally (Figure 1.7) (Huang et al., 2009). In a further development, the effect of ligand density on a local (spacing between ligands at the nanoscale) and a global (micropatterned surfaces) scale was assessed to dissociate physical parameters controlling cell adhesion at different scales (Deeg et al., 2011). Cell response to the local density of ligands, rather than global density, was more pronounced, with FA maturation and cell adhesion strength being more effective when spacing between ligands was below 60 nm. Ligand spacing on the micropatterned surfaces was kept constant at around 60 nm and allowed higher cell spreading compared to unpatterned surfaces presenting higher inter-ligand spacing (74 and 120 nm), despite the fact that these surfaces presented a lower global particle density. These experiments indicate that a small number of sufficiently large FAs is sufficient to sustain cell spreading and that local ligand density and integrin clustering controls the formation of FAs.

In another study, nanocluster-functionalised hydrogel micropillars were used to quantify forces generated by adhesions recruiting different integrins (αvβ3 and α5β1 heterodimers) (Rahmouni et al., 2013). The latter were found to sustain greater maximum forces than the former during adhesion. Also, the ratio of zyxin to actin in FAs at the cell periphery is higher for α5β1, possibly indicating different mechanical roles for these two integrin heterodimers. This is consistent with observations made using a magnetic tweezers assay, which identified α5β1 as an important mediator able to sustain mechanical forces, whereas αvβ3 was found to play a role in mechanotransduction (Roca-Cusachs et al., 2009). However, such integrin specific response is also likely to be dependent on the expression level of the respective integrins and the abundance (and possibly affinity) of the ligands present in the matrix. Hence, engineered cell lines expressing αvβ3 and α5β1 integrins displayed similar abilities to exert traction forces, although their response to external cyclic strain and ability to respond to matrix stiffness was slightly more sensitive in the case of αvβ3 (Balcioglu H. E. et al., 2015).

To further probe the impact of clustering on the ability of cells to exert tension on their matrix, block copolymer micelle nanolithography was combined with molecular tension fluorescent microscopy, in which fluorophores quenched by the close proximity of gold clusters become activated when under tension (Liu et al., 2014). Tension was found to depend on ligand spacing and a threshold of 60-70 nm was found to be necessary for FA formation and tension development. In addition, this work highlighted a two-step adhesion process, in which initial tension at bound integrins is regulated first by F-actin polymerization, followed by the ligand spacing dependent and actomyosin-driven maturation of FAs and the increase of average tension per receptor (up to 6-8 pN per integrin). However, the generation of high traction forces relies on the increase of the number of integrins under tension, rather than a further increase in the tension per molecule. Using a similar technique, the force distribution inside FAs was studied (Morimatsu et al., 2013), and high tensions were observed at the cell periphery, colocalizing with paxillin. In addition, this FRET assay highlighted that various molecules involved in FA regulation, in particular a_vb_3 and paxillin, directly localise at high tension areas (Morimatsu et al., 2015).

In good agreement with these experiments and work carried out on micropillars, optical tweezers assays also provide evidence that traction forces generated at the leading cell edge are stronger than those generated closer to the cell body (Schwingel and Bastmeyer, 2013). The size of beads coated with RGD molecules and the ligand surface density both influenced force transmission, thus confirming the relationship between integrin recruitment and forces generated. A linear correlation was observed between traction forces and retrograde flow. In addition, cell migration was inversely correlated to tension, indicating enhanced migration when low forces are generated.

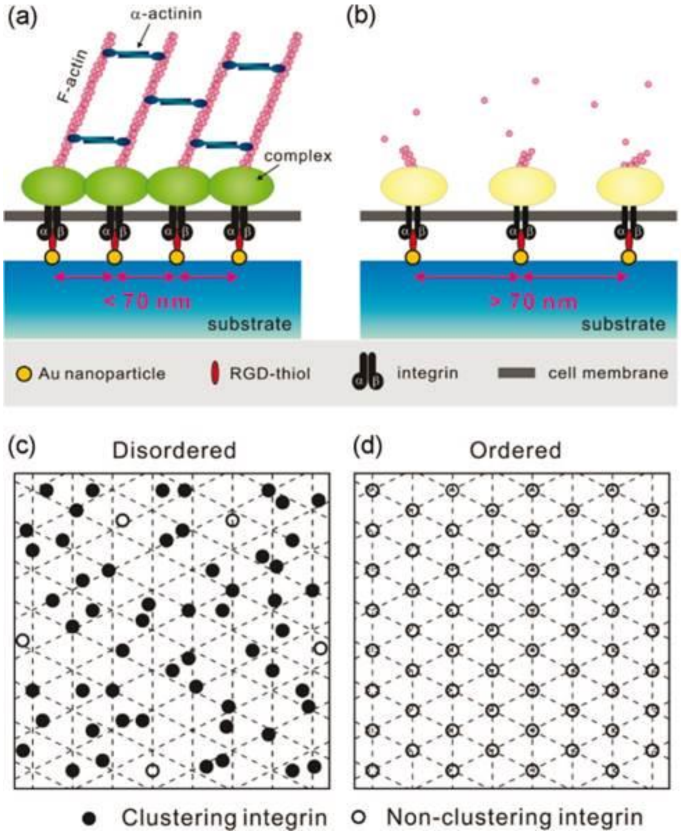

Figure 1.7 Effect of ordered and disordered nanopatterns on integrin clustering. Spacing RGDs further apart than 70 nm (b, d) prevents integrin clustering and FA maturation. Maturation is instead allowed on disordered patterns with similar spacing (a, c). Adapted with permission from (Huang et al., 2009). Copyright (2009) American Chemical Society.

A similar threshold for integrin clustering and cell spreading was measured for cells plated on substrates displaying gold clusters positioned in different geometries (arrays of 2-7 clusters separated by 50-60 nm, assembled in different shapes, spaced by 200 nm distances), and functionalised with RGD molecules (Schvartzman et al., 2011). Cell spreading was dependent on the size of the group of gold clusters (between 2-7). On hexagonal arrays composed of groups of 6 or 7 clusters, cells displayed maximum spreading, despite the large distance between groups (200 nm). On dimer and trimer arrays presenting the same distances between clusters (50-60 nm) and groups of clusters (200 nm), cells were instead struggling to adhere. In addition, it was observed that 4-5 gold clusters within each group was sufficient to sustain cell spreading. This behaviour may suggest that cluster density, rather than distance between ligands, controls cell adhesion. When the density of groups of 7 gold clusters was decreased to the level of the density of groups of 2-3 gold clusters (by increasing the spacing between larger groups up to 370 nm), cell adhesion was not perturbed. Together, these results indicate that clustering of integrins may only be required to occur at a local scale (4-5 integrins) and that cell adhesion may not require the formation of continuous domains of integrins over larger (micron) scales (Schvartzman et al., 2011). The question of whether such discontinuity in integrin clustering enables fully mature FAs to form remains open, but suggests that such adhesions are not based on continuous and homogenous protein assemblies, but rather rely on local clustering of associated proteins.

1.3.2 Geometrical control of FA maturation

Once integrins have been recruited, other molecules associate with growing adhesion sites, mediating coupling to the actin network and enabling the generation of tension and maturation of FAs. The size of adhesions is often used as a hallmark of fully mature FAs, but the relationship between protein recruitment, size or geometry and mechanical coupling is not clear. It is well established that, at the microscale, adhesive area allows integrin clustering, FA assembly and force transmission (Gallant et al., 2005). Adhesion strength increased exponentially with the number of recruited integrins and with increasing the adhesive area on micropatterned surfaces, up to a threshold where no further strengthening is seen. In turn this impacts on a variety of cell phenotypes such as polarity (Thery et al., 2006), cell division (Thery et al., 2005), differentiation (Connelly et al., 2010, McBeath et al., 2004, Kilian et al., 2010) and apoptosis (Chen et al., 1997). However, the geometry of the adhesive landscape rather than the total amount of ECM molecules was found to control cell adhesion. Hence cells are able to bridge across relatively large non-adhesive areas to sustain spreading, without compromising their phenotype (Tan et al., 2013). The size of adhesive patches was identified as a key parameter controlling such cell behaviour. Cells were unable to adhere to adhesive nanoislands with an area below a threshold of 0.11 µm^2, even though their total adhesive area remained unchanged (Coyer et al., 2012). This also correlated with adhesion strength, quantified via a rotating disk assay. Expression of the head domain of talin (binding the cytoplasmic tail of integrins) resulted in the formation of adhesions independently of the size of the adhesive patch. In contrast talin mutants unable to bind integrins did not alter cell spreading. This suggests that stabilisation of integrin clusters by the binding of talin is sufficient to compensate the lack of stability of nascent adhesions at nanopatterns. In addition, expression of the vinculin head domain stabilising integrin clustering, but not vinculin wild-type, resulted in the stabilisation of nascent adhesions even on the smallest nanopatterns. Interestingly, expression of the mutant VinT12 constitutively adopting an open conformation allowing the exposure of talin and actin binding sites (and therefore the transmission of tension) did not result in the stabilisation of adhesions. This suggests that nascent adhesions are unable to sustain mechanical shear forces resulting from actin treadmilling and myosin contractility, resulting in the disassembly of integrin clusters, unless stabilised by the binding of proteins allowing to decouple this phenomenon (as for the head domains of talin and vinculin). These results are in good agreement with studies of vinculin dynamics demonstrating that the head domain of vinculin stabilises adhesions in the absence of tension, but that the actin binding site of the vinculin tail is essential for mechanical sensing (Carisey et al., 2013). Hence, vinculin and talin appear to equally serve as key mediators of the sensing of nanoscale geometry.

The influence of adhesive area size on cell attachment and spreading was also studied via nanopatterned substrates prepared via colloidal lithography and presenting circular adhesive gold patches with diameters ranging from 100 to 1000 nm (Malmstrom et al., 2010). On the smallest patterns, cells can still adhere although weakly, but spreading is limited and only nascent adhesions can be observed. On 500 nm patterns, cell spreading is more evident with the formation of focal complexes and the presence of some actin fibres. On the largest patterns, elongated FAs are formed and connect to better structured and more mature actin fibres. In a further study, the influence of different protein coatings (fibronectin or vitronectin) was assessed on patches ranging from 100-3000 nm (Malmström et al., 2011). On larger patches cell spreading is higher on fibronectin coated patterns and gradually decreases for smaller patches, without any strong evidence for a specific area threshold. Although cells spreading on vitronectin displayed a similar behaviour, their spreading was not as restricted on 200nm patches as compared to cells spreading on fibronectin. Bridging of patches was observed with vinculin stainings on small patterns with vitronectin but not fibronectin and could explain this difference in nanoscale sensing. However, the involvement of different integrins in the binding of fibronectin and vitronectin patches ($\alpha5\beta1$ and $\alpha v\beta3$ respectively), and potentially their respective expression level in the cell type used in this study, could also account for the behaviours observed.

Other phenotypes such as cell motility were also found to be controlled by the nanoscale geometry of adhesions. Adhesion formation and maturation strongly influences migration dynamics and cells seeded on triangle and circular patterns of different sizes produced by colloidal lithography (Slater et al., 2015) formed many small adhesions and displayed enhanced motility on sub-100 nm patterns. On larger patterns (from 222 to 405 nm), adhesions were larger and fewer and cell migration speed decreased. Similarly, the adhesion and spreading of keratinocytes was found to be impaired on small (100-600 nm) adhesive patches, compared to large patterns (3 µm) or homogenous substrates (Figure 1.8) (Gautrot et al., 2014). In addition, this behaviour correlated with an increase in cell differentiation (expression of the cornified envelope protein involucrin) as cell spreading was impaired. Although the restriction of cell spreading was associated with a gradual deterioration of the actin cytoskeleton, the recruitment of key focal adhesion proteins (talin, vinculin, paxillin) and protein phosphorylation were not reduced on the smallest patches, in contrast with the study discussed above by Garcia and co-workers (Coyer et al., 2012). Cells were able to deposit laminin at the adhesive patches further suggesting that, from a biochemical point of view, adhesions formed on nanopatterns were relatively mature. A similar behaviour was observed for proteins associated with hemidesmosomes, a type of matrix adhesion sustained by α6β4 integrins (Sonnenberg et al., 1991), connecting the ECM to the keratin network and not thought to bear tension. However, the dynamics of vinculin binding was found to be faster on small (600 nm) patches, compared to large patches or homogenous substrates, and comparable to vinculin dynamics in cells treated with the myosin inhibitor blebbistatin. Hence these experiments suggest that altered protein dynamics result in uncoupling between adhesions and the actin cytoskeleton and impaired transmission of tension required for cell spreading.

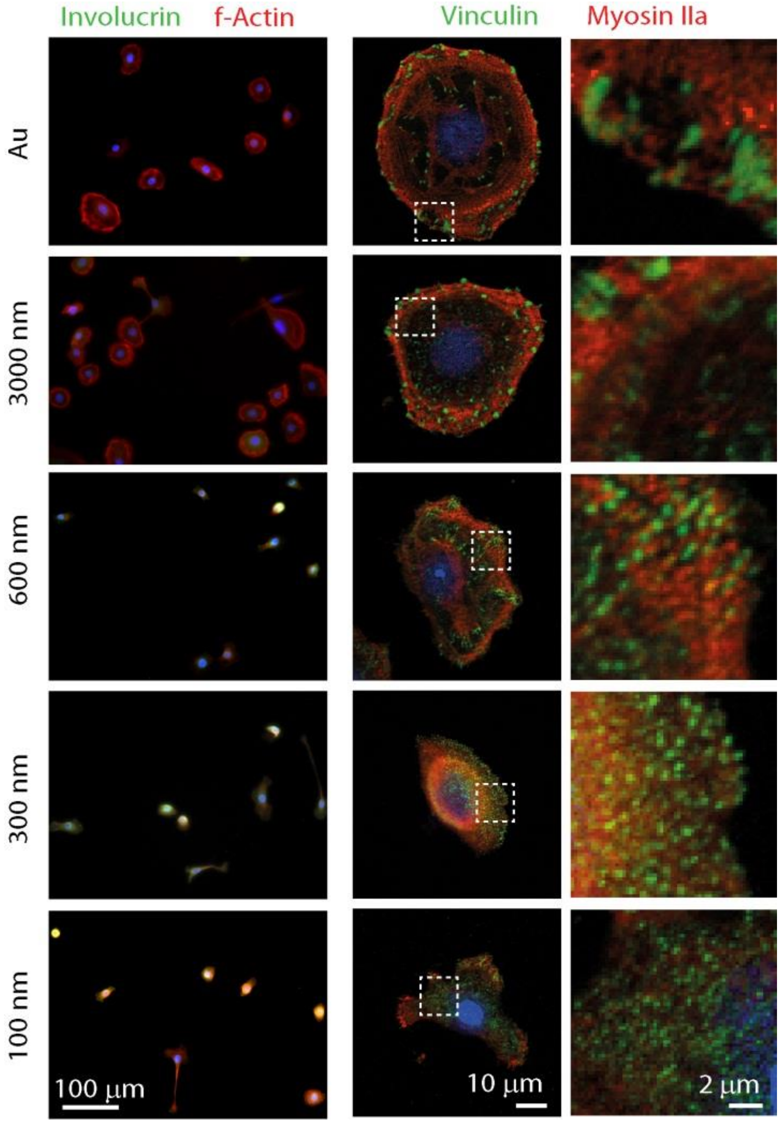

Figure 1.8 Effect of nanopatterns on cell behaviour. Keratinocytes spreading on homogenous surfaces (Au) or on nano-patches with different diameters (3000, 600, 300 and 100 nm). Differentiation (left

column, involucrin is a keratinocytes terminal differentiation marker), focal adhesion formation and keratinocytes spreading (central column, right column showing zooms of areas delimited by the doted boxes) are controlled by the nanoscale geometry of adhesions. Adapted with permission from (Gautrot et al., 2014). Copyright (2014) American Chemical Society.

CYTOSKELETON AND FORCE

The importance of the relationship between matrix geometry and organisation of the actin networks was demonstrated in a series of experiments in which the nucleation of actin polymerisation was controlled by micropatterned substrates. Actin filament orientation and length and the formation of filopodium-like structures are influenced by the spatial organisation and shape of the nucleation area (Reymann et al., 2010). Interestingly, this not only had an impact on the actin network structure but also on the regulation of myosin activity (Reymann A. C. et al., 2012). In addition, this patterning approach allowed the control of the polarisation of actin filaments. When the filaments are antiparallel myosin based contractility results in the deformation and disassembly of the network, whilst parallel bundles are not affected and continue to extend. This so called "orientation selection" mechanism may act as an important nano-to micro-scale sensor of substrate geometry via the regulation of cross-talk between the actin network structure and its ability to sustain contractile forces.

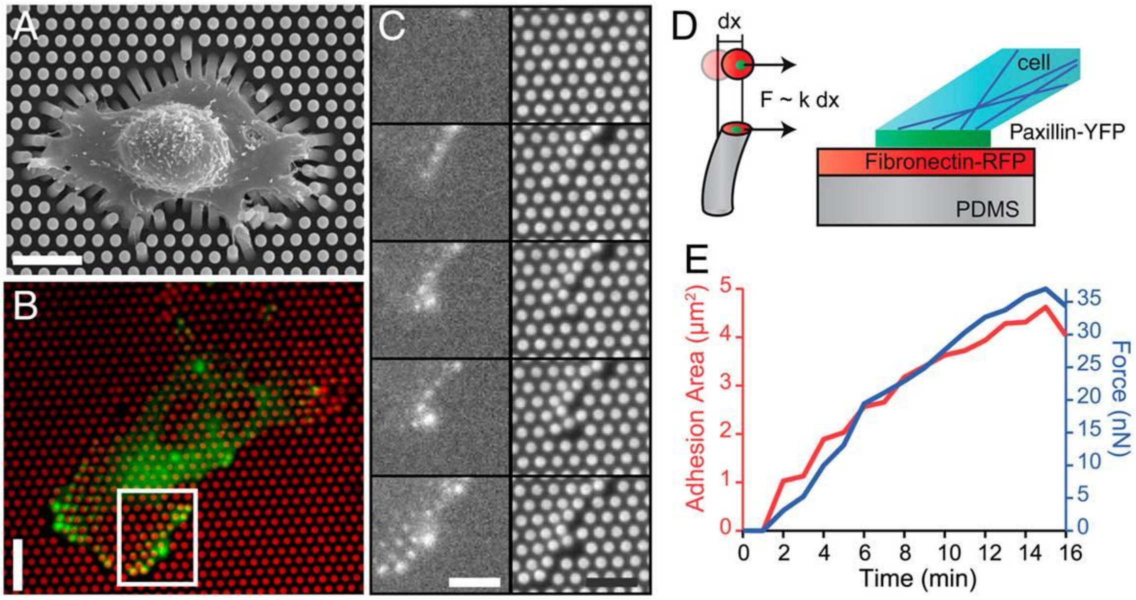

Figure 1.9 Cells adhering and deforming elastic micropillar. SEM (A) and epifluorescent (B, fibronectin coated micropillars are in red and paxillin is in green) images of a cell adhering on elastic micropillars. C represents the inset in B with the sequential FA formation and micropillar displacement. D: schematic of the staining (fibronectin coated micropillars in red and paxillin in green) and force

displacement. E: relationship between force measured and adhesion area over time. Reproduced from (Trichet et al., 2012).

The relationship between adhesion area and force generation was further explored using micropillar arrays allowing the tuning of the rigidity of the substrate via the length of the pillars (Figure 1.9) (Trichet et al., 2012). These experiments highlighted a strong correlation between focal adhesion size and forces generated, consistently with results obtained via an optical laser trap assay (Galbraith et al., 2002) and previous reports by Geiger and co-workers (Balaban et al., 2001). In addition, force generation was increased on stiffer substrates. However, super-resolution imaging of FAs formed on such arrays indicated that large adhesions were in fact composed of multiple small (but elongated and sometimes reaching beyond the boundary of the pillar) adhesions, 100-300 nm across (van Hoorn et al., 2014). The stresses experienced by such adhesions were calculated to be in the range of 10-300 nN/µm^2, one order of magnitude higher than previously measured. Hence the relationship between apparent focal adhesion area and stress may be more complex than the simple linear relationship evidenced by conventional confocal microscopy.

In addition, a detailed analysis of the structure of adhesions and stress field generated by cells spreading on micropillar arrays highlighted significant differences depending on the pillar area (Ghassemi et al., 2012). For micron-size pillars, paxillin staining was localised at the periphery of the pillars and forces applied to neighbouring pillars were correlated. On sub-micron pillars (500 nm), paxillin staining was restricted to the top of the pillars and forces applied to neighbouring pillars appeared to be weakly correlated. This was proposed to result from local contractions generated on sub-micron pillars and uncorrelated to longer range forces. However, it should be noted that the paxillin stainings presented in this work, for large pillars, are significantly different to what others reported (van Hoorn et al., 2014), possibly highlighting cell-dependent phenomena. In addition, although maximum pillar displacement was relatively independent to bending stiffness, it strongly decreased for sub-micron pillars (near 60 nm). Correlated to this behaviour, shear stress was increased 12-fold on the stiffest sub-micron pillars. This behaviour was suppressed in cells lacking the receptor-like protein tyrosine phosphatase α, playing an important role in rigidity sensing. Hence it was proposed that high shear stress and local contractions over 60 nm distances was an important mechano-sensing step via which cells responded to the sub-micron geometry of the matrix on which they spread.

1.3.3 Topography sensing

Cell response to nanofibrous mats and nanogrooves

The ECM often displays a fibrillar morphology and electrospinning has been widely studied to mimic such environment. In many cases, the size of fibres and the dimensions of the gaps that they form were found to control cell fate decision. Rat hippocampus-derived adult neural stem cells (NSCs) were cultured on electrospun Polyethersulfone (PES) fibres with diameters of 300, 750 and 1500 nm, after coating with laminin (Christopherson et al., 2009). Differentiation was found to increase with decreasing fibre diameter, in differentiation medium. Cell morphology was also strongly affected by fibre size, with cells spreading relatively homogenously in all directions on the smallest fibres but stretching and following the main axis of larger fibres. When comparing fibres sizes (300, 500, 700 and 1000 nm) with different fibre orientation (parallel and random fibres), NSCs presented aligned morphologies along the parallel fibre and more polygonal shape on randomly oriented fibres (He et al., 2010). Differentiation was more prominent on parallel patterns with highest level on the 500 nm fibres. No significant difference based on fibre diameter was found on random fibres. It was proposed that fibre diameter affects cell proliferation and differentiation through signalling cascades resulting from changes in FA formation: the MAPK pathway, which affects osteoblastic differentiation, was affected by the size of nanofibres, making such scaffolds attractive for tissue engineering applications (Jaiswal and Brown, 2012)

In contrast to platforms displaying controlled geometry, the size of nanofibres not only controls the potential dimension of focal adhesions that cells may form at their surface, but also the curvature of the membrane at the adhesion sites. In turn, such changes in membrane curvature can affect the binding of membrane associated proteins such as the curvature sensor POR1. The size of fibres (from 100 to 1000 nm) was found to control osteoinduction and the mechanism underlying the activation of a signalling cascade involved in the expression of the osteoinductive marker alkaline phosphatase (ALP) was explored (Higgins et al., 2015). Cells spreading on the smallest fibres displayed higher POR1 binding (as a result of the local increase in membrane curvature), which in turn activated the Rac1 pathway. The largest fibres induced higher ALP activity, as a result of reduced Rac1 signalling, and osteoinductive phenotype. Myosin IIa was also found to sense surface curvature due to increase tension generated on curved surfaces (Figure 1.10) (Ozdemir et al., 2013). Osteogenic differentiation was enhanced on fibrous substrates due to higher tension generated by myosin contractility, in parallel to increased RhoA/ROCK signalling. Finally, beyond the curvature and size of nanofibres, the shape of these objects was also reported to impact the maturation of FAs. Hence, MSCs adhering to mats of silica nanoribbons generated from self-assembled amphiphiles formed larger FAs on helical nanoribbons, compared to twisted ribbons or controlled substrates (Das et al., 2013). This behaviour correlated with increased osteodifferentiation.

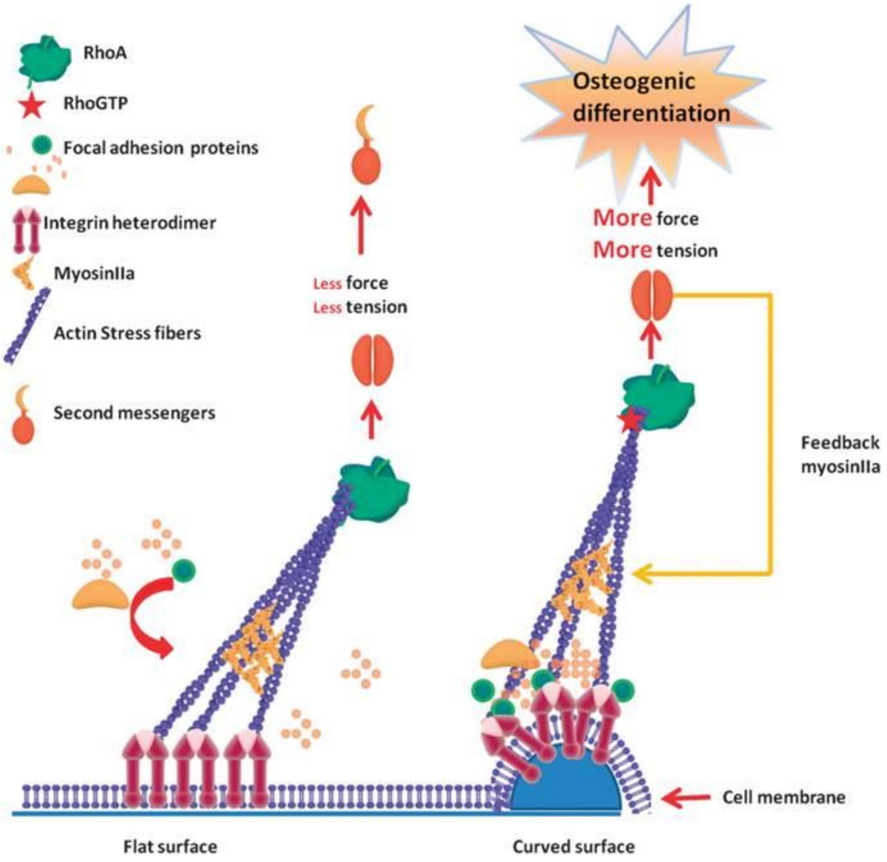

Figure 1.10 Schematic of topography sensing through RhoA/ROCK signalling. Different signalling pathways are activated depending on the surface topography and myosin IIa is involved in the sensing and triggers differentiation depending on the force/ tension felt. On the curved surface there is a higher tension felt that ultimately results in higher levels of differentiation. Reprinted with permission from ref (Ozdemir et al., 2013). Copyright 2013 The Royal Society of Chemistry.

Hence, fibrous networks are significantly more complex physical and geometrical environments than other 2D or quasi 2D substrates. In addition to their intrinsic porosity, the stiffness of the fibres that they are based on (hence the nanoscale mechanics rather than bulk mechanics of the mats) can impact on cell adhesion and phenotype.

When comparing fibrous scaffolds with similar sizes but different porosity, cells were found to proliferate more in mats of poly(3-caprolactone) (PCL) with pore diameters larger than 6 µm, while proliferation was impaired when pores smaller than 3 µm were presented to cells (Lowery et al., 2010). When going to pore sizes above 20 µm, cell deposition of ECM decreased and cells tended to align and spread on single fibres rather than branching across.

Grooves, as fibres, allow the control of cell alignment and morphology. In neonatal rat ventricular myocytes (NRVMs) cultured on substrates with controlled nanotopography (nanoridges/grooves), actin fibres were aligned and more organised along ridges and FA formation was observed at the side of ridges. Such topographically triggered reorganization of the cell cytoskeleton was found to depend on the size of the patterns (Kim et al., 2010). This behaviour is general to a range of materials and cells spreading at the surface of grooved materials are subjected to contact guidance and tend to align in the direction of the grooves, depending on the size (width, depth and spacing) of the features. On 240 and 540 nm deep grooves (12.5 µm wide) cell nuclei were more distorted and greater numbers of focal complexes were formed than on planar surfaces. Such changes in FA formation correlated with a decrease in FAK activation and downregulation of osteogenesis in osteoblast-like MG63 cells cultured on grooved surfaces (Cassidy et al., 2014). On substrates with grooves ranging from 2 to 15 µm wide (2 µm deep), MSCs were found to differentiate in different lineages depending on the width on the groove: adipogenesis was favoured on wider grooves, whilst osteogenic differentiation on the smallest (Abagnale et al., 2015). Migration was also found to be directed parallel to the direction of the grooves.

In order to decouple the respective contributions of nanotopography and stiffness on cell behaviour, cells were cultured on soft nanopatterned (nanogratings of 350 and 500 nm width and 350 nm depth) PDMS substrates (Yim et al., 2010). The sensing of stiffness, rather than topography, was found to control the expression of proteins associated with FA formation (integrins and vinculin) and the organization of actin fibres. On the other hand, surface features were found to impact the ability of cells to exert a higher cytoskeletal tension on stiffer surfaces.

Cell response to nanopits, nanopillars and nanoroughness

The tuning of the nanoroughness of surfaces to control the behaviour of cells and stem cells has recently received considerable attention from the bioengineering community, owing to the implication of such surface texturing for the design of implants. On surfaces presenting different microtopographies and roughness, hMSCs adhered preferentially on homogenous surfaces whilst adhesion was impaired on nanostructured porous silicon (Pereza D.G. et al., 2015). This correlated with the reduced formation of actin fibres and a decrease in cell migration on rough silicon surfaces. Human embryonic stem cell (hESC) proliferation was also decreased and adhesions were disrupted on nanorough surfaces, compared with homogenous controls (Chen et al., 2012). Furthermore, while stemness was retained on smooth surfaces, cells on rough surfaces differentiated more frequently. This behaviour correlated with disrupted FA formation and a change in the expression of non-muscle myosin IIA, known to control stem cell self-renewal. Importantly, the response to surface roughness is often cell dependent: in the same study, the response of fibroblasts to surface roughness was the opposite of that of hESCs and these former cells adhered and spread better on rougher surfaces.

The level of order and disorder of the surface topography was also found to affect the formation of FAs by affecting integrin recruitment, FA maturation and cell spreading (Huang et al., 2009). Dalby et al. produced surfaces textured with nanopits arranged in square, hexagonal and disordered square arrays (with 120 nm diameter, 100 nm deep and an average spacing ranging from 50 to 20 nm). The disordered arrays stimulated osteogenic differentiation of human mesenchymal stem cell (MSCs) while ordered arrays resulted in poorer cellular adhesion and decreased differentiation (Dalby et al., 2007). Ordered arrays disrupted FA formation and cell spreading possibly affecting the ERK/MAPK signalling pathways which in turn downregulated differentiation (Biggs et al., 2009). MSCs were more spread on the ordered square arrays, but FA size and level of actomyosin recruitment at stress fibres were higher on disordered arrays. These cytoskeletal changes were also correlated with changes in nuclear lamina remodelling

(Tsimbouri et al., 2014). However, although ordered nanopit surfaces were not as efficient at inducing osteo-differentiation, they can be used to retain the stemness of MSCs when cultured over long periods of time, hence allowing their expansion from few cells or to higher cell numbers, an important development for the field of cell based therapies (McMurray et al., 2011).

Similarly, hMSC differentiation was found to depend on the density of nanoposts on textured surfaces (Ahn et al., 2014). Cells on surfaces presenting denser topographies were more rounded and softer, favouring adipogenesis, while on sparser nanopost surfaces, cells were stiffer and underwent osteogenic differentiation. Cells spreading on nanopillars with diameters ranging from 200 to 700 nm (Kuo et al., 2014) displayed FAs similar to those of cells spreading on 2D circular patches of similar size range. FAs were decreasing in size with pillar diameter, but on 200 nm bridging of adjacent pillars as a result of forces exerted by cells, allowed larger focal adhesions to be generated. The smallest nanopillars display lower flexural moduli and allow higher cell-substrate interactions. Similarly, the height of Titania nanopillars ranging from 15 to 100 nm was also found to control cell spreading and differentiation (Sjostrom et al., 2009). Shorter pillars maximised cell spreading, cytoskeleton organisation and osteoblastic differentiation.

It is thus evident that designing the size and shape of surface features at the nano- to micro-scale is important to control some of the physical properties of the ECM and the stimuli that cells sense and to which they adjust during fate decision. Such changes in behaviour are directly controlled by changes in focal adhesion formation and cytoskeleton organisation. However, this response is cell type dependent, highlighting the importance of understanding both the biological and physical context in order to design surfaces and implants appropriate for specific applications.

1.4 Conclusions

Cell sensing of the nanoscale physical properties of biomaterials underlies cell spreading and the control of motility and is essential to direct cell phenotypes such as proliferation, differentiation and apoptosis. The molecular processes regulating adhesion formation (molecular clustering, protein complexing, actin polymerisation, bundling and contractility) and their dynamics play a key role in such nanoscale sensing. In addition, increasing evidence indicates that such response to nanoscale properties may in fact dominate cell response to bulk properties of materials, as in the case of the response of cells to matrix mechanics. However, the precise molecular mechanism via which cells sense the nanoscale properties of their microenvironment remains often poorly understood. This is particularly important to elucidate mechanotransduction processes that in turn control cell phenotype. In addition, the role of other components of the extra-cellular matrix (not impacting on integrin-mediated adhesion, such as mucins, lectins, syndecans) and other cytoskeleton components, such as keratins and microtubules, on the sensing of the nanoscale has not systematically been studied. The direct implication of such understanding is the ability to design novel biomaterials allowing an improved control of cell adhesion and behaviour. Engineering the nanoscale properties of biomaterials is particularly appealing for applications in tissue engineering and regenerative medicine as it allows the design of bulk and interfacial properties of implants, scaffolds and cell culture systems independently. Indeed, the structural and mechanical properties of such platforms and their ability to control cell adhesion and phenotype are sometimes hard to reconcile. This is the case for example in the design of implantable brain electrodes or for soft tissue engineering where mechanical integrity is essential, as in cardiac repair. Hence the design of biomaterials for such applications is inherently multidisciplinary and requires technological challenges to be tackled for the synthesis, processing and patterning of relevant materials, with control of the nanoscale, as well as a deeper understanding of the molecular processes underlying their interaction with cells and tissues.

1.5 Aims and Objectives

It is clear from what has been introduced so far that studying the interface between biomaterials and cells is a very broad and multidisciplinary topic and a great amount of research has been focusing on finding synthetic systems that would reproduce the natural environment of cells.

On one hand, this project is inserting in this field with the aim of having a simple 2D platform that could be both easily reproducible and scalable and have geometrical features that mimic the extracellular environment. In this sense we are aiming to produce a randomly organised fibrous pattern with fibres of varying diameter whose topography could reproduce the one of natural collagen or fibronectin fibres. This work would be a follow up of the study of cell behaviour on circular nanopatches (Gautrot et al., 2014) with different diameter sizes, but trying to confine focal adhesion formation to a “2D” level rather than “1D” (which is what happens on nanopatches). Our pattern fibre dimensions would not be in the range of natural ECM fibres, but rather follow the size maturation of focal adhesion, from small, less than a μm^2, focal complexes to mature focal adhesion of few µm long. To our knowledge, such a 2D pattern would be novel in the field.

The second part of the work will then focus on studying cell behaviour on this platform and giving insight in cell mechanotransduction. Despite this field of research is also heavily studied, there are though still lot of gaps in understanding signalling transmission from outside to inside of the cell and vice versa. In particular understanding the precise role of some of the most important proteins in the adhesion plaque is still debated. With this study we thus aim to clarify some of these gaps via studying some of the components of focal adhesion and the cell cytoskeleton and the connection between the two. Assessing this on a constrained geometry where focal adhesion can have determined positions and dimensions will help us understanding cell behaviour at different stages of focal adhesions maturation and how cells react to different topographical “signalling” coming from the outside. We will in particular focus on the link between focal adhesions and the cell cytoskeleton and which are the main proteins orchestrating this linkage and signals transduction.

Chapter 2.

Electrospun Nanofibres Lithography- ENL

2.1 Introduction

The first part of this project focuses on the production and engineering of surfaces mimicking some of the features of the extracellular environment to be used as cell adhesion and proliferation assay. Proteins in the extracellular matrix are often presented in the form of fibrils, as for fibronectin (Klotzsch et al., 2009), displaying defined diameters, but also an organised hierarchical structure, as in the case of collagen fibres (Birk and Trelstad, 1984, Stevens and George, 2005). Fibrillar structures are also very important during wound healing (Mutsaers et al., 1997) and nanofibrous scaffolds have proven a good base for epithelial cells proliferation and stem cell differentiation for application in skin tissue engineering (Chong et al., 2007, Jin et al., 2011). Most studies in the literature focusing on how cells feel and respond to nanopatterned surfaces employ topographies that do not mimic the geometry of the network of proteins that forms the ECM, i.e. fibrillar structures. The work by Spatz et al. has shown the importance of the local density of ligands to enable integrin clustering and focal adhesion formation (Huang et al., 2009, Arnold et al., 2004, Cavalcanti-Adam et al., 2006). The work by Sutherland et al. (Malmstrom et al., 2010, Gautrot et al., 2014) has then shown that the geometry of the growing focal adhesion is also key to control mechano-transduction, cell spreading and differentiation. However, these patterns forced cells to form truncated focal adhesions. Thus, a simple methodology to generate 2D fibrillar patterns enabling the testing of adhesion geometry is needed.

Here we developed a novel patterning platform, electrospun nanofibres lithography (ENL), allowing the generation of cell-adhesive nanofibrous substrates on large scale suitable for the detailed investigation of mechanisms underlying cell sensing of the nanoscale geometry of the ECM. The fibrillar topography is aimed to resemble more the type of networks that proteins, such as collagen and fibronectin, form in the in vivo ECM. Although the aim will not be to reproduce the same sizes as natural protein fibres (as they are only a few nm thick), having a similar patterned morphology will help studying cell behaviour in a more physiological environment.

The process was inspired by colloidal lithography (used for the generation of nanopatches in (Malmstrom et al., 2010) and is composed of 5 to 6 steps (Fig. 2.1). In order to follow the geometrical maturation process of focal adhesion, we aimed to constrain the geometry of adhesions from the size of nascent adhesions (forming patches of around 100nm diameters), up to the diameter of mature focal adhesion (micron size). We thus aimed to produce a fibrous pattern with fibre diameters ranging from 100 nm up to 1µm. In addition, in order to dissociate topographical features from purely geometrical features, and to be able to compare our results with results obtained with 2D nanopatches (Gautrot et al., 2014), we aimed to generate a quasi- 2D fibrous scaffolds.

Two methods were tested for the generation of the nanofibres via electrospun nanofibres lithography (ENL): a sparse electrospun fibre mat was used as a mask for subsequent lithography. Polymer brushes were used as passivation for the background around the fibres (Fig. 2.1).

For the first method (it will be referred here as patterning via etching):

- <u>Electrospinning</u> is used to produce a mesh of random fibres, which will serve as a mask, on silicon wafer/ glass slides coated or not with 1.5 nm Chromium and 15 nm of gold (gold on top).
- <u>Thermal annealing</u> is then used to increase the contact area of the fibres on the substrate.
- <u>Wet etching</u>. The gold in between the fibres is etched after the annealing while the areas protected by the mesh are not removed. The spun fibres left are then dissolved in a proper solvent leaving a gold fibre pattern on the surface.

- Surface functionalization. Gold nanofibres are “protected” and the background surface is coated with an initiator for the following polymerization.
- Atom transfer radical polymerisation (ATRP). The areas surrounding the gold fibre pattern are coated with a layer of non-fouling polymer brushes to prevent unwanted cell adhesion on the non patterned area.

The second method (it will be referred here as patterning via ATRP):

- Silanization. Glass slides/ silicon wafer are functionalised with the ATRP initiator.
- Electrospinning is used to produce a mesh of random fibres, which will serve as a mask, on silicon wafer/ glass slides.
- Thermal annealing is then used to increase the contact area of the fibres on the substrate.
- Atom transfer radical polymerisation (ATRP). The areas surrounding the annealed fibres are coated with a layer of non-fouling polymer brushes to prevent unwanted cell adhesion on the non patterned area. The spun fibres left are then dissolved in a proper solvent leaving a fibrous pattern on the surface.

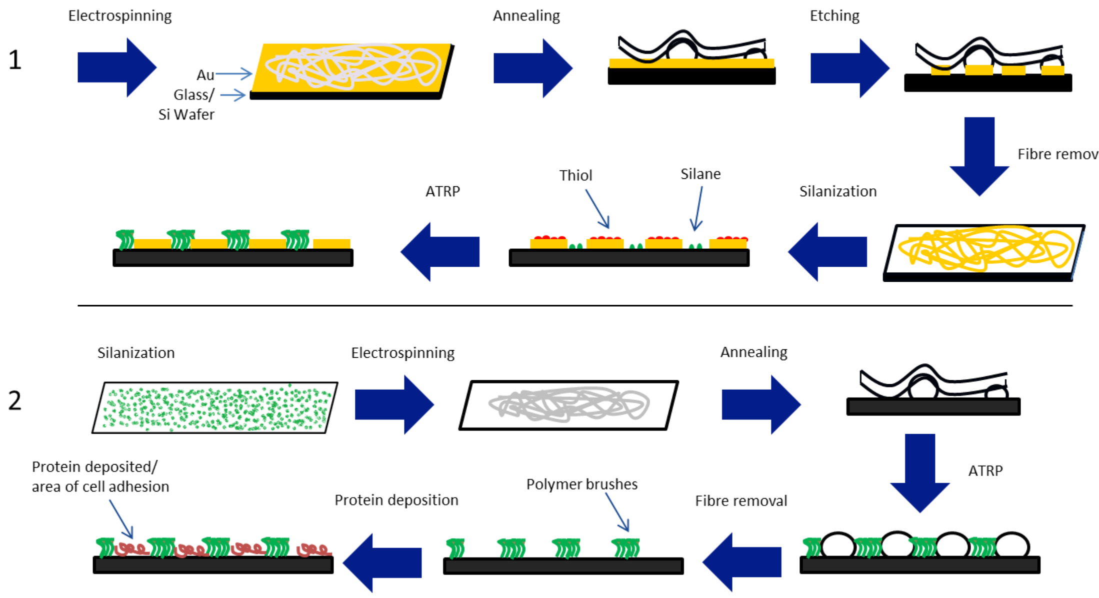

Figure 2.1 Electrospun nanofibres lithography (ENL). Schematic of the two methods tested for the production of the fibrous pattern. Main steps are electrospinning, annealing and ATRP.

Before going into the details of the nanofibres fabrication, some of the technique mentioned above in the patterning protocol will be introduced.

2.1.1 Electrospinning

This process has been briefly introduced in the previous chapter and a few aspects will be here discussed.

The whole process is based on the application of an electric field to a flowing polymer solution and on the interplay between the electric forces generated and the surface tension presents at the tip of the needle from where the polymer solution comes out (Pham et al., 2006).

The setup for this process consists of: a syringe pump that injects the liquid through a syringe ending with a needle through which the solution is ejected, a high-power supplier and a collector (Pham et al., 2006) (Fig. 2.2). The high power supplier is used to charge the polymeric solution while it is pumped out through the needle.

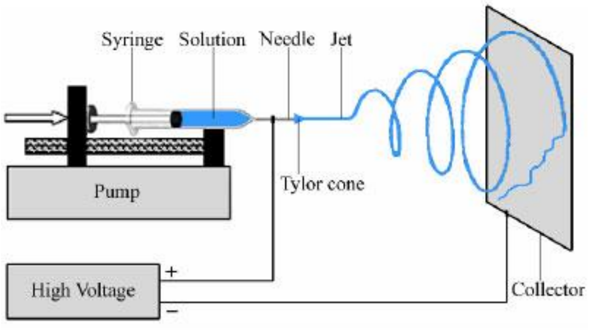

Figure 2.2 Schematic of electrospinning process (Ziabari et al., 2009). The polymer solution flows through a syringe that ends with a needle where the Taylor cone forms. This cone is the accelerated by electrostatic forces and forms a jet directed to the collector.

This process is influenced by many factors, whose effects are often difficult to isolate. Variables can be divided in solution properties, processing conditions and ambient parameters (De Vrieze et al., 2009). These properties should be optimized in order to obtain bead-free and uniform fibres with controlled diameters.

Viscosity is one of the most important parameter. Solutions with too low viscosities can produce beads and junctions, because the fibres are still wet when landing on the substrate. In contrast, if the solution is too viscous the jet is prevented from forming. Viscosity can be controlled by changing the concentration and the molecular weight of the polymer. Several studies have found that fibre diameter increases by increasing the concentration of the polymer (Deitzel et al., 2001). Polymer molecular weight also influences fibre morphology: PMMA fibre beading was found to decrease at high polymer molecular weight (Gupta et al., 2005).

Conductivity of the polymer solutions is another key factor: the higher it is and the more the fibres can stretch. It was shown that with increased conductivity the fibres produced were more uniform, thinner and with fewer beads (Huang et al., 2001).

Surface tension is a solution property that affects bead formation. High surface tension may lead to droplets formation rather than fibres when the solution concentration is low (Deitzel et al., 2001). It has also been shown that decreasing the surface tension was favouring bead- free fibre (Lee et al., 2002b). However, these different properties are interdependent, so discerning the effect of each on the size and morphology of electrospun nanofibres can be relatively difficult or misleading.

Within the processing parameters, the voltage applied and flow rate are the most important. The voltage has to be strong enough to charge the solution and so overcome the surface tension, but if it is increased too much, the Taylor cone is prevented to form and bead formation is observed. The flow rate is also related to fibre diameter: it was shown that fibre diameter decreases decreasing flow rates (Fridrikh et al., 2003).

Another controlling factor is the distance between the needle and the collector: it has to be sufficient to allow the fibres to dry and stretch before being collected (up to 30 cm).

Temperature (an ambient parameter) affects two aspects which contrast each other: when it increases the evaporation rate increases too, whereas the viscosity decreases. The former behaviour leads to a decrease in jet stretch and dominates at low temperatures, while the latter leads to the opposite and predominates at higher temperatures (De Vrieze et al., 2009).

Humidity in general was shown to affect fibre shape and pore distribution (within the fibres), but its influence still remains unclear.

As it appears clear, electrospinning is a complex process governed by several parameters which interplay with each other in a complex fashion. Hence each new electrospinning system and setup must be calibrated and characterised first to determine the level of control achieved on the fibres deposited.

2.1.2 Etching

Etching is a technique used to selectively remove materials from a surface and it can be a step in surface patterning methods (Fig. 2.3) (Lai and Cheng, 2014). In this process, a mask is generally applied on the surface of interest which contains the features that need to be transferred (the pattern): the exposed areas of the target surface are then removed via etching. In photolithography, for example, the mask is normally a photoresist which is patterned via the use of light (DeFranco et al., 2006). In colloidal lithography, colloids can be used as a mask for etching (Yang et al., 2006).

Etching techniques can be divided in two main categories: wet etching, also known as chemical etching, in the liquid phase, and dry etching, in the gas or plasma phase (Ghodssi and Lin, 2011, Kern and Deckert, 1978).

The main characteristics of this process are:

- Isotropy/anisotropy: the isotropic etching works at the same etching velocity in all the directions (like in the wet etching), while in the anisotropic case, the orthogonal velocity is much higher than the horizontal one.
- Selectivity: is the ratio between the etching velocity of the target material and the one of other materials (used as mask). Chemical etching is normally more selective that the physical one.

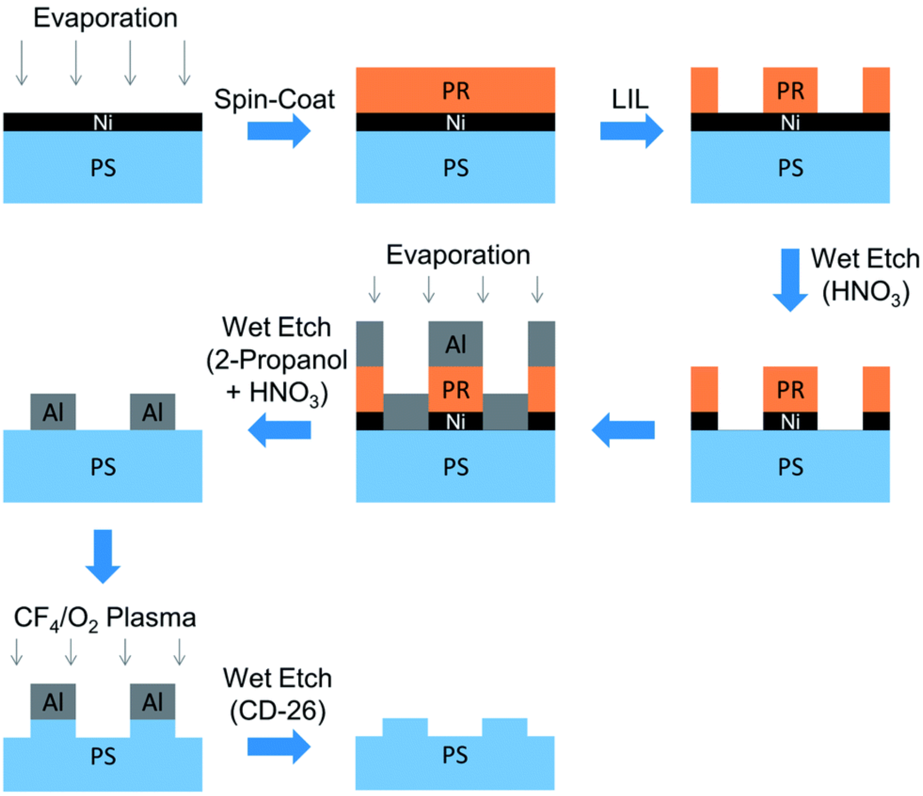

Figure 2.3 Example of combination of dry and wet etching. A photoresist (PR) is deposited on a Nickel coated surface (Ni) and patterned via UV light (LIL). The pattern is then transferred to the surface below via subsequent wet and dry etching. (Lai and Cheng, 2014)

Wet etching. In this process the sample is immersed in a relevant solution (such as acids for metals) that removes the unwanted part of the material to obtain a specific pattern. This process is normally isotropic (Love et al., 2001), although when etching material with different crystallographic planes the etching velocity may be different depending on the direction of the crystal planes (Stocker et al., 1998).

Problems associated with this process are the toxicity of the etchants used, impurities and poor reproducibility, but this method is simple, inexpensive and fast.

Dry etching. This technique exploits the use of plasma or ion beam or e-beam to bombard the sample and reproduce the pattern. It can be either chemical or physical or a combination of both (RIE, reactive ion etching) (Pearton et al., 2000). In the former, a chemical reaction activated by the plasma and by ion bombardment occurs between the etchant and the material on the sample. Dry etching allows for an anisotropic behaviour (optimized for the RIE) and it leads to more uniform and clean results, but is more expensive.

2.1.3 Polymer brushes - ATRP

Polymer brushes are thin films composed of polymer chains attached by the end to a solid substrate (flat or nanoparticles) and with sizes ranging from a few nanometres up to hundreds of nanometres. These polymer chains are typically generated from surface-tethered initiators (Edmondson et al., 2004). Polymer chains can be coupled to the surface via physical or chemical adsorption (*grafting to*) or can be grown via polymerization initiated from the surface (*grafting from*) (see Fig. 2.4). Living/controlled radical polymerization (CRP) techniques are part of the latter category: in this case the polymerization occurs without irreversible chain transfer and chain termination (Matyjaszewski and Xia, 2001). These methods rely on a quick dynamic equilibrium established between growing free radicals and dormant species, normally present in higher quantities. Amongst these methods, atom transfer radical polymerization (ATRP) has been applied to the polymerisation of a very wide range of polymer brushes and rely on the use of alkyl halides as dormant chains and the use of copper based catalysts to mediate equilibria with reactive chains (Barbey et al., 2009). This process is chemically highly versatile and robust, with respect to other CRP.

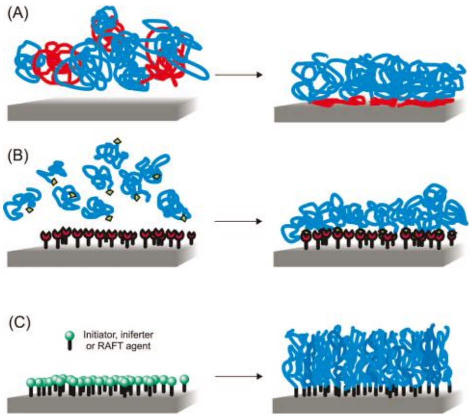

Figure 2.4 Strategies for polymer brush deposition. (A) Physical absorption of diblock copolymers. (B) Chemical absorption via adhesion of end-functionalized polymers with complementary functional groups. (C) Polymer brushes grown via surface-initiated polymerization methods (Barbey et al., 2009).

The ATRP process is based on a reversible redox reaction which activates the dormant species (forming the radicals, $Pn^{\bullet}$) and is catalysed by a transition metal complex (Mt^m/L) in his low oxidation state (Matyjaszewski, 2012). The radical then reacts with the monomer (M) increasing the chain length (Fig. 2.5).

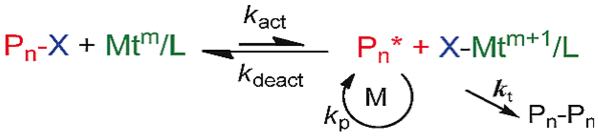

Figure 2.5 Schematic of a conventional ATRP (Matyjaszewski, 2012).

Side reactions and termination reactions also may occur, but in a well controlled reaction these almost vanish. Termination is prevented by ensuring a fast deactivation rate and minimizing the amount of the growing free radicals present at a given time in the system.

A large number of polymers have been fabricated through this technique. In particular, scientists have reported the protein resistance to oligo(ethylene glycol) methacrylate (OEGMA) derived polymers and Poly(2-(methacryloyloxy)ethyl-dimethyl-(3-sulfopropyl)- ammonium hydroxide) (PMEDSAH) (Brown et al., 2005, Tan et al., 2013). On the other hand, polymers that can be functionalized with RGD- peptides were also produced and used for studies on cell spreading and adhesion (Tugulu et al., 2007).

2.2 Nanofibres pattern fabrication: materials and methods

The different steps associated with nanopatterning of substrates with 2D nanofibres, electrospun nanofibres lithography (ENL) will now be explained in detail.

2.2.1 Materials and chemicals

The gold (purchased from Birmingham metal, 99.9% pure) coated glass slides and silicon wafers (purchased from piChem) used were produced by technicians via evaporation of 1.5 nm of Chromium and 15 nm of Gold. Poly (methyl methacrylate) (PMMA) (average M_w ~ 350,000 and 996,000), potassium iodide, iodine (≥99.8%, solid), sodium dodecyl sulfate (SDS), triton X-100, 1-undecanthiol (98%), oligo(ethylene glycol methyl ether methacrylate) (OEGMA, M_w 300), [2-(methacryloyloxy)ethyl]dimethyl-(3-sulfopropyl)ammonium hydroxide (MEDSAH, 97%), triethylamine (≥99%), 2,2'-bipyridyl, copper (I) cloride (CuCl), copper(II) bromide (CuBr2), copper(II) chloride ($CuCl_2$, >99.9%) and gelatin were purchased from Sigma Aldrich. Chloroform ($CHCl_3$) (≥99%), N, N-dimethylformamide (DMF) (≥99.8%) and toluene (>99%) from VWR. Sodium chloride (NaCl) and goat anti-rabbit IgG secondary antibody Alexa Fluor 488 were from Fisher. 3-trimethoxysilylpropyl 2-bromo-2methyl-propionate was from Fluoro Chem. Fibronectin from human plasma (1 mg/ml) was from Millipore. Foetal bovine serum (FBS) was from PAA. Polyclonal anti-fibronectin antibody (100 µg) from rabbit was from abcam. Deionised water was obtained using a Synergy system from Millipore.

2.2.2 Silanization

The surface of the wafer had to be functionalised with a silane which served as initiator for the ATRP process: this was the first step in the patterning via ATRP method and an intermediate step for the patterning via etching one. Silicon wafers were treated for 10 min with air plasma (ZEPTO Plasma Etcher from Diener Electronic Plasma Surface Technologies) and then incubated overnight in a solution of 30 µl of 3-trimethoxysilylpropyl 2-bromo-2methyl-propionate (**1**) and 50 µL of triethylamine dissolved in 40 mL toluene. The substrates were then rinsed with DI water, acetone and ethanol and stored under inert atmosphere until used for further treatment.

2.2.3 Electrospinning

PMMA was chosen to produce the spun fibres for its versatility and range of molecular weight. The polymer was dissolved in a mixture of chloroform and DMF. Different ratios between the two solvents were tested: 7:3, 8:2 and 6:4. These ratios were selected to control the conductivity and rate of evaporation of the solvent during spinning: the chloroform has a lower boiling point (which increases the evaporation rate) and DMF provides some conductivity. Thus, increasing the ratio of the former can increase the speed of evaporation of the solution, whilst increasing the latter it is possible to increase solution conductivity and so allow the fibres to stretch more and to achieve smaller diameters. In order to obtain a set of fibre diameter, different concentrations of PMMA were tested: 3.5%, 4%, 5%, 6%, 7%, 10% and 12% w/w (although this latter concentration was found to be too viscous and was not used anymore). The highest M_w PMMA was used for preparing the lowest concentrated solutions (3.5, 4 and 5 w/w%): because it was shown that for very low viscosity solutions (less concentrated) higher M_w leads to more homogeneous and less beaded fibres, while the opposite occurs for more concentrated solutions (Gupta et al., 2005). The prepared solutions were kept in sealed bottles until used. To completely allow the PMMA to dissolve, the solutions were kept stirring at 50°C overnight on a Stuart ceramic hotplate stirrer.

In the setup, shown in Fig. 2.6, a Kent Genie syringe pump was used to supply the PMMA solution flowing through a needle fixed at the top of the system. The needle was connected to the high DC power supplier, a Glassman EQ high voltage power supplier. The collector was a metal plate which was grounded.

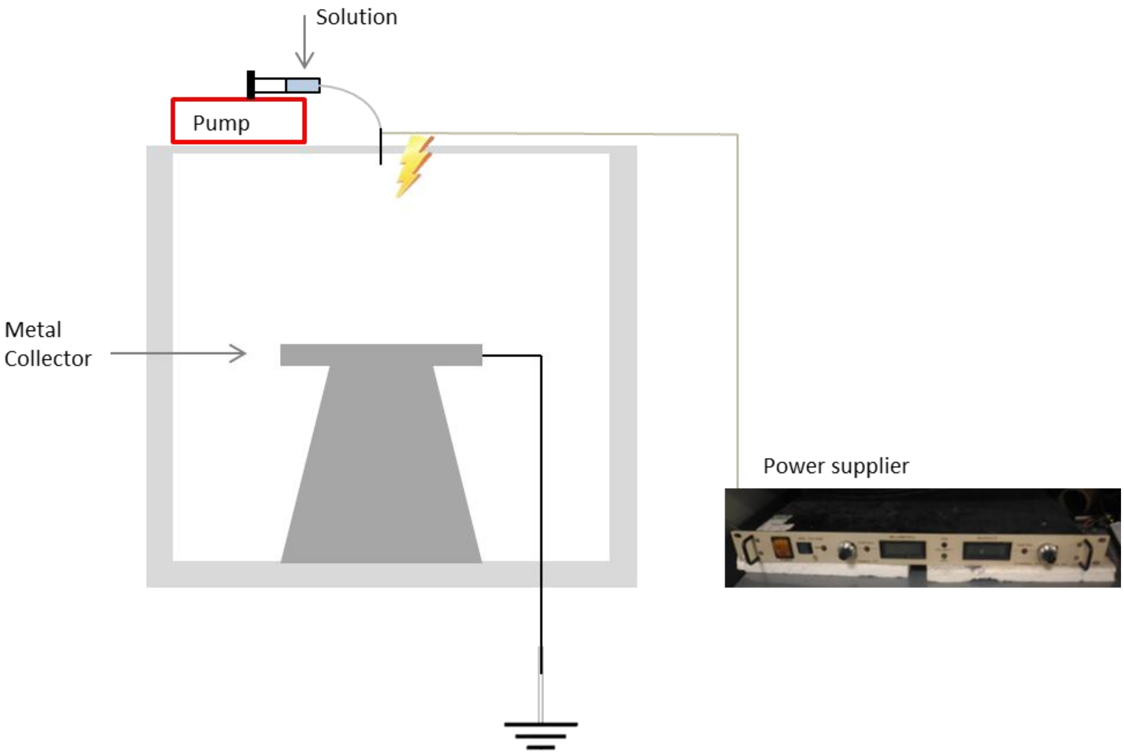

Figure 2.6 Experimental set-up for electrospinning. The polymer solution flows through a needle where an electric field is applied; this charges the solution so that the jet is formed. A plastic box of 1 X 1 m (grey square) protects the area where the Taylor cone is formed and the metal collector where the fibres are deposited. The metal collector is supported by a metal structure that is grounded.

During electrospinning, process parameters such as flow rate and the voltage applied were controlled and optimized to obtain uniform, bead-free fibres and to allow a constant jet production (flow rate ranging from 0.08 to 0.8 mL/hr and voltage from 19 to 26 kV, see table 2.1). Particular attention was given to maintain a continuous and regular "jet" coming out from the needle during the process (assessed by naked eye). The distance between the needle and the collector had to be far enough to allow the jet sufficient flight to stretch and form fibres. In our experiments, it was kept at 19 cm. In order to check uniformity and beads, fibres were collected first on glass slides and observed under an optical microscope. The flow rate and voltage were consequently adjusted to improve the morphology and uniformity of fibres (at low flow rate beads can be almost suppressed). Another important factor that in our case could not be controlled is humidity: if humidity was too low it was very difficult to prevent beads formation, especially for solutions with too high or too low viscosities. For these (3.5%, 4% and 10%), the addition of salt (NaCl) in 0.1% in weight, which allows to further increase the conductivity of solutions and thus the fibres to stretch better, was required.

For our purpose we tried to obtain nanofibres with different densities of the fibre mesh. To do so, the electrospinning time (during which collection on the target substrate was allowed) was controlled. Different fibre densities were obtained at different collection times and their density was determined via microscopy. Deposition time for small fibre was about 30 sec and up to 1-2 minutes for low and high densities respectively; for thicker fibres was about 1 min for low and a few minutes for high densities.

Fibres were also collected on foil to check the morphology and diameter via scanning electron microscopy (SEM).

The samples obtained from electrospinning (gold coated glass slides and silicon wafers and pristine silicon wafers) were kept for further processing as illustrated in the next paragraphs.

2.2.4 Annealing

Deposited fibres were thermally annealed in an oven in order to improve their contact area with the underlying substrate and their adhesiveness to it. Various temperatures were tested in order to preserve the fibre dimensions whilst ensuring a good contact with the underlying substrate; incubation time was kept constant. The smallest fibres are especially sensitive: if kept at too high temperatures, the surface contact area increased too much, thus increasing dramatically the initial fibre diameter. Samples were left in the oven for one hour and a set of temperatures ranging from 140°C to 190°C was tested to understand how the dimension of fibres was affected by the increase of the temperature. Substrates were directly placed in the oven, on a metal tray. The fibres were then analysed (after gold coating) via SEM to confirm that their morphology was unaltered and to quantify changes in diameters.

2.2.5 Wet etching

For our purpose, chemical (or wet) etching was used, due to its ease and low cost, to remove the unprotected gold in the patterning via etching method. A mixture of potassium iodide/ iodine and distilled water ($KI/ I_2/H_2O_d$) was used, as reported in previous work (Zhang, 2013). The etching process is based on an oxidation reaction:

$$2Au + I_2 = 2AuI.$$

The solution was prepared dissolving potassium iodide and iodine in distilled water. Two concentrations were tested:

(1) $KI/ I_2/H_2O_d = 4:1:400$ (KI 0.06M and I_2 0.01M) and **(2)** $KI/ I_2/H_2O_d = 4:1:800$.

The solution was kept in a glass vial, in the dark, and allowed to dissolve with sonication if needed.

The etching solution **(1)** was used initially for gold coated glass slides. It was found that for samples with fibres produced from the 3.5% and 4% PMMA solutions, this solution led to over- etching, thus **(2)** was used for these concentrations. Slides were left in the etchant solution first and then quickly rinsed with distilled water, to stop the reaction and eliminate any residual solution from the slides, then washed with 95% ethanol and dried. They were then left in chloroform for about ten minutes in order to dissolve the spun PMMA fibres. Samples were then removed from the chloroform solution, washed with 99% acetone, water and ethanol and dried. Different etching times were tested in order to optimize the process, ranging from 50 sec to 75 sec. After etching and fibre removal, the remaining nanofibres were qualitatively assessed with naked eye and via optical microscopy to determine whether there was residual gold on the background and examine the fibre morphology. The time of etching was adjusted depending on these preliminary results. SEM images were taken for a more precise investigation. Silicon wafers were found to be over-etched with **(1)**, thus **(2)** was used varying the etching times.

All samples were analysed with energy dispersive spectroscopy (EDS) to confirm their composition and whether any gold was left in the background and via SEM and atomic force microscopy (AFM) for topography analysis (only samples prepared on silicon wafers were analysed with AFM).

As the contour of fibres was found not smooth, probably due to poor surface wettability during the etching process, other techniques were tested. Air or even some contaminations between the PMMA fibres may restrict contact and access of the etchant solution, preventing the etching process to occur. Two main actions are generally employed for increasing surface wettability: cleaning the surface or the use surfactants.

Both techniques were employed here and the conditions tested on glass slide are here listed:

- Adding 0.1% w/w of sodium dodecyl sulfate (SDS) to the etchant solution.
- Adding 0.1% w/w of triton X-100 to the etchant solution.
- Adding 0.1% in volume of ethanol, for cleaning the surface, to the etchant solution.
- Pre-clean the surface with a "soft" plasma treatment via a ZEPTO, Electric Diener (plasma surface technologies), to remove the dust and make surface more hydrophilic. This treatment was carried for one or two minutes.
- Combining the surface cleaning with the plasma etching together by adding ethanol to the etchant solution.

Not all the above conditions were tested on silicon wafers as clearly resulting in poor etching.

2.2.6 Polymer brushes growth - ATRP

For the patterning via etching method, the polymer brushes were grown after the etching step and PMMA fibre removal on the background between the gold fibres left: thus the gold areas have to be protected from the subsequent polymerization. Silicon wafers were treated for 10 minutes with air plasma and then incubated overnight in a solution of 60 mg of 1-Undecanthiol (which covalently bonds to the gold fibres left via the sulphur atom) in 40ml ethanol. The substrates were then rinsed with DI water, ethanol and then dried with Nitrogen. They were then incubated overnight in a silane solution prepared as mention in the paragraph “silanization”. The 3-trimethoxysilylpropyl 2-bromo-2methyl-propionate silane acts as the initiator for the ATRP, while the triethylamine catalyses its attachment to the surface. The substrates were then rinsed with ethanol and water, dried and kept for the ATRP process.

For the patterning via ATRP method, substrates have already been functionalised with the initiator before electrospinning as in paragraph “silanization”. In this case, the spun fibres were retained on the substrate: the brushes will grow in between them to cover the background. POEGMA was used for both methods, while PMEDSAH was only tried with the patterning via ATRP one. The method for ATRP for both polymers is here reported.

The polymerization was carried out under inert gas (typically nitrogen) to avoid the oxidation of the metal catalyst used in the ATRP process. Two round-bottom flasks with the monomer/catalyst solution were prepared, containing respectively the monomer (OEGMA, 12.6 g), the ligand 2,2'-bipyridyl (320 mg) and the deactivation catalyst copper(II) bromide ($CuBr_2$, 18 mg) into a mixture of de-ionized water and ethanol (4:1, total volume of 30 mL) for POEGMA brushes and the monomer ([2-(Methacryloyloxy)ethyl]dimethyl-(3-sulfopropyl)ammonium hydroxide, 20 g), the ligand 2,2'-bipyridyl (560 mg), and the deactivation catalyst copper(II) chloride (CuCl2, 76.8 mg) into a mixture of water and methanol (1:4, total volume of 40 ml) for PMEDSAH brushes. The flasks were sealed and degassed via an inert gas inlet (needle) and stirred for 45 min to allow the dissolution of reagents whilst bubbling with nitrogen to remove oxygen from the flask and solution.

Copper (I) chloride (CuCl, 82 mg for POEGMA and 144 mg for MEDSAH) was then quickly added to the solution which was subsequently stirred whilst bubbling with nitrogen for another 15 minutes. MEDSAH polymerisation was found to lack reproducibility due to the possible formation of glue at the bottom of the flask. The solution was then transferred using a syringe to sealed vials containing the samples (previously degassed and left under inert gas). During the polymerization samples were kept under nitrogen. The polymerisation time was selected depending on the height of the polymer brush required.

POEGMA brushes height was found to be around 30 nm after 30 min reaction. In contrast, PMEDSAH does not display a linear growth and it was left to polymerise for 90 min to obtain a film of about 20 nm (Tan et al., 2013). Water was quickly added to the system to stop the polymerization and samples were washed with plenty of water to remove any catalyst, then ethanol and dried. As PMEDSAH polymerisation generates a glue (free polymer) during the reaction, the samples were left overnight in a saline solution of water and NaCl to dissolve the polymer mass. The samples are then washed with water, ethanol and dried.

For the patterning via ATRP method, the PMMA fibrous mask was then removed from the substrates using chloroform for 10- 15 min and samples were finally rinsed with water and ethanol and dried. The densities and dimensions of the nanofibres were confirmed via SEM and AFM and EDS analysis.

During the polymerizations, homogenous reference substrates (without fibres) were also produced in order to quantify the height of the layer of polymer brushes grown. The thickness of these homogenous brushes was evaluated via ellipsometry. This method measures the change in polarization of an incident radiation after reflection from the substrate of interest and compares it to a model. Thickness as well as composition and optical properties of the film can be quantified.

2.2.7 Fibronectin deposition

After fibre removal, samples were functionalised with fibronectin (FN), which selectively deposited in the fibre-shaped gaps left between the polymer brushes coated areas. Samples were incubated for 45 min in a FN solution (10 µg/mL in PBS) at room temperature and then washed with PBS first by diluting twice and then completely replacing the buffer twice more. Cell seeding or immunostaining was carried out directly after this.

2.2.8 Fibronectin immunostaining

To assess the quality of FN deposition, fibronectin was immunostained. After deposition, samples were blocked with a solution of 10% FBS and 0.25% gelatin in PBS for 1 h at room temperature, then incubated with a fibronectin antibody (1:200) for 1 h, washed with PBS, incubated with the secondary antibody (1:1000; Alexafluor 488 anti-rabbit) for 1 h and finally washed again. All steps were carried out at room temperature. The samples were then characterized via epifluorescence microscopy.

2.2.9 Characterization

Ellipsometry. Ellipsometry was used to quantify the thickness of polymer brushes after polymerization on a reference homogenous (no fibre) silicon substrate functionalised with silane **1**. The dry polymer thickness (h_d) was measured using an α-SE® spectroscopic ellipsometer (J. A. Woollam) at an incident angle of 70°. A silicon substrate/Cauchy film model was used and fitting was carried between 400 nm and 900 nm.

SEM. Samples were characterized via scanning electron microscopy (Inspect F from FEI) after each step to characterise the fibre morphology and dimensions. Fibre diameter was assessed after electrospinning, annealing and polymer brush growth. Electrospun fibres were coated with Gold (SC7620 Mini Sputter Coater, Quorum Technologies), 60 sec coating and 20 mA process current, whilst this step is not required to image nanofibres after their removal and after etching. A voltage of 20 kV, a spot size of 3.5 and an aperture of 30 µm were used and magnification up to 20,000X. The SEM software was used to assess fibre diameter. SEM images were used to assess the nanofibres density (area where the ECM protein is deposited) and the gap area between the fibres at different fibre sizes using ImageJ. The SEM images were first transformed in black and white images and then the area of the objects (the fibres if density is needed or the area between fibres when assessing the gaps) is measured. Fractal dimension was also computed using ImageJ plug- in “FracLac”. Images are transformed in binary and then analysed with the software.

AFM. Atomic force microscopy (AFM- NT-MTD, NTEGRA) was carried out on the patterned samples before and after fibronectin deposition to quantify the depth of the nanofibres and their roughness. Semicontact mode was used and the row pictures were corrected with a first order function by the software (Nova). Non-contact NSG01 cantilevers from NT-MDT were used (force constant 1.45-15.1 N/m and resonant frequency 87-230 kHz).

Immuno-fluorescence microscopy and data analysis. Fluorescence microscopy images to quantify fibronectin deposition (after immunostaining) were acquired with a Leica DMI 4000B epifluorescence microscope (EL6000 lamp, 20x0.7 NA lens, 63x1.40 Oil lens). Profiles for fibronectin stainings were obtained from the corresponding images of immunostained samples, using ImgeJ.

Statistical analysis. Statistical analysis was carried out using Origin 8 and one-way ANOVA with Tukey test for posthoc analysis. Significance was determined by * $P < 0.05$, ** $P < 0.01$, *** $P < 0.001$, **** $P < 0.0001$, ***** $P < 0.0001$. A full summary of statistical analysis is provided in appendix A2.

2.3 Nanofibres pattern fabrication: results and discussions

2.3.1 Electro-spinning of fibres

The first step of the protocol is the deposition of a mesh of fibres with controlled diameters in the sub-micron range, which will serve as a mask for subsequent patterning. Fibres were deposited via electrospinning. This technique was chosen above direct writing method (like inkjet printing and dip-pen nanolithography) or replication method (like micro- contact printing or photolithography) thanks to the ability to go to 100 – 200 nm range and cover at the same time large areas. Also the apparatus used is inexpensive.

Fibres collected on foil were analysed via SEM to quantify their diameter. They ranged from 120 nm to near 1500 nm (see Fig. 2.7/Table 2.1). A ratio of 7:3 ($CHCl_3$/ DMF) was used in previous work (Zhang, 2013) and was found to afford an optimal balance of evaporation rate and conductivity. A ratio of 8:2 was also tested but resulted in significant bead formation, possibly because the fibres did not stretch sufficiently due to the decreased conductivity. With our setup, we found that the solvent ratio had to be pushed to 6:4 in order to prevent beading, possibly to allow better stretching of fibres during their flight. We propose that, especially when environmental conditions are not optimal, the fibres need more time to stretch (slow evaporation rate, thus less $CHCl_3$) and form a more uniform mesh on the collector.

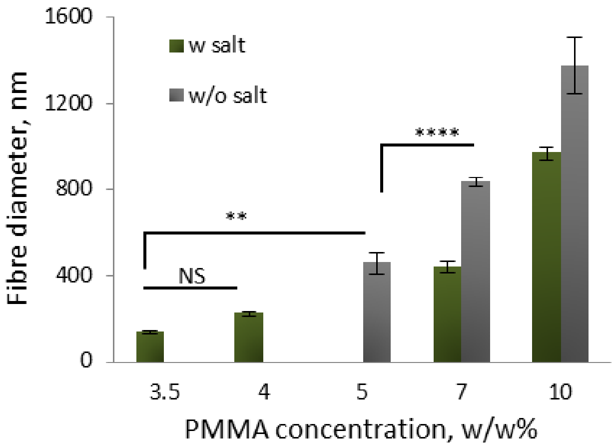

Figure 2.7 Fibre dimensions (diameter) obtained using different PMMA concentrations (x axis) and with or without the use of an electrolyte (salt, NaCl 0.1% in weight). Bars are standard errors, n≥3, number of experiments. For statistical test: *, $P < 0.05$; **, $P < 0.01$; ***, $P < 0.001$; ****, $P < 0.0001$.

Environmental parameters play an important role in fibre formation but it was not possible to control them with our setup. Most importantly, when the humidity was low (<20%) it was very difficult to obtain bead-free fibres. Adding an electrolyte (NaCl in this case) improved the conductivity thus allowing fibres to stretch further during the spinning process. Hence the formation of beads was almost suppressed. When fibres stretched further, their diameter also decreased, and this should be considered when producing the thickest fibres (e.g. from 10% PMMA solutions).

The flow rate and voltage applied were shown here to have a more modest effect on fibre dimensions (see Table 2.1) but they were adjusted during the process to suppress the occurrence of beading. This is in good agreement with previous reports that demonstrated the control of Polyethersulfone (PES) (Christopherson et al., 2009) and PMMA (Liu et al., 2009) nanofibres ranging from few hundreds nanometres to microns based on the molecular weight and concentration of materials deposited. The voltage in particular has to be adjusted so that the electric field is not too high and fibres have the correct time to stretch and the solvent to evaporate.

The conditions used so far and the dimensions of the fibres obtained are reported in table 2.1.

Table 2.1 Conditions used for electrospinning of PMMA fibres and the corresponding fibre dimensions. In order in the table: PMMA concentration, molecular weight (Mw), ratio of CHCl3 to DMF, presence of salt, Humidity, Flow rate, Voltage, average fibre diameter (nm) and relative standard deviation.

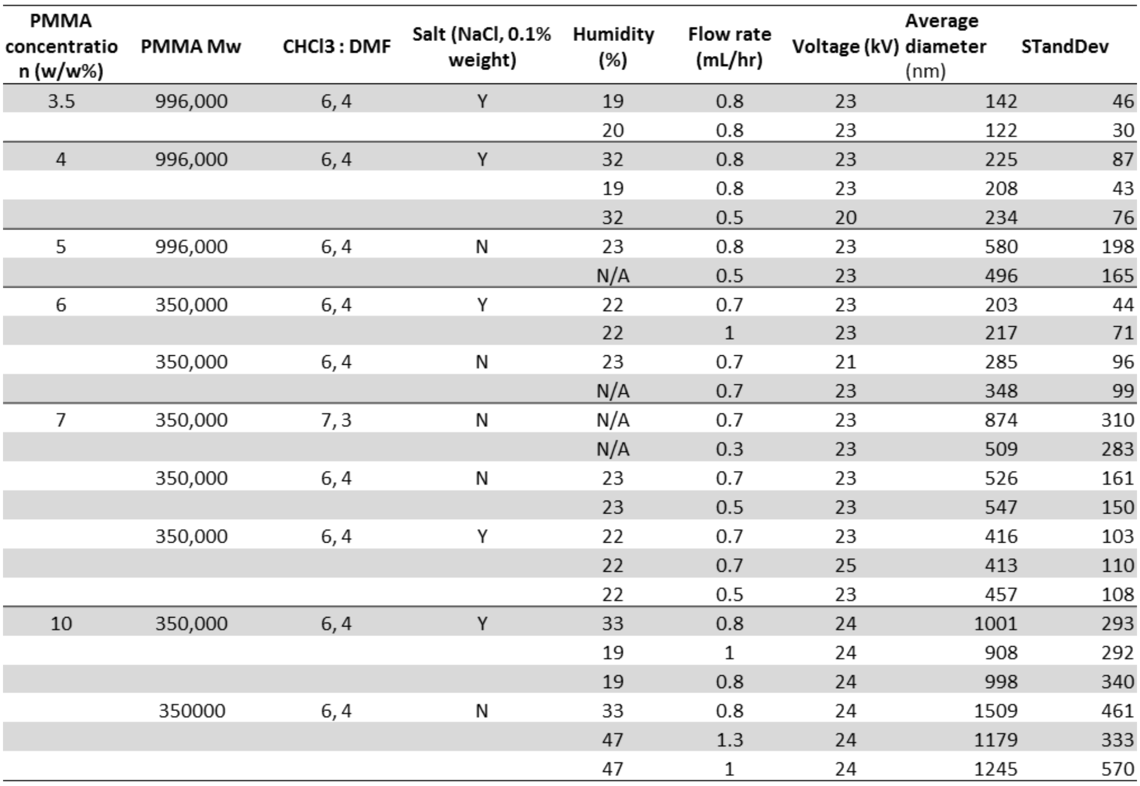

PMMA concentration (w/w%)	PMMA Mw	CHCl3 : DMF	Salt (NaCl, 0.1% weight)	Humidity (%)	Flow rate (mL/hr)	Voltage (kV)	Average diameter (nm)	STandDev
3.5	996,000	6, 4	Y	19	0.8	23	142	46
				20	0.8	23	122	30
4	996,000	6, 4	Y	32	0.8	23	225	87
				19	0.8	23	208	43
				32	0.5	20	234	76
5	996,000	6, 4	N	23	0.8	23	580	198
				N/A	0.5	23	496	165
6	350,000	6, 4	Y	22	0.7	23	203	44
				22	1	23	217	71
	350,000	6, 4	N	23	0.7	21	285	96
				N/A	0.7	23	348	99
7	350,000	7, 3	N	N/A	0.7	23	874	310
				N/A	0.3	23	509	283
	350,000	6, 4	N	23	0.7	23	526	161
				23	0.5	23	547	150
	350,000	6, 4	Y	22	0.7	23	416	103
				22	0.7	25	413	110
				22	0.5	23	457	108
10	350,000	6, 4	Y	33	0.8	24	1001	293
				19	1	24	908	292
				19	0.8	24	998	340
	350000	6, 4	N	33	0.8	24	1509	461
				47	1.3	24	1179	333
				47	1	24	1245	570

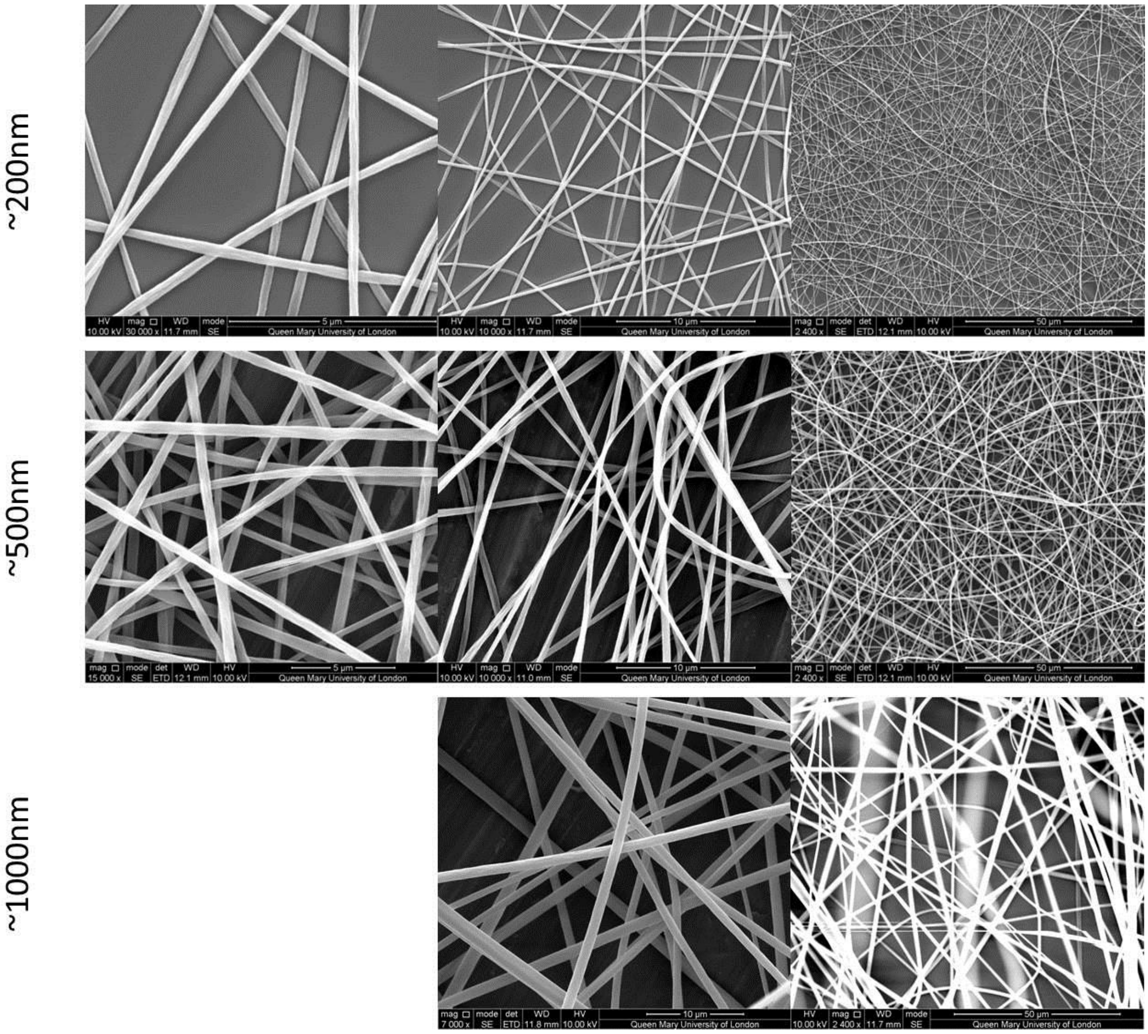

Figure 2.8 SEM images of electrospun fibres from different solution concentration. Small fibres (200 nm, top row) were produced from 3.5% PMMA solution; intermediate fibres (500 nm) from 5% PMMA solution; and biggest fibres (1000 nm) from 10% solutions. Images are taken at different magnifications (see label).

For our purpose, we aimed to generate a set of fibre mats with fibre dimensions ranging from 100 nm to 1000 nm (Fig. 2.8), ideally near 200-300 nm, 500-600 nm, 700-800 nm and 1000 nm, to match dimensions achieved in previous work focusing on nanopatterns generated via colloidal lithography (Gautrot et al., 2014). Therefore PMMA concentrations that suits these conditions were found to be 3.5, 5, 10 (6:4 ratio) and 7% (7:3 ratio) in order to produce around 200/ 300, 500, 1000 and 800 nm fibre diameter respectively.

2.3.2 Thermal annealing

The different annealing temperatures were tested with fibres spun from three different PMMA concentrations: 3.5%, 7% and 10%. This choice was made because fibres produced by the first were thought to be the most sensitive to temperature as they are the smallest, and the opposite reason for the latter. In fact, the thickest fibres were found to require higher annealing temperature in order to deform and bond with the substrate, while the thinner fibres require very low temperature in order to collapse. The increases in fibre diameter, after annealing, are reported in Fig. 2.9.

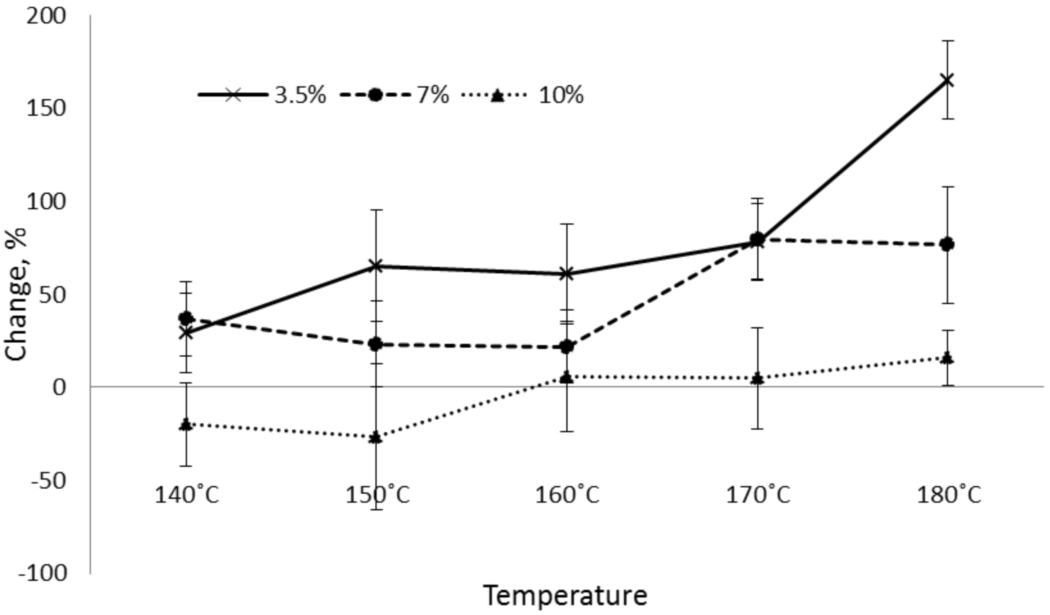

Figure 2.9 Percentile change of three sizes of fibre dimension (obtained from 3.5, 7 and 10% w/w PMMA solution concentration) at different annealing temperatures. Error bars are SD.

Fibres after annealing were also collected for SEM analysis (Fig. 2.10). As can be noticed, bridging of fibres is quite evident for the smallest fibres (around 200 nm) at already 140 ˚C. When increasing temperatures too much it is possible to see that fibres completely deform with much frequent bridging occurrence (as for 800 nm fibres annealed at 180 ˚C).

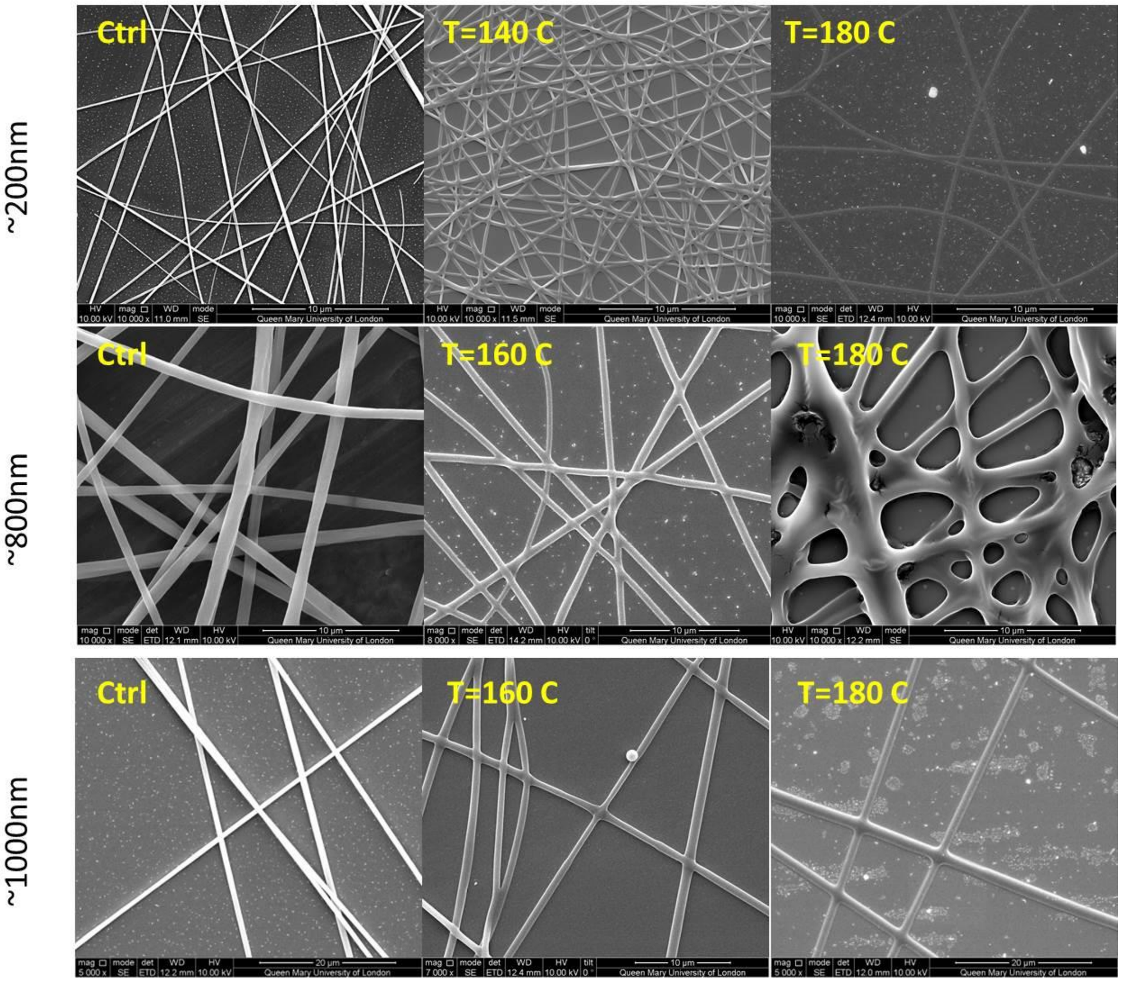

Figure 2.10. SEM images of fibres (200, 800 and 1000 nm diameters as spun) after thermal annealing at various temperatures. The first column represents the fibres as spun.

As shown in the picture (Fig. 2.9, 2.10), the small fibres diameter (around 200 nm) may change sensibly even at lower temperatures (their diameter increases of already 30% even at the lowest temperature) which is not the case for the fibres generated from 10% PMMA solutions. From these results, annealing temperatures were selected for each initial fibre diameter (Table 2.2).

Table 2.2 Annealing temperatures chosen for the fibre diameter of interest.

Initial fibre diameter(nm)	200/300 nm (3.5%)	500 nm (5%)	800 nm (7%)	1000 nm (10%)
T (°C) for annealing	140	150	160	170

2.3.3 Wet etching

Chemical (or wet) etching was performed for the patterning via etching method after fibre annealing. This process is isotropic (Kern and Deckert, 1978, Love et al., 2001), and so etching rate are expected to be the same in all directions. In this case, the layer of gold to be etched was only 15 nm thick, thus it is likely that on the horizontal direction (below the spun fibre) there was also going to be a loss of about 30 nm (15 nm for each fibre side), which is relatively small compared to fibre diameters (from about 200 to 1000 nm). The loss will also be further reduced considering the presence of PMMA annealed fibres covering the gold, thus protecting the area from the access of the etchant. Etchant concentrations and etching times were controlled to optimise the quality of the process aiming to remove gold from the background between fibres and not over-etch the patterned gold fibres themselves, causing so a significant decrease of their diameter.

The starting solution is a mixture of potassium iodide/iodine/water (solution **(1)** from method paragraph) and it was found to lead to irregular contours (Fig. 2.11 A, B), particularly with the thinner fibres. This behaviour is probably caused by hydrophilicity issues: the solution cannot wet properly the gold surface, either due to dust or air bubbles trapped while immersing the sample in the solution.

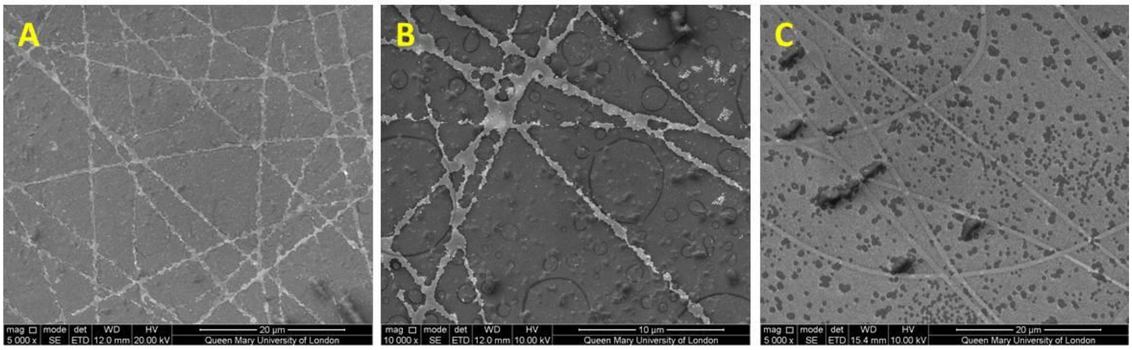

Figure 2.11. Gold etching on glass. Gold exposed areas were etched with solution (1). SEM images showing 700nm fibres (at different magnification) on glass etched with solution (1) without (A, B) and with (C) 0.1% SDS.

The addition of surfactants was used to improve wettability of the nanofibres, but didn't solve the problem and worsened it probably because it was leading to the precipitation of one of the reagents, slowing down the etching reaction and the removal of gold (Fig. 2.11 C).

Cleaning the surface with a plasma treatment improved the contour of the nanofibres. It can also be combined with the addition of ethanol to the solution, to lower surface tension and improve the surface wetting. In Fig. 2.12, examples of nanofibres etched with the original solution after 1 min of plasma oxidation are shown.

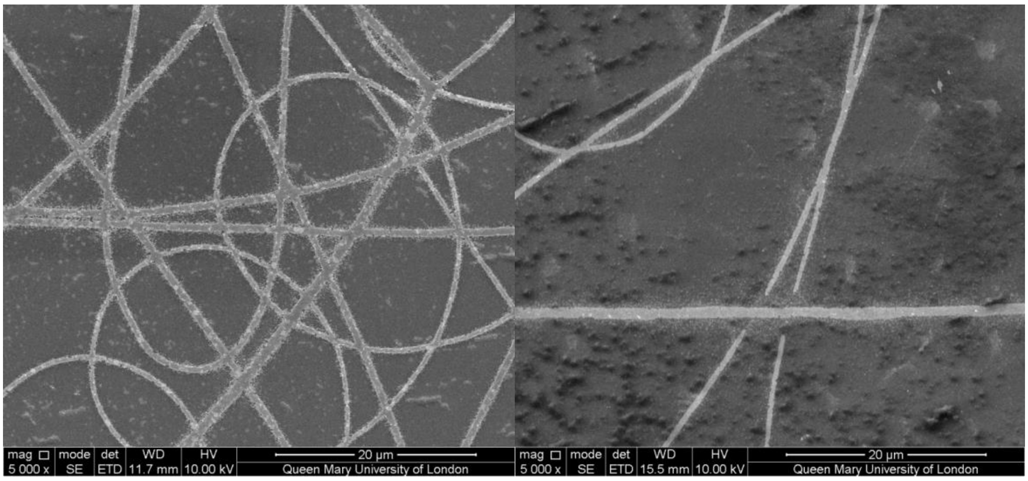

Figure 2.12 SEM images representing 800 nm (left) and 550nm (right) fibres on glass after 1min plasma treatment and etching with solution (1).

For the smallest fibres (spun from 3.5% PMMA solution) the solution used was found to over-etch these fibres, due to their thinner diameter. For these, a less concentrated solution (**(2)**) was used and different times of etching were tested as well (see Tab. 2.3). It was possible, in this way, to optimize the etching time and etchant concentration to obtain continuous and quite regular nanofibres with controlled dimensions (Fig. 2.13 C).

These conditions were then used for etching on gold coated silicon wafers for AFM imaging. It was found that solution **(1)** led to over-etching of the fibres for these samples and solution **(2)** was used thereafter (Tab. 2.3). In this case, it was also possible to find the correct time to produce fine nanofibres.

One minute plasma treatment was performed for both nanofibres on wafer and with the smallest fibre size on glass (around 200/ 300 nm diameter) before the etching.

Table 2.3. Etching conditions tested on wafer and glass. W= gold coated silicon wafer (different fibre dimensions); G= 200/ 300 nm diameter fibres on gold coated glass slides. Etching via solution (1) – the more concentrated – led to over-etching for all the time tested; with solution (2) it was possible to obtain continuous nanofibres by optimizing the etching time.

Conditions		**Sample**	**Conditions**		**Sample**
Solution **(1)**	45 s	G	Solution **(2)**	65 s	W, G
	55 s	W, G		70 s	W, G
	60 s	W		75 s	G
	65 s	W		80 s	G

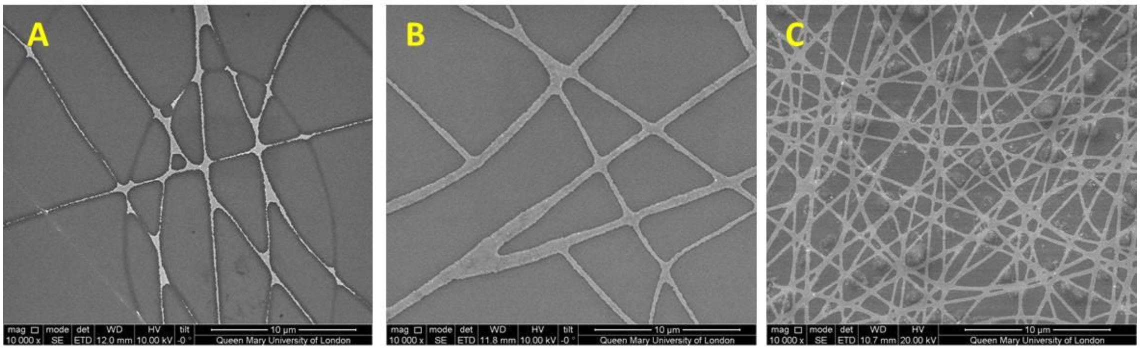

Figure 2.13. SEM images of about 600 nm diameter gold fibre on wafer (A, B) etched for 65 sec with solution (1) (A) and (2) (B). Solution (1) over etches the sample. 300 nm diameter fibres on glass after 70 s with solution (2) (C).

The best results were obtained using solution **(2)** and etching for 60/65 seconds on wafer and 70 seconds for the smallest fibres on glass slide. Another mentioned problem with etching is that the longest the etching time the higher the decrease in fibre diameter, so for high etching time even if the nanofibres obtained are clear, the fibres have undergone significant changes in diameter (Fig. 2.14).

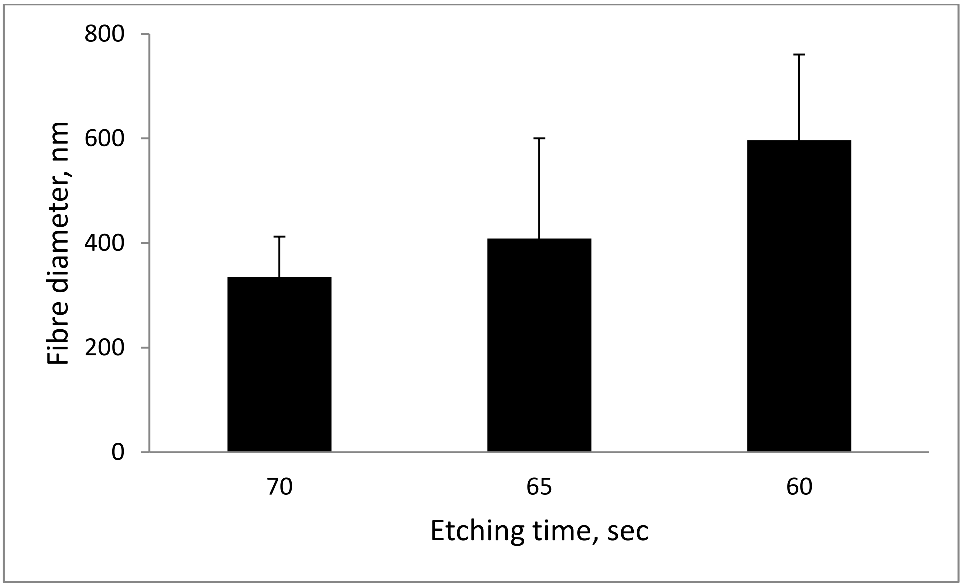

Figure 2.14. Effect of etching time for about 600 nm fibre diameter. Increasing the etching time decreases the fibre diameter. Error bars are SD.

AFM imaging was also performed to characterise the topography and in particular the thickness of the nanofibres. As evidenced by images (Fig. 2.15), the height measured (around 12 nm) is similar to the expected thickness of the gold layer deposited on the wafer (15 nm).

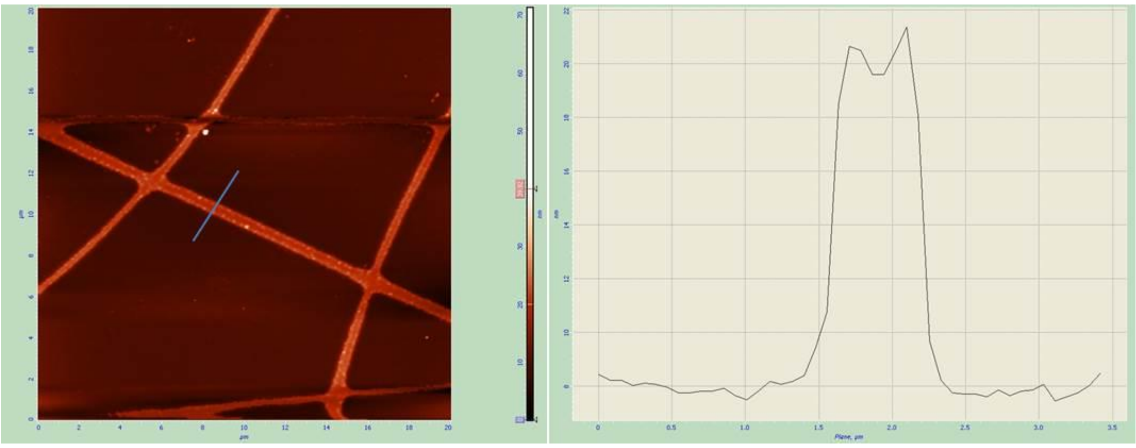

Figure 2.15. AFM image (left) and height profile (right) of the gold nanofibres left after etching (fibres diameter around 600 nm). The height of the gold fibre left is about 15 nm.

EDS was used to characterise the chemical composition of the sample. The technique relies on the interaction of a source of X-ray and the sample. Analysing the energy emitted by the surface after the excitation, it is possible to know which atoms enter in its composition and their relative ratios. The outcome is a spectrum where each atom possesses a unique peak: the area beneath the peak is proportional to the content of this atom for the surface analysed.

Fig. 2.16 shows a picture from EDS with the related composition. As shown in the image, gold was almost completely removed from the background, where only silicon is detected.

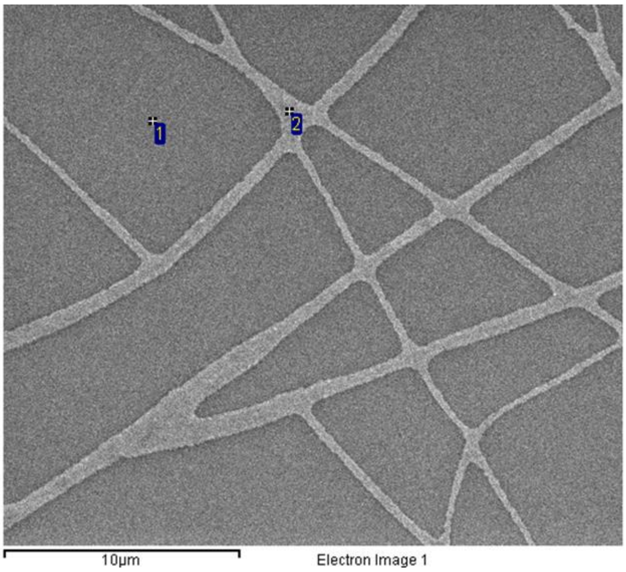

	Si	Au
1	99.57	0.43
2	85.99	14.01

Figure 2.16. SEM image of the nanofibres left after 65 s etching on wafer. Spectra are detected in points 1 and 2 on the image and a table with the detected elements and concentration (% in weight) is shown

2.3.4 Polymer brush growth

Polymer brushes are an effective and versatile method to engineer surface chemistry and prevent or promote protein adhesion (Brown et al., 2005, Tan et al., 2013, Tugulu et al., 2007). For our purpose, preventing protein adhesion is required to analyse the response of cells when they are "forced" to adhere and proliferate selectively on the areas of the nanopatterned fibres.

Two polymers were used for this purpose: poly oligo(ethylene glycol methyl ether methacrylate) (POEGMA) and poly(2-(methacryloyloxy)ethyl-dimethyl-(3-sulfopropyl)-ammonium hydroxide) (PMEDSAH). Such polymer brushes display excellent protein resistance, due to their hydrophilicity and high packing density and have proved particularly robust for the design of micropatterned cell arrays, even after long incubation times and at high cell densities (Gautrot et al., 2012, Gautrot et al., 2010, Tan et al., 2013). The polymer brushes were grown via ATRP on the target surfaces pre- functionalized with initiator **(1)** (from par. 2.2.2 “silanization”). Brush thickness and density can be controlled by manipulating polymerization parameters, such as time of polymerization and catalyst composition.

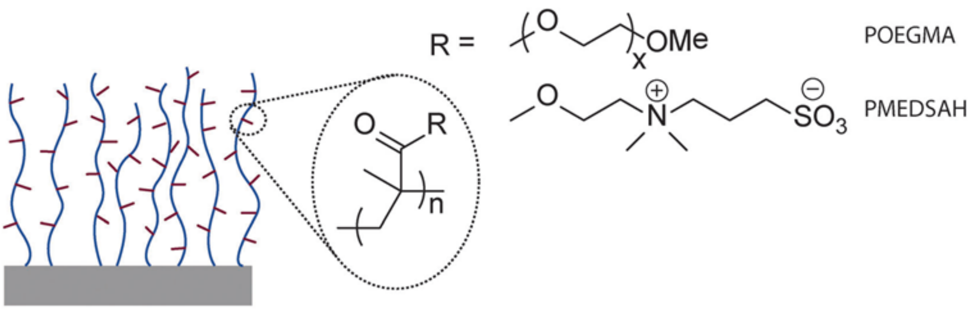

Figure 2.17 POEGMA and PMEDSAH brushes structure grown via ATRP (Tan et al., 2013). Brushes grow perpendicular to the surface with the R group on the side of the chains.

In order to assess if the thermal annealing was damaging the silane initiator, samples coated with homogenous brushes were compared, where the brushes were grown after the silane coated surface underwent heat treatment or not. A slight decrease was observed in the height of the polymer brushes layer grown from annealed and not substrates (not annealed = 50.44 nm, annealed at 140˚C = 46.59 nm and annealed at 170˚ C = 43.11 nm brushes).

It was furthermore found that a very thin layer of PMMA (~1nm) remains attached to the silicon surface even after chloroform treatment (Fig. 2.18, AFM): this probably represents a chemical bound that is very hard to eliminate. In the figure, PMMA fibres were spun, annealed and removed. EDS analysis after ATRP reveals as well that there may be some PMMA left on the nanofibres, because carbon was found in correspondence of that and may derive from PMMA spun (Fig. 2.18, EDS).

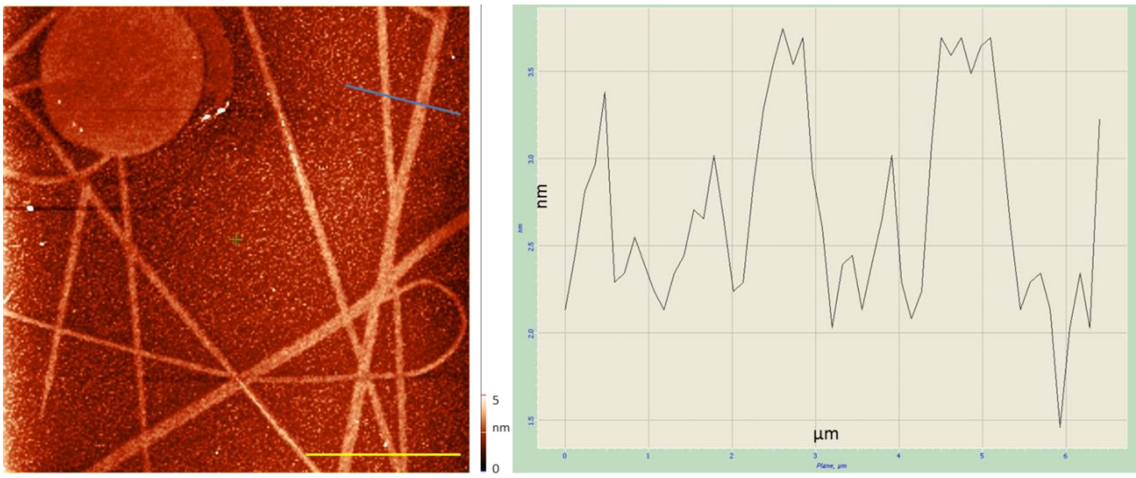

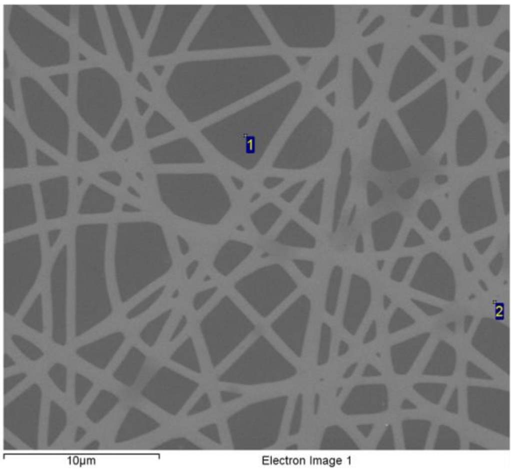

	Si	C	O
1	85.36	12.98	1.66
2	90.63	9.00	0.37

Figure 2.18. Top. Fibres were electrospun, annealed and then removed with $CHCl_3$. The surface was then characterised via AFM (top left) showing a very thin layer of residual PMMA left on the silicon (see height profile of the blue line, right). Scale bar 10 µm. Bottom. After polymer brushes growth and PMMA fibre removal, EDS analysis was performed to check the composition of the resulting pattern: some carbon is detected on the nanofibres even after removal of the PMMA fibres, suggesting there may be some PMMA left.

AFM images of nanofibres obtained after etching and brush growth are shown in Fig.2.19. As it can be noticed, the gold fibres are higher (see the AFM profile) than the background (25 nm gap, POEGMA brushes in this case), while it was expected to be the opposite as they should be only 15 nm compared with the polymer brush coating, which should be around 30 nm in this case (polymerization time set at 30 min for POEGMA): so there should theoretically be a 15 nm step between the background and the gold fibre.

The reason of this behaviour were not elucidated: hypothesis are that either the undecanthiol is not protecting the gold fibres efficiently and some polymer brushes may actually grow on gold areas, or if the gold is not etched completely from the background that may cause a decrease in the density of tethered ATRP initiators, which will in turn result in less dense brushes, collapsed on the surface and displaying significantly reduced overall coating thicknesses.

Due to difficulties in obtaining a proper passivation of the background and the uncertainties of the etching step, the second nanopatterning method was explored, for ENL, based on the direct growth of polymer brushes between electrospun nanofibres (patterning via ATRP).

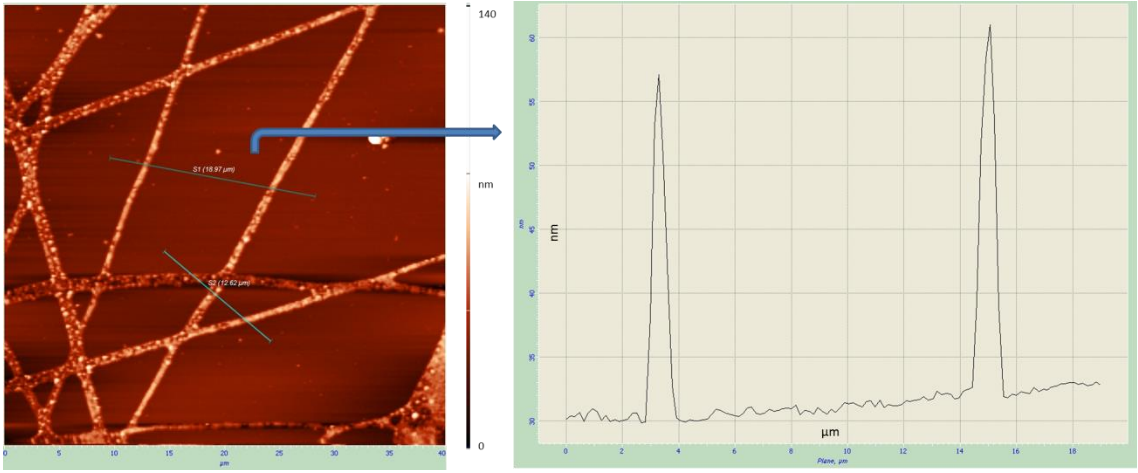

Figure 2.19. AFM imaging of nanopatterned substrates after polymer brush growth (POEGMA), prepared via the patterning via etching method. Left, topography image; right, height profile. The gold fibres left are higher (see profile) than the POEGMA functionalised background.

For this method, after removal of fibres, we found that the height of the brush layer, defining the remaining fibrous patterns, was 30 ± 2 nm high (for POEGMA), comparable to the thickness predicted and that of homogenous brushes grown in identical conditions and evaluated by ellipsometry (Fig. 2.20, 2.21). The contour profile of the resulting nanofibres is sharp (90 nm/µm, from AFM profiles) and the width of the resulting fibres closely matches that of the corresponding annealed fibres (Fig. 2.22), confirming the efficiency of the fibrous masks to control the localisation of the polymer brushes generated via ENL. In addition, it was possible to directly image the resulting nanofibres using SEM (Fig. 2.20 and 2.21), due to the difference in electron density between the exposed silicon substrate and the insulating brush coating. This allowed us to confirm the size of the fibres generated but also their density (Fig. 2.24).

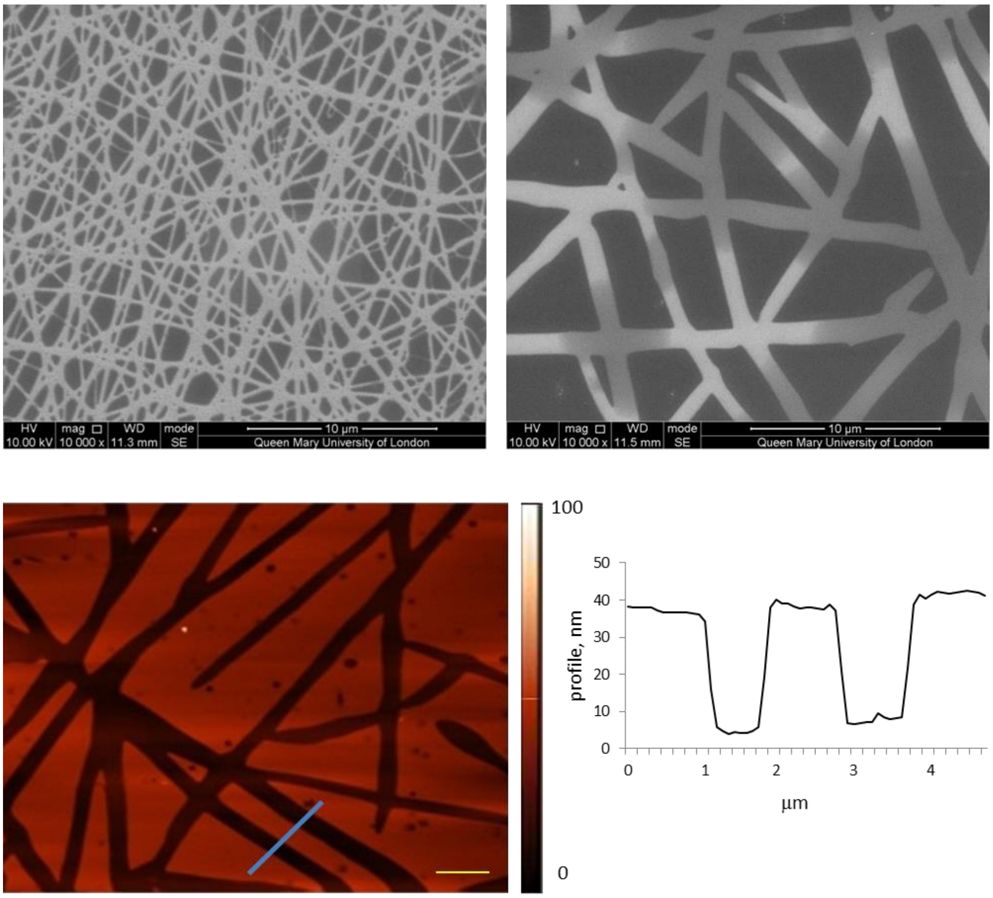

Figure 2.20. POEGMA brushes produced following the patterning via ATRP method. SEM images (top row) of nanofibres with 250 nm (left) and 1000 nm (right) diameter. AFM (bottom row) of 1000 nm nanofibres with height profile. Scale bar is 2 µm.

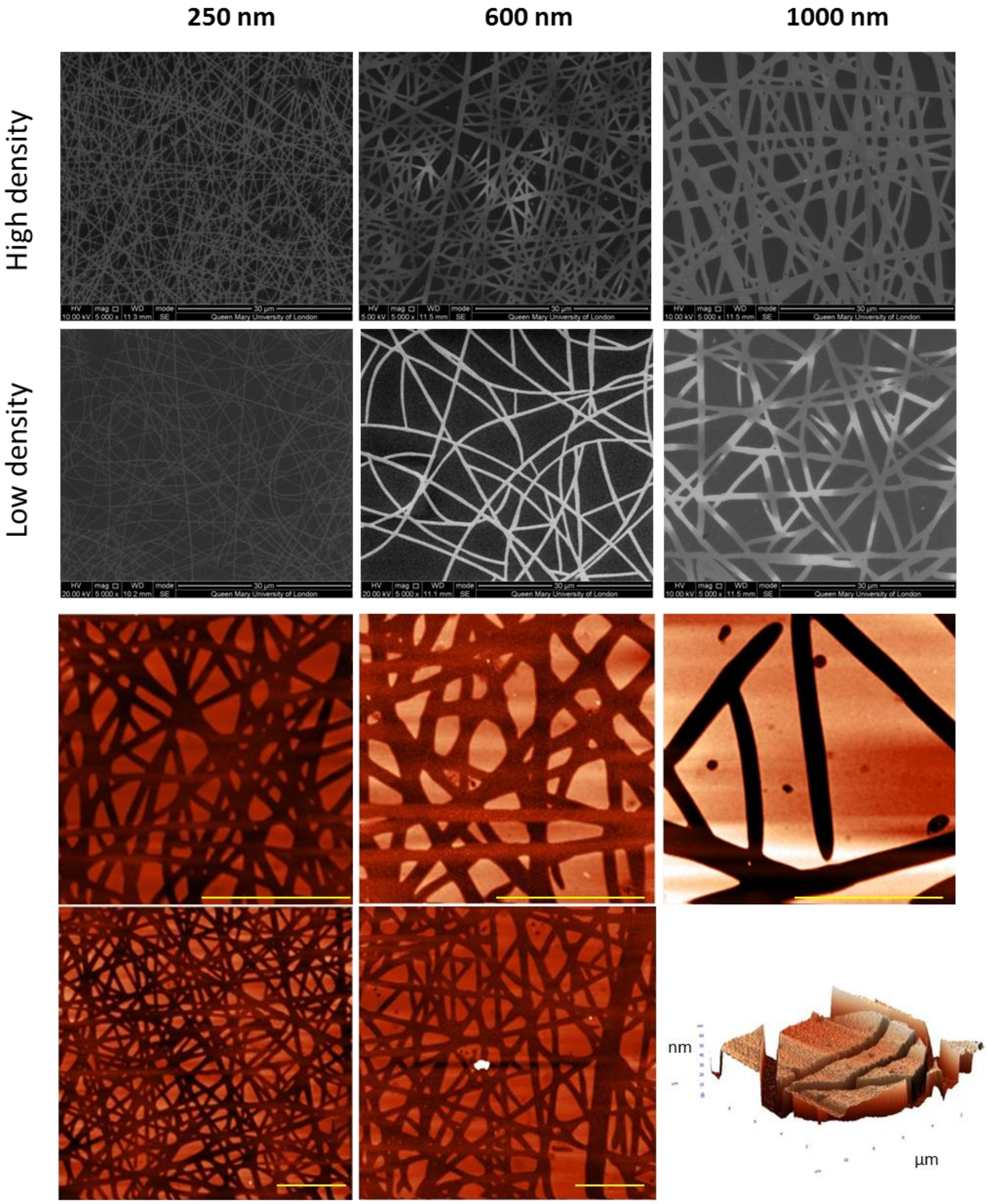

Figure 2.21. Patterns produced via ATRP method. Representative SEM (upper row, high density nanofibres and lower row low density) and AFM (high density nanofibres) images of the pattern after polymer brushes and mask removal. First column is 250 nm diameter nanofibres, second column is 600 nm nanofibres and last column is 1000 nm nanofibres (including a 3D AFM image). Scale bar in AFM images is 5 µm.

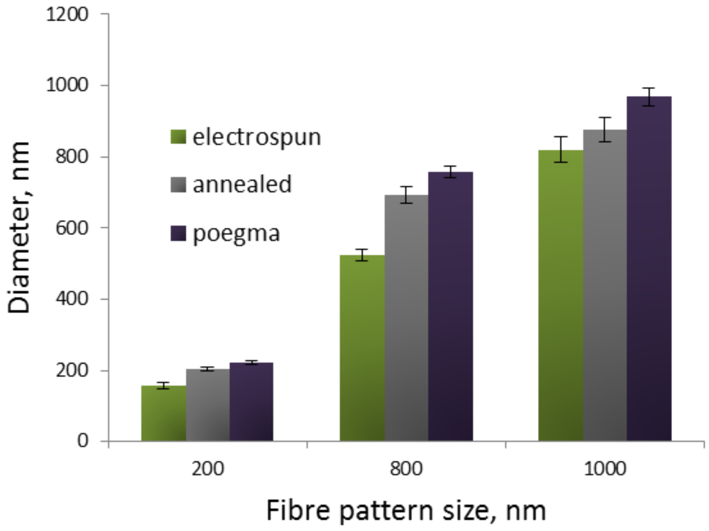

Figure 2.22 Evolution of fibre diameter over the patterning process following ATRP method: after electrospinning (green), annealing (grey) and polymer brushes functionalization (purple). Error bars are standard errors (n ≥ 3).

It was also assessed if there is any loss in the brushes layer height due to the treatment with chloroform. Data show that the differences in height before and after the treatment are not significant (Fig. 2.23).

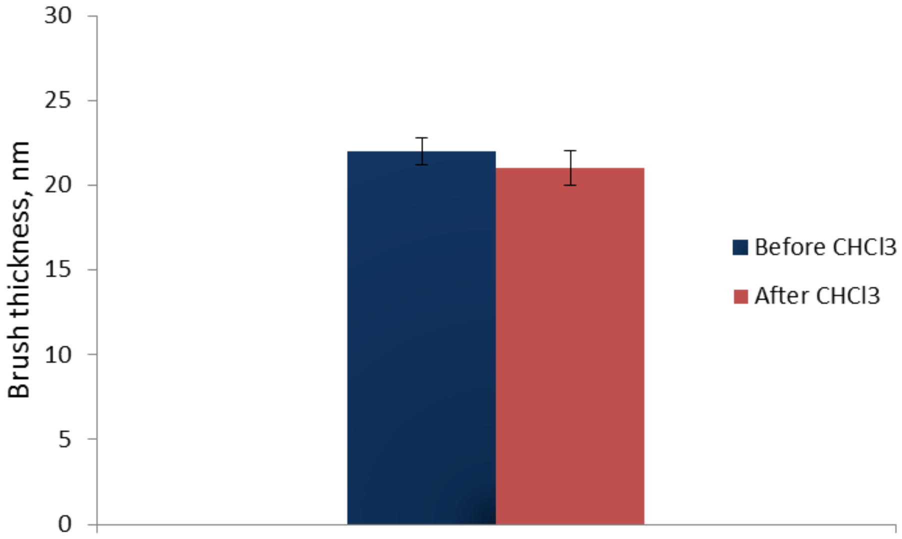

Figure 2.23. Change in brush layer thickness (measured via ellipsometry after ATRP) before and after treatment with chloroform for removing PMMA fibres. Error bars are SE. No significant differences can be noticed.

We successfully managed to obtain nanofibres with different densities; in particular the aim was to have low (around 20% of the area covered by fibres), intermediate (around 40%) and high (around 60%) nanofibres density. As expected, nanofibres with the smallest diameters (around 250 nm) presents also smaller gaps between fibres, while for the 550 and 800 nm fibre patterns the gap distributions are similar (Fig. 2.24). We found that large fibres (e.g. 800 nm and 1 µm) displayed a poorer control of the distance between fibres and their density (especially when high densities are desired), presumably due to the difficulty of fully annealing the rigid fibres generated with these dimensions. Fractal dimension of the nanofibres with 250, 550 and 1000 nm diameter at low density were also assessed. This measurement helps further characterising complex patterns. The data show that average fractal dimensions were comparable across patterns with similar density and different fibre diameters.

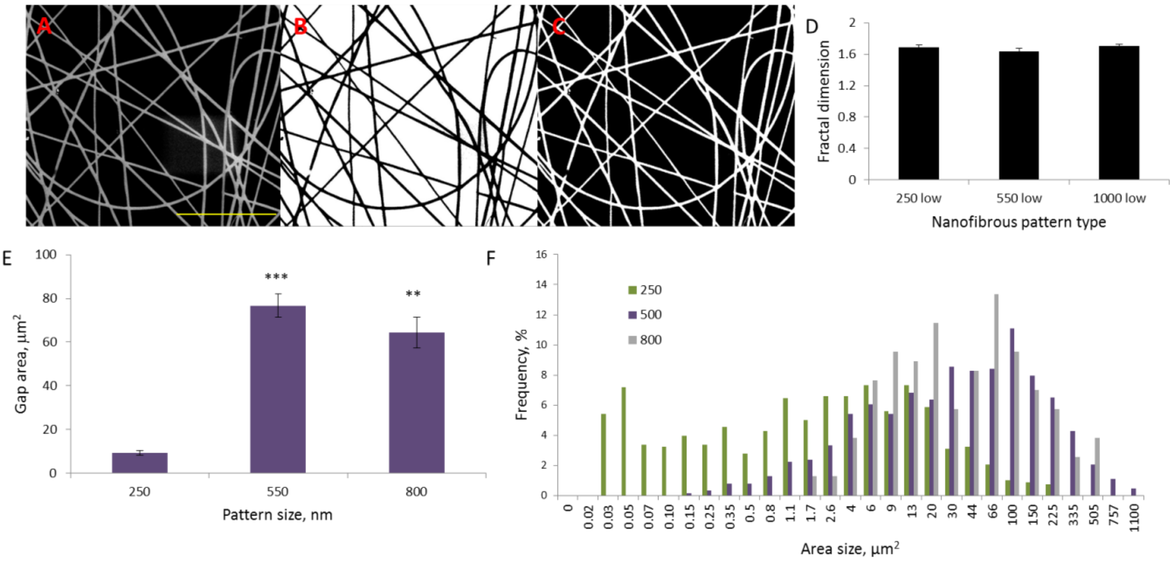

Figure 2.24. Methodology used to assess fibre density and the gap area between the fibres. From a starting SEM image (A, 550 nm fibres and low density nanofibres. Scale bar is 30 µm) a threshold was applied to get a BW image (B and C inverted) from which the % of area covered from fibres (B) and the area of the gap in between fibres (C) was calculated. Average area of the gap between the fibres for 250, 550 and 800 nm diameter low density nanofibres (E). Error bars are standard deviation, n≥ 200, number of sampling. Comparisons are referred to the 250 nm. For statistical test: *, P < 0.05; **, P < 0.01; ***, P < 0.001; ****, P < 0.0001. Gap area distribution on different nanofibres diameters, 250 (green), 500 and 800 nm, at low density (F). Fractal dimension of the pattern with low density fibres and diameters of 250, 550 and 1000 nm was also assessed using ImageJ (D).

The MEDSAH system (which was only tested with the patterning via ATRP method) was found to be less reliable (in terms of thickness achieved, see Fig. 2.25) and more difficult to manage due to the formation of glue during polymerization. Although it was possible to passivate the background (Fig. 2.25) with this polymer too and some cell assays were carried out, this system was then left aside and POEGMA was chosen as final polymer brush coating due to the ease of its handling and better reproducibility.

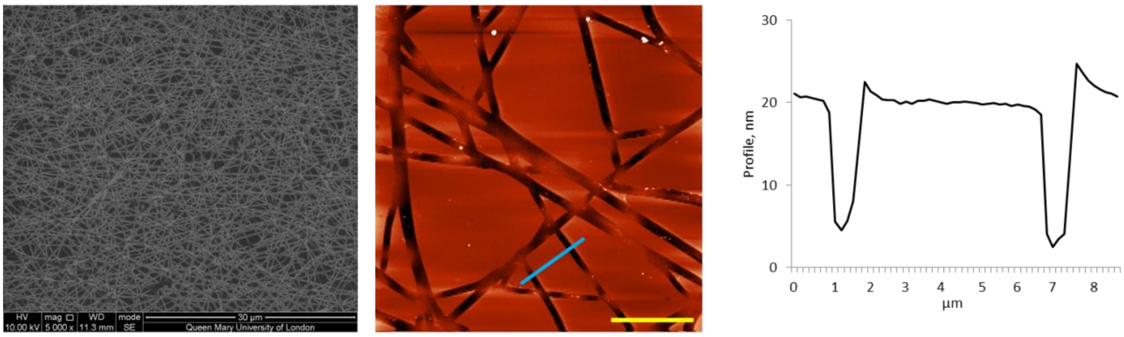

Figure 2.25. PMEDSAH brushes grown via the patterning ATRP method. SEM of 300 nm diameter fibrous pattern (left) and AFM of 1000 nm fibrous pattern with height profile (right). Scale bar is 10 µm.

2.3.5 Fibronectin deposition

To enable integrin-mediated cell adhesion, fibronectin was deposited on the nanofibres (Fig. 2.26) after POEGMA and PMEDSAH brushes growth. Fluorescence imaging confirmed that fibronectin selectively adsorbed to areas unprotected by the brushes and formed fibrous fibronectin nanofibres with controlled dimensions: POEGMA coating results in a better control of fibronectin adsorption than PMEDSAH. The intensity profile across fibres within the resulting nanofibres, with sharp peaks associated with fibronectin fibres (Figure 2.26, inset), confirmed the specificity of the protein adsorption and the quality of the resulting patterns. This is in good agreement with results obtained for micro-patterned POEGMA brushes (Gautrot et al., 2010), indicating that the initiator layer deposited in the first step of the ENL process remained intact during electrospinning and annealing steps and enabled dense brushes to be generated, with high protein resistance. This also indicates that fibronectin adsorbs well on the exposed fibres to provide a high contrast between fibres and the background.

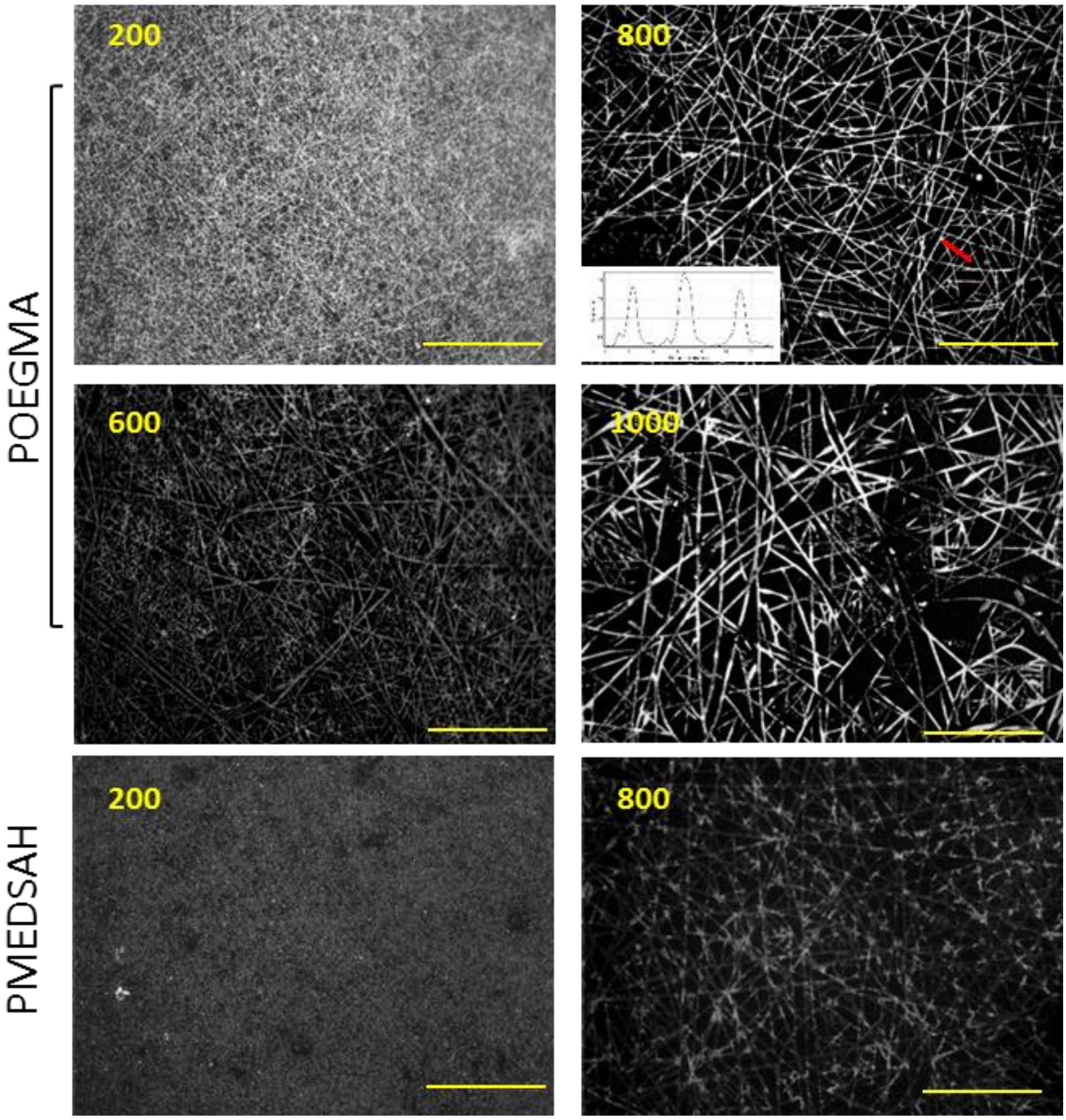

Figure 2.26. Images from epifluorescent microscopy showing nanofibres after fibronectin deposition and immunostaining. POEGMA and PMEDSAH brushes coating with different fibre size: 200, 600, 800 and 1000 nm for POEGMA and 200 and 800 nm for PMEDSAH. The inset shows the corresponding fibronectin intensity profile. Scale bar 50 µm.

In addition, we examined whether the hydrophobic initiator layer exposed within nanofibres led to the formation of protein clusters and associated changes in nanoscale topography, as was observed during the adsorption of fibronectin to hydrophobic polymers (Guerra et al., 2010, Bathawab et al., 2015). Measurements of surface roughness via AFM did not highlight any major change in nanoscale topography, either along fibres themselves or within POEGMA-coated areas (Figure 2.27). This confirms that fibronectin deposited homogenously on the nanofibres.

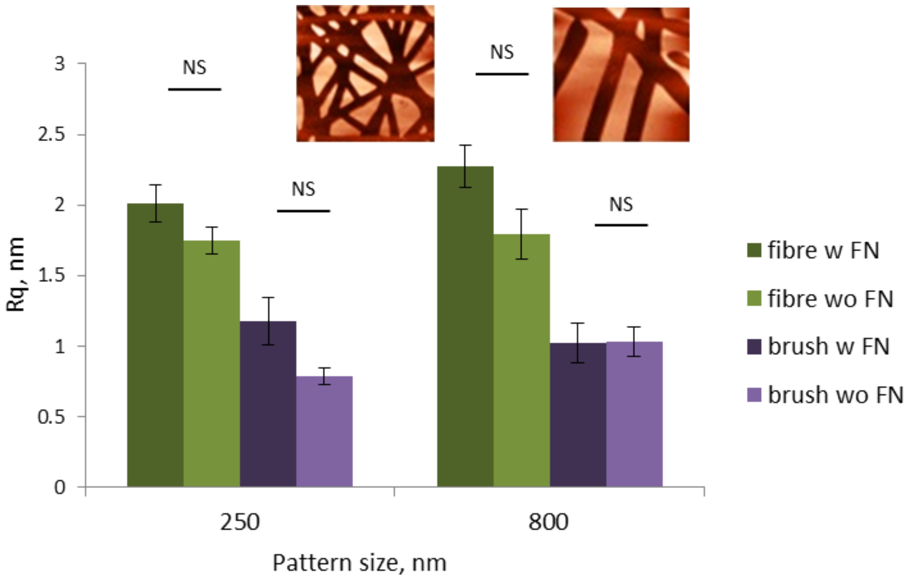

Figure 2.27 Roughness analysis of 250 and 800 nm nanofibres (see representative AFM images for the two nanofibres size in the inset) with POEGMA brushes. Roughness was assessed before (wo FN) and after (w FN) FN deposition. Error bars are standard errors (n = 3). No significant differences are noticeable for these values (see tab. S3 for the details of statistical analysis).

2.4 Conclusions

This chapter introduced the fabrication of fibrous nanopatterns using a novel, scalable and inexpensive method – Electrospun Nanofibre Lithography, ENL. The nanofibres produced will be used for cell assays in order to study cell adhesion, spreading and trying to elucidate signalling cascade involved in cell sensing of the extracellular matrix. For this reason, the nanofibres produced have to present certain characteristics which will allow this study: in particular, the size and geometry of the nanofibres have to be controlled so that cell sensing of the nanofibres dimensions can be studied systematically. Forcing cell to adhere to certain area with a defined shape and size has proven to give insight in how cells sense the extracellular environment (Dalby et al., 2007, Cavalcanti-Adam et al., 2006, Tan et al., 2013, Gautrot et al., 2010).

As will be explained in the following chapters, the main features that were controlled are the size of the fibrous patter and the density: these two parameters were successfully controlled using ENL, allowing the preparation of nanofibres ranging from 200 to 1000nm and different densities.

The nanofibres have been produced in a stepwise process and two procedures were followed. The second one (which does not include the etching step) was then chosen due to its faster and more reliable process. Electrospinning was first carried out to allow the deposition of a mesh of polymeric fibres on the surface. The resulting fibres were then annealed and a layer of polymer brushes were grown in the background. The spun fibres were then removed leaving a quasi- 2D nanopatterned area with fibrous shape and producing a cell adhesive area (the fibre), surrounded by a layer of non-fouling polymer brush which will prevent unwanted cell adhesion.

Electrospinning is a crucial step in defining fibre size: parameters like the polymer concentration (PMMA in this case), and the ratio of the solvents (DMF and $CHCl_3$) were optimized to obtain a range of fibre spun from 200 to 1000nm. Process parameters such as flow rate and voltage applied were adjusted during the spinning.

Thermal annealing was then used to improve the contact area between the fibre and the surface: for this step temperatures were carefully selected in order to not modify excessively the geometry of the fibres achieved via electrospinning.

Controlled growth of polymer brushes in between fibres was finally obtained via the polymerisation of POEGMA or PMEDSAH. The former was finally selected for use as passivating background due to the ease of its production.

Fibronectin, an extracellular matrix protein that allows and promotes cell adhesion, was then deposited on the nanofibres showing that the passivating background is preventing protein adhesion while these selectively attach on the areas of the fibrous pattern.

The next chapters will describe how cell assays were performed in order to understand how cells feel the different size and density of the nanofibres. Proliferation, morphology and focal adhesion maturation were assessed, comparing especially the geometrical maturation of FA on different size adhesion sites.

Chapter 3

Cell sensing of the matrix nanoscale geometry

3.1 Introduction

Cells are not “free-standing” objects but require to adhere to the extracellular matrix (ECM) and to other cells in order to survive, carry out their function and form more complex structures (tissues). It has been shown in the last decades that cells feel and respond to the physical properties of the complex environment constituted by the ECM, contact with neighbouring cells and soluble growth factors and cytokines. Focal adhesion (FA) formation and maturation are important processes via which cells sense and adhere to the ECM and impact on signalling pathways eventually controlling cell phenotype (Berrier and Yamada, 2007, Parsons et al., 2010). Such cellular sensing of the adhesive landscape occurs at different length scales, from the microscale, at which cell shape and multi-cellular assemblies are controlled (McBeath et al., 2004, Connelly et al., 2010, Gautrot et al., 2012), to the nanoscale, at which the formation and dynamics of single adhesions are regulated (Huang et al., 2009, Schvartzman et al., 2011, Cavalcanti-Adam et al., 2006, Dalby et al., 2007, Gautrot et al., 2014). Importantly, underlying these phenomena, the prevention of FA assembly leads to the disruption of the cell cytoskeleton: when cells are forced to adhere on small areas or when adhesion points are too far apart to allow integrin clustering and the interaction of key adapter proteins, cell spreading is impaired and other signalling pathways are disrupted leading, for example, to stem cell differentiation (Biggs et al., 2009, Lee et al., 2010).

FAs are initiated and regulated by the binding of integrins to the ECM (Petit and Thiery, 2000), as described in Chapter 1. This phenomenon is followed by their clustering and the recruitment of other molecules, amongst which vinculin, talin, VASP, zyxin, paxillin, p130 Cas, focal adhesion kinase (FAK) and integrin-linked kinase (ILK) play an important role in determining FA stability and cell phenotype. In addition, the precise positioning of these molecules and 3D organisation of the structure of FAs is important to the stability of FAs formed, their ability to sustain mechanical forces and transmit downstream signals (Kanchanawong et al., 2010, Case et al., 2015). The dynamics of such processes is regulated by the transmission of forces bidirectionally, inside-out and outside-in: when cells cannot exert adequate grip on their surrounding environment, FAs are destabilised (Gallant et al., 2005). In turn, the reorganisation of the cell cytoskeleton and formation of stress fibre (contractile actin bundles) are strongly dependent on transmission of intracellular forces. Adapter proteins such as talin and vinculin play an important role in such processes and regulate adhesion size, shape, as well as cell spreading and shape (Liu et al., 2015, Carisey et al., 2013, Humphries et al., 2007). Upon activation of vinculin FAs are generally stabilised, increase in size and, as a result, cell migration decreases. Considering the essential role of integrin clustering to the formation and development of FAs, it is clear that integrin expression itself should have a profound impact on cell adhesion and associated mechanotransduction. Indeed, integrin expression level and the type of heterodimers expressed (e.g. α5β1 vs αvβ3) was found to impact on cell shape, the architecture of the cytoskeleton, as well as cell motility (Gimond et al., 1999, Danen et al., 2005, Truong and Danen, 2009). Such changes are associated with marked changes in signalling via Rho GTPases (Gimond et al., 1999, Danen et al., 2005, Truong and Danen, 2009, Danen et al., 2002) and, strikingly, the scattering of cell clusters (Gimond et al., 1999). The shape, number and size of FAs were also found to be strongly correlated with such changes in phenotype. Such effect may be explained by the differential regulation of Rho GTPases Rac and RhoA (Danen et al., 2005), as well as the differential binding affinity of β1 and β3 integrins for soluble fibronectin (and associated impact on fibrillogenesis). These phenomena also correlate with important changes in the dynamics and nanoscale organisation of α5β1 and αvβ3 integrins (Danen et al., 2005, Rossier et al., 2012). Differential regulation of FA maturation and cell phenotype was also evidenced between different β1 heterodimers (e.g. α5 and α4) (Mostafavi-Pour et al., 2003). In addition, α5β1 and αvβ3 integrins play important roles in the ability of cells to generate forces, respond to applied mechanical stimulations and associated mechanotransduction (Roca-Cusachs et al., 2009, Balcioglu H. E. et al., 2015). Hence, these studies highlight a direct relationship between integrin expression, the regulation of the shape and size of adhesions and the sensing of physical properties of the ECM.

The sensing of the ECM is thus of particular importance to the regulation of cell phenotype. To investigate the role of different microenvironmental cues, engineered biointerfaces presenting controlled chemistry, topography and mechanical properties have been developed. In particular, the modification of surfaces to create micro- to nano-scale features has been exploited to regulate FA maturation and cell phenotype (see Chapter 1).

It was previously showed that the size of adhesions (100 nm to 3 µm circular patches) primarily controls the assembly of the cytoskeleton, and that blocking the geometrical maturation of adhesions does not restrict protein recruitment significantly, nor the phosphorylation of proteins recruited to adhesions or the assembly of ECM proteins at adhesion sites (Gautrot et al., 2014). In contrast, we found that adhesion dynamics (rate of diffusion of vinculin to the adhesions) was altered. This may highlight the role of adhesion dynamics, assembly and disassembly, as important stages involved in nanoscale sensing. In this respect, the continuity of the matrix, its geometry and topography are expected to regulate such dynamic processes. How such nanoscale geometrical cues impact on adhesion size and shape as well as cell spreading and shape is not understood. In addition, how the differential expression of integrins impacts on the sensing of nanoscale geometry is not clear.

The nanopatterns produced as explained in the previous chapter were then used for the detailed investigation of mechanisms underlying cell sensing of the nanoscale geometry of the ECM. The nanofibers generated using this method mimic better the fibrous structure of some natural matrices, but without introducing complex 3D effects (topography and changes in fibre curvature). In addition, these quasi-2D nanofibers allow comparison with other 2D nanopatterns displaying circular patches of controlled diameters, previously studied (Gautrot et al., 2014). This allows to investigate relationships between adhesion size and geometry and cell shape and spreading in a more realistic scenario, including with respect to the continuity of the matrix. As ENL allows the patterning of thin glass coverslips and does not introduce structures with strong refractive index mismatch, it is compatible with a broad range of high resolution live imaging microscopy techniques. This platform was then used to investigate the influence of adhesion geometry on cell spreading and shape. We make comparisons between cell response to the size of nanopatterns in the case of circular discrete patches and continuous nanofibers with similar range of sizes and density. Finally, the role of integrin expression on nanoscale sensing of the geometry of the adhesive landscape was investigated.

3.2 Materials and methods

3.2.1 Materials and chemicals.

Triton X-100, gelatin, Phallodin –Tetramethylrhodamine B isothiocyanate, PFA (paraformaldehyde), Monoclonal AntiVinculin antibody produced in mouse, Mowiol 4-88, glycerol, DAPI (4,6-diamidino-2-phenylindole), GTA (glutaraldehyde), phosphate buffer (PB) 0.1M, phosphate-buffered saline (PBS, 150 mM), and labelled BSA (Albumin, Tetramethylrhodamine isothiocyanate bovine) were purchased from Sigma Aldrich. Fibronectin from human plasma (1 mg/ml) was from Millipore. Foetal bovine serum (FBS) was from PAA. DMEM (500 mL), trypsin, versene (100 mL), Alexa Fluor goat anti-mouse 488 were from Life Technologies. Polyclonal anti-Fibronectin antibody (100 µg) from rabbit, polyclonal anti-laminin from rabbit, αv (Anti-Integrin alpha V antibody [EPR16800]) and β1 (Anti-Integrin beta 1 antibody [P5D2]) integrin monomer were from abcam. Penicillin-Streptomycin (5,000 U/mL), L-glutamine, Alexa Fluor donkey anti rabbit 594 and goat anti rabbit 488 were from Fisher. Deionised water was obtained using a Synergy system from Millipore.

3.2.2 PLL-PEG functionalization of circular patches

Circular nanopatterns of 300, 500 and 800 nm were obtained from Prof. Sutherland, (iNANO) and fabricated as described in (Di Cio et al., 2016, Malmstrom et al., 2010) The resulting substrates were then washed twice with 70% ethanol and left to sterilise in 70% ethanol for 5 min before washing twice with phosphate buffer saline (PBS, Sigma). The substrates were incubated in a solution of poly(L-lysine)-g-poly(ethylene glycol) PLL(20)-g[3.5]-PEG(2) (Surface Solutions, Switzerland, 25 mg/mL) in (HEPES, 10 mM, pH 7.4, Gibco) for 45 min, then washed with PBS twice. Substrates were incubated in a fibronectin solution straight after (see details for FN deposition in Chapter 2).

3.2.3 Cell culture and seeding.

HaCaT and GE cells were cultured in DMEM supplemented with 10% FBS, glutamine and antibiotics. GE β1-deficient epithelial cells (GE) and GE cells in which α5β1 and αvβ3 integrins are stably expressed (GEβ1 and GEβ3, respectively, obtained by retroviral expression (Danen et al., 2002)) have been previously described (expression levels of α5β1 and αvβ3 integrins are reported in previously published work). Cells were cultured to confluency (about 80% density) and were detached using trypsin/versene (1:9) and reseeded on either fibrous patterns functionalised with fibronectin (see Chapter 2 for details) or on circular patches after PLL –PEG treatment and fibronectin functionalization. HaCat were seeded in a 24 well plate containing the fibronectin functionalised patterns at a density of 7500 cells/mL (1mL/well) in DMEM medium. GE cells were seeded in 48 well plate containing the fibronectin functionalised nanofibres at a density of 7500 cells/mL (0.5mL/well) in DMEM medium. Cells were then allowed to adhere for 24 hrs and then fixed for staining.

3.2.4 Immunostaining.

For triple staining of actin, nucleus and vinculin, after 24 h incubation cells were fixed with 4% paraformaldehyde (in PBS) for 10 min, permeabilized with 0.2% Triton X-100 (in PBS) for 5 min and blocked with a solution of 10% FBS and 0.25% gelatin in PBS for 1 h at room temperature. Phalloidin (1:500) was added at this stage too. Samples were then incubated with the primary antibody (anti-vinculin, 1:200) for 1 h at room temperature, washed and incubated with the conjugated secondary antibody (1:1000; Alexafluor 488 α-mouse) and DAPI (1:1000) for 1 h at room temperature and washed again before being mounted on glass slides with Mowiol solutions.

Double staining of fibronectin and vinculin was also carried out with HaCat cells. After cells were allowed to spread for 24 hrs, samples were incubated for 1h at room temperature with primary antibodies (rabbit-anti-fibronectin and mouse-anti-vinculin mouse) first and then washed and incubated in secondary antibody (in this case using Alexafluor 594 anti-rabbit for fibronectin) solutions in blocking buffer (as above) for 1h. For laminin-332 and fibronectin staining, samples were treated first with a 1:1 mixture of FN and labelled BSA (10µg/mL) and after cell seeding for 24 hrs and blocking they were incubated with primary antibody (rabbit anti-laminin, 1:200) and secondary antibody (Alexafluor 488-conjugated, 1:1000).

In order to assess integrin expression in the different cell line (GE, GE β1 and GE β3) double staining of fibronectin/ labelled BSA (as previously described) and either αv or β1 integrin monomer was performed: Anti-Integrin alpha V and Anti-Integrin beta 1 respectively as primary antibody and respectively conjugated secondary (488).

3.2.5 Cell characterization

SEM.

SEM was used to investigate HaCat cells morphology after adhesion to the patterns and to control homogeneous substrate. Cells were fixed after 24 h adhesion with 2.5% glutaraldehyde in PB for 2 h at room temperature. Samples were then washed 3 times with PBS 0.1M and dehydrated with a series of ethanol washings increasing the ethanol content from 20% to 100%, each wash repeated twice for 5 minutes. Critical Point Drying was then performed (EMS 850 Critical Point Dryer). Samples were then coated with Gold (SC7620 Mini Sputter Coater, Quorum Technologies), 60 sec coating and 20mA process current. A voltage of 20 kV, a spot size of 3.5 and an aperture of 30 µm were used.

Immuno-fluorescence microscopy and data analysis.

Fluorescence microscopy images to quantify cell spreading (after phalloidin staining) and cell density (after nuclear staining with DAPI) were acquired with a Leica DMI 4000B epifluorescence microscope (EL6000 lamp, 20x0.7 NA lens, 63x1.40 Oil lens). Fluorescence microscopy images for vinculin staining, double staining of fibronectin and vinculin or laminin in HaCat cells and integrin expression in GE cells of αv or β1 integrin monomer were obtained with a Leica TCS SP2 confocal and multiphoton microscope (X-CITE 120 LED lamp, 63X1.4 Oil lens). ImageJ was used for cell spreading and density quantification: for cell area, between 100 and 150 cells were analysed for each condition in each experiments and experiments were carried out in triplicate. Objects were analysed after thresholding the images. For density analysis thresholding and watershed were used in ImageJ on the dapi staining images in order to identify individual nuclei.

Statistical analysis.

Statistical analysis was carried out using Origin 8 and one-way ANOVA with Tukey test for posthoc analysis. Significance was determined by * $P < 0.05$, ** $P < 0.01$, *** $P < 0.001$, **** $P < 0.0001$. A full summary of statistical analysis is provided below in Appendix A2. In figure captions, "n" means the number of independent replicates of the experiment presented.

3.3 Results and discussions

3.3.1 Control of cell adhesion.

To investigate the control of cell adhesion using the nanofibres generated via ENL, HaCaT cells were seeded on nanofibrous substrates (passivated with POEGMA and functionalised with fibronectin) with fibre widths ranging from 250 to 1000 nm (specifically, 250, 550, 800 and 1000 nm width). In order to assess whether cell adhesions are controlled by the nanoscale geometry of the fibrous pattern, confocal imaging of vinculin (focal adhesion marker) and fibronectin immunostained substrates was carried out (Fig 3.1 A). Colocalization of the two markers was observed, indicating that the geometry of the fibronectin adhesive nanofibres was efficiently controlling cell adhesion and the maturation of adhesive complexes. This is in good agreement with previous work on circular nanopatches that showed a good control of adhesion geometry using substrates generated via sparse colloidal lithography (Gautrot et al., 2014, Malmstrom et al., 2010). These experiments were repeated on 800 nm diameter patches (Fig. 3.1 C) and confirmed the colocalization of vinculin and fibronectin, although some level of bridging of FAs over a few patches was also observed, as previously reported (Malmström et al., 2011). These observations were supported by SEM images of HaCaT cells spreading at the surface of nanofibrous substrates (Fig. 3.2). In these images, cell protrusions can be observed to make links with shapes defined by the fibres (despite the low contrast with which quasi-2D fibrous mats can be observed after gold coating of the substrates). In addition, the distal part of these protrusions was found to extend from fibres and be associated with changes in membrane curvature. This led to more irregular geometry of the cell edge and lamellipodiae, compared to cells spreading on homogenous substrates. Lamellipodiae are structures playing an important role in the sensing of physical properties of the matrix and their dynamics and stability controls the formation of stable focal adhesions (Giannone et al., 2004, Gardel et al., 2008). Hence, changes in their geometry and dynamics are likely to have an impact on cell spreading and cell shape. Interestingly, cells seeded on wide fibres (800 nm) displayed an increase in contrast in structures observed at areas of lamellipodiae overlapping with fibres (Fig. 3.2). This was not observed on smaller fibres and may indicate an enrichment in cytoskeletal components associated with the recruitment of adhesion molecules at wide fibres and associated stabilisation of lamellipodiae.

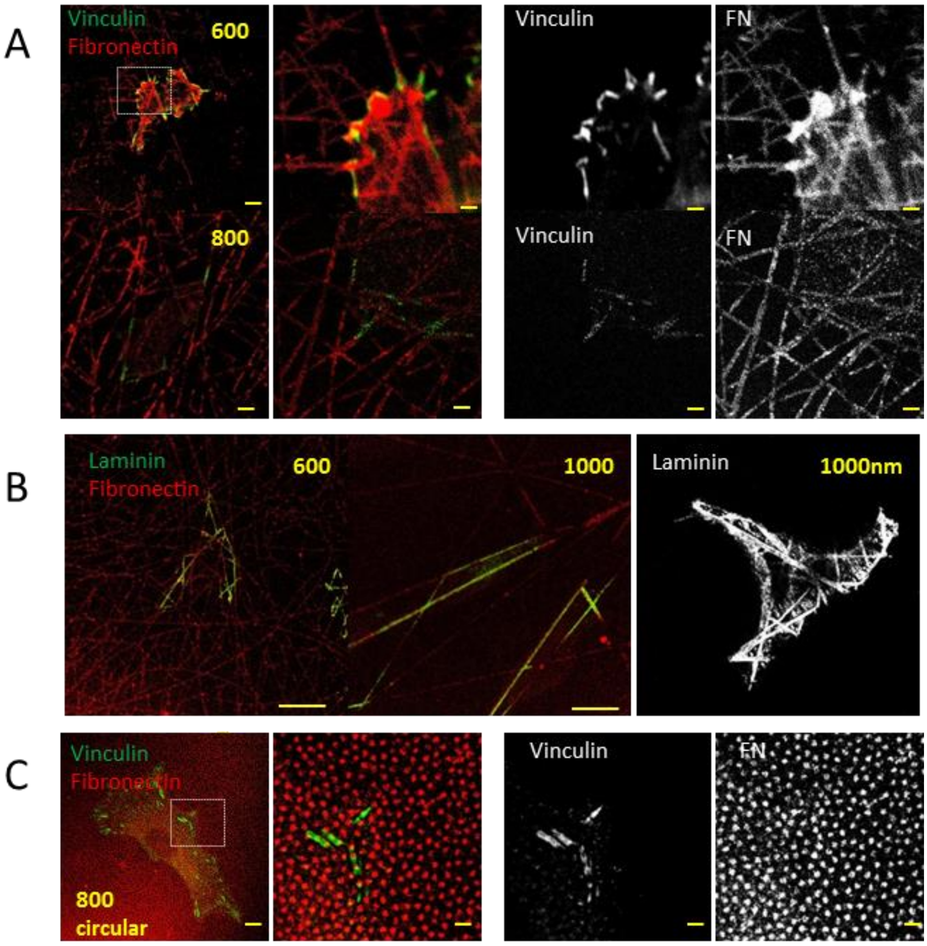

Figure 3.1 A. HaCat cells spreading (for 24 hr) on nanofibres with different diameters. A. Confocal microscopy images of cells on 600 nm (top) and 800 nm (bottom) diameter nanofibres (passivated with POEGMA): colocalization can be noticed of vinculin (green) on fibronectin (red). Scale bar of the first images (normal size) is 10 µm, in the zoomed images the scale bar is 2 µm. B. Confocal images of immunostained samples for laminin (green) and FN/BSA (1/1, 594nm, red) of cells seeded on 600 nm and 1000 nm nanofibres (first two images) and laminin on 1000 nm nanofibres (last images on the right). Scale bar is 10 µm. C. Double staining for vinculin and fibronectin of cells seeded on circular patched (800 nm diameter). Scale bar is 10 µm in the first image and 2 µm in the zoomed images.

Finally, cells can effectively remodel their microenvironment, via deformation of the matrix (Huebsch et al., 2010), its degradation (Khetan et al., 2013) or deposition of new ECM proteins (Malmström et al., 2011). Hence keratinocytes were found to leave trails of laminin-332 during migration (Frank and Carter, 2004) and deposit this protein at the surface of circular nanopatches (Gautrot et al., 2014). Such processes may lead to a complete remodelling of the nanoscale geometry of the adhesive landscape as cells spread at biointerfaces. We examined the extent of such phenomena via the immunostaining of HaCaTs spreading on fibronectin nanofibres, probing for the deposition of laminin-332 (Fig. 3.1 B). Confocal microscopy indicated that, after 24 hrs of spreading at the surface of nanofibrous patterns, cells deposited laminin-332 to nanofibres directly in contact with their basal membrane. In addition, double stained cell-seeded substrates (simultaneously probed for fibronectin and laminin-332) showed that the laminin-rich fibres directly extended from the fibronectin fibres onto which cells spread. These results indicate that, although ECM protein deposition occurs at the surface of nanopatterned substrates, this phenomenon remains localised to the fibres themselves and therefore should not significantly impact the geometry of the adhesive landscape, at least during relatively short-term cell adhesion and culture.

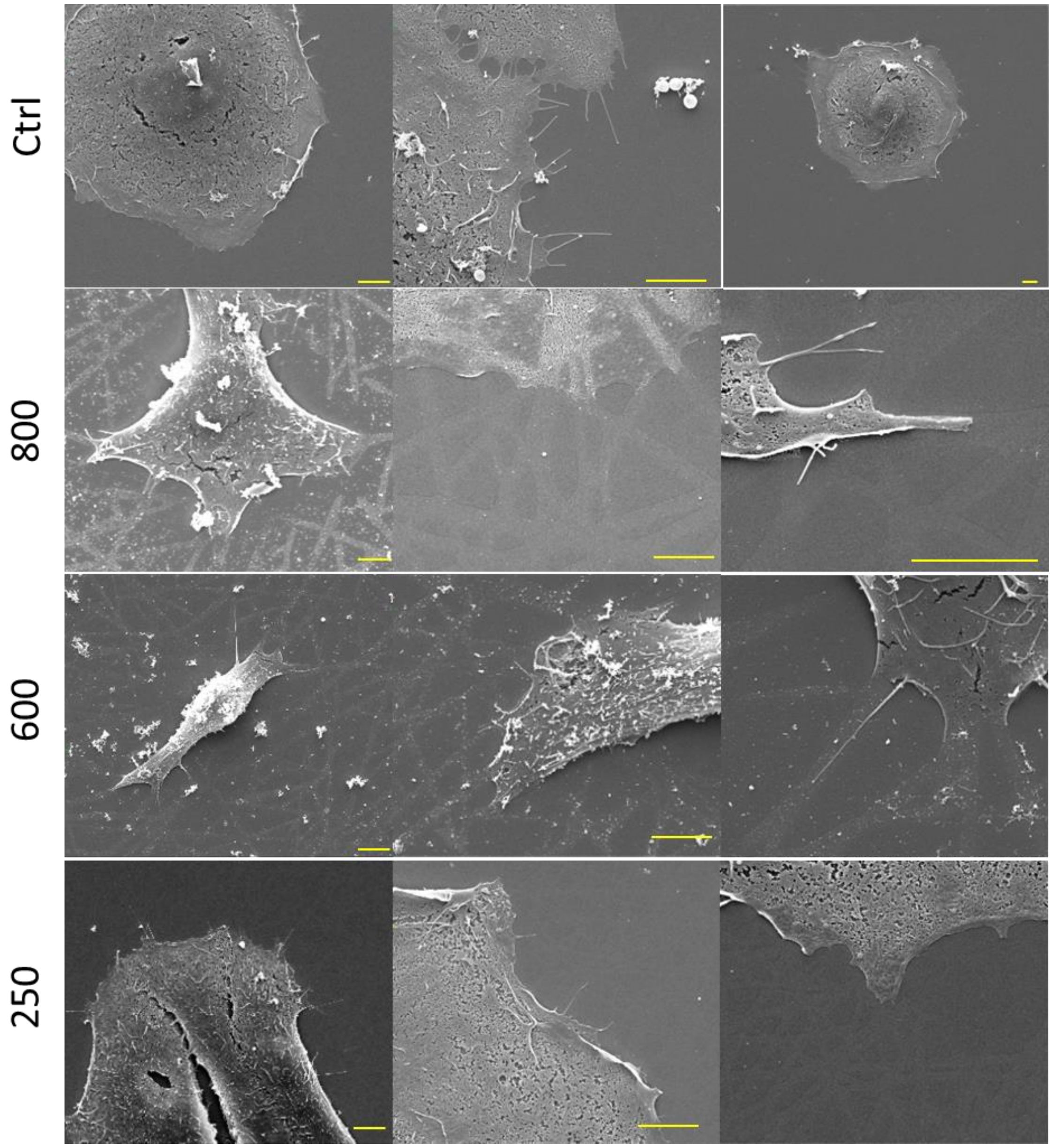

Figure 3.2 HaCat cells after 24 hr spreading. SEM images representing cells adhering on control homogenous surfaces, 800, 600 and 250 nm diameter fibres (different magnification). Scale bar is 5 µm.

3.3.2 Impact of nanoscale geometry on cell spreading and shape.

The extent of cell spreading at the surface of nanofibrous patterns was investigated next. The impact of fibre dimension and density was explored first (Fig. 3.3 and 3.4). HaCat cells were seeded on nanofibres with diameter of 250, 550 800 and 1000 nm (POEGMA background) and at three different densities (ratio of ECM-coated area over the total area of the substrate): in this case 60 ± 5 % for high, 40 ± 5% for intermediate and 22 ± 8 % for low density nanofibres. The density of cells found to adhere at the surface of nanofibres after 24 hrs was relatively insensitive to the size and density of nanofibres (Fig. 3.4). A slight decrease compared to homogenous substrates was observed, potentially due to the lower overall density of ECM proteins. This effect was more pronounced on the largest fibres, perhaps as a result of larger distances between fibres required to preserve the ECM coated area comparable across the range of fibre dimension. This prevented the study of cells on the largest fibres at the lowest density. Cell area was more sensitive to the fibre dimensions at low fibre density (22 ± 8 %), although, at intermediate (40 ± 5%) and high (60 ± 5 %) density, changes in cell spreading were still significantly different on the smallest fibres (250 nm) compared to controlled substrates (P = 0.00165 and 0.0002 respectively). Such impact of fibre density may be a result of some level of fibre fusion at higher fibre densities. In general the cell area size increases when increasing the nanofibres density (verified for all dimensions apart the 550nm, where the maximum cell spreading is at the intermediate densities) or the fibre size (the diameter). This was not the case for the biggest fibres, in fact at intermediate densities the spreading decreases on them (compared to the 800 nm nanofibres) probably due to larger gaps between them that the cells have to overcome: at intermediate densities thus the spreading actually decreases going towards the biggest fibres. When then moving at higher densities this is balanced due to the higher contact area that cells can feel. In addition, changes in cell spreading were found to occur gradually, rather than be sensitive to a specific dimension or density. This is in good agreement with changes in cell spreading reported for adhesion to circular nanopatches (Gautrot et al., 2014), but contrasts with observations made in the case of cells spreading on mixed patterns presenting one large adhesive island surrounded by nanopatches, for which an area-threshold was reported (Coyer et al., 2012).

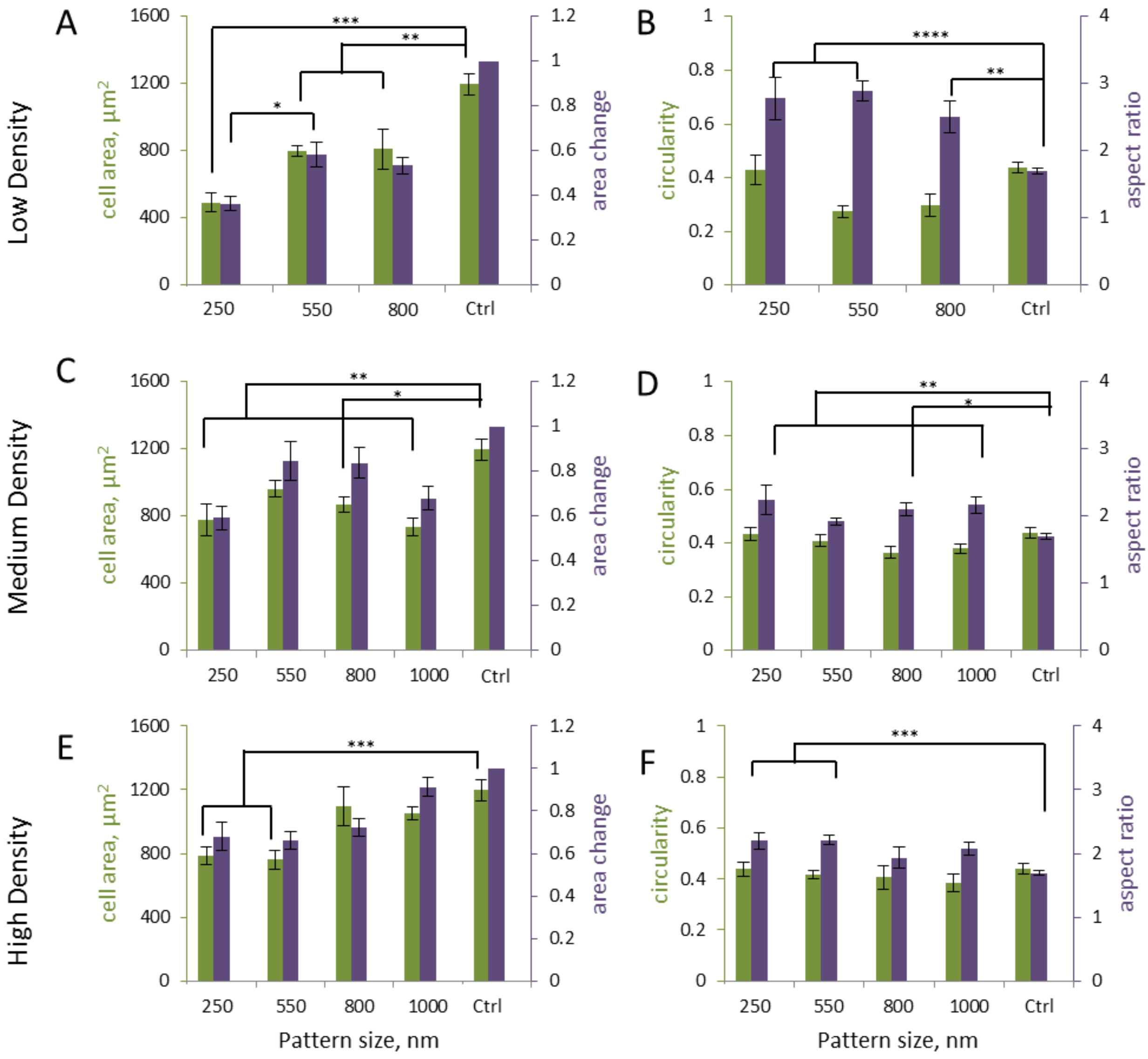

Figure 3.3 . HaCat cells after 24 hr spreading. Data showing ell area (green) and relative area change (purple, relative to control surfaces) on low (A), medium (C) and high (E) density nanofibres with 250, 550, 800 and 1000 nm diameters (POEGMA patterns). Ctrl is the homogenous control surface. Cell morphology quantified via circularity (green) and aspect ratio (purple, longer cell axis divided by the smaller axis) on low (B), medium (D) and high (F) density nanofibres. Error bars are SE, n ≥ 3, with n representing the number of experiments. For statistical test: *, P < 0.05; **, P < 0.01; ***, P < 0.001; ****, P < 0.0001.

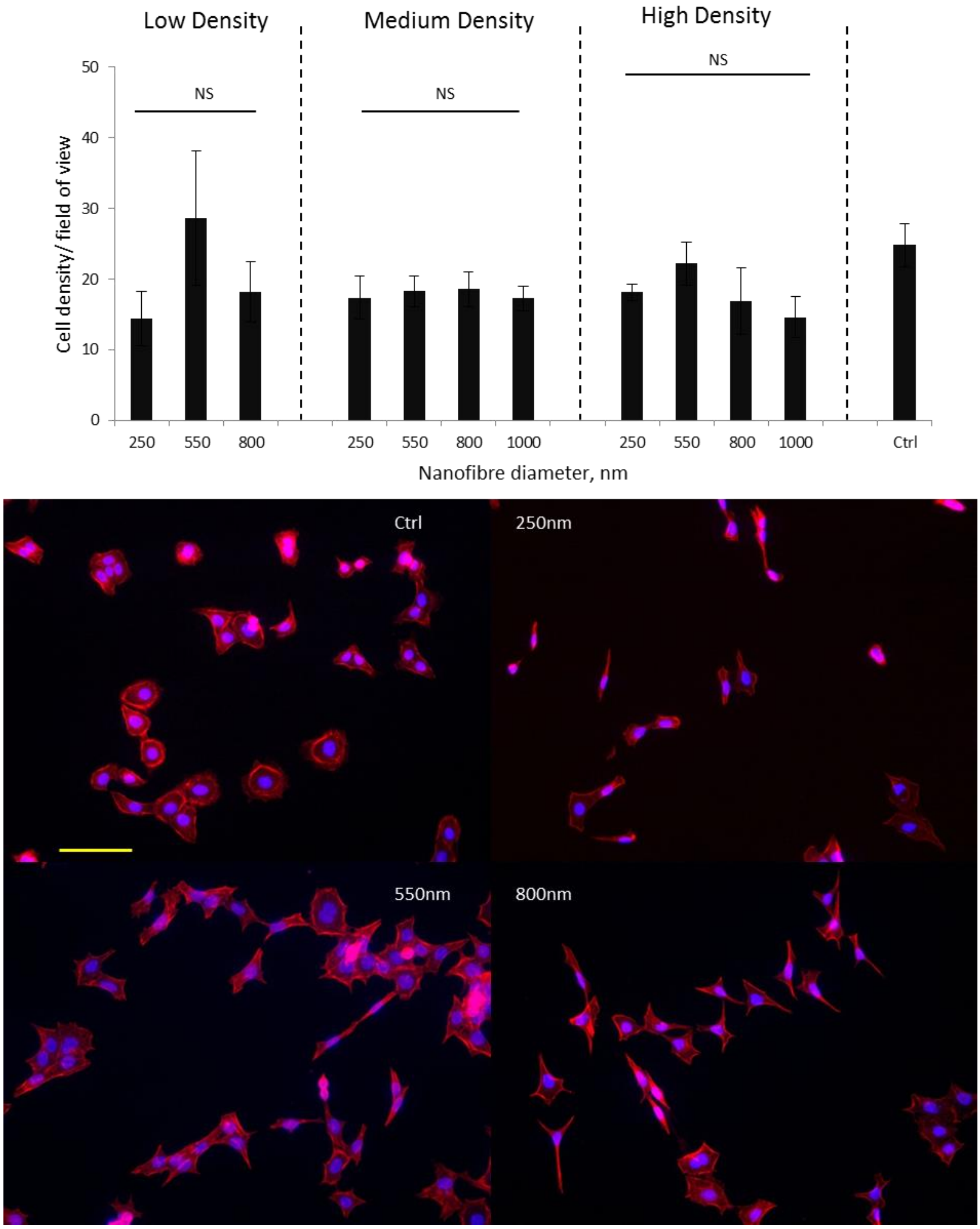

Figure 3.4 Graph: HaCat cell density on low, medium and high density nanofibres, with fibres of different diameters. Ctrl is the homogenous control surface. Error bars are SE, n ≥ 3. No significant differences are noticeable from this data, across different densities and nanofibres dimensions. Bottom: representative epifluorescent microscope images of cells seeded on low density nanofibres with different fibre sizes (see picture). Scale bar is 100 µm.

Cell shape was also strongly affected by nanofibres (Fig. 3.3 B, D and F and Fig. 3.5). Whereas HaCaT cells spread isotropically on homogenous control substrates, cells adhering to nanofibres displayed asymmetric polarized shapes. This resulted in an increase in cell aspect ratio on all fibres and a decrease in circularity down to 550 nm fibres on the low density nanofibres, beyond which circularity increases again as a result of the marked decrease in cell spreading observed for cells adhering to 200 nm fibres. At intermediate and high fibre densities, in agreement with the weaker changes observed in cell spreading, cell shape change was not as significant (cell circularity remained unchanged and cell aspect ratio only rose up to 2.2 ± 0.08 for 550 nm fibres on high density and 2.24 ± 0.2 and 2.2 ± 0.12 for 250 nm fibres on medium and high density nanofibres respectively).

The changes in cell spreading and shape were correlated with marked changes in the structure of the cytoskeleton (Fig. 3.5). Whereas peripheral transverse actin bundles were typically observed in cells spreading on homogenous substrates (Tee et al., 2015), cells displayed thick concave stress fibres when spreading on wide nanofibres (800 nm). As the size of nanofibres decreased to 550 and 250 nm, so did the thickness and length of stress fibres, in agreement with the reduction in cell spreading. The formation of stress fibres with associated stable focal adhesions correlates well with the increase in cell polarity and aspect ratio. As the nanofibres size decreased, despite the formation of relatively large focal adhesions, the assembly of stress fibres seems to be gradually prevented, suggesting that, as for cells adhering to circular nanopatches (Gautrot et al., 2014), the nanoscale geometry of the adhesive landscape regulates cytoskeletal assembly rather than focal adhesion protein recruitment.

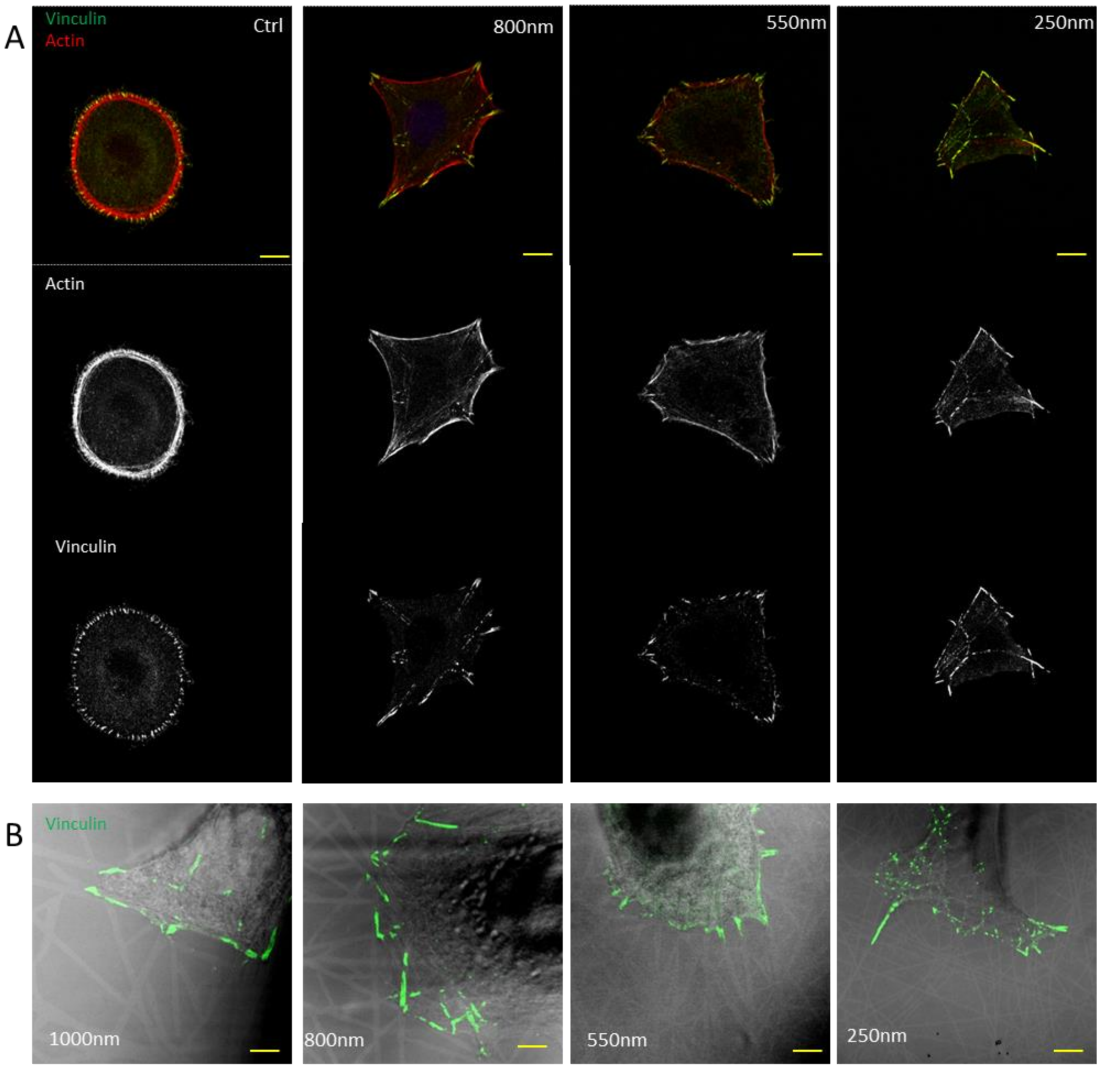

Figure 3.5 A. Confocal images of HaCat cells spreading (24 hr) on different nanofibre diameter (POEGMA brushes): vinculin (green) and actin (red) staining of cell spreading on control homogenous surfaces (first column, Ctrl), 800 nm (second column), 550 nm (third column) and 250 nm (last column) nanofibres (low density). Scale bar is 10 µm. B. Confocal images of HaCat spreading on 1000 nm (average nanofibres density), 800 nm (average nanofibres density), 550 nm (high nanofibres density) and 250 nm (average nanofibres density). Green represents vinculin and the background is taken in reflection mode. Scale bar is 20 µm.

HaCat cells were also tested on patterns functionalised with PMEDSAH at different densities and fibre sizes: 250 nm and 550 nm high density and 800 and 1000 nm at intermediate densities. Although it was possible to control cell adhesion with this system too, POEGMA was chosen as preferred passivation background due to easier production, as explained in the previous chapter.

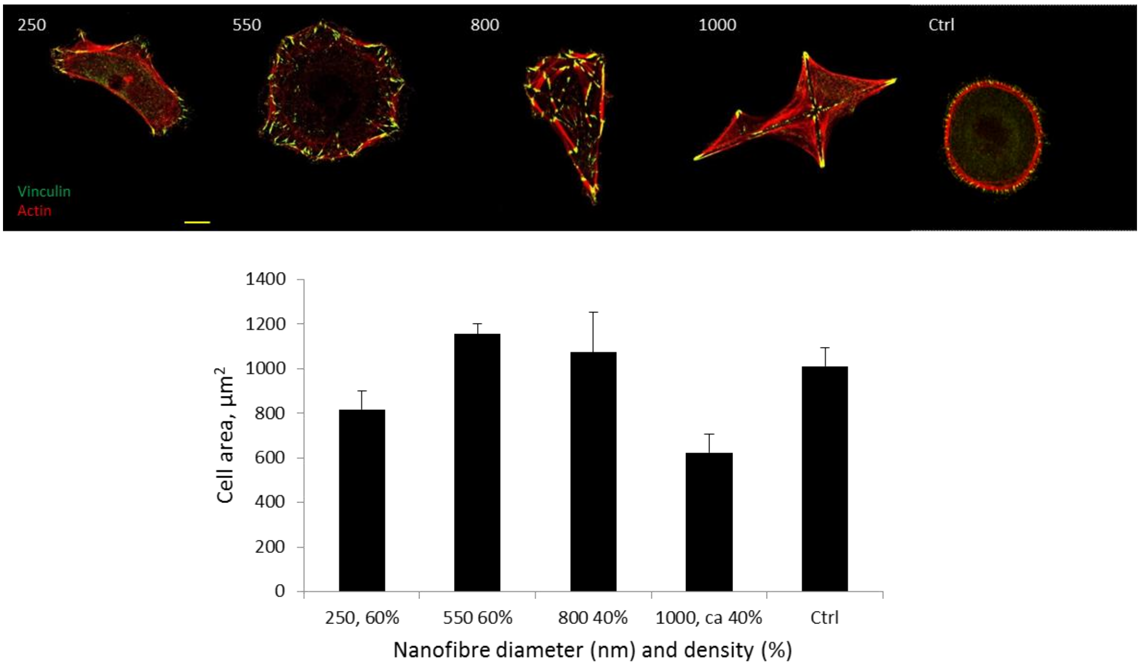

Figure 3.6 HaCat cells seeded on nanofibres with PMEDSAH functionalised background (24 hr spreading). Here there is a mixture of intermediate and high densities. Cell area for cell seeded on different nanofibres size and at different density. Scale bar is 10 µm.

Having established that cell spreading and shape are determined by fibre diameter, we investigated whether the shape of focal adhesions could influence cell spreading and shape, comparing cell adhesion experiments on nanofibres and circular nanopatches (Fig 3.7). To this aim, we seeded HaCaT cells on circular nanopatches generated via sparse colloidal lithography (with ECM densities comparable to those of the sparse fibres, 20 % of the overall area, Fig. 3.7 top) (Malmstrom et al., 2010, Malmström et al., 2011). We found a similar trend in cell spreading, as cell area decreased to 449 ± 33 µm2 on 300 nm patches (Fig. 3.7, A), although the larger cell areas observed on the gold control substrates used to compare nanopatches resulted in a stronger decrease in the relative cell spreading for the smallest nanopatches (0.26 ± 0.03 for 300 nm patches, compared to 0.36 ± 0.03 for 250 nm nanofibres). However, cell shape remained largely unaffected by the size of nanopatches and cells spread relatively homogenously and presented only weak polarisation, compared to their behaviour on nanofibres (Fig. 3.7, B). Hence, in addition to focal adhesion size, the shape of adhesive clusters, as determined by the nanoscale geometry of the adhesive landscape, has an important impact on cell spreading and shape.

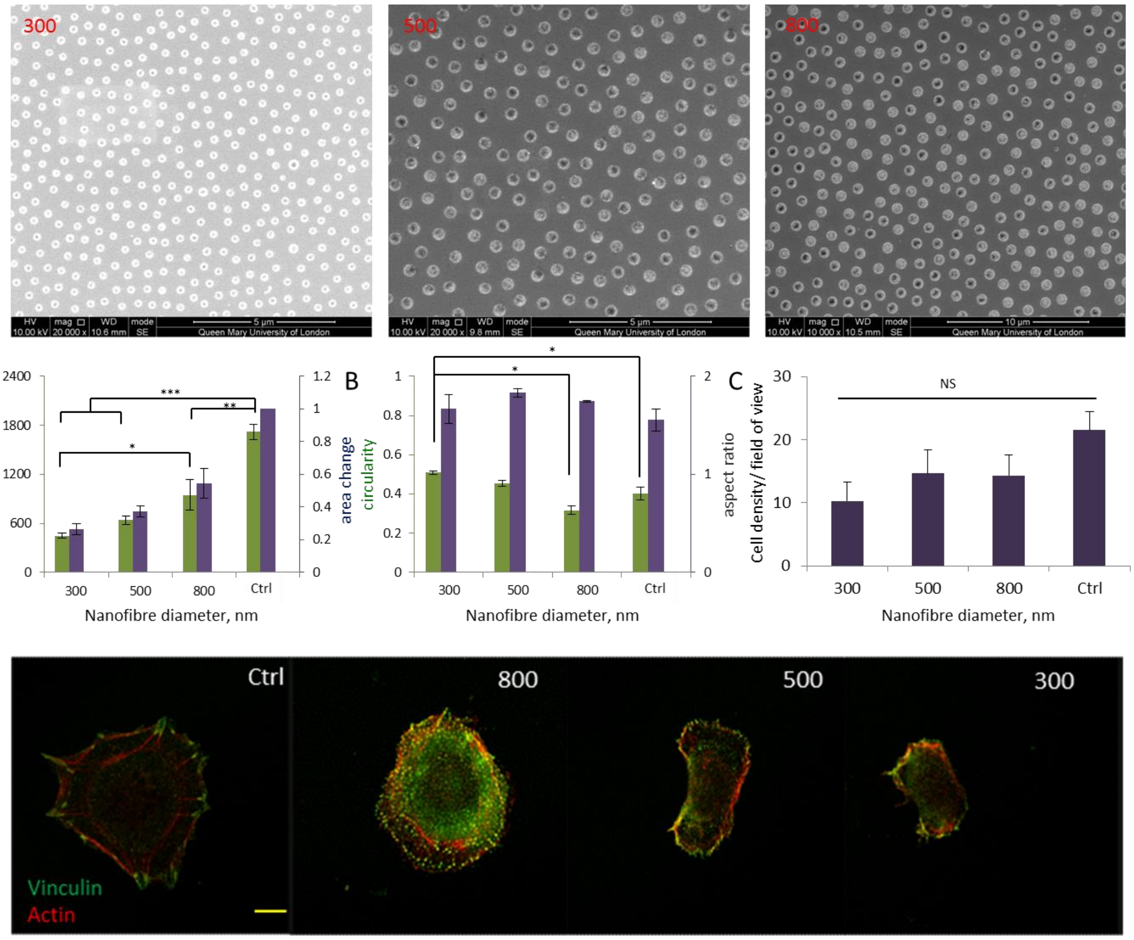

Figure 3.7 First row: SEM images of the circular patches (in order: 300, 500 and 800 nm diameter). Second row. HaCat cells spreading (24 hr) and relative area change (to control) on circular patches (A), cell shape descriptors (B) and cell density (C). Third row. Representative confocal images of cells spreading on the different size patches: vinculin (green) and actin (red). Scale bar is 10 µm. Error bars are SE, n ≥ 3, with n representing the number of experiments. For statistical test: *, P < 0.05; **, P < 0.01; ***, P < 0.001; ****, P < 0.0001.

3.3.3 Impact of integrin expression on nanoscale sensing of ECM geometry.

The expression of different types of integrins strongly influences the size and shape of focal adhesions and this impacts on cell spreading and shape (Danen et al., 2002). We next examined whether differential integrin expression could also act as an important sensing element of the nanoscale geometry of the adhesive landscape. The GE cell line is a β1-defficient epithelioid cell line (established from β1-null mouse embryos after clonal culture and selection) expressing low levels of αv and β3 integrins, whereas the GEβ1 and GEβ3 cell lines express high levels of α5β1 and αvβ3 integrins heterodimers, respectively (Fig. 3.8) (Danen et al., 2002, Gimond et al., 1999). Such integrin expression strongly influences cell morphology and phenotype (e.g. fibrillogenesis, cohesiveness of colonies mimicking an epithelial-mesenchymal transition).

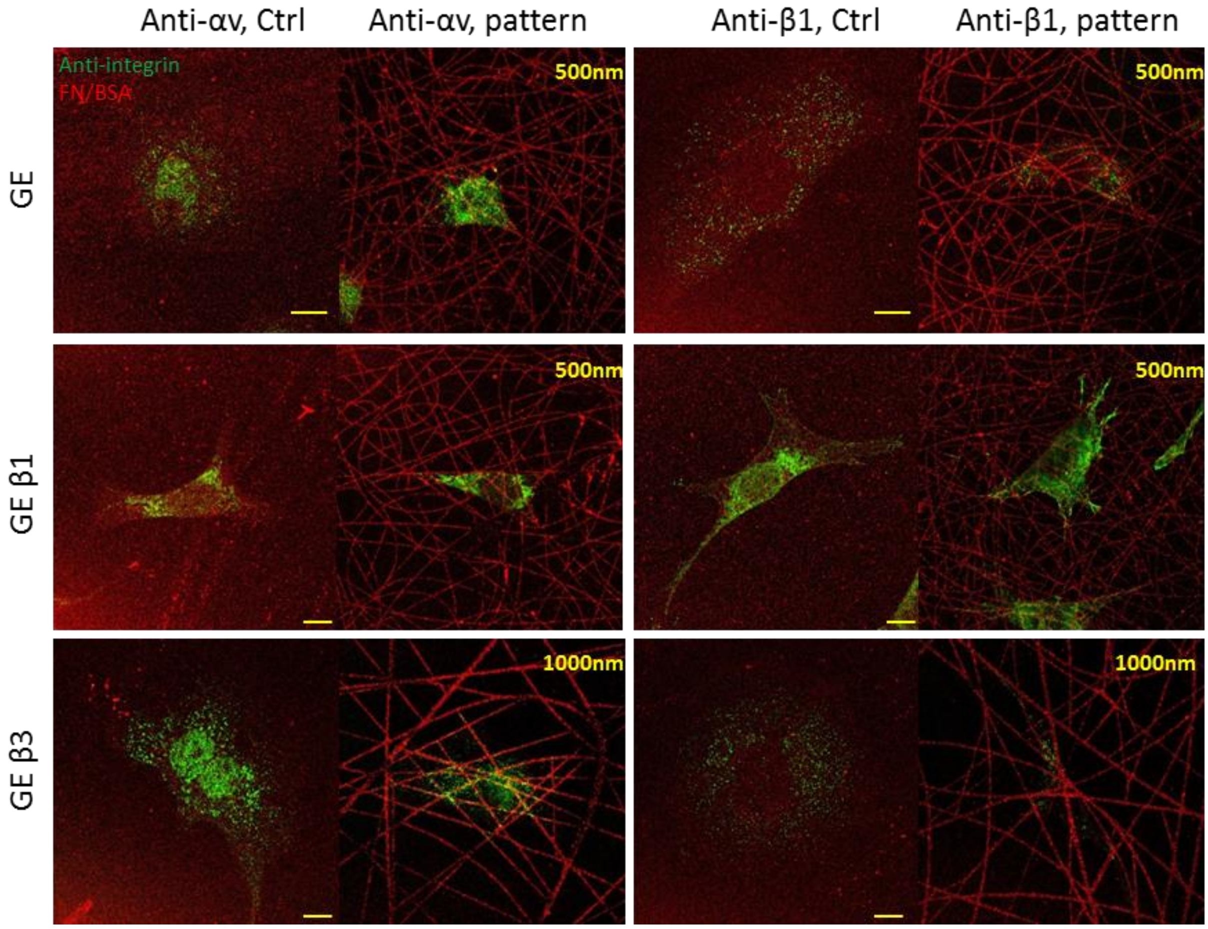

Figure 3.8 Expression of β1 and αv integrins by GE cells spreading on control homogenous surfaces and 500 and 1000nm diameter nanofibres (as indicated in the figure). The anti- integrin antibodies are shown in green and the FN/ BSA (1/1) in red (confocal images). Scale bar is 10 µm.

In order to study the impact of integrin expression on cell sensing of the nanoscale environment, these three cell lines were seeded on nanofibrous patterns with fibre diameter of 250, 550 and 1000 nm and with low density (because these nanofibres were found to be more effective in influencing cell spreading, Fig. 3.9, 3.10, 3.11 and 3.12). Although all three cell types responded to the dimensions of nanofibres, the decrease in cell spreading occurred for wider nanofibres and was stronger in the case of αvβ3 expressing cells, in particular GEβ3 cells. Side experiments were performed to confirm that the specific integrins expressed were recruited at the nanofibres (Fig. 3.8). Hence whereas the relative cell spreading of GEβ1 cells remained relatively high on 1000 nm-wide fibres (0.8 ± 0.03), it had already decreased significantly on GE and GEβ3 cells (0.63 ± 0.02 and 0.62 ± 0.03, respectively; P = 0.003 and 0.012, respectively). On the thinnest fibres (250 nm), the relative cell spreading of GEβ3 cells was the lowest (0.25 ± 0.03, compared to 0.42 ± 0.03 and 0.44 ± 0.04 for GE and GEβ1 cells, respectively; P = 0.00001 and 0.0010, respectively). These results contrast with those previously obtained for GE cells spreading onto circular nanopatches, which had indicated that nanoscale sensing of the pattern geometry was insensitive to integrin expression (Gautrot et al., 2014).

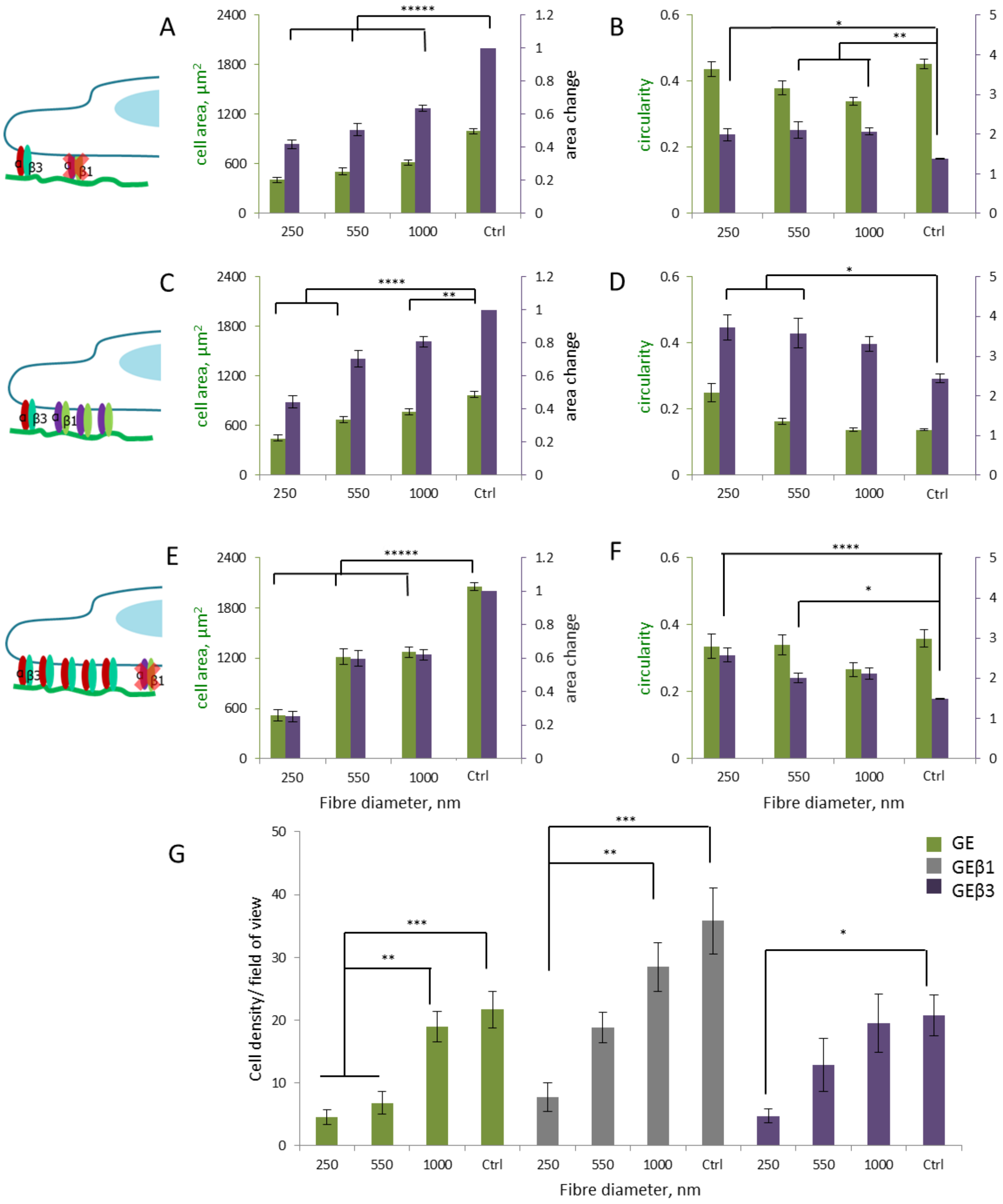

Figure 3.9 GE cells after 24 hr spreading. Cell area (green) and relative area change of GE (A), GEβ1 (C) and GEβ3 (E) on fibrous patterns (see schematics of integrin expression on the side). Shape descriptor

(circularity and aspect ratio), for GE (B), GE β1 (D) and GE β3 (F) cells on different nanofibres sizes. GE cell density on different nanofibres size (G).Ctrl is the homogenous control surface. Error bars are SE (n ≥ 6, with n representing the number of experiments). For statistical test: **, $P < 0.01$; ***, $P < 0.001$; ****, $P < 0.0001$; *****$P < 0.00001$.

Focal adhesions assembled by the three types of GE cells were characterised by confocal microscopy. Consistent with previous reports (Danen et al., 2002), it was found that GEβ1 cells adhering to homogenous substrates displayed few elongated focal adhesions, associated with a more polarised morphology, whereas GE and GEβ3 cells displayed many punctate adhesions, with less polarised morphologies (Fig. 3.9 B, D and F and Fig. 3.10, 3.11 and 3.12). The qualitative changes in morphologies observed as a result of differential integrin expression correlated with changes in shape descriptors measured for the three types of GE cells, with higher aspect ratios and lower circularities measured for GEβ1 cells (Fig. 3.9 B, D and F).

These results suggest that, although cell adhesion is correlated with the size of nanofibres, differential expression of integrin heterodimers is an important mediator of the sensing of the nanoscale geometry of the adhesive landscape. Hence, β1-expressing cells are less susceptible to the dimension of nanofibres compared to β3-expressing cells. It can be hypothesised that the ability of β1-expressing cells to retain a spread morphology on nanofibres may be related to their polarised morphology, even on homogenous substrates. Therefore, spreading on nanofibres does not force β1-expressing cells to adopt an abnormal polarised phenotype, whereas β3-expressing cells are strongly induced to polarise on nanofibres.

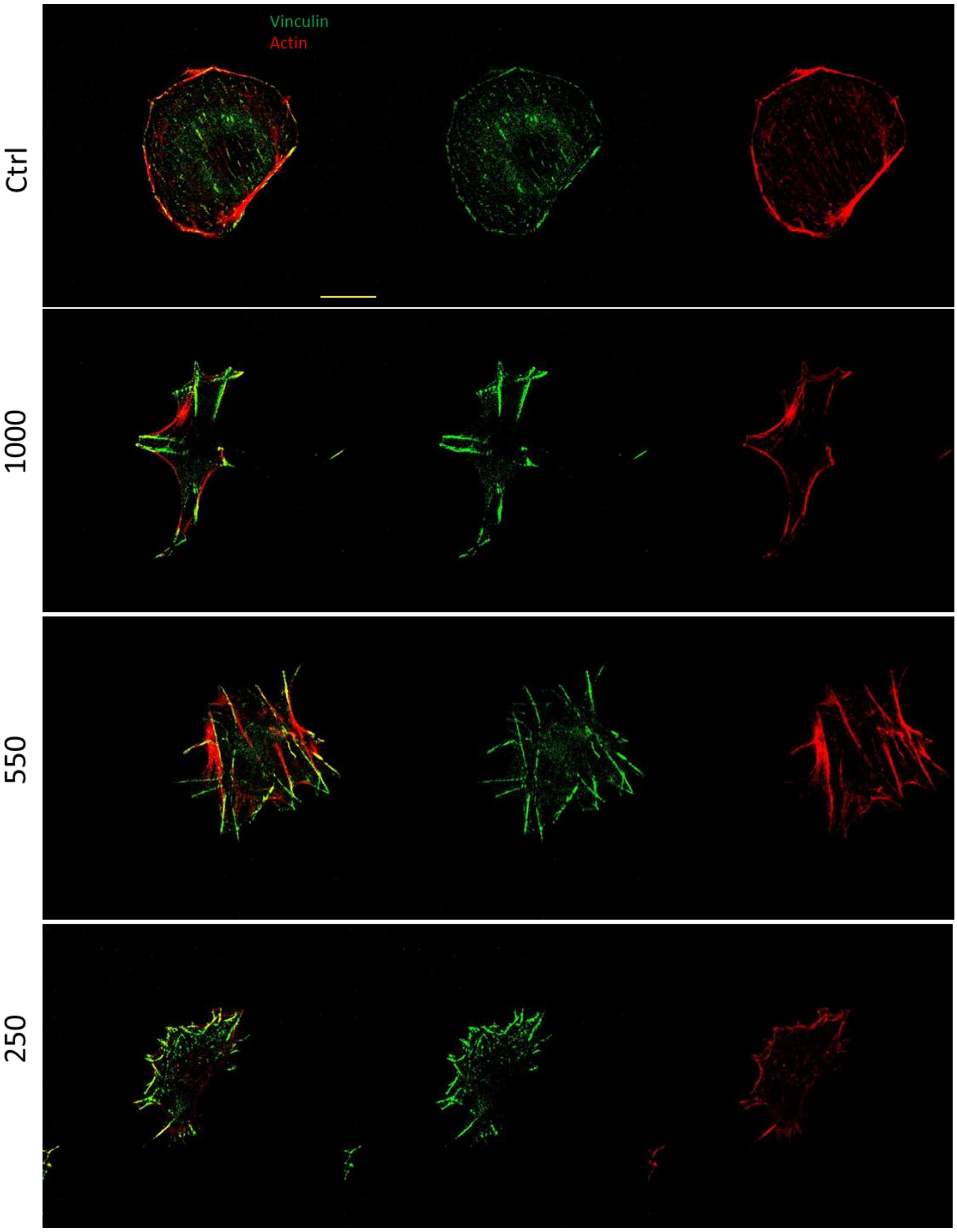

Figure 3.10 GE cells spreading on nanofibrous patterns (after 24 hr). Confocal images representing vinculin (green) and actin (red) staining of GE cells spreading on control homogenous (Ctrl) surfaces and 1000, 550 and 250 nm diameter fibres (from top to bottom). Scale bar 15 µm.

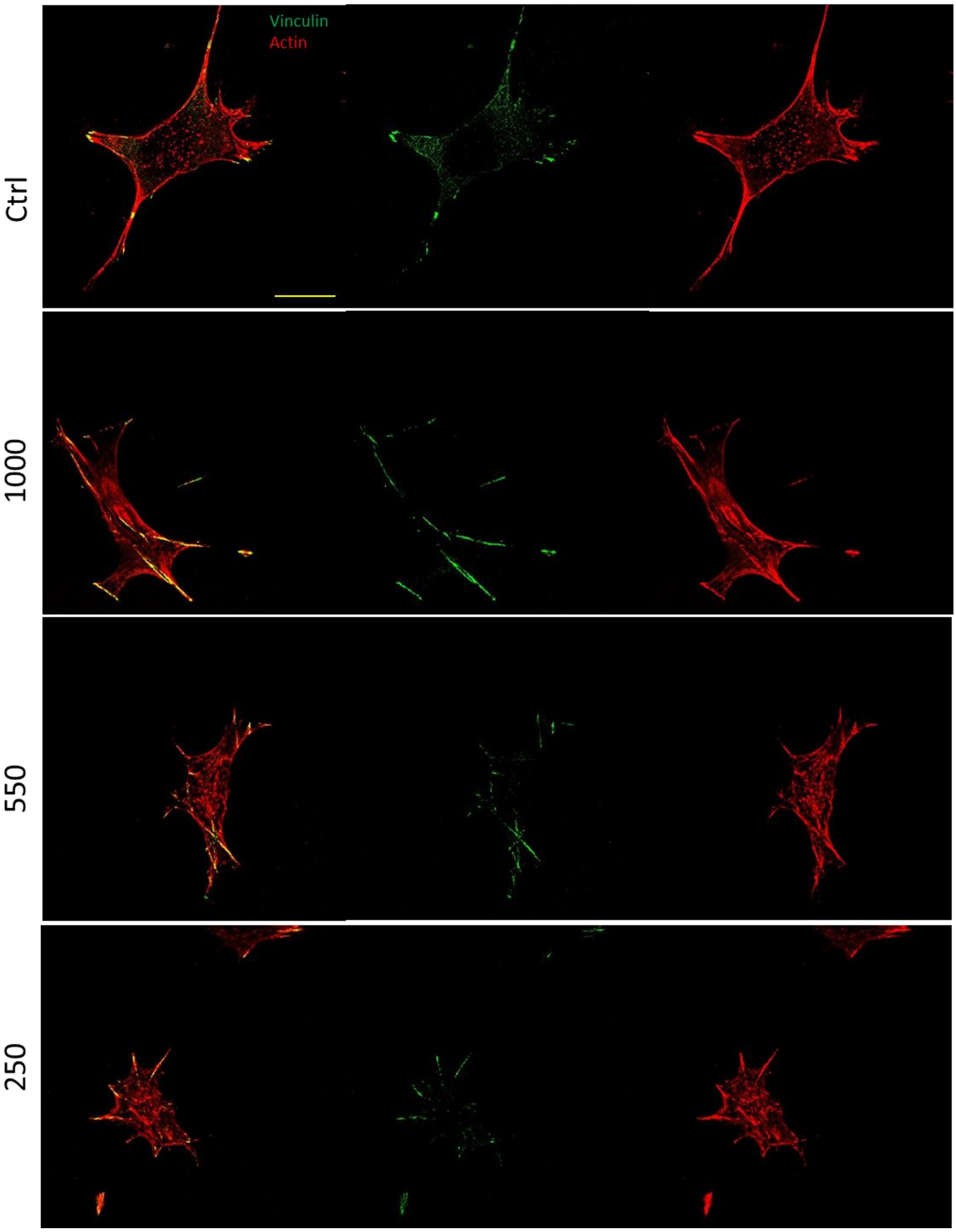

Figure 3.11 GEβ1 cells spreading on nanofibrous patterns (after 24 hr). Confocal images representing vinculin (green) and actin (red) staining of GE β1 cells spreading on control homogenous (Ctrl) surfaces and 1000, 550 and 250 nm diameter fibres (from top to bottom). Scale bar 20 µm.

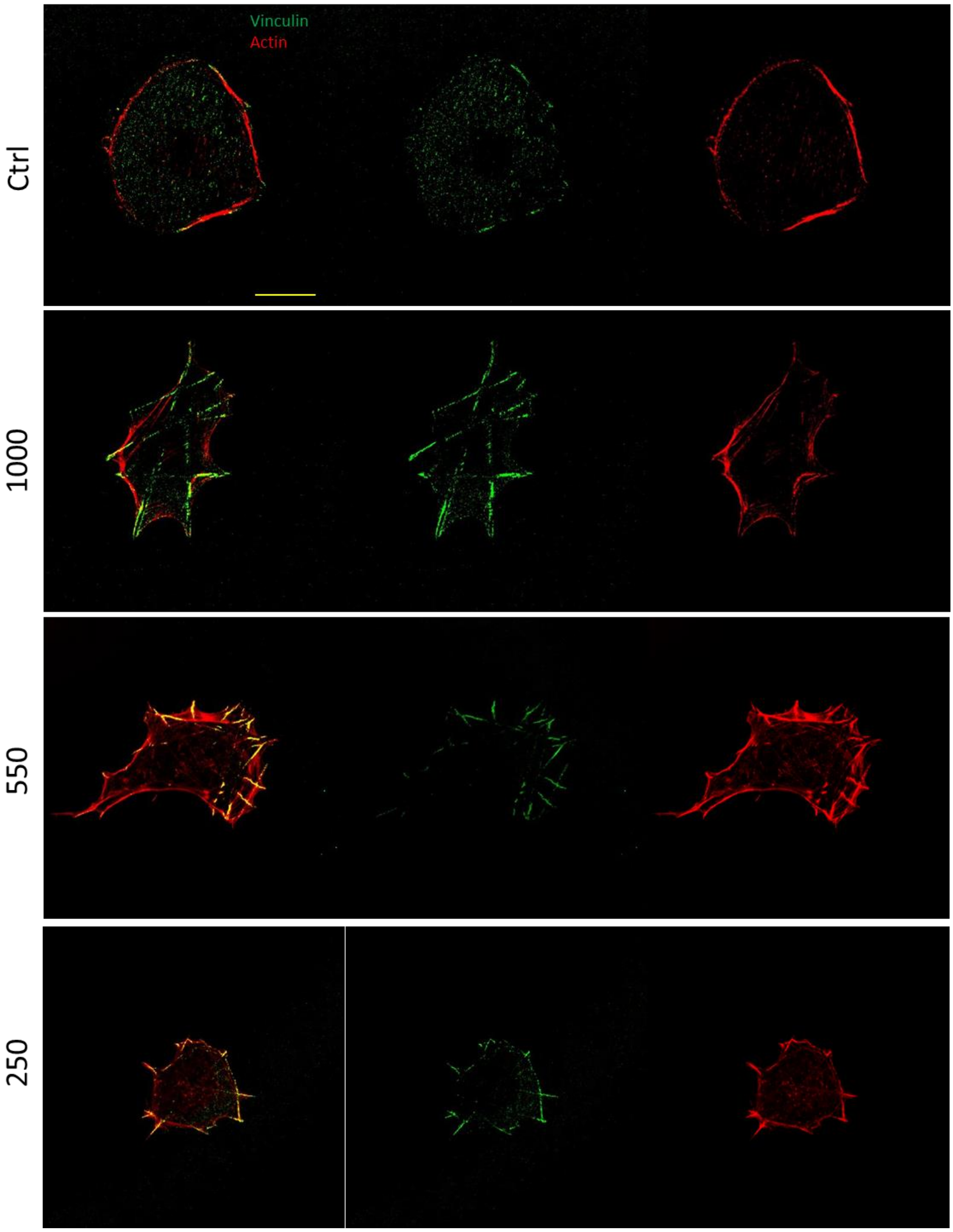

Figure 3.12 GEβ3 cells spreading on nanofibrous patterns (after 24 hr). Confocal images representing vinculin (green) and actin (red) staining of GE β3 cells spreading on control homogenous (Ctrl) surfaces and 1000, 550 and 250 nm diameter fibres (from top to bottom). Scale bar 20 µm.

3.4 Conclusion

Overall, the results show that the nanoscale geometry of adhesions is an important regulator of cell spreading and shape. In contrast to circular nanopatches that restrict the geometrical maturation of adhesions via the control of their size, nanofibres allow adhesions to develop along one axis. From this point of view, nanofibrous patterns, although 2D, mimic better the continuity and geometry of natural fibrous matrices, often found for example in the mesenchyme and stroma. The parallels observed between cell spreading on circular and fibrous patterns indicate that the size of adhesions regulates the assembly of the actin cytoskeleton. However, the ability of adhesions to develop along one dimension on nanofibres results in the polarisation of cells that otherwise would adopt symmetric shapes on homogenous substrates. Polarization and cytoskeleton organization seemed to be affected by the size of the adhesion areas: cell spreading and focal adhesion maturation are impaired on the smallest sizes (at least on the low density nanofibres) thus possibly affecting protein recruitment at the adhesion site and cytoskeleton stabilization. Such sensing of the nanoscale geometry of the adhesive landscape offers strong parallels with the spreading of cells on surfaces regulating the topography of self-assembled fibronectin (Vanterpool et al., 2014). These results also demonstrate that differential expression of integrins modulates sensing of nanoscale geometrical cues. Considering the importance of differential integrin expression to the mechanical sensing of the matrix and response to deformation (Roca-Cusachs et al., 2009, Balcioglu H. E. et al., 2015), integrin-specific physical sensing of the microenvironment appears as a general phenomenon. In this respect, developing differential expression of integrins may provide an adaptive advantage for cells able to sense and respond to the physical properties of their micro-environment. This may explain some of the differences typically observed in integrin expression between epithelial and mesenchymal tissues. These findings highlight the importance of understanding the specific sensing mechanisms of nanoscale physical cues in order to develop appropriate implant texturing designs for promoting the adhesion of specific cell types (and potentially controlling their phenotype). However, the detailed mechanism via which integrin ligation mediates the sensing of nanoscale geometrical cues remain elusive. The reorganisation of the cytoskeleton seems to play an important role in this process, but key steps and parameters controlling this phenomenon are not clearly understood.

Chapter 4

Vinculin sensing of the geometry

4.1 Introduction

Vinculin is a key component of focal adhesions and its activation and binding with other proteins inside the adhesion plaque plays a prominent role in adhesion formation and maturation (Atherton et al., 2016, Atherton et al., 2015, Carisey et al., 2013). As described in Chapter 1, cell adhesion and mechano-transduction are not unidirectional, but rather involve inside-out and outside-in mechanisms. Hence vinculin recruitment and activation are stimulated and reinforced by the presence of other adhesion components. Clearly, its position in the adhesion complex is a hint of its complex and central role: although vinculin does not directly bind the cytoplasmic tail of integrins, it is situated in the adjacent layer of focal adhesion molecules, the so called “force transduction layer” together with talin (Kanchanawong et al., 2010). However talin is direct binder of both integrins and actin, it is also activated by traction forces to enable the binding of several vinculin molecules allowing further coupling to the actin network. Vinculin actually moves between the different layers of focal adhesions depending on its conformation and the maturation stage of the focal adhesion (Case et al., 2015): being closer to integrin when adhesion complex are forming and recruiting further up near to actin during focal adhesion maturation.

The precise interaction mechanisms of vinculin with other proteins and the subsequent downstream signalling events derived from it have been the topic of much investigation. Vinculin is divided in three major domains: an N-terminal head, a flexible neck region, and a C-terminal tail domain (Eimer et al., 1993). Vinculin is activated when the head and the tail domain of the protein dissociate (Bakolitsa et al., 2004) and this activation is mediated via protein interaction and force generation. Different vinculin constructs were tested in order to elucidate the detailed function of the different fragments of this molecule on the regulation of interactions with other focal adhesion proteins and their influence on focal adhesion maturation and stability (Humphries et al., 2007, Grashoff et al., 2010). Vinculin constructs in which the molecule was kept in a constitutive active state (vinT12), by impeding interactions between the tail and head of the molecule, and vinculin mutants that lack a tail fragment (vin880 and vnc258) were associated with an increase in the number and size of focal adhesions. This indicates that the head domain is involved in focal adhesion stabilization (recovery kinetics are also slower with these constructs compared with a full length vinculin – vinFL) (Humphries et al., 2007). While the head domain, by binding with talin, is responsible for integrin clustering and focal adhesion growth, the tail was found to be responsible for the linkage with the cytoskeleton and thus force transmission. This interaction with both the lower (integrin-talin) and higher (actin) compartments of focal adhesions, allows vinculin to control the dynamics of other proteins in the adhesion plaque (Carisey et al., 2013).

This chapter will investigate the role of vinculin on the sensing of nanoscale topography and geometry of the ECM. The role of different integrins was assessed in the formation of focal adhesions on homogenous surfaces and on the different nanofibres sizes (250, 550 and 1000 nm diameter) at low density. Furthermore vinculin dynamic in GEβ3 cells was assessed via fluorescence-recovery after photobleaching (FRAP) in order to compare the kinetics of assembly and disassembly of the protein at adhesion sites stabilised at the surface of nanofibres. Finally, vinculin-deficient mouse embryonic fibroblasts (MEFvin^{-}/$^{-}$) were seeded on homogenous surfaces and nanofibres with different size (300, 500 and 1000 nm) at low density and cell spreading and morphology was evaluated.

4.2 Materials and methods

4.2.1 Materials and chemicals.

Advanced DMEM, DMEM (500 mL), Keratinocyte- SFM (KSFM), Penicillin-Streptomycin (5,000 U/mL), L-glutamine were from Thermo Fisher. Foetal bovine serum (FBS) was from PAA. jetPEI HTS DNA (1mL) and 50 mL Sodium Chloride were from Polyplus. Alexa Fluor goat anti-mouse 488 was from Life Technologies. Phalloidin – Tetramethylrhodamine B isothiocyanate, DAPI (4,6-diamidino-2-phenylindole) and monoclonal Anti- Vinculin antibody produced in mouse were from Sigma. Vinculin-venus plasmid was from addgene. Vinculin construct T12 and Vnc880 were provided by Dr Christoph Ballestrem (University of Manchester, Manchester, UK, (Carisey et al., 2013)). 6 and 48- well plates were from Corning Costar. Silicone elastomer curing agent and silicone elastomer base (Sylgard).

4.2.2 Cell culture and seeding.

Vinculin -deficient mouse embryonic fibroblast ($MEFvin^{-}/^{-}$) were provided by Dr Christoph Ballestrem (University of Manchester, Manchester, UK, (Carisey et al., 2013)). Cells were cultured in Advanced DMEM supplemented with 10% FBS, glutamine and antibiotics. Cells were cultured to confluency (about 80% density) and were detached using trypsin/versene (1:9) and reseeded on fibrous patterns or in culture plastic well plate for experiments.

GEβ3 cells for FRAP experiments were cultured as described in the previous chapter. Cells were seeded overnight in 6 well plates at a density of 200000/ well for transfection the day after.

4.2.3 GEβ3 transfection for FRAP experiments

GEβ3 cells were transfected with vinculin venus in order to study the dynamics of the protein. For the transfection, 7 µg of vinculin venus DNA and 8 µL of the transfecting agent jetPEI were separately dissolved in 100 µL of a Sodium Chloride solution (150 mM, from Polyplus). The jetPEI solution was then added to the DNA solution, flicked for mixing and left 15-20 min to complex. The solution was then added to the culture plate where cell medium was already replaced with KSFM (serum free medium for enhanced transfection). Cells were left for 4 hrs to transfect, after which medium was switched back to the DMEM. Small Petri dishes were appositely prepared for live imaging: a hole was drilled at the bottom of the dish with a diameter of 13 mm where a clean coverslip or a patterned glass slide was then sealed with Polydimethylsiloxane (PDMS, 1:10 ratio of curing agent and base) and left overnight to cure. After 24 hrs from transfection cells were detached using trypsin/versene and 100 μL of the cell suspension was reseeded in the prepared Petri dishes with nanofibres size of 250, 550 and 1000 nm. Cells were analysed the day after.

4.2.4 MEFvin^{-}/$^{-}$ vinculin transfection

MEFvin^{-}/$^{-}$ were seeded in 6 well plate at a density of 200000/ well (so that the day after they would be confluent to about 80%). After 24 hrs spreading they were transfected with three different fluorescent vinculin construct: vinculin venus (our control, normally working vinculin molecule), vinculin T12 (constitutively active form of vinculin, the head and the tail domains are never in contact so that the molecule is always in its active form) and vinculin 880 (lacking the tail, so the head cannot bind it). 7 μg of each DNA were separately dissolved in 100 μL of a Sodium Chloride solution and 8 μL (for each DNA) of the transfecting agent jetPEI were diluted in 100 μL of a Sodium Chloride solution. The solution containing the jetPEI was then added to the DNA solution, flicked for mixing and left 15-20 min to complex. The solution was then added to the culture plate where cell medium was already replaced with KFSM (serum free medium for enhanced transfection). Cells were left for 4 hrs to transfect, after which medium was switched back to the DMEM. After 24 hrs from transfection cells were detached using trypsin/ versene and reseeded in 48 well plate on the fibrous patterns and an homogenous control at a density of 15000 cells/ mL and 0.5 mL/well. After about 7 hrs of spreading cells were fixed and stained for phalloidin and dapi for further analysis.

4.2.5 Immuno-fluorescence microscopy and data analysis.

To quantify FA size, shape and intensity of the GE, GEβ1 and GEβ3 cells (experiments described in the previous chapter) 10-15 cells were analysed and experiments were carried out in triplicates. Confocal images of vinculin staining were analysed with ImageJ: images were thresholded at about 1% and data extrapolation (area, shape descriptor and mean intensity) were performed on each object (adhesion). The data were then grouped in three categories: focal complexes (nascent FA, from 0 to 1 µm^2), mature focal adhesions (1- 5 µm^2) and fibrillary adhesions (5 - 40 µm^2).

Fluorescence microscopy images to quantify MEFvin$^-$/$^-$ cell spreading (after phalloidin staining) of the transfected and not transfected cells were acquired with a Leica DMI 4000B epifluorescence microscope (EL6000 lamp, 20x0.7 NA lens, 63x1.40 Oil lens). To quantify MEFvin$^-$/$^-$ cell area, 50-150 cells were analysed and experiments were carried out in triplicates or more. Around 40 transfected cells were analysed in total for the experiments on the smallest nanofibres, due to the lower densities obtained.

Fluorescence-recovery after photobleaching (FRAP)

GEβ3 cells expressing vinculin venus and seeded on either the patterned surfaces or homogenous substrates where analysed for live cell microscopy with a Zeiss Super resolution LSM 710 ELYRA PS.1 equipped with an environmental chamber where level of CO_2 was kept at 5% and temperature at 37.5 ˚C. Live cell images were acquired using a 63X 1.4NA oil DIC M27 objective using confocal mode. Venus fluorescence was detected using a 488-nm diode laser. For FRAP experiments, 4- 5 single focal adhesions were bleached using a 488nm laser at 80% power with a pixel dwell time of 12.61 µsec and scan time 1.94 sec. 10 cells were analysed for each experiment and experiments were carried out in triplicate. The evolution of the fluorescent intensity was monitored for 5 min, imaging every 5 sec: initial intensities were monitored for 4 scans before starting to bleach. Bleaching was performed in two iterations and stopped when densities dropped to about 50%. During the scan, the intensity was measured by the ZEN software and stored for post processing. The intensity at each time point (*I(t)*) was referred to the initial intensity (I_0, intensity before photobleaching):

$$I_{rel}(t) = \frac{\mathrm{I(t)}}{I_0}$$

There was no need for background correction as the intensity of this was always 0. The experimental data were fitted using the software Origin 8 with and exponential growth equation:

$$I_{rel}(t) = A_0(1 - e^{-\tau t})$$

Where τ is the rate constant of the fluorescent recovery and A_0 is the mobile fraction. Results are reported as averages with standard errors of the mean.

4.2.6 Statistical analysis.

Statistical analysis was carried out using Origin 8 and one-way ANOVA with Tukey test for posthoc analysis. Significance was determined by * $P < 0.05$, ** $P < 0.01$, *** $P < 0.001$. A full summary of statistical analysis is provided below (Supplementary Tables). In figure captions, “n” means the number of independent replicates of the experiment presented.

4.3 Results and discussions

4.3.1 How integrin expression affect focal adhesion formation

Focal adhesions formed from the GE, GEβ1 and GEβ3 cells were further analysed in order to assess differences depending on the integrins expression and the different nanofibres sizes.

All three cell lines, upon adhesion to nanofibres, displayed more large and elongated adhesions, a phenomenon that was most striking for GE and GEβ3 cells (Fig. 4.1): the population of the largest adhesions (above 1 μm^2) assembled on the nanopatterns is larger than for adhesions formed on homogenous substrates (excluding the smallest fibre patterns). Furthermore for GE and GEβ3 cells the biggest adhesions on control are up to 7.78 μm^2 while on the 1000 nm nanofibres they go up to 39 μm^2; this is not observed for GEβ1 cells. However, for all three cell types, the size and number of adhesions decreased with the size of nanofibres (Fig. 4.1), especially for GEβ3 cells, confirming the control of cell adhesion geometry through ENL, irrespective of integrin expression. This reduction in size was apparent for the largest adhesions, which displayed reduced populations on smaller nanofibres. This may indicate that the restricted nanoscale geometry determined by nanofibres contributes to the merging or stabilisation of adhesions into larger complexes. This is however insufficient to maintain the spreading area observed for cells on control homogenous substrates and is consistent with the notion that ECM geometry may directly impact on the assembly of other structures than focal adhesions, such as the actin cytoskeleton, to regulate spreading. Overall, the reduction in ECM adhesion size and numbers was associated with a disruption of the structure of the cytoskeleton, with shorter and thinner actin fibres originating from adhesions formed on smaller nanofibres (Fig. 3.10-12, from previous chapter).

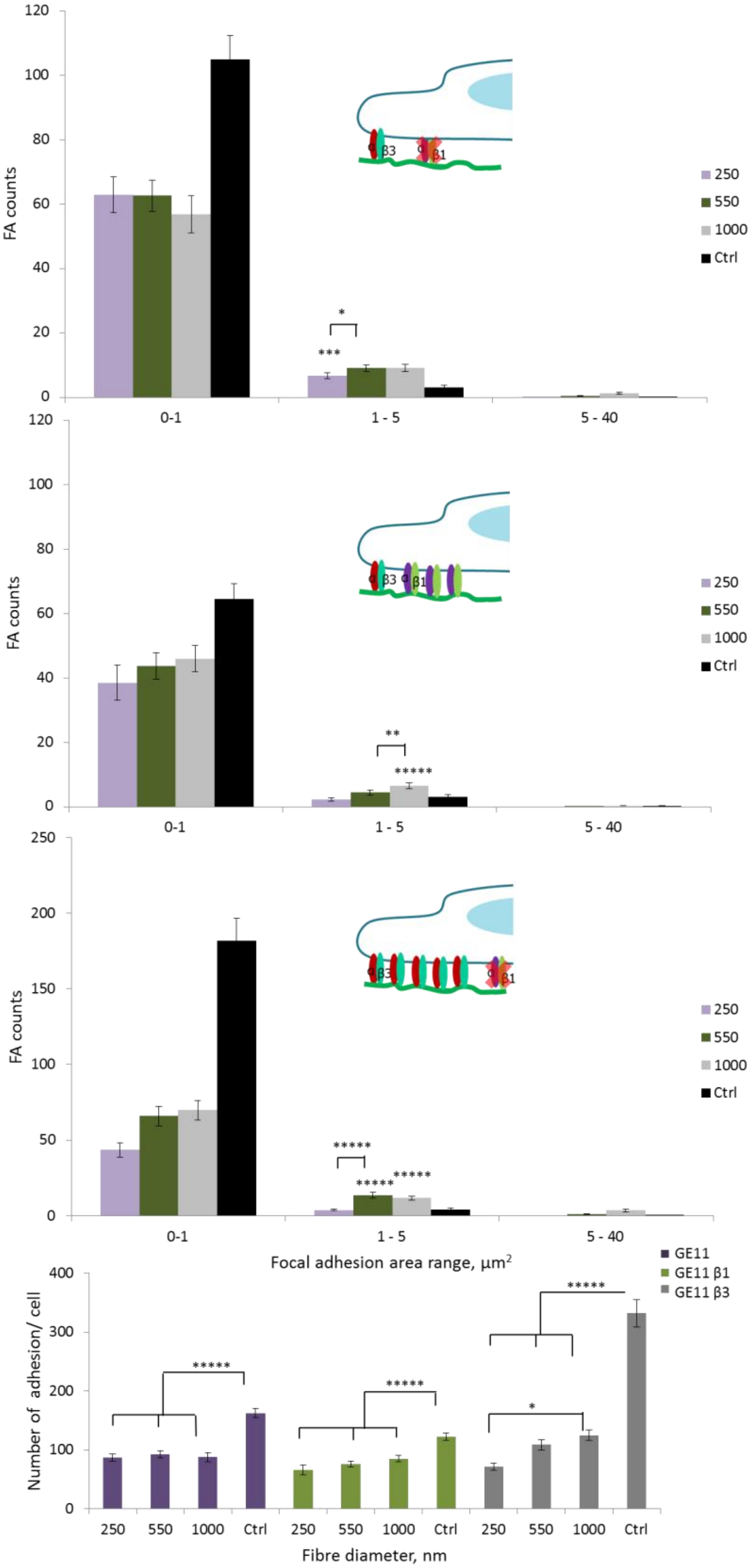

Figure 4.1 Focal adhesion distributions. A, B and C: focal adhesion size distribution for the GE, GEβ1 and GEβ3 cells (respectively) on the different nanofibres size. Focal adhesion sizes are divided in three

ranges: from 0 to 1 μm^2 for focal complexes, from 1 to 5 μm^2 for mature focal adhesion and from 5 to 40 μm^2 for fibrillar adhesion. D: total number of FA per cell for each condition. Ctrl is the homogenous control surface. Error bars are SE, n = 3, with n representing the number of experiments. For statistical test: *, $P < 0.05$; **, $P < 0.01$; ***, $P < 0.001$; ****, $P < 0.0001$.

Circularity of focal adhesions (Fig. 4.2) seems to be unaffected for the three cell types on the different nanofibres, for focal adhesion range between 0 to 5 μm^2. GE and GEβ3 cells show a decrease in circularity for the biggest adhesion range (5 to 40 μm^2). The focal adhesion aspect ratio is instead more affected. For the GEβ1 and GEβ3 cells, adhesions formed on fibres present higher aspect ratio with increasing size of the adhesions (above 1 μm^2) compared with adhesions formed on the controls. GEβ3 cells in particular show the highest aspect ratios for adhesion assembled on the smallest nanofibres, in agreement with the low circularity found.

These results are in agreement with the observation that the FAs (Fig. 3.10-12, from previous chapter) follow the nanofibres paths and thus adopt a “fibre-like” shape with more elongated features. Furthermore, for the GEβ3 cells the adhesions formed on the intermediate size nanofibres (550 nm) show the highest intensities (Fig. 4.3), although this is not statistically significant. For the GE cells, the adhesions on the smallest nanofibres present the highest intensities (not statistically significant). The GEβ1 cells show a pronounced decrease in intensity for the smallest fibre size, while no major differences can be noticed for the other nanofibres sizes and the homogenous substrates (Fig. 4.3).

It is thus clear that the geometry of the nanopattern is influencing the formation and maturation of focal adhesions, but that different integrins have also a major role in sensing the topography.

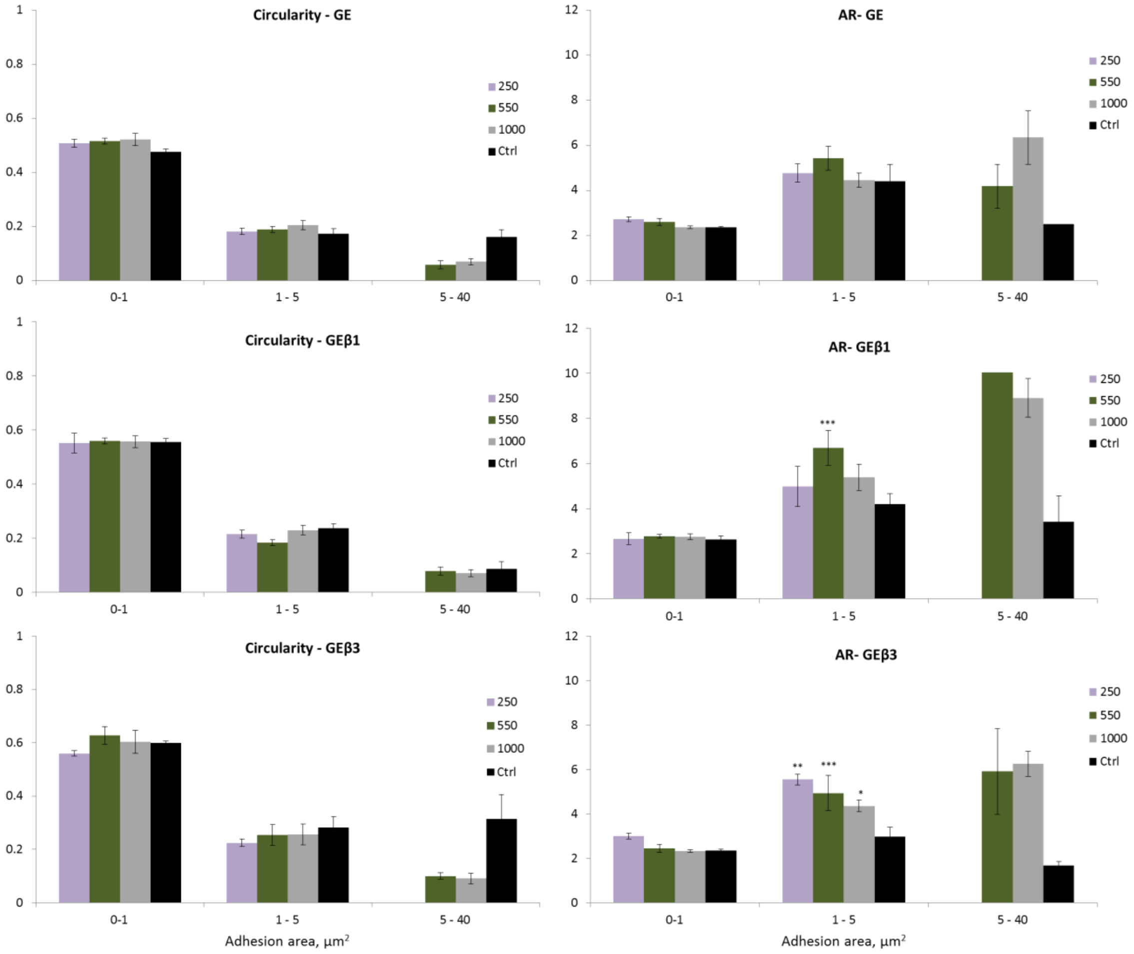

Figure 4.2 Focal adhesion shape descriptors distribution (for the three focal adhesion size ranges) of the GE, GEβ1 and GEβ3 cells on the different nanofibres size: circularity (left) and aspect ratio (AR, right). Ctrl is the homogenous control surface. Error bars are SE, n = 3, with n representing the number of experiments. For statistical test: *, P < 0.05; **, P < 0.01; ***, P < 0.001; ****, P < 0.0001.

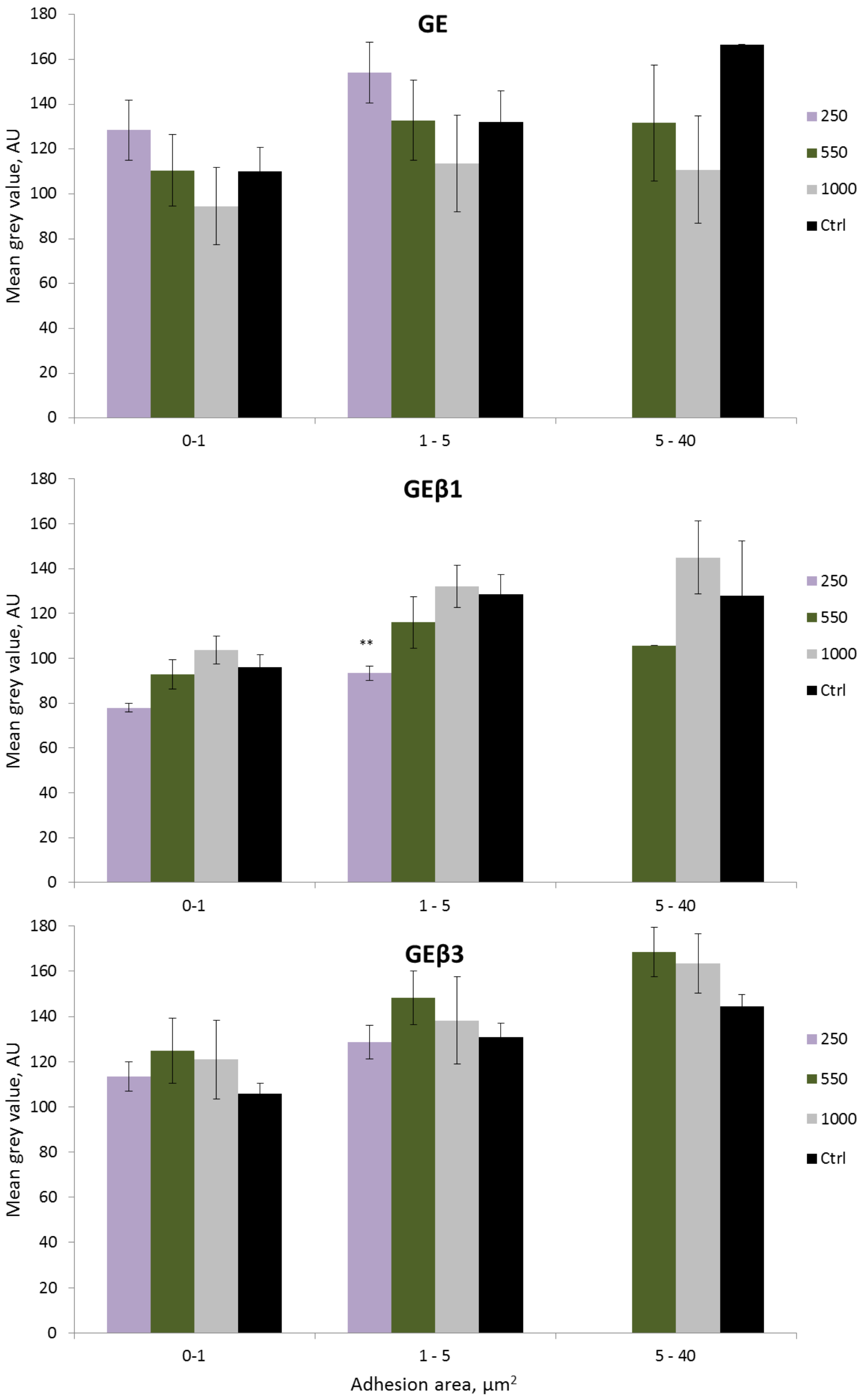

Figure 4.3 Focal adhesion intensity distribution of the GE, GEβ1 and GEβ3 cells on the different nanofibres size. Ctrl is the homogenous control surface. Error bars are SE, n = 3, with n representing the number of experiments. For statistical test: *, P < 0.05; **, P < 0.01; ***, P < 0.001; ****, P < 0.0001.

4.3.2 How is vinculin regulated at the nanoscale

The FA distributions data indicate that there are changes in the way focal adhesions assemble on the fibrous patterns, so we performed FRAP in order to see if the dynamic regulation of this protein is differentially regulated on the nanofibres. We decided to perform the next set of experiments on the GEβ3 cells as they were found to be more sensitive to the geometry of the patterns (see results from last chapter).

Vinculin dynamic regulation was assessed on control homogenous surfaces and on 550 and 1000 nm diameter nanofibres. The smallest size nanofibres were excluded because it was found to be challenging to have distinguishable focal adhesions under conditions required by our live microscopy assay. In previous reports (Gautrot et al., 2014), vinculin dynamics were measured for keratinocytes seeded on homogenous and patterned surfaces, with patch sizes of 600 and 3000 nm. Dynamics were found to be increased when going to smaller patch sizes (600 nm), as the recovery velocity of FRAP was more than doubled. These experiments were carried out with primary keratinocytes. Here GEβ3 cells were seeded on 500 and 1000 nm nanofibres and on homogenous controls and FRAP experiments were performed. Recovery velocities and immobile fraction (the amount of molecules which do not move inside a focal adhesion) were measured. The data (Fig. 4.4) indicate that vinculin recovery (*k*, s^{-1}) was faster for cells seeded on the nanofibres than on the homogenous surfaces: k = 0.027, 0.03 and 0.0168 s^{-1} on 550, 1000 nm and homogenous substrates respectively (P = 0.024 between 1000 nm and control). Velocity found on homogenous surfaces were comparable with velocity reported in other reports (k_{on} = 0.012 and k_{off} = 0.018 (Lavelin et al., 2013)). No significant differences were observed for the immobile fraction. The kinetics found for these cells are slower than kinetics measured on homogenous and nanopatterned substrates for keratinocytes (Gautrot et al., 2014): this may not be surprising considering that the type of integrins are different and β_3 integrins are known to reinforce focal adhesion and stabilise the cell (Schiller et al., 2013) thus possibly leading to slower dynamics (Danen et al., 2005, Schaufler et al., 2016).

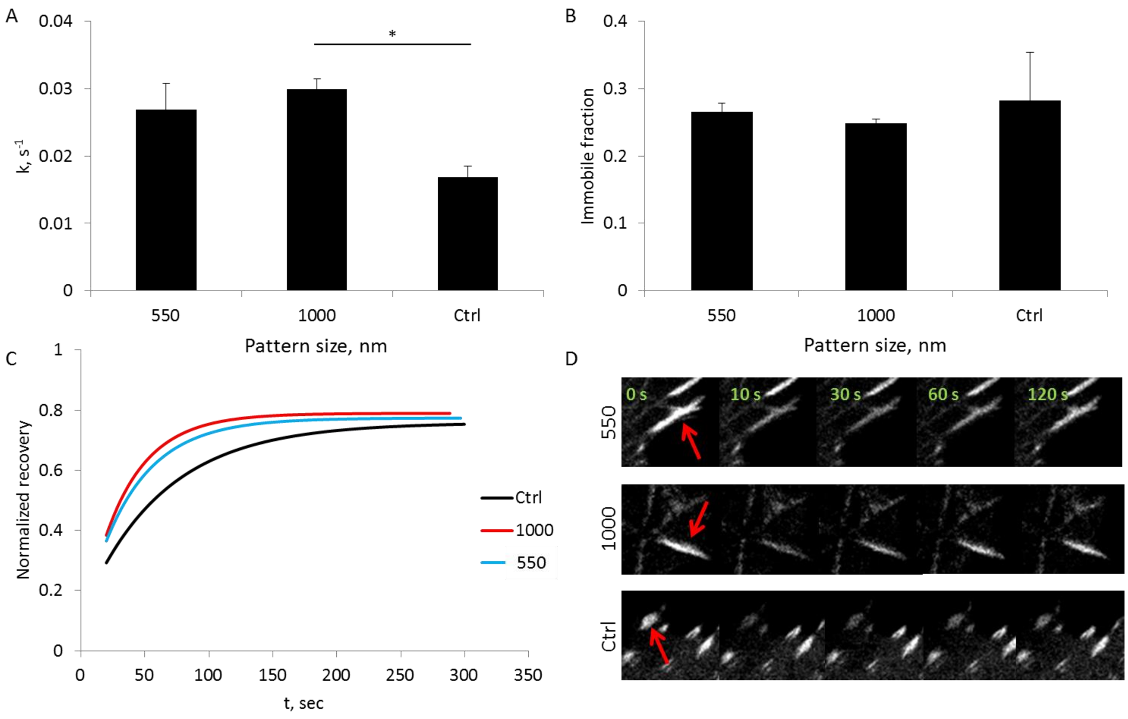

Figure 4.4 FRAP analysis for vinculin dynamics. Focal adhesions were selected at the cell edge and bleached to about 50% of the initial intensity. Vinculin recovery rate (A- *k*, s^{-1}) and immobile fraction (B) for cells seeded on homogenous surfaces (Ctrl) and patterned surfaces (550 and 1000 nm fibre diameter). The graph (C) shows typical recovery curves in the three conditions. Kymographs (D) of a sample focal adhesion for each condition during FRAP are also presented.

These dynamic studies showed a small but significant increase in the exchange rate of vinculin on the patterned surfaces compared with the homogenous. We thus tried to further assess vinculin role in the sensing of the geometry.

Mouse embryonic fibroblasts where vinculin had been knocked out (MEFvin$^-$/$^-$) were tested on fibrous patterns with fibre dimensions of 300, 500 and 1000 nm (low nanofibres densities of 20 %). Previous studies have found that these cells were less spread than wild type cells expressing vinculin and that rescuing vinculin expression in MEFvin$^-$/$^-$ cells rescued the normal spreading phenotype of these cells (Saunders et al., 2006). Here the MEFs vin$^-$/$^-$ were transfected first with vinculin plasmids and subsequently seeded on the nanofibrous patterned substrates. Cells were then analysed depending on the expression or not of vinculin (after immunostaining). Three different plasmids were used: vinculin venus (Grashoff et al., 2010), a full length vinculin tagged with venus, a variant of GFP (Nagai et al., 2002); vinculin T12, a constitutively active form of vinculin presenting mutation that impair head – tail associations; vinculin 880, truncated on the N-terminal 880 amino acids, thus lacking the tail domain able to bind actin (Humphries et al., 2007). Cells expressing the latter two constructs were shown to assemble denser and larger focal adhesions (Carisey et al., 2013) displaying slower dynamics, possibly due to changes in affinity for vinculin binding proteins due to conformational changes, ultimately resulting in the higher stability of those vinculin constructs within focal adhesions.

MEFvin^{-}/$^{-}$ and those expressing the three different vinculin constructs tested displayed similar responses to the diameters of the nanofibres (Fig. 4.5 A): cells spreading gradually decreased with decreasing fibre size (cells spreading on the smallest nanofibres, 300nm, were found to struggle to adhere and there is a more than two folds decrease in cell area compared to cells spreading on the homogenous surfaces, $P < 0.00001$). However, no significant differences were found between transfected and non-transfected cell areas for the vinculin venus and T12 plasmid. Surprisingly, cells treated with the vinculin 880 appear to be more sensitive, with statistically differences in cell spreading between the transfected cells and non-transfected on the homogenous surface (779 ± 25 and 962 ± 103 µm^2 respectively for cells transfected or not, $P = 0.00155$) and the 1000 nm nanofibres (624 ± 39 and 753 ± 87 µm^2 respectively for cells transfected or not, $P = 0.01135$). This is not consistent with what was found in other works, where vinculin null cells were found to be more spread after rescuing vinculin expression (Saunders et al., 2006). When comparing cells transfected with the three different plasmids and spreading on nanofibrous substrates, no significant differences were found either, although there is a slight tendency for cells expressing the vinculin venus construct to be more spread than the others, while the cells expressing the vinculin 880 plasmid present lower spreading on control and 1000 nm nanofibres.

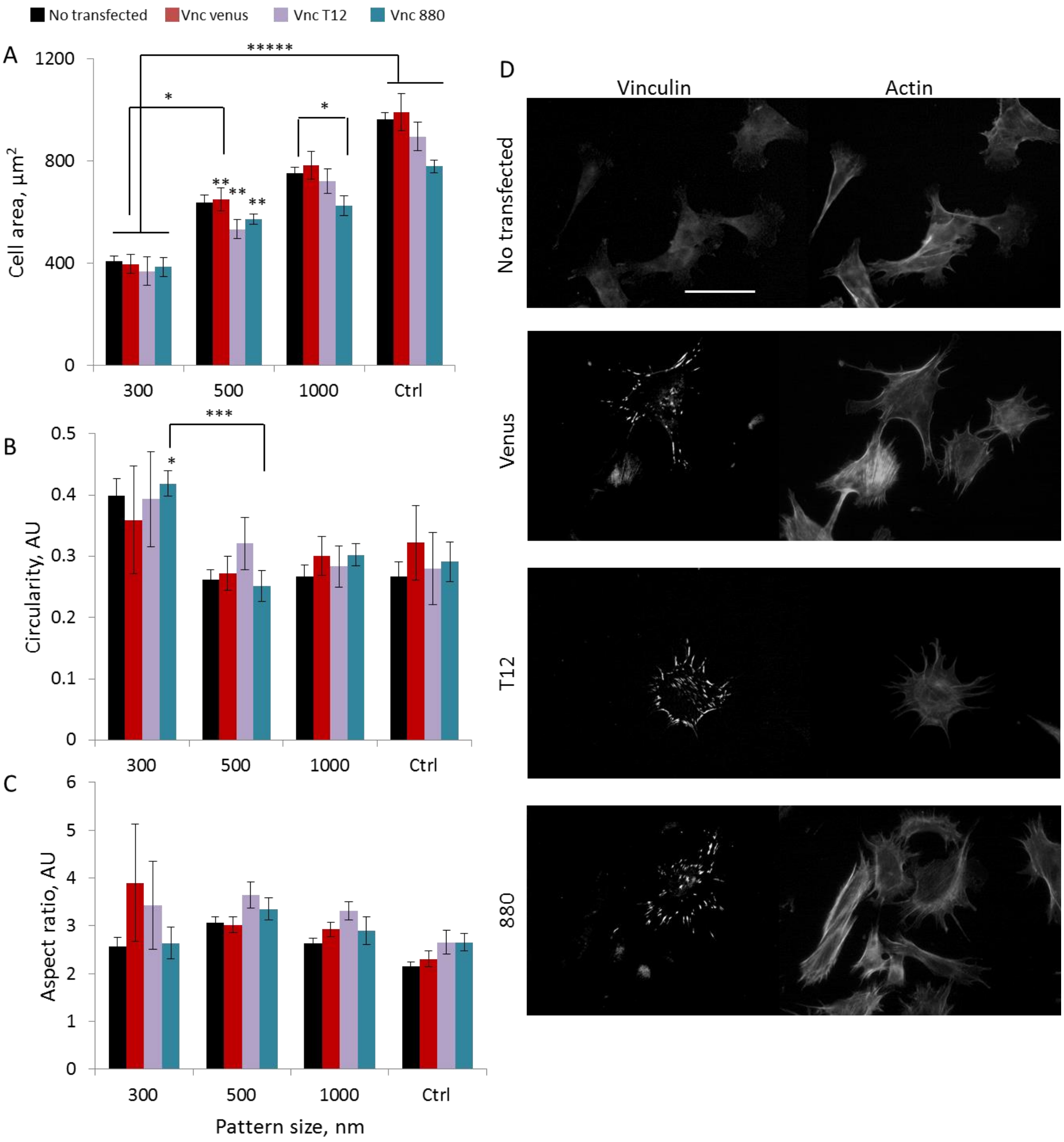

Figure 4.5 MEFvin^{-}/$^{-}$ cells transfected or not with the specific plasmid (vinculin venus, T12 and 880). Cells were spreading on nanofibres (300, 500 and 1000 nm diameter) or on homogenous surfaces (Ctrl) for 24 hr. Cell area (A), circularity (B) and aspect ratio (C) data are shown in the graphs. Error bars are SE (n ≥ 3, with n representing the number of experiments). For statistical test: **, P < 0.01; ***, P < 0.001; ****, P < 0.0001; *****P < 0.00001. (D). Representative epifluorescent images of non-transfected cells and cells expressing the three different plasmid and spreading on homogenous surfaces. Scale bar is 50 µm.

Cell shape was also found to be relatively insensitive to vinculin expression on the different nanofibres (Fig. 4.5 B, C). For cells expressing the vinculin 880 construct, there is a significant increase in circularity for cells spreading on the 300 nm fibres (and circularity are generally higher on this nanofibres for all conditions): this is probably due to the fact that cells struggle to spread when seeded on these nanofibres and therefore cannot form stable cell protrusions leading to elongation. Non transfected cells seem to present less elongated morphologies (lower aspect ratio, Fig. 4.5 C), and this is more evident on the 300 nm nanofibres: this may be a symptom that these cells may sense the geometry of the substrates more than those expressing the various vinculin constructs studied.

The epifluorescent images (Fig. 4.6 and 4.7) show that there is a slight tendency for transfected cells seeded on the nanopatterns to adopt more polarised morphologies. It seems evident that on the homogenous surfaces (Ctrl) focal adhesions are arranged in a different fashion for the three vinculin plasmid. These differences are lost when cells are spreading on the nanofibres, which may indicate a stronger effect of the geometry of the nanopatterns than of the differences in vinculin expression.

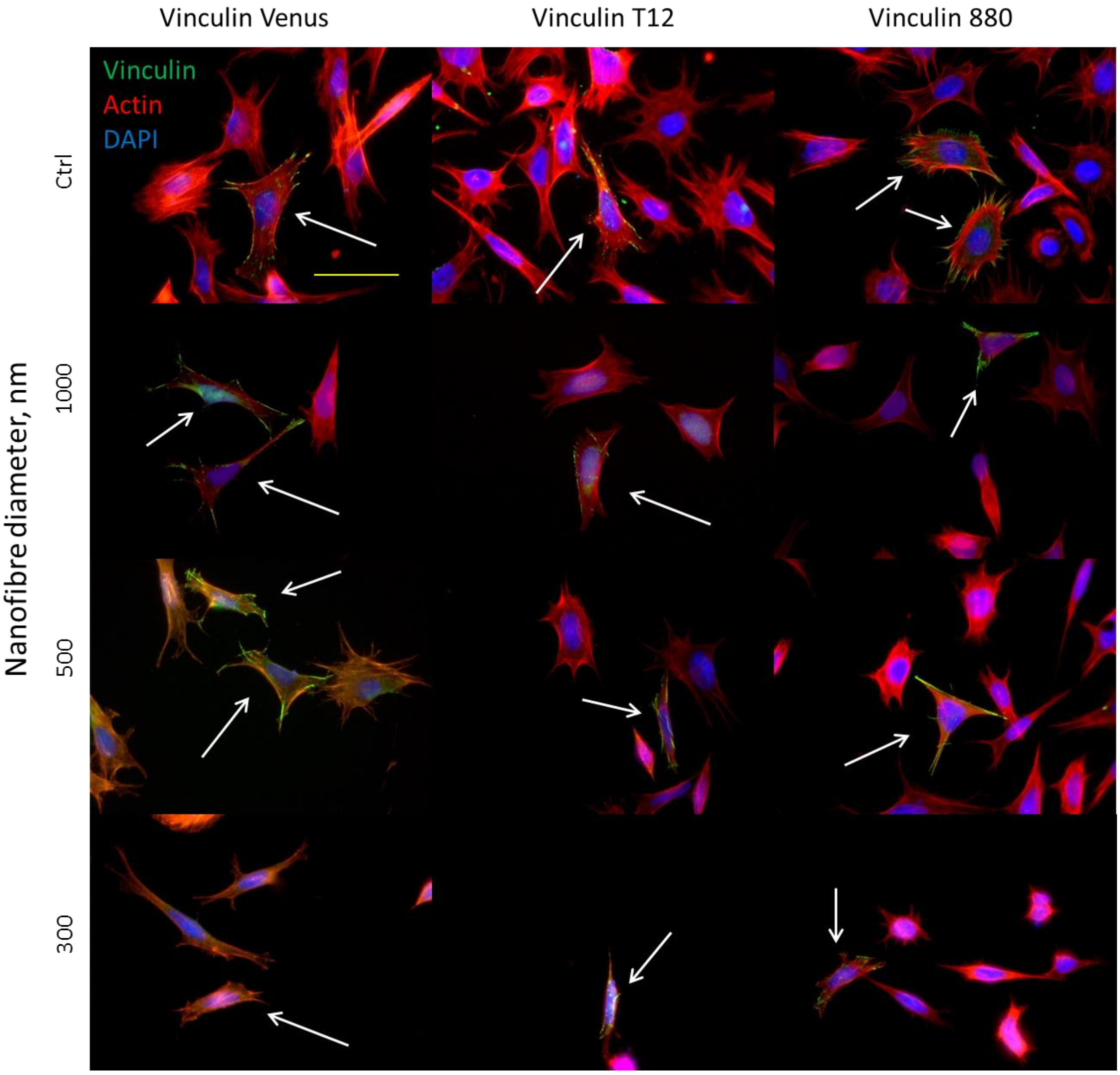

Figure 4.6 Epifluorescent images of MEFvin⁻/⁻ cells spreading on nanofibres at different diameters (300, 500 and 1000 nm) and on homogenous surfaces (Ctrl). Cells were transfected or not with the specific vinculin plasmid (green in the images, vinculin venus, T12 and 880) . The white arrows point at transfected cells. Scale bar is 50 µm.

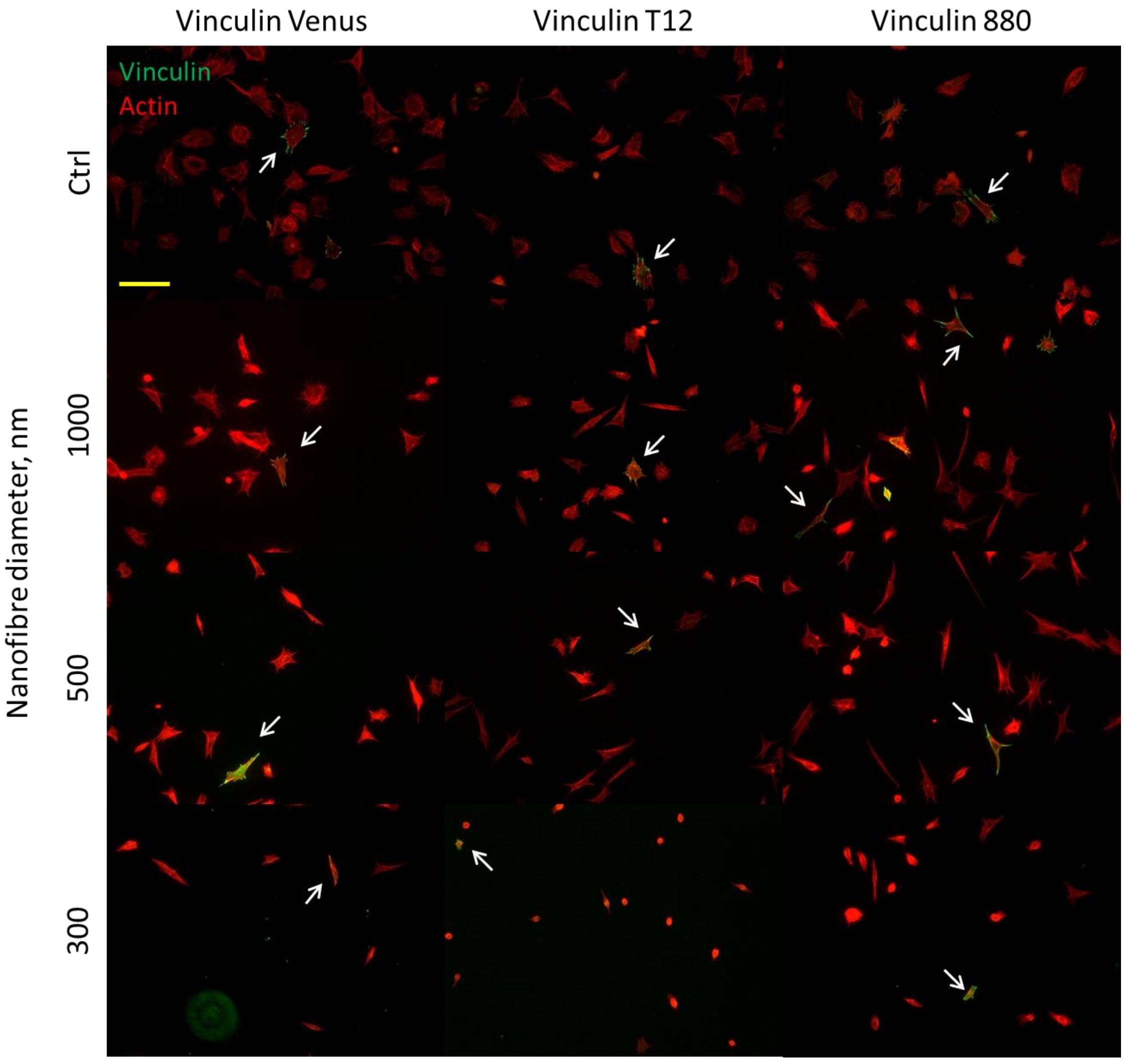

Figure 4.7 Epifluorescent images of MEFvin⁻/⁻ cells spreading on nanofibres at different diameters (300, 500 and 1000 nm) and on homogenous surfaces (Ctrl) (lower magnification). Cells were transfected or not with the specific vinculin plasmid (green in the images, vinculin venus, T12 and 880). The white arrows point at transfected cells. Scale bar is 100 µm.

Together, these results suggest that although a clear focal adhesion rearrangement appears from the images and FA data and the kinetics of vinculin is altered on the nanofibres, it fails to alter cell phenotype and it may thus not represent a major player in nanoscale sensing, but that other molecules may be primarily involved in this as focal adhesion maturation (Fig. 4.6 and 4.7), cell morphology (see Fig. 4.5) and spreading are still affected by the nanofibres diameters.

4.4 Conclusions

Focal adhesions are a complex network of more than 100 components which are linked and interplay with each other in a complex fashion (Zaidel-Bar et al., 2007a, Petit and Thiery, 2000). Vinculin, talin and integrins have attracted the most attention and have been proven to be key components in the cell sensing and adhesion process (Roca-Cusachs et al., 2009) (Schiller et al., 2013, Humphries et al., 2007, Liu et al., 2015). Vinculin in particular is linked to and was found to orchestrate many adhesion components (Case et al., 2015).

Here we focused on the role of vinculin in sensing the geometry of the extracellular environment. Although there is a growing number of reports on how cells behave when adhering on constrained topographies or geometries and on how molecules in the adhesion plaque behave in “physiological” conditions, a systematic study mixing these two aspects and studying the mechanosensing when cells are forced to attach to a determined geometry is still missing or poorly addressed.

We reported that the geometry of the adhesive surfaces is affecting the geometry and maturation of focal adhesions with cells failing to spread when fibre like adhesion sites are decreased to about 250 nm in diameter. For cells seeded on nanofibres patterns with diameters ranging from 250 to 1000 nm, focal adhesions were found to be differently distributed compared to adhesions assembled on homogenous surfaces. On controls, adhesions are higher in number but they are smaller in size compared to the biggest nanofibres. Cells expressing different integrins were also compared, with cells expressing β_3 integrins being more sensitive to this pattern geometry. The decrease of focal adhesion number, but the increase of their sizes for cells spreading on the 550 and 1000 nm diameter nanofibres may suggest that adhesions are clustering on these surfaces.

Furthermore vinculin was found to be more dynamic on nanofibres of 550 and 1000 nm diameters, showing that cells possibly generate less stable adhesions on these substrates than cells spreading on homogenous surfaces, despite the observed increase in adhesion size and length.

Experiments with vinculin -deficient mouse embryonic fibroblast (*MEFvin*$^{-}$/$^{-}$) show that cell spreading and morphology do not present significant differences between cells where the protein has been recovered and cells lacking it on both homogenous and patterned surfaces. Cells are still affected from the geometry, showing a decrease in cell area as the nanofibres sizes decrease.

These results suggest that although focal adhesion formation and geometry is affected from the fibre diameter and faster vinculin dynamics are observed when cells are seeded on the nanofibres versus homogenous substrates, this molecule may not be the key player in cell sensing, but that other molecules in the adhesion plaque may be more important.

Chapter 5

Actin sensing of the geometry

5.1 Introduction

Vinculin has been previously introduced for its role in mechanosensing and for its ability to transmit and sustain forces via the link to the actin cytoskeleton (Dumbauld D.W. et al., 2013, Chang and Kumar, 2013, Thievessen et al., 2013). This connection was found to be crucial for changes in cell shape and migration and for sensing ligation to the ECM. Actin assembly is thus directly connected to the sensing of the biochemical and physical properties of the extracellular environment and it is essential to sustain cell spreading and morphological changes, as well as cell motility on both 2D (Thery et al., 2006, Reymann A. C. et al., 2012, Gautrot et al., 2010, Schwingel and Bastmeyer, 2013, Schvartzman et al., 2011, Slater et al., 2015) and 3D matrices (Prager-Khoutorsky et al., 2011, Fraley et al., 2010, Miron-Mendoza et al., 2010). Cells seeded on nanopatterns showed increased motility with decreasing size of adhesion sites (Slater et al., 2015). Lamellipodia were also found to have enhanced kinetics when cells were seeded on 8 nm adhesion patterns, a phenomenon that was modulated by the spacing between adhesion sites (Cavalcanti-Adam et al., 2007). As mentioned in the introduction chapter, F-actin polymerization in the lamellipodium correlates with small stresses, while in presence of mature focal adhesion, thicker stress fibres are formed that are associated with higher stresses (Gardel et al., 2008). Therefore thicker stress fibres have been generally associated with more static cells (Pellegrin and Mellor, 2007). Despite numerous studies focusing on actin dynamics (Ponti et al., 2004, Reymann et al., 2010) and the correlation of actin motion with other focal adhesion proteins (Hu et al., 2007, Brown et al., 2005), little is known on how these dynamics correlate with constrained adhesions, that is when cell are seeded on surfaces/ matrices displaying defined topographies or geometries.

Given the apparent insensitive response of cell rearrangement to the mechanotransducer protein vinculin in nanoscale sensing of matrix topography, and given the apparent changes in cytoskeleton rearrangement, we focused on understanding in more detail how the cytoskeleton is regulated by nanofibre diameters and propose that it acts as the primary nanoscale sensor.

An in-depth examination of actin cytoskeleton organization for GE, GEβ1 and GEβ3 cells spreading on the different nanofibres after immunostaining is here proposed. Actin dynamics of GEβ1 and GEβ3 cells were also assessed for cell spreading on the different nanofibres sizes. Finally, the role of contractility in sensing the extracellular environment was investigated assessing the degree of colocalization with actin of two proteins involved in actin arrangement (α-actinin and myosin II) for GEβ1 and GEβ3 cells on the nanofibres and how the “curvature” imposed from the brush height influences cell spreading and focal adhesion formation. Actin cytoskeleton inhibitors were also tested for this purpose and in order to understand the role of contractility in the geometry sensing.

5.2 Matherials and methods

5.2.1 Materials and chemicals

Keratinocyte- SFM (KSFM), Penicillin-Streptomycin (5,000 U/mL), L-glutamine, secondary goat anti –rabbit 488 were from Thermo Fisher. Foetal bovine serum (FBS) was from PAA. jetPEI HTS DNA (1mL) and 50 mL Sodium Chloride were from Polyplus. Mouse monoclonal Anti-α Actinin antibody was from abcam. DMEM (500 mL), trypsin, versene (100 mL), Alexa Fluor goat anti-mouse 488 was from Life Technologies. Rabbit polyclonal Anti-Myosin IIA, non muscle antibody (0.2 mL), monoclonal Anti- Vinculin antibody produced in mouse, Phallodin –Tetramethylrhodamine B isothiocyanate, DAPI (4,6-diamidino-2-phenylindole), myosin inhibitor Blebbistatin, Dimethyl sulfoxide (DMSO) were from Sigma. Rock inhibitor Y-27632 was from R&D Systems. LifeAct-TagRFP plasmid was from Ibidi. 6 and 48- well plates were from Corning Costar. Silicone elastomer curing agent and silicone elastomer base (Sylgard).

5.2.2 Cell culture and seeding

GEβ1 and GEβ3 cells were cultured as described in Chapter 3 and seeded in 48 well plate containing the fibronectin functionalised nanofibres at a density of 7500 cells/mL (0.5mL/well) in DMEM medium. Cells were then allowed to adhere for 24 hrs and then fixed for staining for colocalization study.

GEβ1 and GEβ3 cells were also seeded overnight in 6 well plates at a density of 200K/ well for transfection with LifeAct.

GEβ3 cells were seeded in 48 well plates on fibronectin- coated nanofibres with different polymer brush height (30 nm and 10 nm dry thickness) for vinculin immunostaining and for cytoskeleton inhibitor treatment.

5.2.3 Cytoskeleton inhibitors treatment

Inhibitors Y-27632 and Blebbistatin were diluted in DMSO so to have a starting solution of 10mM. GEβ3 cells were seeded on nanofibres with different diameters and brush height in 48 well plate at density of 7500 cells/ mL and 0.5mL/ well. After 24 hrs they were treated with one of the two inhibitors for 4 hrs at a concentration of 10 μM in DMEM medium. Non treated cells were incubated in DMEM/ DMSO at the same concentration used for the inhibitors. They were then fixed and stained for actin, nucleus and vinculin for cell spreading and FA characterization.

5.2.4 Immunostaining for myosin II and α-actinin

GEβ1 and GEβ3 cells were immunostained for α-actinin and myosin II to see expression and colocalization with the actin cytoskeleton for cells seeded on the nanofibres. After 24 hrs spreading cells were fixed and stained with anti-myosin II and anti - α-actinin (dilution 1:200) and relative secondary (488 nm). Phalloidin and dapi staining were also performed.

5.2.5 GEβ1 and GEβ3 transfection

GEβ1 and GEβ3 cells were transfected with LifeAct plasmid (actin marker for the visualization of F-actin in living cells) after overnight spreading in 6 well plate. The procedure for transfection is the same as illustrated in Chapter 4. The amount of DNA/ jetPEI used was 3 μg/ 4 μL. After 24 hrs from transfection cells were detached using trypsin/versene and 100 µL of the cell suspension was reseeded in the prepared Petri dishes with nanofibres size of 250, 500 and 1000 nm. Cells were analysed the day after.

5.2.6 Immuno-fluorescence microscopy and data analysis

Fluorescence microscopy images for α-actinin and myosin II staining in GEβ1 and GEβ3 cells and for vinculin staining of GEβ3 cells on different brush heights and after inhibitor treatment were obtained with a Leica TCS SP2 confocal and multiphoton microscope (X-CITE 120 LED lamp, 63X1.4 Oil lens). To quantify α-actinin and myosin II colocalization with the cytoskeleton, 10-15 cells were analysed (one experiment only). For colocalization analysis of α-actinin and myosin II with the cytoskeleton, ImageJ plug in "JaCoP" was used. It is possible to measure several colocalization coefficients, between which the Pearson's coefficient is the one we are interested in. Focal adhesion analysis was carried out as illustrated in Chapter 3.

Fluorescence microscopy images to quantify GEβ3 cells spreading and cell density on different brush height and after inhibitor treatment were acquired with a Leica DMI 4000B epifluorescence microscope (EL6000 lamp, 20x0.7 NA lens, 63x1.40 Oil lens). 100 cells per condition were analysed and experiments were carried out in triplicates.

Live imaging

GEβ1 and GEβ3 cells expressing LifeAct and seeded on either the patterned surfaces or homogenous substrates were analysed for live cell microscopy with a Zeiss Super resolution LSM 710 ELYRA PS.1 equipped with an environmental chamber where the level of CO_2 was kept at 5% and temperature at 37.5 ˚C. Live cell images were acquired using a 63X 1.4NA oil DIC M27 objective using confocal mode. LifeAct fluorescence was detected using a 543-nm diode laser. For live imaging experiments, images were collected over 150 min taking pictures every 1 min and 5 to 10 cells were analysed per experiments and repeated in triplicate.

The cell area change and trajectories over time were measured via ImgeJ. Cells were thresholded and the area and the centre of mass were extracted for each time point. Velocities were then calculated. For the protrusion velocity, a line was drawn over the cell edge at a certain angle with the cell centre and the position of the edge was detected via ImageJ. 5 cells were analysed for each condition.

Analysis of actin cytoskeleton: MatLab

Cytoskeleton analysis was performed by Dr. Núria Gavara (Queen Mary University of London) and the live imaging videos of actin cytoskeleton were analysed using a MatLab code (courtesy of Dr. Núria Gavara, London, (Gavara and Chadwick, 2016)). Briefly the code is based on optimization steps in order to identify single actin fibres and get measurements of them. The process is based on image segmentation and then application of filters in order to identify the fibres. Checkpoints are inserted at each step to verify the consistency on the fibre selected. For the live imaging, the algorithm requires to circle the cell that need to be analysed (in case more objects are present in the same image) and then it follows it at each time point, although no single fibre dynamic cross correlation can be done. Although cross-correlation is not possible with this technique, a sense of how certain fibres variables change over time can be obtained. The algorithm measures several fibres parameters and the one we are considering here are fibre length, apparent thickness, chirality and convexity. The apparent thickness does not represent the real thickness, which would be impossible to calculate with the microscopy techniques used here, but more an average of pixel intensities in each fibre: the thickest the fibre the highest is the intensity value for the pixels composing the fibre, for example stress fibres will show higher values than a single actin fibre. Chirality measures whether fibres point circumferentially (showing a value close to 0) or to the cell centre (having a value assigned close to 90). Convexity gives an indication of how cells morphology looks like: if cells look more like a star (they have a higher value) or a petal (they have a lower value) (see Fig. 5.1 for schematic).

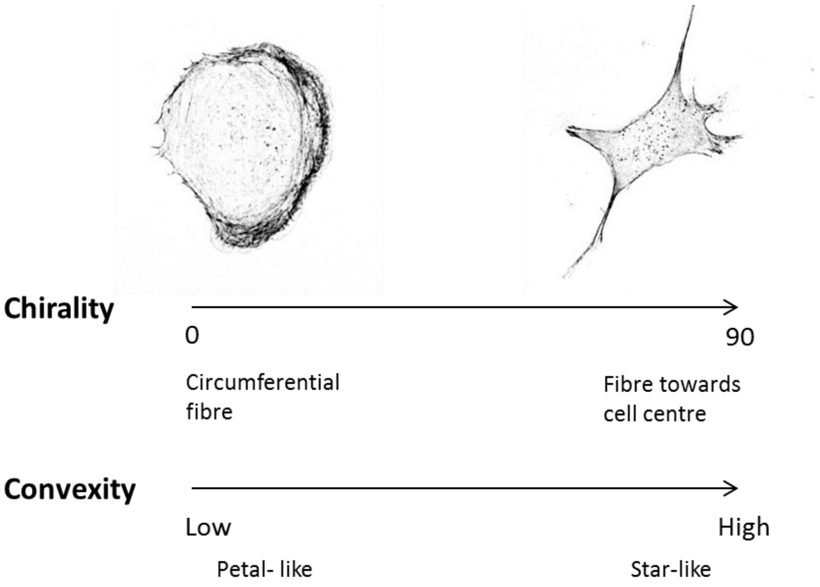

Figure 5.1 Example of cell with low/ high chirality and convexity.

5.2.7 Statistical analysis

Statistical analysis was carried out using Origin 8 and one-way ANOVA with Tukey test for posthoc analysis. Significance was determined by * $P < 0.05$, ** $P < 0.01$, *** $P < 0.001$, ****$P < 0.0001$. A full summary of statistical analysis is provided below (Supplementary Tables). In figure captions, “n” means the number of independent replicates of the experiment presented.

5.3 Results and discussions

5.3.1 Actin cytoskeleton organisation on nanofibres

The cell cytoskeleton is mainly composed of actin filaments and microtubules (Fletcher and Mullins, 2010). Filaments then associate into thicker fibres called stress fibres, which are the main players in force bearing and cell contractility.

The organization of the cytoskeleton has been widely studied (Pellegrin and Mellor, 2007, Tojkander et al., 2011, Hotulainen and Lappalainen, 2006, Thery et al., 2006), but quantification of what happens on constrained substrates (when cells are forced to adhere on micro or nanopatterns for examples) is still missing or poorly characterised. Here we are quantifying some differences between stress fibres features when GE, GEβ1 and GEβ3 cells are adhering to nanopatterns with different fibre diameters (250, 550 and 1000 nm) or to homogenous- coated surfaces. This analysis has been carried out using a MatLab code (kindly by Dr. Nuria Gavara, see methods section) which identifies and quantifies some properties of the actin cytoskeleton. In Fig. 5.2 there is an example of how the fibre extrapolation is visualized. The results are shown as four maps, two intensity maps (with the fibres identified, top right) and two directionality maps (with direction of the fibres identified).

Features that we were particularly interested in and that were showing a change for the three cell types were: fibre length and thickness, chirality and convexity.

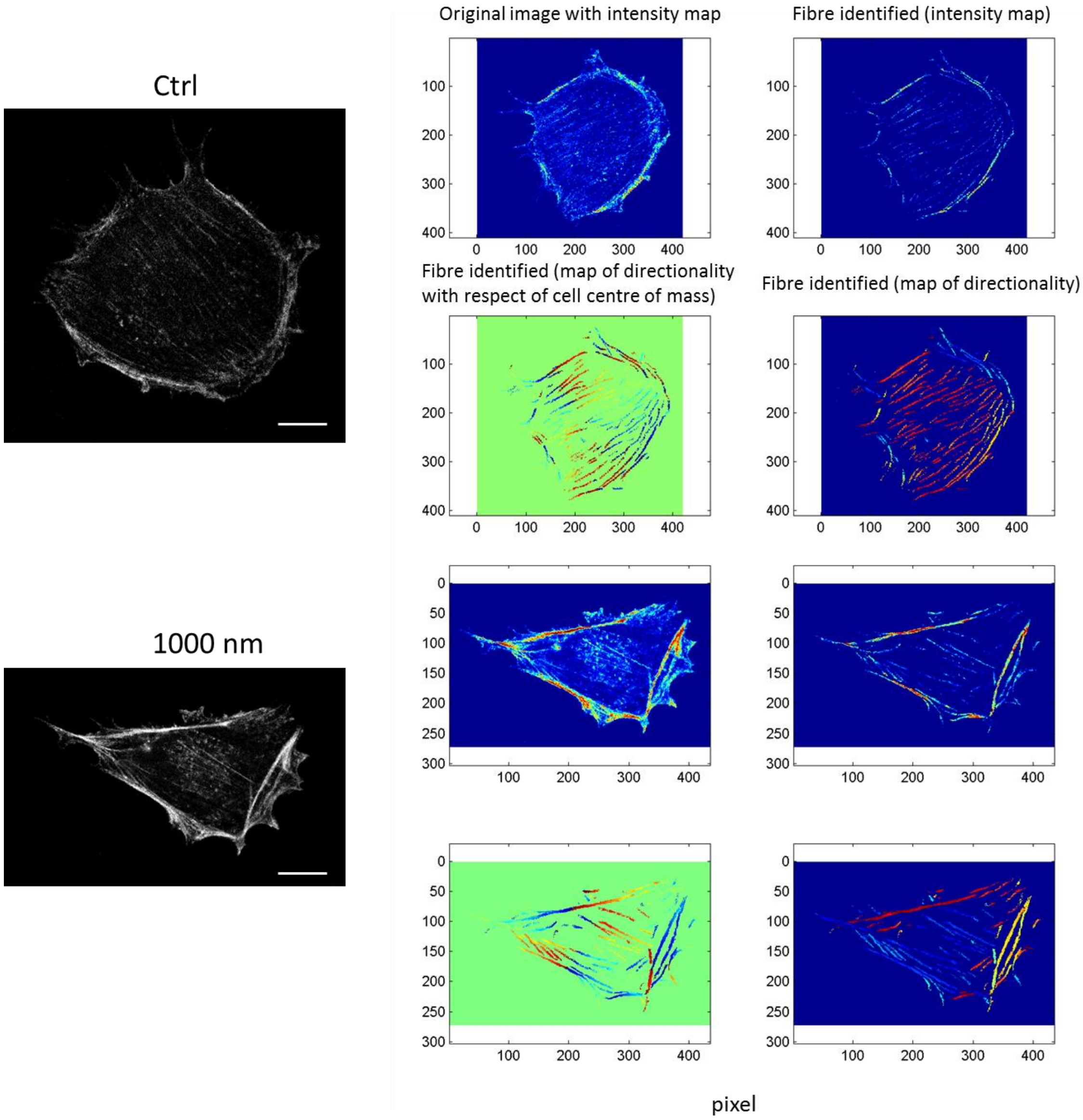

Figure 5.2 GEβ3 cells. Confocal images of the actin cytoskeleton (grey scale image on the left, scale bar is 10 µm) of cells spreading on nanofibres (1000 nm diameter) and homogenous surfaces (Ctrl) were analysed with a MatLab code to extract actin fibres measurements. On the right there are examples of maps extracted from the code: intensity of the F-actin, actin fibres identified (intensity map) and fibre direction. Axis units for the maps are pixels: 1µm = 0.19 pixel.

Data (Fig. 5.3) show that, consistent with previous observations, GE and GEβ1 cells present thicker stress fibres on the 1000 nm nanofibres, followed by the control while GEβ3 cells present thicker stress fibres on the 550 and 1000 nm nanofibres. These cells also present the thickest stress fibres for all conditions, showing that maybe a higher reorganisation is needed in order for the cells to spread on these nanofibres. Cell spreading on the 1000 nm nanofibres also present the longest fibres, that is apart for

GEβ3 cells, which presents the longest fibres on the 550 nm nanofibres. In agreement with the cell shape results obtained (Fig. 3.9 from Chapter 3) GEβ1 cells present the highest convexities, as they have more a “star” morphology and this does not change significantly for all the nanofibres (apart between the 250 and 1000 nm). GEβ3 cells exhibit again more significant changes between cells seeded on control and patterned surfaces than the other cell types. As expected, chirality is lower for cells seeded on control surfaces for GE and GEβ3 cells (with most significant changes for the latter) as these cells present generally thick stress fibres around the cell periphery (Fig. 5.4), while they have more randomly organised and directed fibres for cells seeded on nanofibres. Due to the nature of their morphology, GEβ1 cells generally show fibres directed more toward the centre of the cells and do not present significant differences between the various conditions.

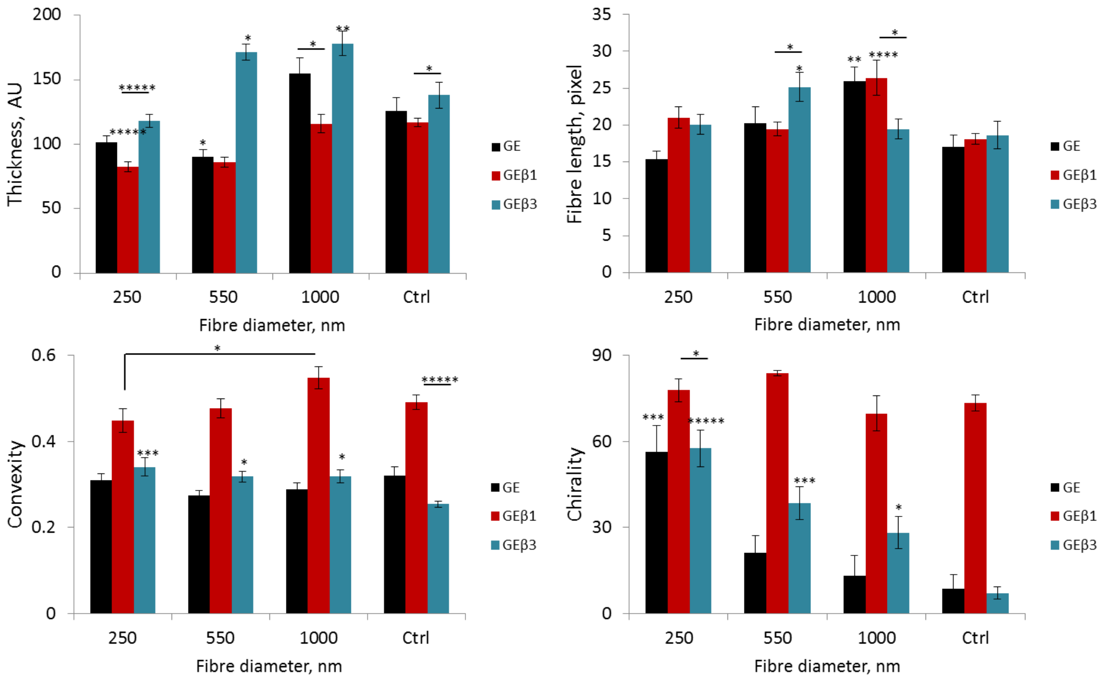

Figure 5.3 Actin fibres characterization for GE, GEβ1 and GEβ3 cells seeded on control and nanofibres (250, 550 and 1000 nm diameter). From confocal images after 24 hr spreading. Apparent thickness, length, convexity and chirality were measured from confocal images. Error bars are SE, n = 3, with n representing the number of experiments. For statistical test: *, $P < 0.05$; **, $P < 0.01$; ***, $P < 0.001$; ****, $P < 0.0001$. Comparisons are with the control surface for each cell type, unless differently specified.

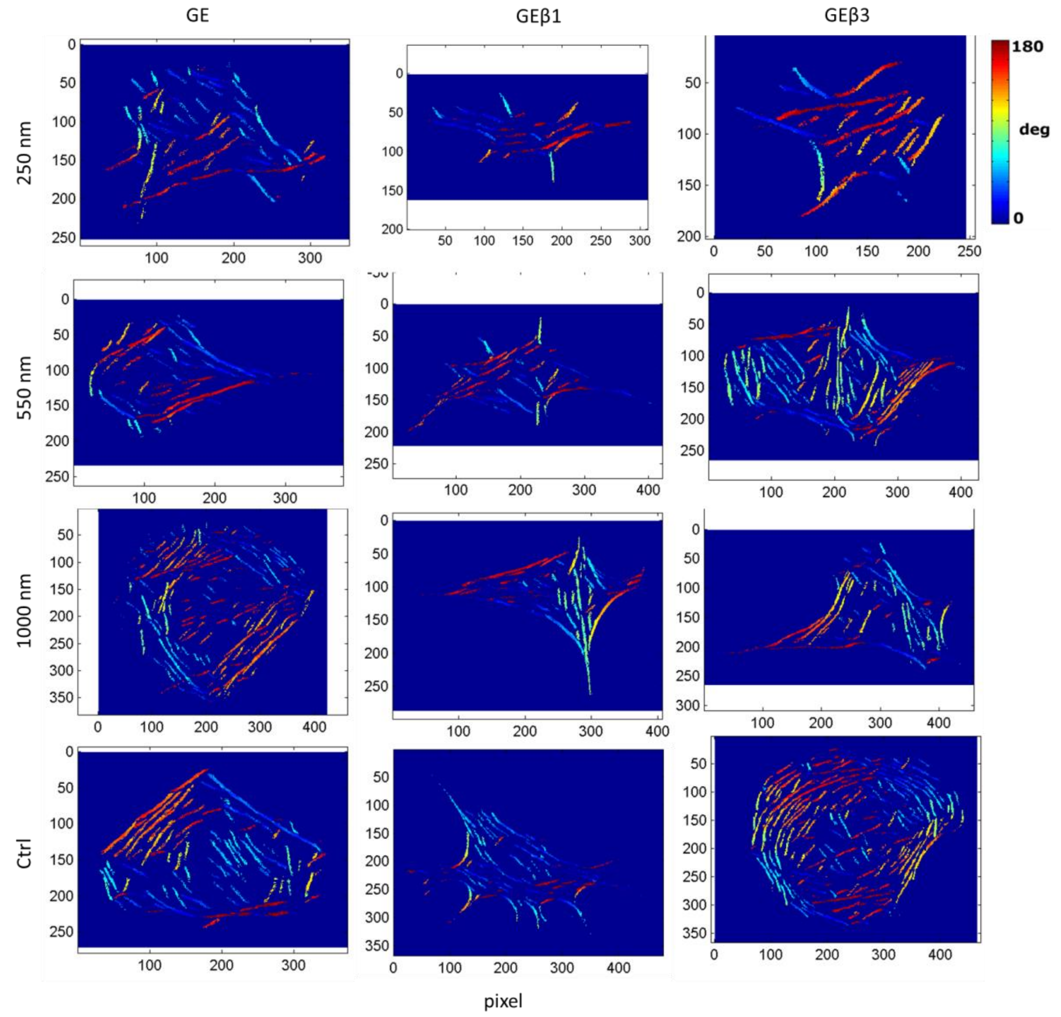

Figure 5.4 Directionality map of actin stress fibres. Examples of directionality maps of actin stress fibres for GE, GEβ1 and GEβ3 cells seeded on control and nanofibres (250, 550 and 1000 nm diameter). Maps were extracted from confocal images of actin staining after 24 hr cell spreading. For angular direction: dark blue indicates direction toward the left of the paper (0°C), red indicates the opposite direction, toward right (180 °C) and yellow green indicates the up-down direction (90 °C).

These results suggest that fibres within β3 expressing cells are more mature (thicker and longer), especially with the high β3 expressing cells, whose fibres are also more affected by the fibre diameters.

GEβ1 and GEβ3 cells were then transfected with red LifeAct and seeded on nanofibres with different sizes (250, 500 and 1000 nm diameters) and on control homogenous substrates and their behaviour (motility and cytoskeleton rearrangement) was monitored for 150 min. As can be observed from Fig. 5.5, cell morphology changes faster and more radically when cells are seeded on the nanofibres rather than on homogenous surfaces. This phenomenon seems to be linked to a faster reorganization of the cytoskeleton too, with stress fibres being less stable on patterned substrates. There are also quite clear differences between GEβ1 and GEβ3 cells, where the latter show more pronounced and clear stress fibres.

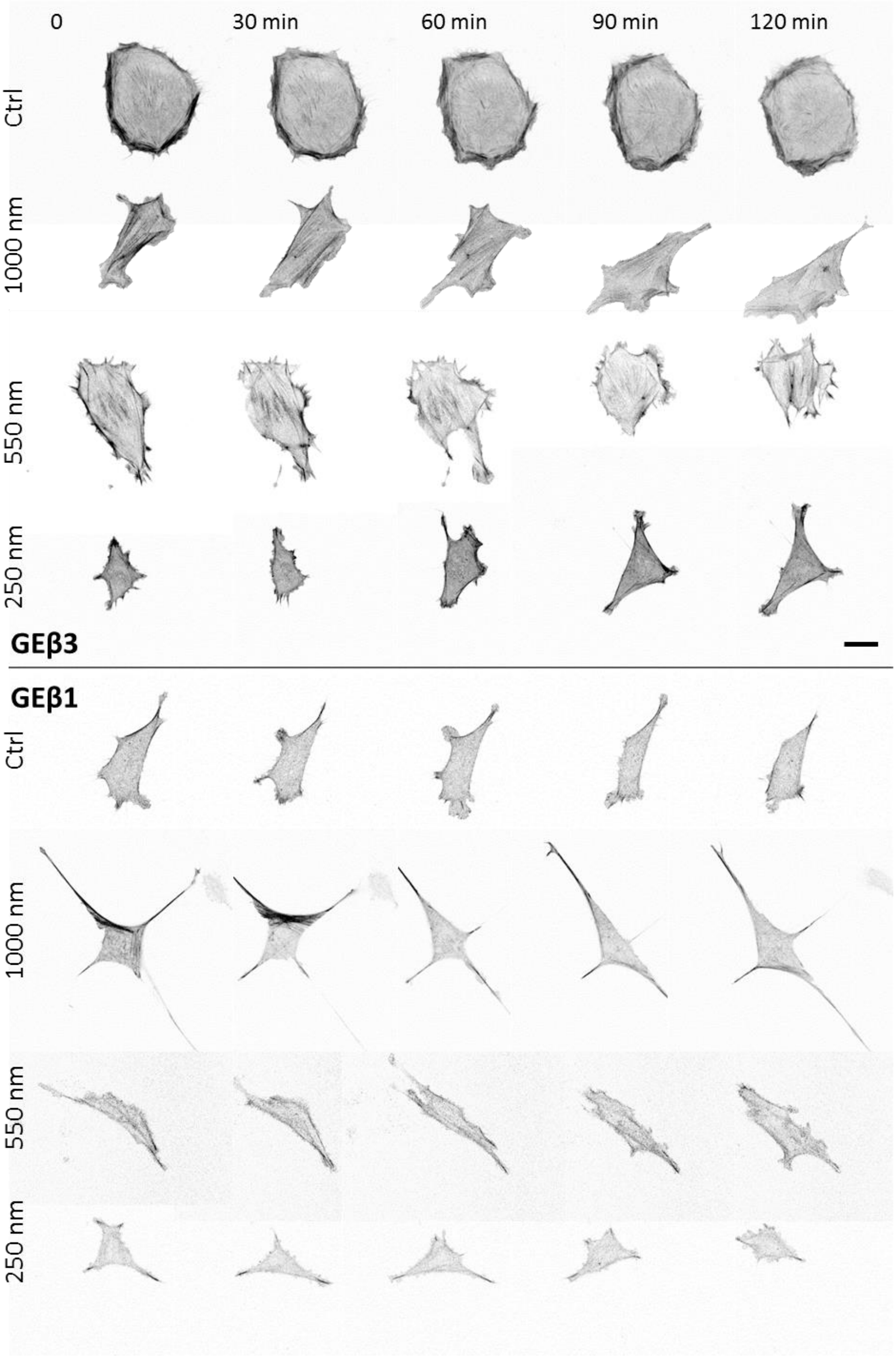

Figure 5.5 Confocal images of the actin cytoskeleton. GEβ1 and GEβ3 cells spreading on nanofibres (250, 550 and 1000 nm diameter) and homogenous surfaces (Ctrl) at different time points. Scale bar is 20 µm.

Cell area variation and cell trajectories were then assessed over time. As can be noticed in Fig. 5.6 (A and B), the cell area is relatively stable over time for cells seeded on control surfaces, while it varies significantly more with decreasing fibre sizes (the most pronounced variation is observed for cells on the 250 nm nanofibres). In agreement with this observation, cells migrate less on the homogenous surfaces (see Fig. 5.6 C and D) while they travel longer distances on nanofibres. GEβ3 cells seem to be more motile on the 250 nm nanofibres, while GEβ1 cells do not show significant differences in terms of migration velocities (Fig. 5.6 E and F). In general GEβ1 cells appear to be more mobile than GEβ3, and this is in agreement with other reports that show that GEβ1 cells present lower persistence but higher velocity than GEβ3 cells (Danen et al., 2005) (see also the protrusion velocities, Fig. 5.7). Furthermore, cell adhesion mediated by α5β1 integrins leads to faster spreading than cell adhesion mediate by αvβ3 integrins (Schaufler et al., 2016), when cells were seeded on nanopatterns with controlled ligand densities. This is linked to the observation that cells spreading on αvβ3 integrin selective ligands form larger focal adhesions, but they are not involved in initial spreading and adhesion. This is also in agreement with the results obtained from the focal adhesion size analysis presented in the previous chapter, where the number of focal adhesions per adhesion size is higher in GEβ3 cells than GEβ1, not only on homogenous surfaces but also on all the nanofibres.

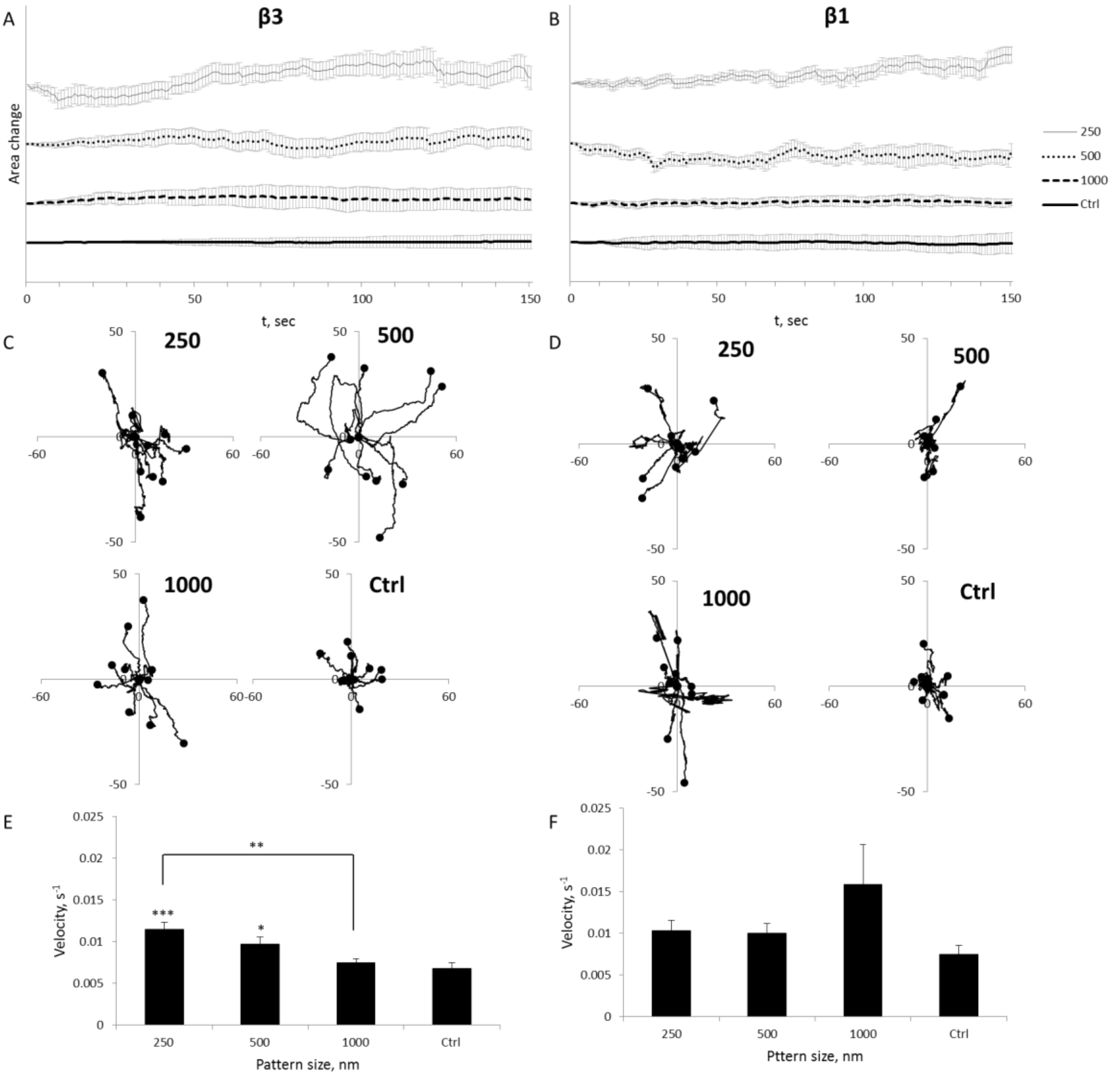

Figure 5.6 Cell cytoskeleton analysis from confocal images acquired over a period of 150 min (every 1 min). Cell area change (A and B), cell trajectories (C and D) and velocity (E and F) of GEβ3 (left) and GEβ1 (right) cells spreading on 250, 500 and 1000 nm nanofibres and homogenous substrates (Ctrl). Area change graph (arbitrary units), the error bar are SD. Velocity error bars are SE.

Activity at the protrusions is faster on the patterned surfaces (Fig. 5.7). The cell edge moves slower for cells seeded on control for both GEβ1 and GEβ3 (average velocities measured are 0.009 and 0.012 µm/sec for GEβ3 and GEβ1 respectively and is lower than on nanofibres). The highest velocities are observed for cells spreading on the 500 nm nanofibres for both the GEβ3 and GEβ1 cells and GEβ1 cell edges move generally faster than GEβ3 ones. Such membrane activity is often observed on materials with nanotopography or on softer materials (Cavalcanti-Adam et al., 2007). When cells are sensing the matrix in order to “decide” whether to adhere or not, there is a great amount of activity at cell protrusions (Giannone et al., 2004), in the lamellipodium area, consisting of actin polymerization and retrograde flow. The resulting actin network hooks up to nascent adhesions and stabilises them whilst maturing (through the exertion of contractile forces). Owing to the geometry of ECM molecules presented to cells on our nanofibres, integrins are not allowed to anchor to the substrate homogenously, but are restricted to specific locations. Hence, the actin network is only able to hook up to adhesions at the locations defined by the ECM pattern. As a result, increased membrane activity would be expected at the surface of our materials, a phenomenon that was also reported for other nanomaterials (Cavalcanti-Adam et al., 2007).

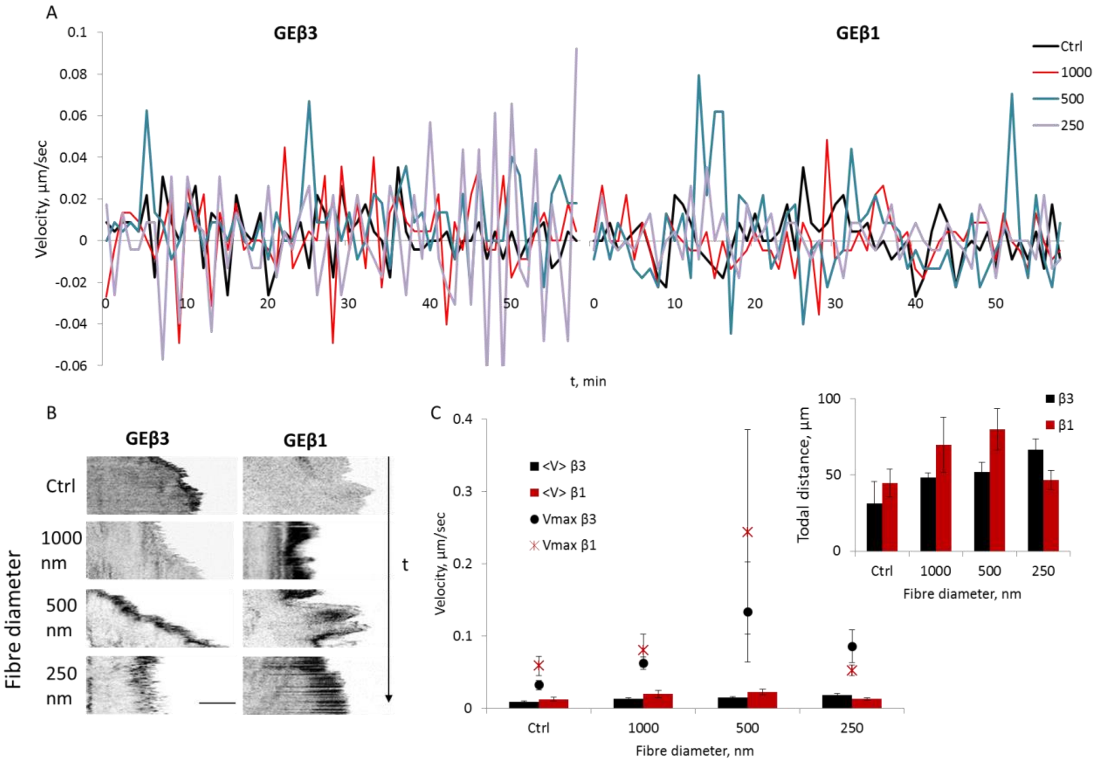

Figure 5.7 Cell protrusion dynamics. A. Example of protrusion dynamics for GEβ1 (right) and GEβ3 (left) cells seeded on homogenous and nanofibres (1000, 500 and 250 nm fibre diameter). Velocity is measured by following the movement over time of the cell edge at a certain angle respect to the cell centre of mass. B. Kymographs from confocal images showing the evolution over time(y axis) of cell edge at a certain angle with respect of the cell centre. Scale bar is 10 µm. C. Data for cell edge velocity. Average velocity (<v>), max velocity (Vmax) of the cell edge and total distance travelled by the cell edge (average of 5 cells) are represented in graph C. Total distance is measured summing all the distances travelled for each time point.

The dynamic of the actin network during cell spreading and motility on homogenous and patterned surfaces was then assessed (Fig. 5.8). What seems to emerge from the videos is that actin fibres remodel faster when cells are spreading on the nanofibres. Showing some fibres as example, for GEβ3 cells spreading on homogenous surfaces (control) the life time of a stress fibre appears to be longer (around 43 minutes in Fig. 5.8 following the fibre highlighted from the red arrow) than in cells spreading on the nanofibres (it decreases to around 23 minutes for the 1000 and 500 nm nanofibres and less than 20 min for the 250 nm ones). These are qualitative results, but considering the change in area over time and the distances and velocity measured, it seems plausible that cells on the nanofibres rearrange their cytoskeleton in a more dynamic way than on the homogenous surfaces. Another feature noticeable on the nanofibres is the appearance of “dots” in the actin cytoskeleton (Fig. 5.8, blue arrows). These resemble foci of F-actin and appear in area of higher actin rearrangement. They only appear very rarely on homogenous substrates and mainly in the lamellipodium. On patterned substrates, they normally appear in the cell centre (where they are easier to identify) or in areas of intense actin assembly, within or at the boundary of the lamellipodium, and travel along the cell body before disassembling. These actin foci are forming less frequently in the GEβ1 cells (Fig. 5.9) and they appear to have much shorter life times.

In the GEβ1 cells, stress fibres have a different shape to GEβ3 cells and for cells spreading on homogenous surfaces they appear mainly at the periphery (Fig. 5.9). Fibre dynamics appear to be qualitatively similar to GEβ3 cells, although from Fig. 5.9 cells spreading on the 1000 nm fibres seem to have longer life time. An optimized way of analysing actin dynamic is still under examination.

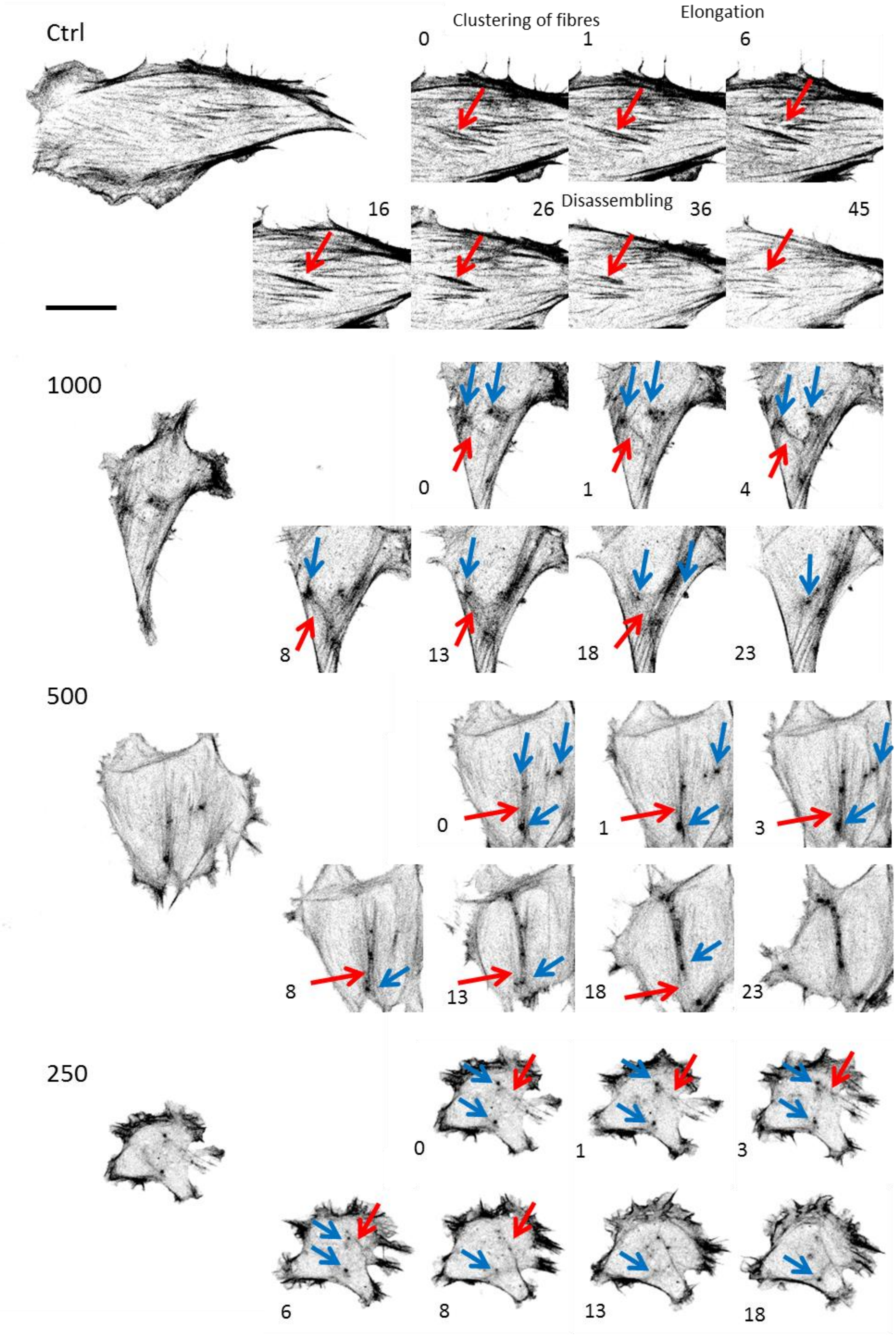

Figure 5.8 GEβ3 cells. Confocal images of actin cytoskeleton dynamics (at different time points) for cells spreading on homogenous (Ctrl) and nanofibres (1000, 500 and 250 nm fibre diameter). Red arrows show fibre assembly and disassembly and blue arrows point at actin foci noticeable on patterned surfaces. Numbers in the images represent time in minutes. Scale bar is 20 µm.

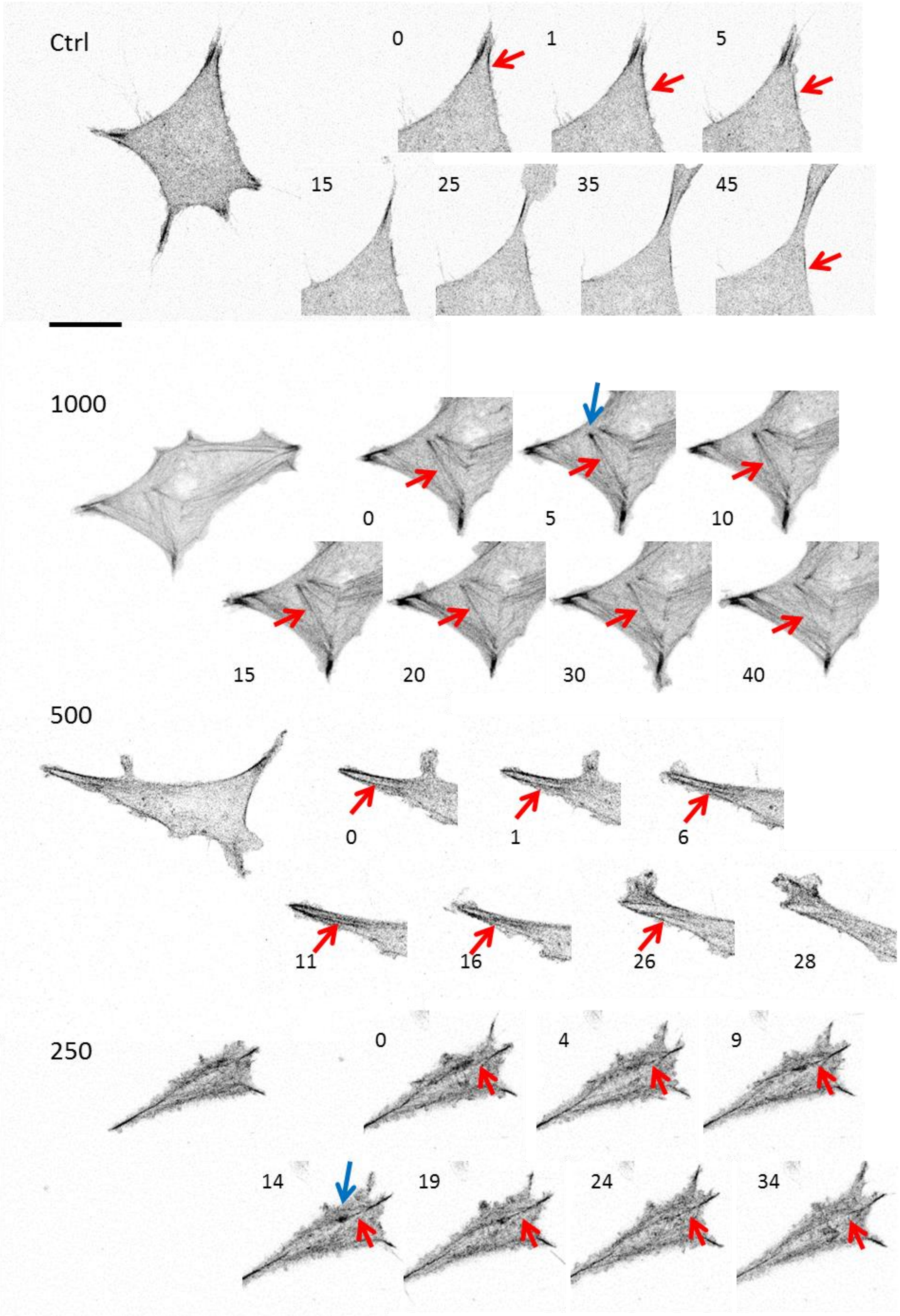

Figure 5.9 GEβ1 cells. Confocal images of actin cytoskeleton dynamics (at different time points) for cells spreading on homogenous (Ctrl) and nanofibres (1000, 500 and 250 nm fibre diameter). Red arrows show fibre assembly and disassembly and blue arrows point at actin foci noticeable on patterned surfaces. Numbers in the images represent time in minutes. Scale bar is 20 µm.

Another common behaviour observed on patterned substrates is an abrupt change of the cell edge, with a sudden retraction of the rear edge of the cell (Fig. 5.10): the retraction generally happens within one or two minutes. This is possibly due to the topography of the pattern beneath and a forced polarization/ way of migration of the cells. The discreet nature of the pattern (fibres separated by non-adhesive areas) could result in rapid re-balancing of forces upon disassembly of an adhesion site. This could result in fast reorganisation of the cell body.

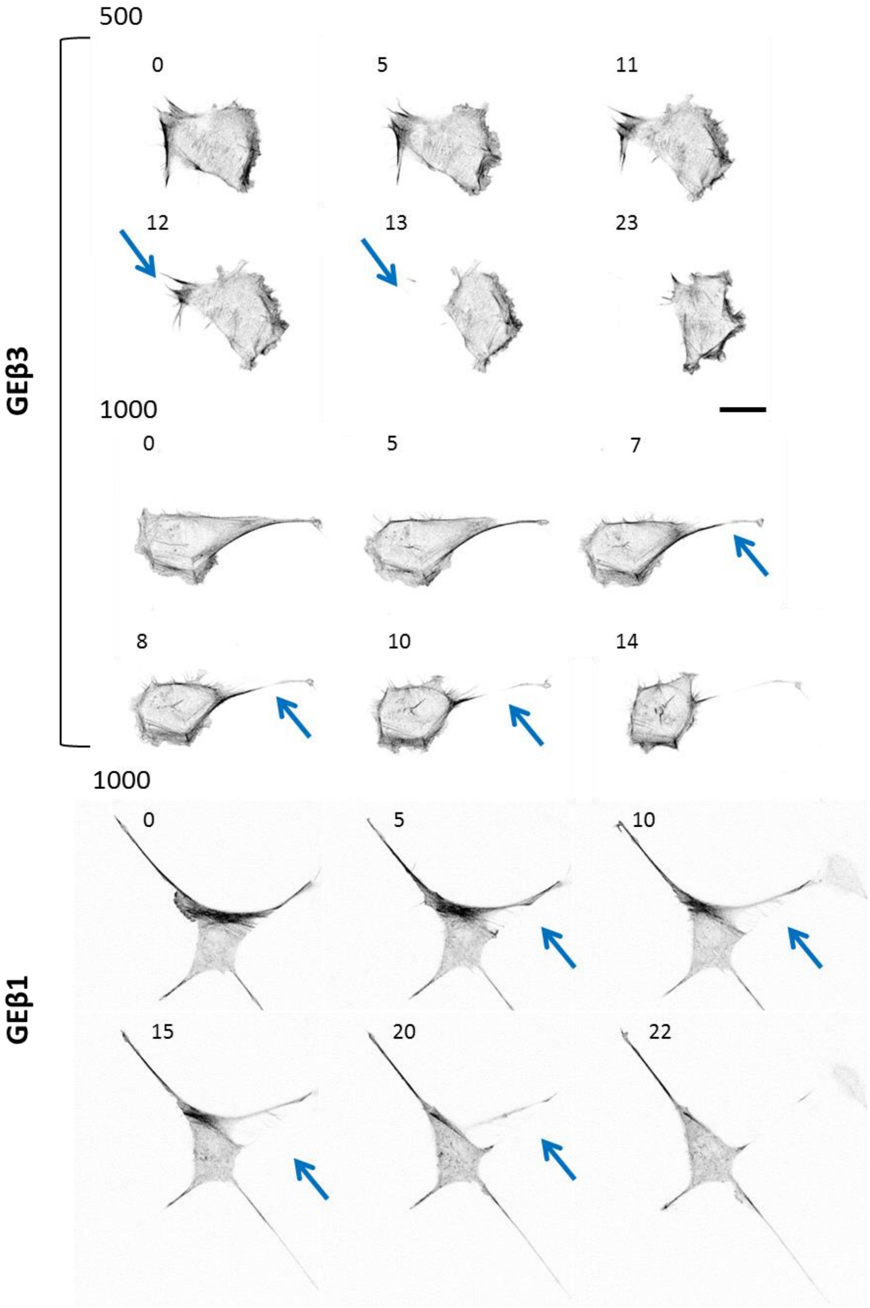

Figure 5.10 Confocal images of actin cytoskeleton dynamics. Sudden edge retraction of GEβ1 and GEβ3 cells spreading on 500 and 1000 nm nanofibres. Number is each tiles represent time in minutes. Scale bar is 20 µm.

We then followed actin fibre evolution over 120 min for the GEβ1 and GEβ3 cells using the MatLab code (kindly provided by Dr. Nuria Gavara) used for the cytoskeleton analysis of immunostained samples. The code works separately on each image and cannot cross- correlate fibre changes over time, thus it is not possible to follow the evolution of one single fibre. These results give a broad sense of how the cytoskeleton evolves over time, showing some of the above described parameter changes in time. Fig. 5.11 shows the change over time of fibre length, thickness, chirality and convexity for one cell for each condition. The parameter that shows the highest changes over time is chirality, while for the others there does not seem to be significant differences between cells spreading on the control and on the patterned surfaces. These results are qualitative, and a method for analysing fibre by fibre change over time is still to be optimized.

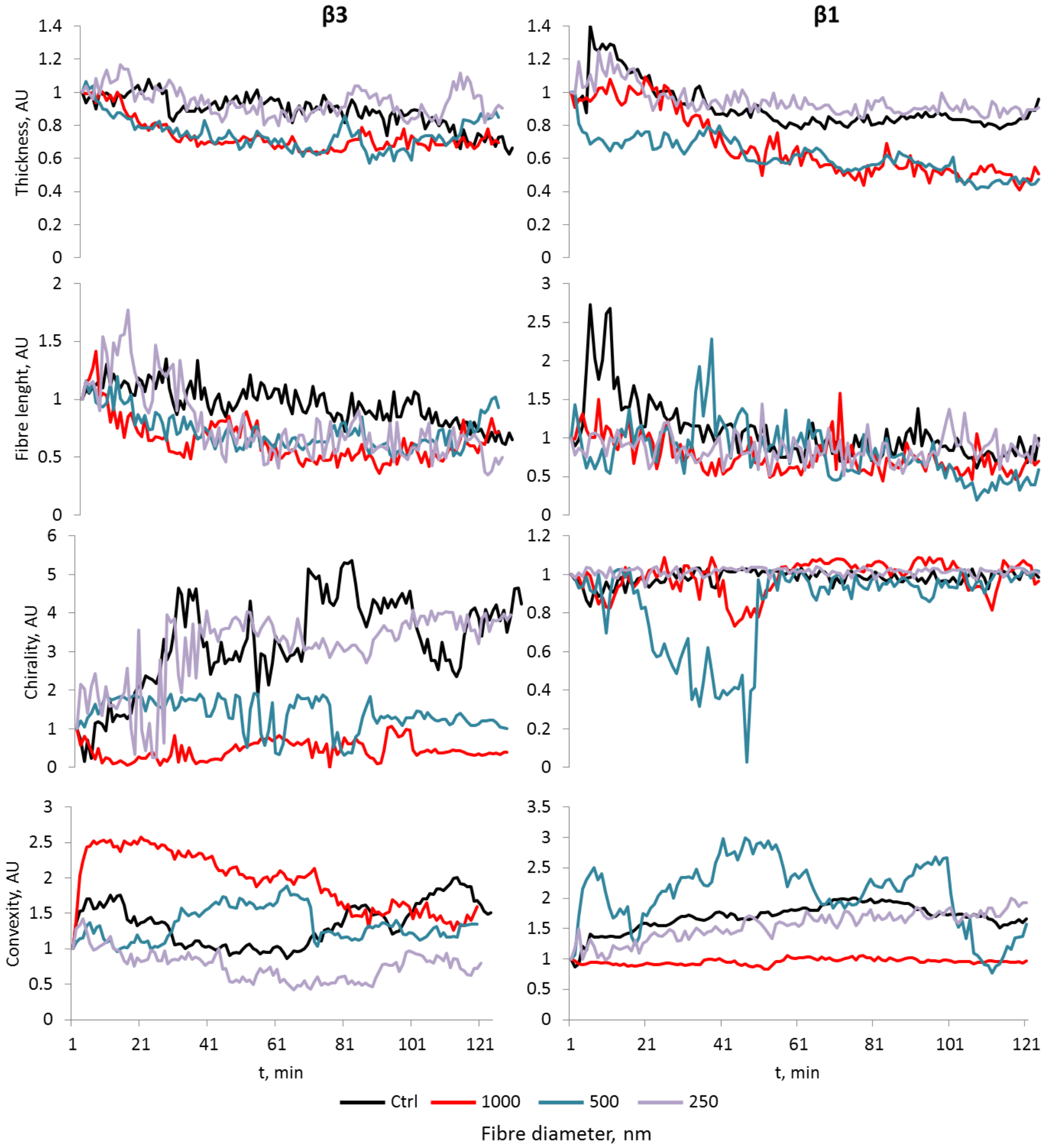

Figure 5.11 Example of actin fibres evolution over time of GEβ1 and GEβ3 cells (for one cell) spreading on homogenous and nanofibres (1000, 500 and 250 nm fibre diameter). Actin fibres were analysed via a MatLab from confocal images taking during 2 hr period time. Parameters analysed were apparent fibre thickness and length, chirality and convexity.

From the results and observations presented above, it seems clear that the cytoskeleton has a prominent role in cell sensing of the extracellular environment and this is combined with a differential integrin expression.

5.3.2 GEβ3 cells sensing of the topography is associated with an impaired cytoskeleton organization

α-Actinin and myosin II are proteins that associate with actin and stress fibres (Shroff et al., 2007, Hotulainen and Lappalainen, 2006). Myosin II is generally associated with fibre contractility and α-actinin plays a role in the crosslinking of actin fibres into thicker bundles. Here we analysed the distribution of these two proteins in GEβ1 and GEβ3 cells seeded on the different nanofibres and their association with the actin cytoskeleton.

It can be noticed in the images (Fig. 5.12) that α-actinin appears to be localized at the end of thick stress fibres or at the cell periphery: this in agreement with studies that found that this protein also partially overlaps with vinculin in focal adhesions (Shroff et al., 2007) and it elongates together with actin at the cell periphery (Choi et al., 2008). It is also found in a punctate, periodic pattern along stress fibres in agreement with other studies (Edlund et al., 2001). This behaviour is clearly seen for GEβ1 cells seeded on the 1000 nm nanofibres, while it is disrupted when decreasing the nanofibres size (550 and 300 nm). Interestingly, on the homogenous control substrates this is also less evident and similar patterns are seen only along the cell edge. Similar behaviour can be noticed for GEβ3 cells: on control surfaces the alternate pattern is observed mainly on the stress fibres at the cell periphery while it is clearly visible along stress fibres presented in the cell body on the 1000 and 550 nm nanofibres. Myosin II seems more distributed in the cell body (Fig. 5.12) and it is associated along the stress fibres too in an alternate punctuate fashion on both homogenous surfaces and the nanofibres: the two proteins normally associate in this alternate fashion along ventral stress fibres and transverse arc (Tojkander et al., 2011, Tojkander et al., 2012). Myosin II seems to be more expressed in the GEβ3 cells than in the GEβ1 and it appears to present a fibre-like shape maybe masking the pattern below.

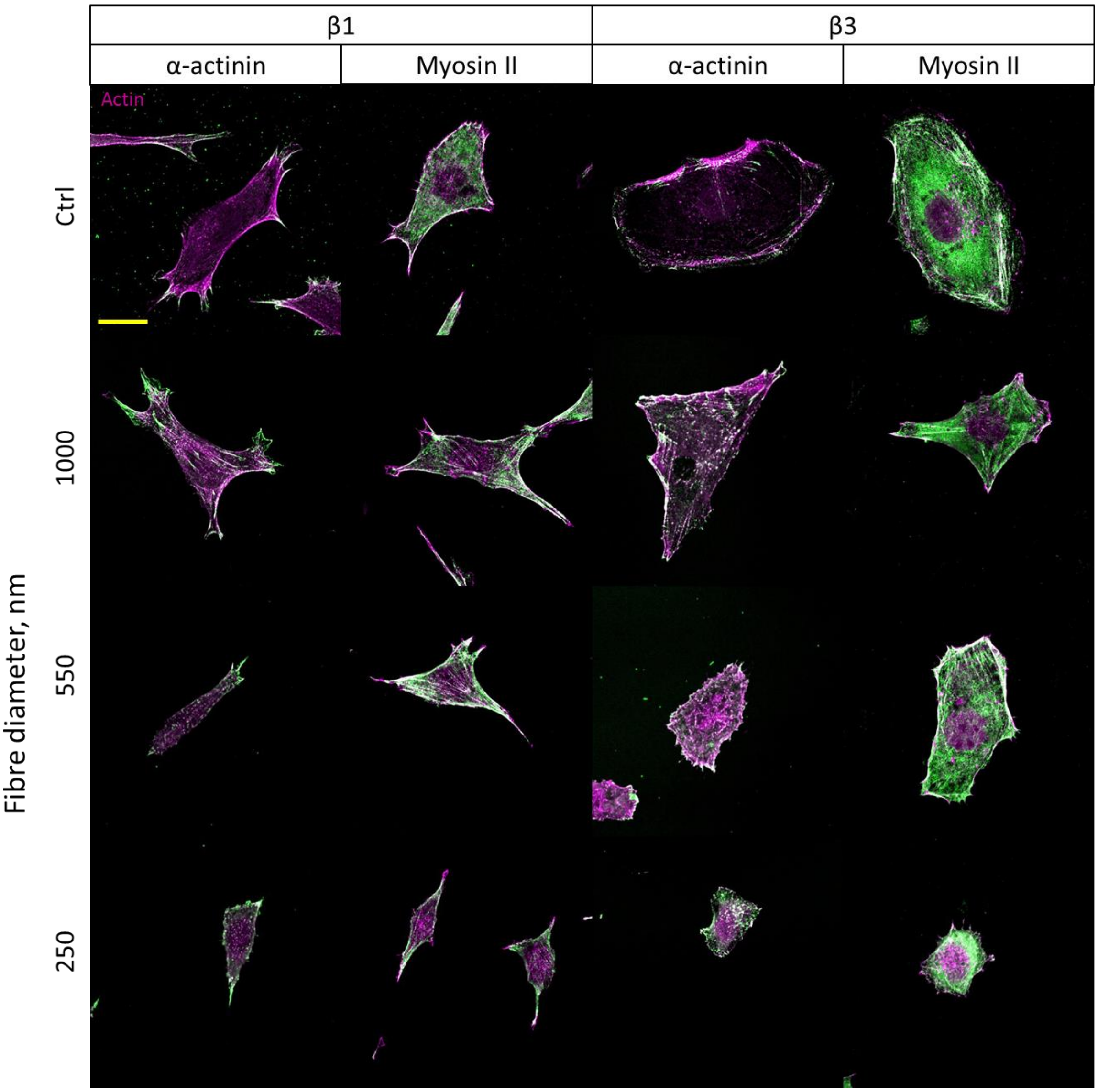

Figure 5.12 Colocaliation experiments myosin II/ actin and α-actinin/actin. Representative confocal images for GEβ1 and GEβ3 cells seeded on 250, 550 and 1000 nm nanofibres and homogenous control surfaces for 24 hr and stained for actin (magenta) and either myosin II or α-actinin (green). Scale bar is 20 µm.

We next analysed the colocalisation of α-actinin and myosin II with actin fibres. The Pearson's coefficient of α-actinin/actin and myosin II/ actin association was measured for GEβ1 and GEβ3 cells seeded on 250, 550 and 1000 nm nanofibres and homogenous control surfaces. This coefficient ranges from 0 to 1 and quantify the correlation of two signals, in this case the red channel for actin and the green channel for either myosin II or α-actinin. A Pearson's coefficient of 1 stands for perfect correlation and 0 for no correlation. Our data (Fig. 5.13) indicate that in GEβ3 cells myosin II shows higher correlation than α-actinin for all conditions apart for the 1000 nm nanofibres, where the trend is reverted. Myosin II appears to be more correlated with actin on the 250 and 550 nm nanofibres than 1000 and control surfaces. No significant differences for GEβ1 cells are instead observed between the two proteins apart for the control, where correlation for myosin II is higher than for α-actinin. Furthermore α-actinin shows higher correlation on the nanofibres than on the homogenous substrates for these cells although is not affected from the nanofibres size. Myosin correlation seems unaffected from the nanofibres, differently from GEβ3 cells.

The higher colocalization of α-actinin on the nanofibres (Fig. 5.13) could represent a symptom of rearrangement of the structure of focal adhesion due to the constrained geometry: it is possible that due to the brushes thickness there could be a shift upwards of the force transmitting layer and maybe more of this protein could be recruited at the adhesion site, causing a higher match with actin. Furthermore, GEβ1 and GEβ3 cells present larger focal adhesions on patterned surfaces than on homogenous (excluding the 250 nm nanofibres) and this could be the source again of higher overlap of protein in the adhesion plaque with the actin cytoskeleton.

Any of these conclusions should be repeated for statistical significance.

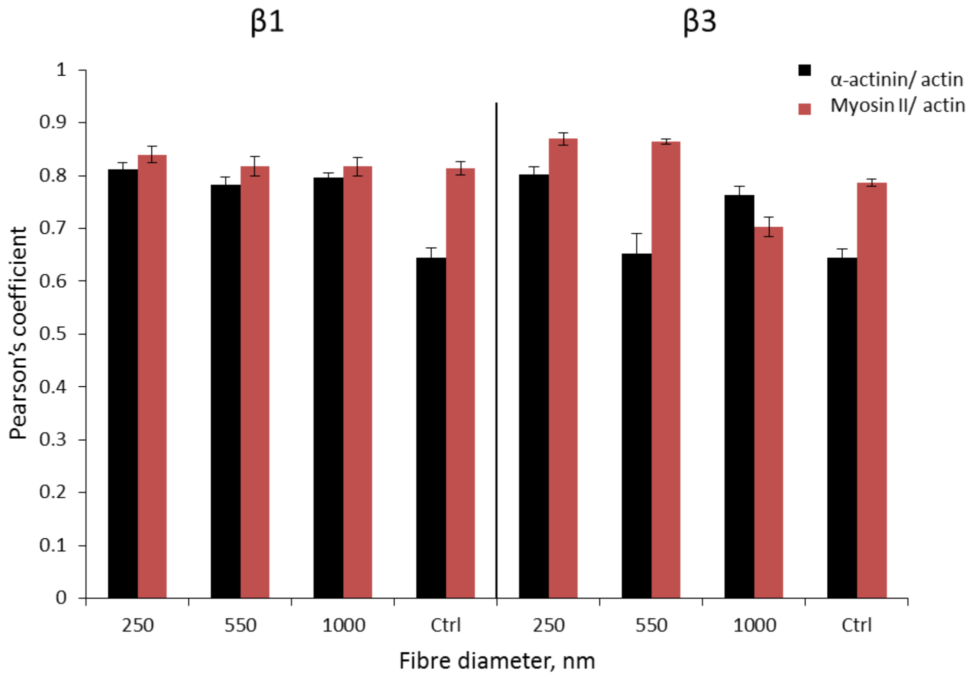

Figure 5.13 Colocalization analysis. Pearson's coefficient of α-actinin/ actin and myosin II/ actin colocalization measured for GEβ1 and GEβ3 cells seeded on 250, 550 and 1000 nm nanofibres and homogenous control surfaces. Error bars are SE (n = 10-15, where n is the number of cells analysed).

Hence our data suggest that myosin assembly is altered by adhesion to nanofibres in the case of β3 expressing cells, but not β1 expressing cells. In this model, the actin cytoskeleton and its dynamics appear to be important elements responsible for sensing nanoscale topography, in an integrin-dependant manner.

To further understand the mechanism via which the actin cytoskeleton is able to sense the ECM nanotopography, it is here proposed that actin fibres can either align along ECM fibres, in which case they can strengthen as is typically observed on homogenous substrates, but may have to deviate from such organisation and branch across 2 or more ECM fibres in order to reinforce with other actin fibres, in which case they become sensitive to the topography of the substrate. Therefore, the topography of the nanofibres, defined by polymer brushes, may be an important parameter resulting in disruption of actin assembly and stability.

In particular, it has previously been shown that cells can feel the curvature of the surface they are adhering to via for example the curvature sensor POR1 (Higgins et al., 2015) or myosin IIa (Ozdemir et al., 2013) activating different signalling pathways in interfaces displaying higher curvature. The passivating polymer brush layer is expected to impose a level of membrane curvature, considering that cells have to adhere within "nanopits". The height of these features is defined by the height of the swollen brushes, 60 nm in the case of the nanofibres tested. This may cause a significant constraint on cytoskeleton assembly, whilst not altering significantly the recruitment of FA-associated proteins. In order to explore the occurrence of such constraint, we exploited the ability of precisely control the height of polymer brushes via changes in polymerisation times (Gautrot et al., 2010). The thickness of brushes was decreased to 10 nm to study whether cell sensing of the nanoscale geometry was affected by the height of the polymer coating. GEβ3 cells were thus seeded on 250, 550 and 1000 nm nanofibres sizes and with a brush height of either 10 or 30 nm. It is worth noting that these heights are dry polymer thicknesses and that these structures are expected to swell by approximately 100 % (Tan et al., 2013), therefore resulting in features with heights of 20 and 60 nm, respectively.

The most striking observation is the lack of cell response in cell spreading to the nanofibres size when the brush height was dropped to 10 nm (Fig. 5.14), although cell spreading was generally still lower than for cells seeded on homogenous surfaces (cell spreading areas on control substrates are near 2000 µm^2, as shown in Fig. 3.9 E). The main difference between the two brush heights is observed when comparing the smallest nanofibres sizes (250 nm). Cell spreading was not significantly impaired on 250 nanofibres with 10 nm brushes, compared to 1000 nm fibres (1291 ± 136 and 1380 ± 68 µm^2), whereas cell spreading was only 517 ± 65 µm^2 on 250 nm fibres with 30 nm brushes). Focal adhesions are more developed on 250 nm fibres with 10 nm brushes too (greater numbers and larger areas, see Fig. 5.14 and 5.17). The cytoskeleton of cells spreading on fibres generated from 10 nm brushes appears to present better structured stress fibres too (see Fig. 5.14 and 5.22). The aspect ratio of these cells is also lower than cells seeded on the smallest fibres with 30 nm brushes. Cell densities and circularities were not affected by the nanofibres size with such thin brushes. Finally, as will be highlighted in the next paragraphs, although cell spreading is not significantly affected by the fibre diameter with 10 nm brushes, focal adhesions formed on these nanofibres were generally larger for all nanofibres sizes than the focal adhesions formed on nanofibres with 30 nm brushes. Hence these results clearly indicate that the cell response to nanofibres is conditional of a pitted geometry and that the step imposed by 30 nm brushes is affecting the cell ability to form stable adhesions in addition to its impact on the assembly of stress fibres. This is suggesting that such a step is destabilising the focal adhesion structure, where talin typically assembles at a 15^o angle with respect to the focal adhesion plane followed by stress fibres assembled at an angle of 2 to 6^o (Liu et al., 2015). Focal adhesions composition was also found to be strongly affected when cells were growing on pitted or grooved surfaces rather than flat surfaces and this behaviour was enhanced with decreasing the spacing between the nanofeatures (Yang et al., 2013).

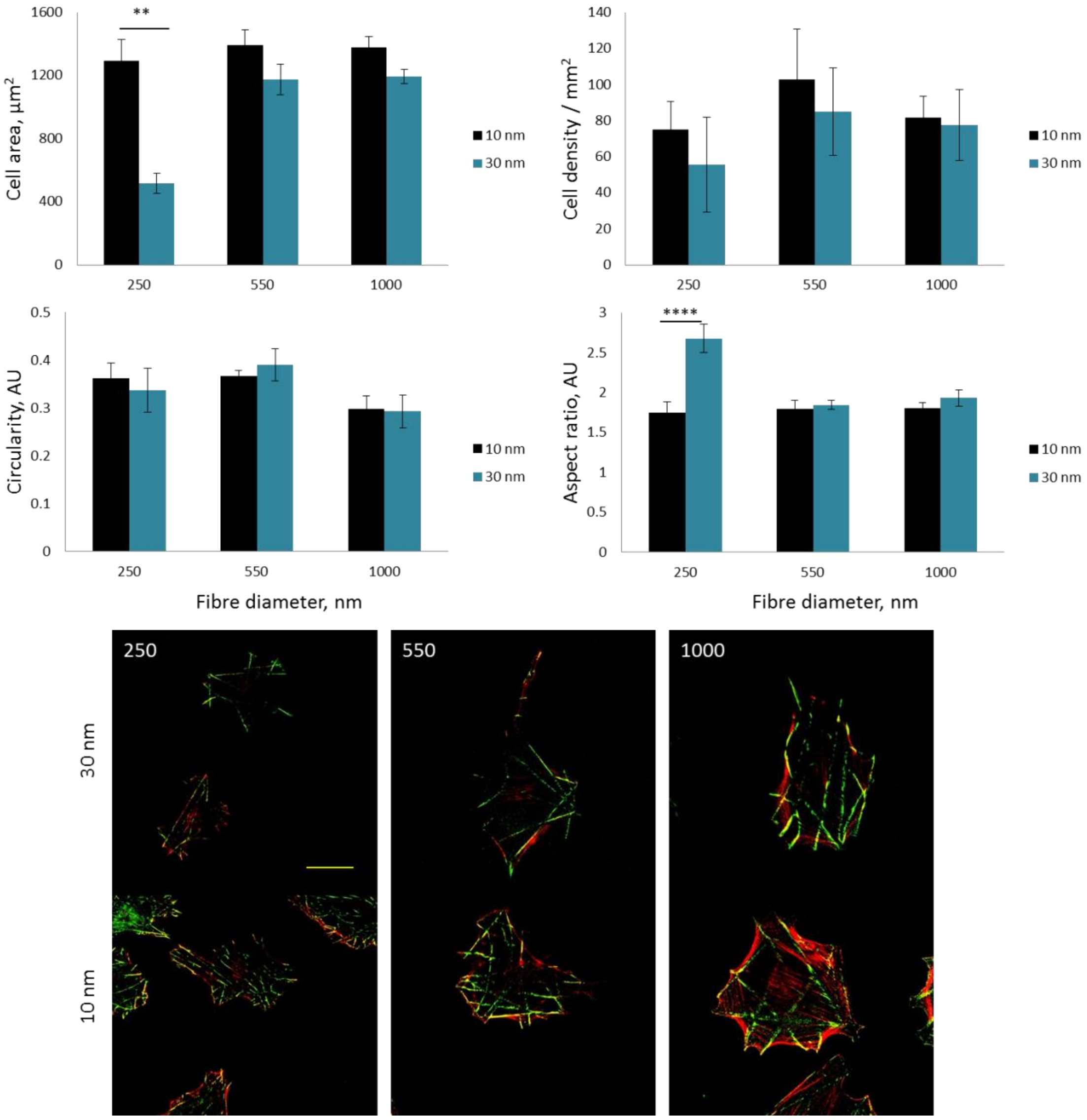

Figure 5.14 Cell area, density and shape (circularity and aspect ratio) of GEβ3 cells seeded on different nanofibres sizes (250, 550 and 1000 nm diameter) presenting two polymer brushes heights (10 and 30 nm). Error bars are SE, n = 3, with n representing the number of experiments. For statistical test: *, P < 0.05; **, P < 0.01; ***, P < 0.001; ****, P < 0.0001. Confocal representative images of GEβ3 cells spreading on the different nanofibres types (250, 550 and 1000 nm fibre diameter and 10 and 30 nm brush layer). Scale bar is 20 μm.

The role of cytoskeleton tension on cell spreading on nanofibres was therefore next investigated. In order to do so, cells were treated with inhibitors of cytoskeleton dynamics: the ROCK inhibitor Y-27632 (Ishizaki et al., 2000) and the myosin II inhibitor blebbistatin. The use of these molecules was proven to perturb the organization of the cytoskeleton (Xu et al., 2012) and resulted in the impairment of actin stress fibres and the release of proteins from FAs and associated rapid disassembly of these structures

(Lavelin et al., 2013). GEβ3 cells were seeded on nanofibres with different sizes (250, 550 and 1000 nm) and brush height (10 and 30 nm) and treated after 24 hours spreading with these two inhibitors (separately) or with DMSO (as a control, 10 µM) for 4 hrs. Cell shape (Fig. 5.16) was significantly altered by inhibitor treatment on all nanofibres. Cell edges were not delimited anymore by the formation of thick stress fibres but instead appeared swollen and branched. No significant differences (Fig. 5.15) could be observed in cell spreading for the different conditions (fibre diameter and brush height) between treated and untreated cells, apart for cells seeded on the smallest substrates (250 nm) with 30 nm brushes, where cells were much more spread after inhibitor treatment. A decrease in cell area compared to homogenous surfaces can still be observed for the cells seeded on the different nanofibres sizes even after inhibitor treatment. Generally, cell circularities were lower for cells treated with inhibitors, compared to cells treated with carrier reflecting the higher level of branching observed after inhibitor treatments. Cell density remained unaffected, confirming that cells remained adhered to the substrates after treatment with inhibitors (Fig. 5.15).

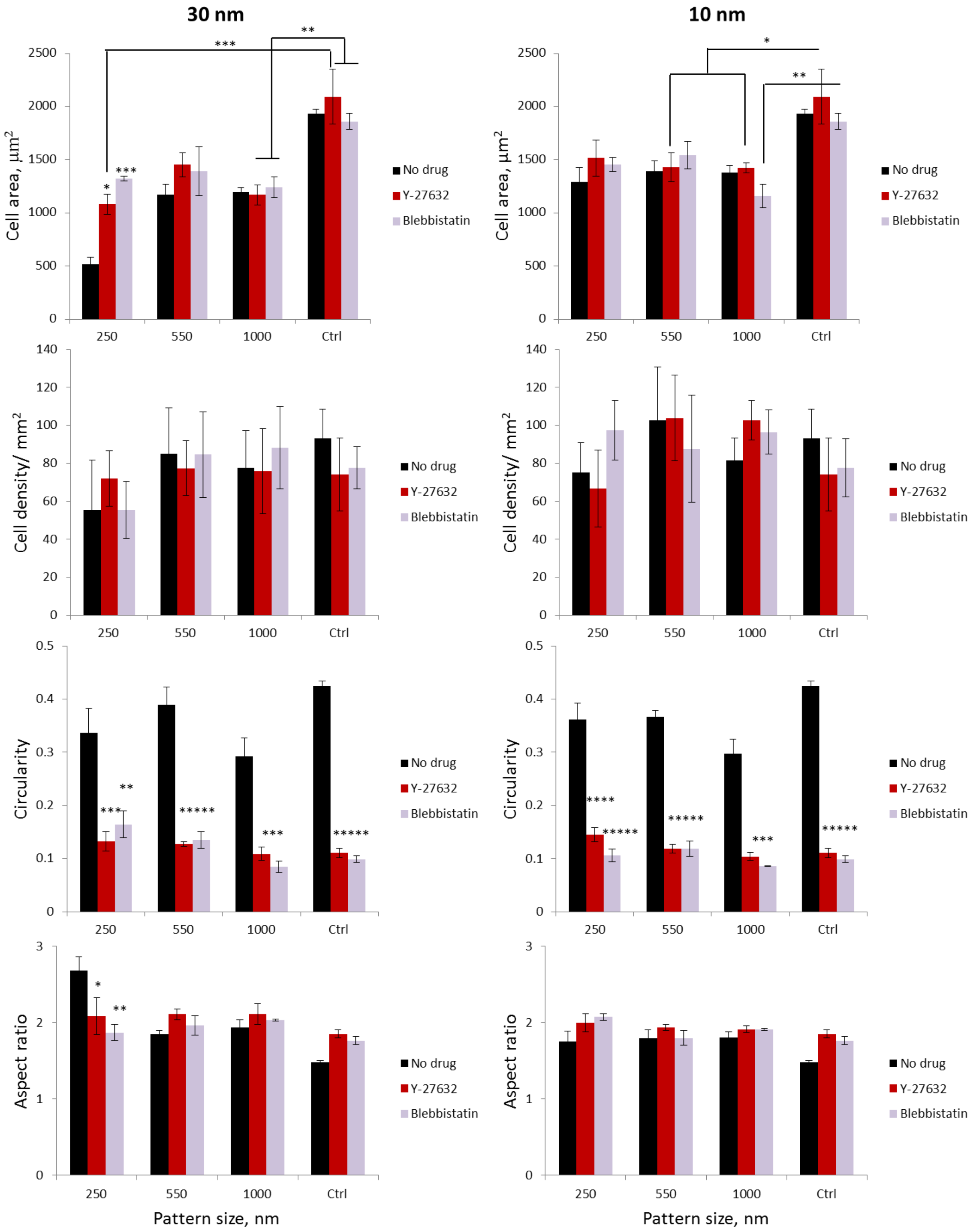

Figure 5.15 Geβ3 cells seeded on different nanofibres sizes (250, 550 and 1000 nm) and two brushes heights (10 and 30 nm) and treated or not with cytoskeleton inhibitors: Y-27632 (red) or Blebbistatin (light purple). Cells were allowed to spread for 24 hr and then treated with the proper inhibitor for 4 hr. Control samples were treated with DMSO (10 µM). Cell area, density and shape descriptors (circularity and aspect ratio) are shown in the graphs for the two inhibitors. Error bars are SE, n = 3, with n representing the number of experiments. For statistical test: *, $P < 0.05$; **, $P < 0.01$; ***, $P < 0.001$; ****, $P < 0.0001$.

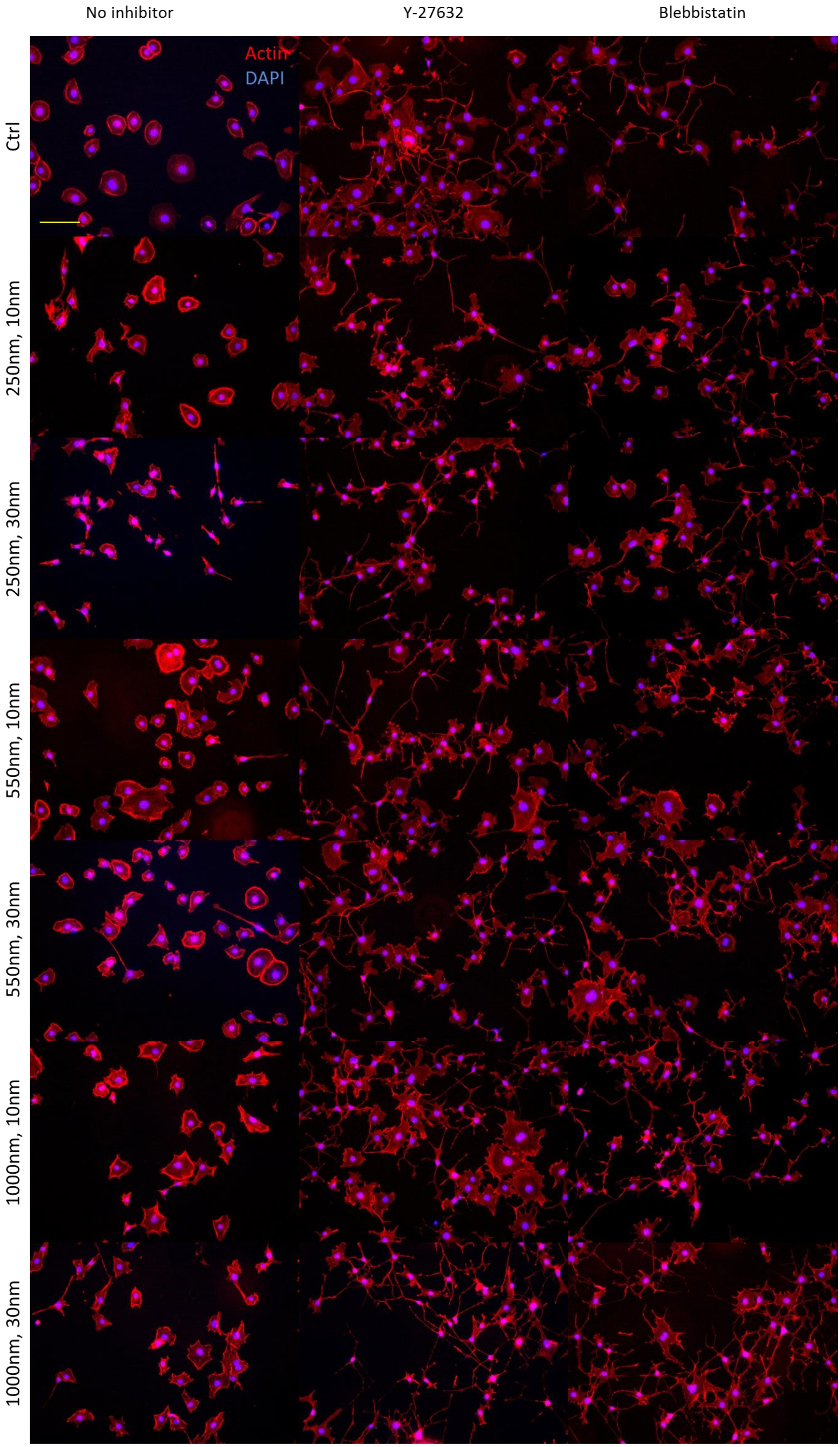
No inhibitor
Y-27632
Blebbistatin
Actin
DAPI
Ctrl
250nm, 10nm
250nm, 30nm
550nm, 10nm
550nm, 30nm
1000nm, 10nm
1000nm, 30nm

Figure 5.16 Representative epifluorescent images for GEβ3 cells seeded on different nanofibres diameters (250, 550 and 1000 nm) and two brushes height (10 and 30 nm) and treated or not with cytoskeleton inhibitors: Y-27632 (second column) or Blebbistatin (third column). Scale bar is 100 µm.

Focal adhesion analysis showed that the number of focal adhesions with sizes below 1 µm^2 is generally higher for cells treated with inhibitors on all substrate types (Fig. 5.17 and 5.18). The fact that cells treated with the inhibitors present greater numbers of smaller adhesion is expected, due to the disruptive impact of the inhibitors on these structures (Lavelin et al., 2013, Wolfenson et al., 2011, Zaidel-Bar et al., 2007b). Larger focal adhesions disassemble and are thought to persist as large numbers of small persistent adhesive complexes. As expected, the total number of focal adhesions per cell is higher for cells treated with the two inhibitors for all patterns, but not for the homogenous substrates and the 1000 nm nanofibres with 10 nm brush height (Fig. 5.19). This may indicate that the patterns still restrict the formation of diffuse, short lived adhesion complexes resulting from binding kinetics of integrins with the underlying matrix and associated complexation of adapter proteins such as vinculin. In addition, staining intensities at focal adhesions decreased after inhibitor treatment (Fig. 5.21 and 5.22), reflecting the lower level of recruitment of focal adhesion proteins after actin cytoskeleton disassembly.

Above 1 µm^2 adhesion sizes (Fig. 5.17 and 5.18), the number of focal adhesion between treated and untreated cells even up and it became higher for untreated cells as adhesion size increases. Similar observations were made on homogenous surfaces (Ctrl). Interestingly, after treatment with inhibitors, no differences were observed between focal adhesion distributions of cells spreading on fibres defined by 30 and 10 nm brushes. In fact, longer adhesions were observed for cells spreading on nanofibres defined by 30 nm brushes after treatment with inhibitors. This further suggests the strong impact of actin contractility and stress fibre organization and orientation with respect to the basal plane on nanoscale sensing.

It is worth noting that here vinculin was used as a marker for focal adhesion and using only one focal adhesion marker may not be sufficient to identify a focal adhesion. The co-localisation with a second protein may have served the purpose better.

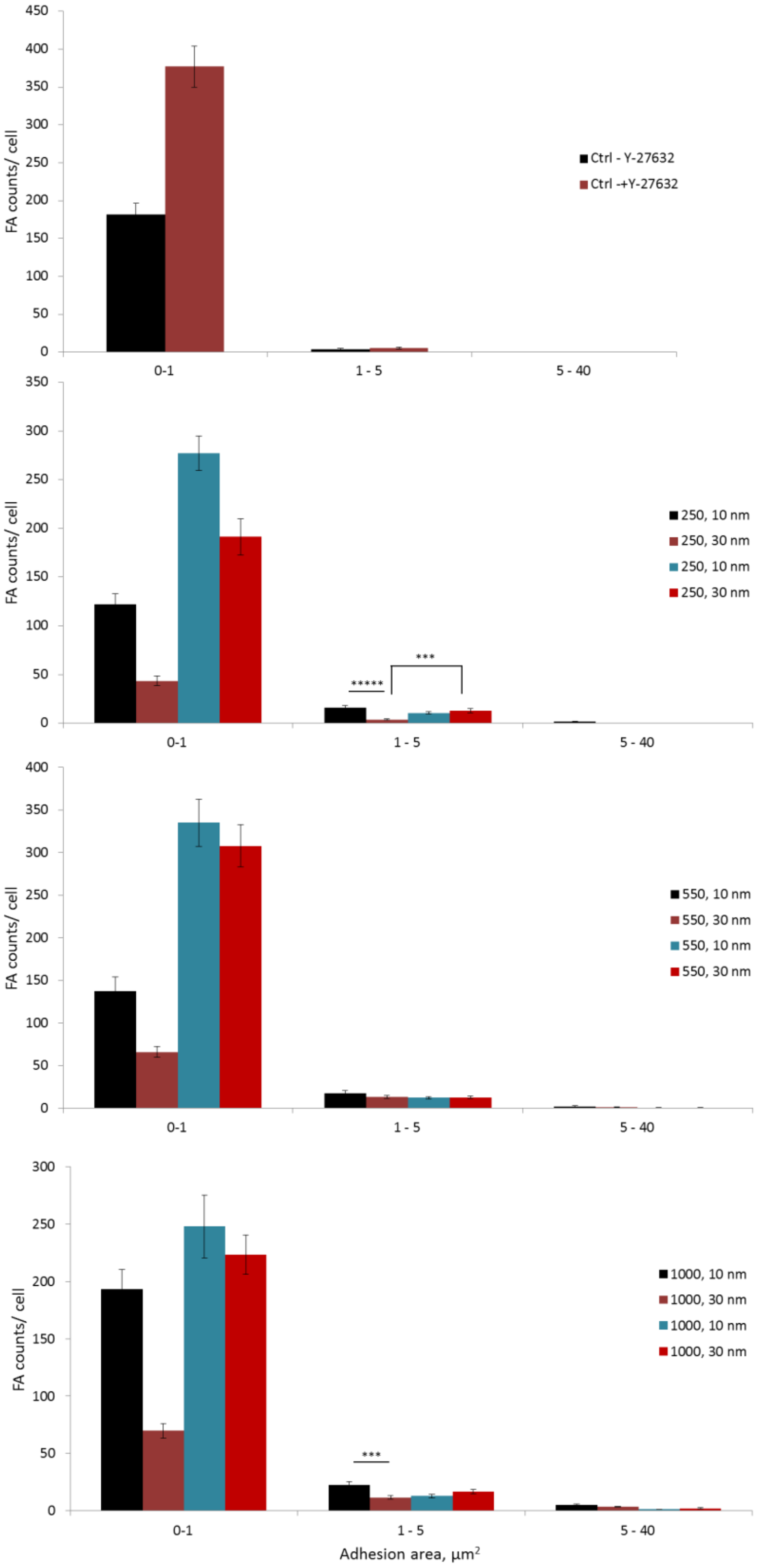

Figure 5.17 Focal adhesion (vinculin staining)size distributions for the GEβ3 cells treated or not with the Y-27632 inhibitor and spreading on the different nanofibres diameters (250, 550 and 1000 nm) and brush height (10 or 30 nm). Ctrl is the homogenous control surface. Adhesion sizes were divided in three ranges: 0 to 1 μm^2, 1 to 5 and 5 to 40 μm^2. Error bars are SE, n = 3, with n representing the number of experiments. For statistical test: *, $P < 0.05$; **, $P < 0.01$; ***, $P < 0.001$; ****, $P < 0.0001$.

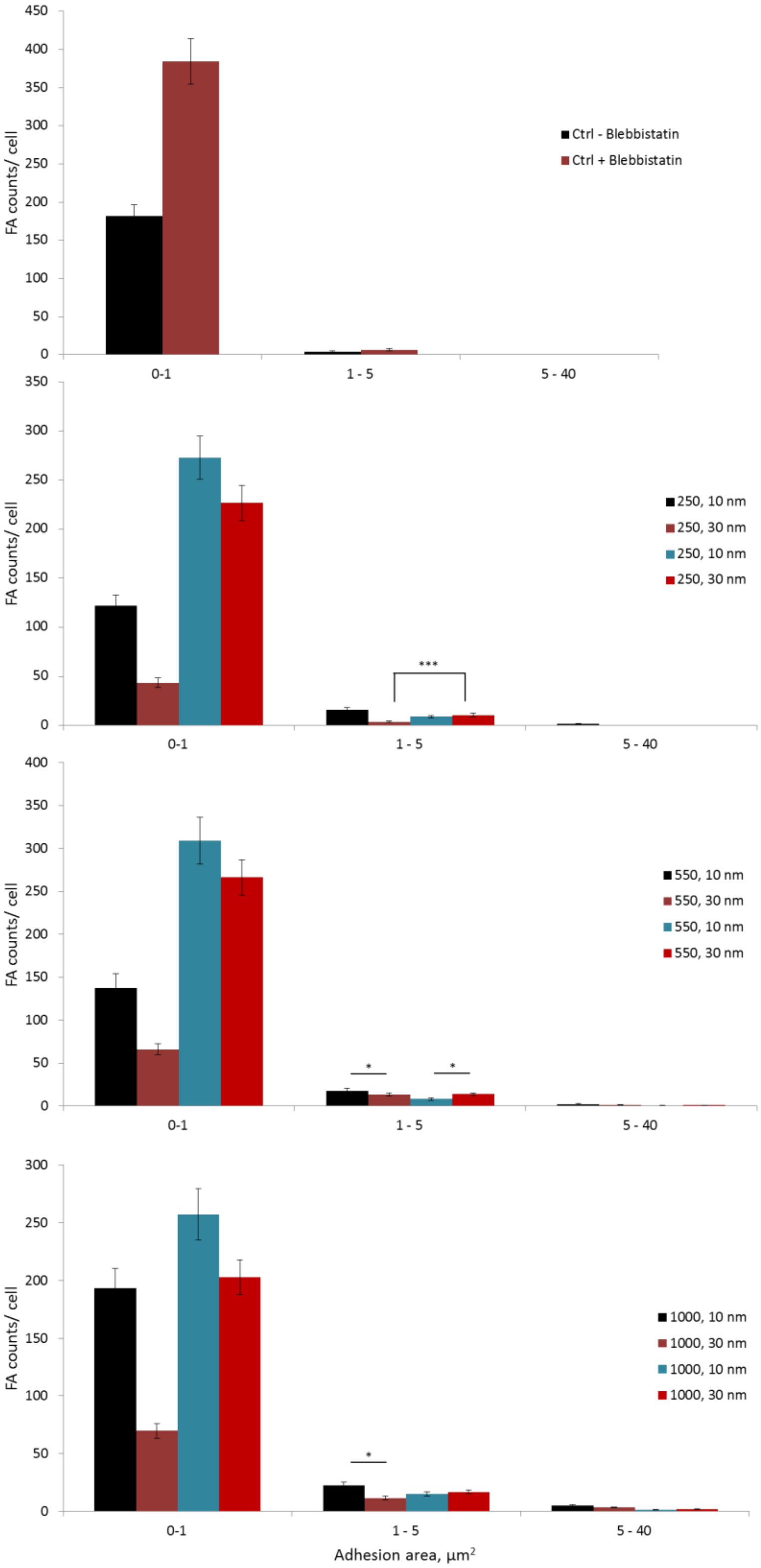

Figure 5.18 Focal adhesion size distributions for the GEβ3 cells treated or not with the Y-27632 inhibitor and spreading on the different nanofibres diameters (250, 550 and 1000 nm) and brush height (10 or 30 nm). Ctrl is the homogenous control surface. Adhesion sizes were divided in three ranges: 0 to 1 µm^2, 1 to 5 and 5 to 40 µm^2. Error bars are SE, n = 3, with n representing the number of experiments. For statistical test: *, P < 0.05; **, P < 0.01; ***, P < 0.001; ****, P < 0.0001.

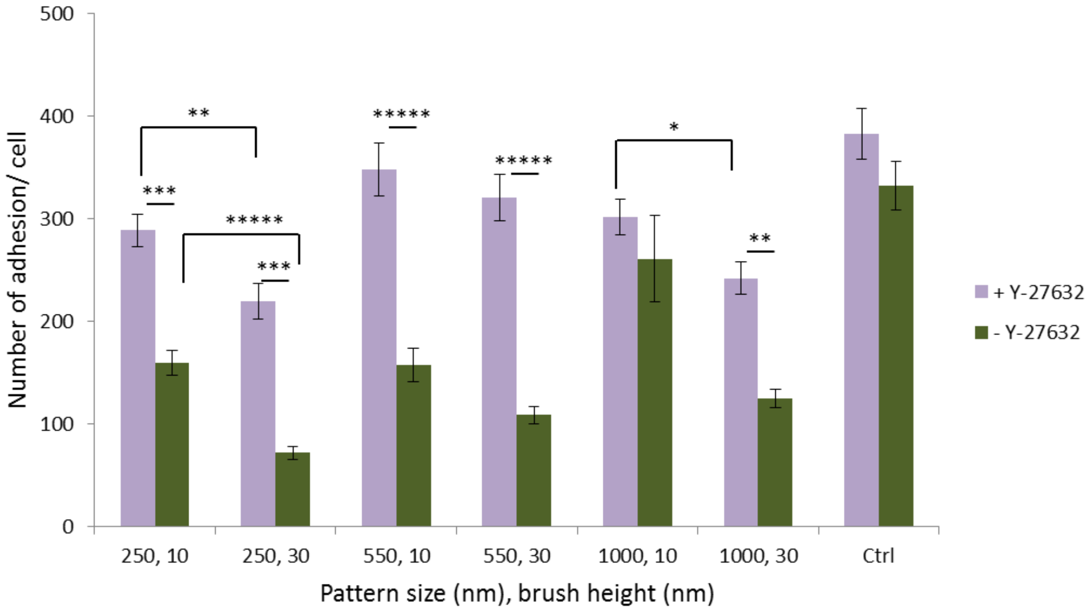

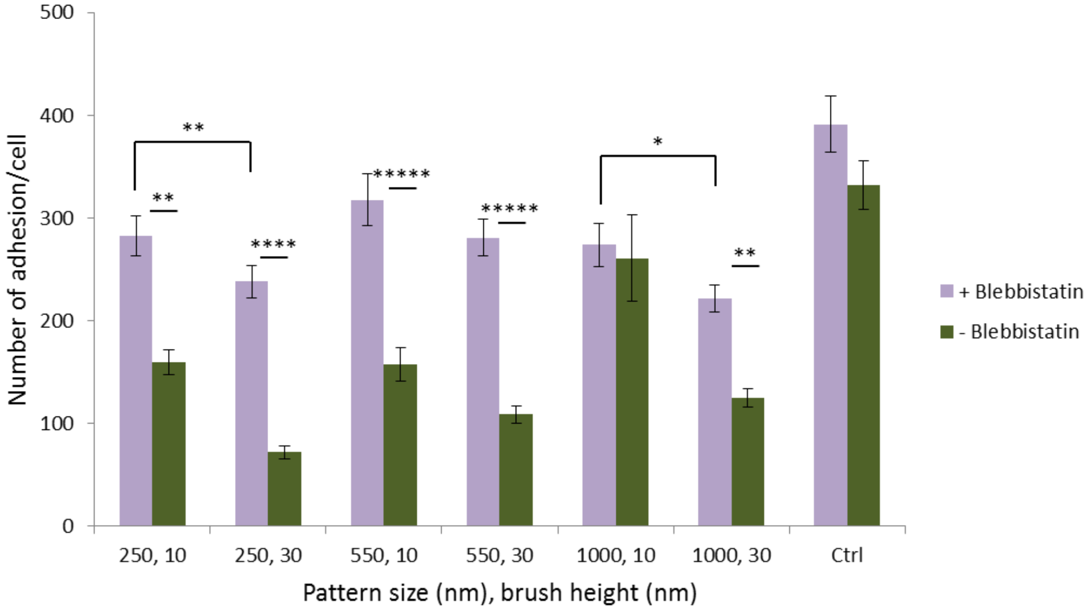

Figure 5.19 Total number of FAs per cell for GEβ3 cells seeded on different nanofibres diameters (250, 550 and 1000 nm) and brush height (10 and 30 nm) and treated or not with the either Y-27632 or Blebbistatin. Ctrl is the homogenous control surface. Error bars are SE, n = 3, with n representing the number of experiments. For statistical test: *, P < 0.05; **, P < 0.01; ***, P < 0.001; ****, P < 0.0001.

Interestingly, focal adhesion circularities are higher for cells seeded on 10 nm brush patterns. After inhibitor treatment FA circularities are comparable for nanofibres generated with both brush sizes (Figure 5.20 and Appendix A1.1). This effect is particularly pronounced at small adhesion sizes (up to about 1 μm^2). Aspect ratio was accordingly found to be generally higher for non-treated cells (Fig. 5.20 and Appendix A1.1). This observation further points towards the combined impact of nanoscale geometry and brush height on the directed assembly of focal adhesion and actin stress fibres: when the cell membrane has to curve into deeper features in order to make contact with the substrate, the actin cytoskeleton will preferentially align parallel to the fibres in order to accommodate an optimal 15^{o} angle. Hence such assembly results in more oriented, less circular adhesions.

In agreement with other studies (Wolfenson H. et al., 2010), mean intensities were significantly decreased for focal adhesions after inhibitor treatment (Fig. 5.21)

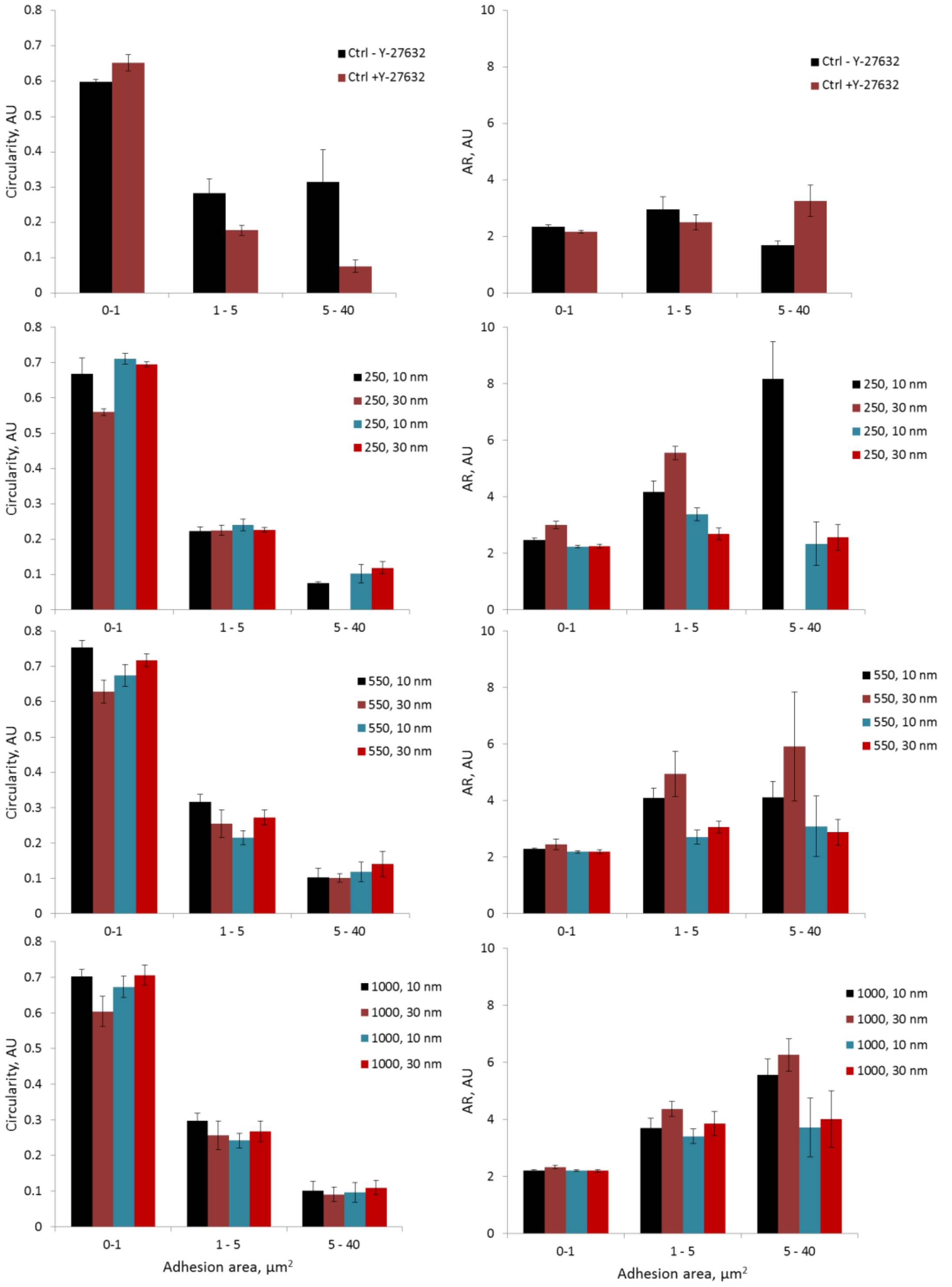

Figure 5.20 Focal adhesion shape descriptor distributions of the GEβ3 cells on the different nanofibres diameters (250, 550 and 1000 nm) and brushes heights (10 and 30 nm) and treated with Y-27632: circularity (left) and aspect ratio (right). Ctrl is the homogenous control surface. Error bars are SE, n = 3, with n representing the number of experiments. For statistical test: *, P < 0.05; **, P < 0.01; ***, P < 0.001; ****, P < 0.0001.

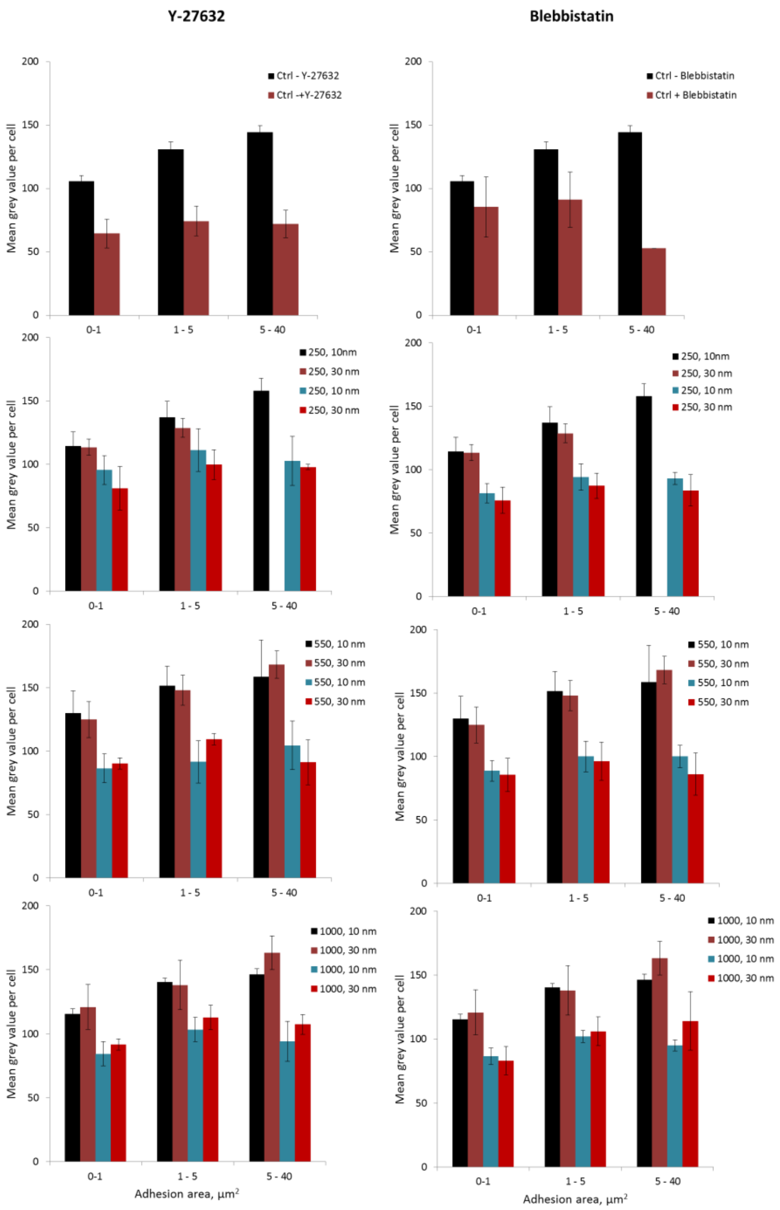

Figure 5.21 Focal adhesion intensity distributions (vinculin marker) of the GEβ3 cells on the different nanofibres diameters (250, 550 and 1000 nm) and brushes height treated with either Y-27632 or Blebbistatin. Ctrl is the homogenous control surface. Error bars are SE, n = 3, with n representing the number of experiments. For statistical test: *, P < 0.05; **, P < 0.01; ***, P < 0.001; ****, P < 0.0001.

These data are consistent with confocal images (Fig. 5.22 and Appendix Fig. A1.2 and A1.3) of the cells before and after treatment: although for treated cells on the nanofibres there are a few adhesions that still present a reminiscent fibre- like shape that follows the nanofibres beneath, most adhesion are more dots like and very faint. The actin cytoskeleton also presents strong differences between the two conditions, with the absence of stress fibres for treated cells, swollen boundaries and branching formation.

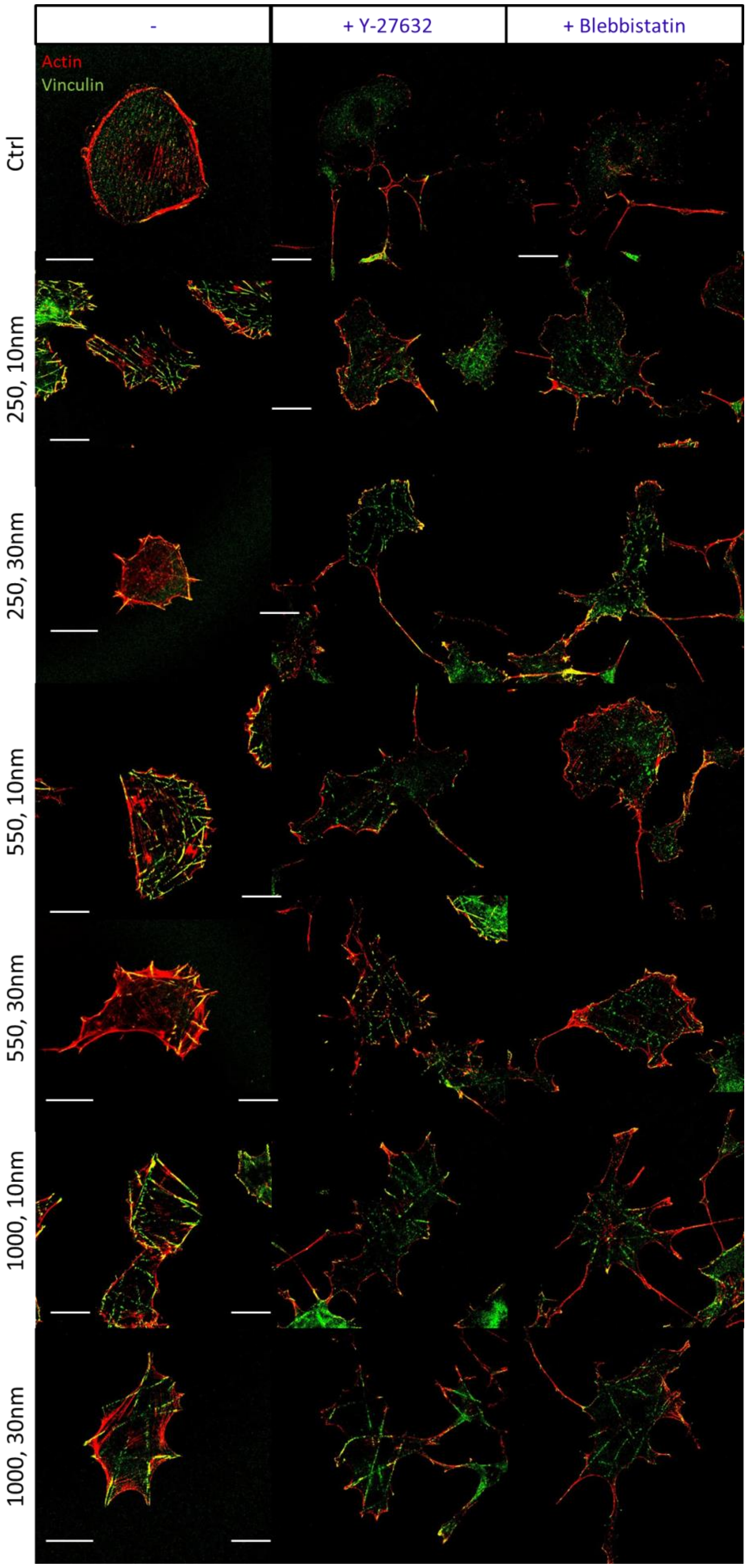

Figure 5.22 Confocal images of GEβ3 cells seeded on different nanofibre diameters (250, 550 and 1000 nm) and brush heights (10 and 30 nm) and treated or not with the cytoskeleton inhibitor Y- 27632 or Blebbistatin. Red is actin cytoskeleton and green is vinculin marker for FAs (for separate channel see Appendix 1). Scale bar is 20 µm.

These results show that the actin reorganization is probably the key step in cell sensing of the nanoscale. The thicker brush layer, over than the constrained fibre geometry, can be destabilizing for actin reorganization and its connection to focal adhesions. Decreasing this barrier leads to increased cell spreading for cells seeded on the smallest geometries. Furthermore, upon cytoskeleton contractility inhibition, cell morphologies, focal adhesions and cytoskeleton reorganization are strongly affected. This may indicate that actin contractility and assembly is the main director of nanoscale sensing.

5.4 Conclusions

In this chapter we have identified the actin cytoskeleton as an important sensing element of the nanotopography of the ECM. Due to the constraints determined by the topography of the matrix, the actin cytoskeleton and the tension it sustains result in the collapse of actin fibres, resulting in altered cell adhesion and spreading.

Differences in cytoskeletal organisation were first analysed for cells expressing β1, β3 or low levels of β3 integrins, and cells were found to present thicker stress fibres, and more centrally oriented fibres, on the largest nanofibres (550 and 1000 nm). Results suggest that cells expressing β3 integrins present more mature fibres and are more sensitive to the nanofibres. When moving to analyse cell motility on these nanofibres, cells seeded on the fibrous nanopatterns were found to be more motile and with less stable cell edges. GEβ1 cells were also observed to be more mobile than GEβ3. Interestingly, associated with an observed higher cytoskeleton rearrangement (at both cell periphery and inside the cell body), GEβ3 cells present highly dynamic actin networks and display the occurrence of foci presumably generated in areas in which stress generated along actin fibres can be sustained considering the geometry and topography of the matrix. Preliminary results on myosin II and α-actinin colocalization also demonstrate an increase in sensitivity for the nanofibres in GEβ3 but not GEβ1 cells (although these results need to be repeated).

The geometry presented here may be comparable to grooved surfaces with groove dimensions and depth in the range of our nanofibres (from 200 to 1000 nm and around 60 nm depth). In this case cells can only form adhesions at the bottom of the groove (due to the passivation polymer brush layer). Although there are still no clear molecular mechanisms, cells have generally been found to align to such grooved surfaces along the major axis of the groove. The alignment though is dependent on the ridge/ grove dimension and the depth of the geometry (Teixeira et al., 2006, Teixeira et al., 2003). In particular, the smaller the features of the pattern, the less aligned the cell morphologies are: cells were found not to align to geometries with depths below 35 nm or ridge widths smaller than 100 nm (Loesberg et al., 2007). Focal adhesions and actin fibres are thus aligned with the grooves above a certain threshold, and it was observed that if the grooves are spaced enough (more than 100 nm), cells manage to adhere in between them as well. Similarly to what happens with grooved geometry, the fibrous patterns where the cells are forced on in this study can determine a focused actin flow along the fibres or perpendicular to them depending on how much constrain the cytoskeleton can bear. In our case though, cells are forced into the “depth” of the fibres and this can cause misalignment in the structure of focal adhesions and the actin network above (Liu et al., 2015). Actin fibres may then be forced to align along the nanofibres behind in order to not perturb the internal structure of focal adhesion or they can grow perpendicular to them when they manage to overcome the tension required: cells on the smallest nanofibres (250 nm) are probably not able to sustain this force and this is why we cannot observe many thick stress fibres. When decreasing the obstacle formed by the brushes wall (10 nm brushes) cell cytoskeleton can then more freely reorganise and this is the significant difference noticed on the smallest nanofibres with shorter brushes.

There is then a cooperation of the fibres size and brush height that dictate how the cells will in the end sense and respond to the geometry. Finally, cytoskeleton inhibitors were used to show that this sensing is very much mediated by contractility: a floppy network is not significantly affected by the height of the brush, that is why there is a lower response on the smallest nanofibres (cell area is significantly higher for cells spreading on the 250 nm fibres after inhibitor treatment compared with before the treatment).

Chapter 6.

Summary of conclusions and future directions

This project focuses on cell sensing and response to a novel fibrous nanopattern with the aim of giving more insight about cell mechanistic behaviour.

Surface engineering is widely used to produce functionalised substrates at the nano and micro scale in order to study cell behaviour and improve cell- biomaterials interface. Here we successfully produced a quasi 2D fibrous nanopattern with fibre diameters ranging from 200 to 1000 nm. These dimensions have been chosen in order to follow cell adhesion maturation from small focal complex to developed focal adhesions. The technique developed for this purpose was called Electrospun Nanofibre Lithography (ENL), due to the fact that electrospinning was used to create the mask with the features to reproduce on the surfaces and this is the determining step for the fibre dimensions. The areas around the electrospunspun fibres were passivated using controlled polymer brush growth (ATRP in this case), which allowed specific functionalization with a protein resistant polymer (POEGMA). The polymerization time can be varied in order to obtain different brush thicknesses. Once the electrospun fibre mesh is removed what is left is a random fibrous pattern surrounded by a non-fouling layer of polymer brushes that can be functionalised with adhesive protein on the fibrous area in order to favour cell attachment. This process is easy, scalable and inexpensive and is compatible with most microscopy techniques (like TIRF or SIM and live imaging). Further developments could include going further down with the fibre sizes, for example testing new polymers (rather than PMMA) that could produce electrospun fibres thinner than 100/50 nm. This technique can also be easily scaled up for high throughput, allowing test of different polymer brushes in parallel.

The fibrous nanopatterns produced were then tested with several cell type and it was found that not only fibre dimensions, but also fibre density affected cell adhesion, restricting focal adhesion formation and cell spreading as the fibre diameter decreases from 1000 nm to 250 nm. Lower nanofibres densities (fibronectin functionalised fibre patterns approximately 20% of the total area) were found to be more disruptive, while cells feel less the geometry when the patterned area coverage is above 40 %. Low density nanofibres were then chosen for further studies. Cell response was also compared between the fibrous nanopattern and circular nanopatches with similar densities (around 20%) and diameter sizes (300, 500 and 800 nm). Similar response was found for cell spreading, although decreasing the size of the nanopatches had a stronger impact on the cell area: this is probably due to the fact that the fibrous patterns restrict adhesion on one dimension only, while with the patches it is a 2D restriction. Cell shape was instead found to be much more polarized on the fibrous patterns: cytoskeleton rearrangement was particularly strong on the smallest nanofibres (250 nm), showing that restriction of cell adhesive areas leads to a reorganization of the focal adhesion and thus actin structure.

Differential integrin expression was also found to be very important in the sensing of the extracellular environment. β1-defficient epithelioid cell lines expressing low levels of αv and β3 integrins (GE cells) and cell lines expressing high levels of α5β1 (GEβ1) and αvβ3 (GEβ3) integrins heterodimers were tested on the fibrous patterns. Changes in cell spreading and morphology were observed for all cell types, but GEβ3 cells were found to be more sensitive to the restricted geometry, confirming that different integrins can be involved in different stages of cell sensing and focal adhesion maturation.

The role of vinculin in the sensing process was then tested. Focal adhesion analysis of GE cells expressing different level of β1 and β3 integrins showed significant differences in the number and sizes of adhesion, with cells growing on homogenous surfaces having higher number of adhesion, but generally smaller than cells seeded on the 550 and 1000 nm nanofibres. The constraint geometry may lead cells to merge or to mature oversized adhesions in order to stabilise and counterbalance a possible increase in tension that cells undergo on the nanofibres. These findings led to further vinculin characterization, and the dynamic regulation of this protein was studied in

GEβ3 cells seeded on homogenous or fibre patterned surfaces. Vinculin was found to have faster turnover for cells seeded on the latter. Cells lacking vinculin were further tested. No significant differences in cell spreading were although found for MEF vin^{-}/$^{-}$ cells re-expressing or not vinculin and seeded on the nanofibres. These results may suggest that although vinculin dynamics seems to be regulated differently on fibrous patterns (from FA distributions and FRAP experiments), this protein may not be the primary nanoscale sensor (from MEF vin^{-}/$^{-}$ experiments).

Due to the strong differences noticed in the cytoskeleton rearrangement, we finally decided to focus the attention on the actin, proposing that its link to focal adhesion is a major mediator of the geometry sensing.

GE, GEβ1 and GEβ3 cytoskeleton structure was analysed for cells seeded on homogenous and patterned substrates showing strong differences in the actin fibre organization and structure depending on the integrin expressed and the type of surfaces cells were adhering on. β3 expressing cells presented more mature actin fibres, more pronounced with the high β3 expressing cells. This is further modulated by the nanofibres size, in a bimodal fashion. In addition, β3 expressing cells display actin fibres that are far more affected (in terms of shape, not just size) by the nanofibres, compared to β1 expressing cells.

GEβ1 and GEβ3 dynamics were further analysed over a period of time of 120 min. Cells seeded on nanofibres displayed higher motility and qualitative observations seem to show that the dynamic of the cytoskeleton and stress fibres is also higher: cell protrusion move faster on the nanofibres and sudden changes of the cells edge can be observed. In GEβ3 cells seeded on the patterned surfaces, and less in GEβ1, was interestingly noticed the formation of actin foci that move quickly inside the cell body and are associated with areas of strong actin remodelling. These structures may be associated to higher tension that cells may feel on these surfaces and actin misassembly due to the constrained geometry. Furthermore, the increased maturity of GEβ3 cells actin fibres may be underlying an increase in contractility exerted across these structures, which may underlie their lower stability (catastrophic collapse).

Considering the geometry proposed here, it seems that the actin fibres could either align along the nanofibres, but may have to deviate in order to reinforce with other actin fibres thus bridging more nanofibres. The topography of the brush could then come in the way of this rearrangement, considering we are using dry thicknesses of 30 nm. We then tested this hypothesis decreasing the brush height to 10 nm, and actually noticed that focal adhesions were higher in number and sizes. The most striking difference though is noticed on the smallest nanofibres (250 nm), where cells presented much higher spreading compared to cells seeded on the same size but with the 30 nm brushes. This proves that the obstacle formed by the brushes may be disruptive for the connection focal adhesion- cytoskeleton.

Finally, we tested cell contractility using cytoskeleton inhibitor and noticed that although spreading is not much affected, focal adhesions dismantle and the cytoskeleton show swollen and highly brunched morphologies on all nanofibres sizes and brush heights and homogenous surfaces. We thus propose that the sensing is mediated by contractility and cytoskeleton arrangement and when these are impaired the brush height is not felt anymore.

Future of tissue engineering and regenerative medicine will rely on modifying the interface material/ cells or tissue so to optimize cell proliferation, for wound healing for example, or to guide stem cells differentiation. Finding the right dimensions and features and thus optimizing biomaterial interfaces so that they resemble more the physiological environment will allow this process and is a vital step in this branch of science.

Bibliography

ABAGNALE, G., STEGER, M., NGUYEN, V. H., HERSCH, N., SECHI, A., JOUSSEN, S., DENECKE, B., MERKEL, R., HOFFMANN, B., DRESER, A., SCHNAKENBERG, U., GILLNER, A. & WAGNER, W. 2015. Surface topography enhances differentiation of mesenchymal stem cells towards osteogenic and adipogenic lineages. *Biomaterials,* 61**,** 316-26.

AGARWAL, S., GREINER, A. & WENDORFF, J. H. 2009. Electrospinning of Manmade and Biopolymer Nanofibers-Progress in Techniques, Materials, and Applications. *Advanced Functional Materials,* 19**,** 2863-2879.

AHN, E. H., KIM, Y., KSHITIZ, AN, S. S., AFZAL, J., LEE, S., KWAK, M., SUH, K. Y., KIM, D. H. & LEVCHENKO, A. 2014. Spatial control of adult stem cell fate using nanotopographic cues. *Biomaterials,* 35**,** 2401-10.

ALBERTS, B., JOHNSON, A., LEWIS, J., RAFF, M., ROBERTS, K. & WALTER, P. 2002. Molecular biology of the cell. new york: Garland science; 2002. *Classic textbook now in its 5th Edition*.

ARNAOUT, M. A., GOODMAN, S. L. & XIONG, J.-P. 2007. Structure and mechanics of integrin-based cell adhesion. *Current opinion in cell biology,* 19**,** 495-507.

ARNOLD, M., CAVALCANTI-ADAM, E. A., GLASS, R., BLÜMMEL, J., ECK, W., KANTLEHNER, M., KESSLER, H. & SPATZ, J. P. 2004. Activation of integrin function by nanopatterned adhesive interfaces. *ChemPhysChem,* 5**,** 383-388.

ATHERTON, P., STUTCHBURY, B., JETHWA, D. & BALLESTREM, C. 2016. Mechanosensitive components of integrin adhesions: Role of vinculin. *Experimental cell research,* 343**,** 21-27.

ATHERTON, P., STUTCHBURY, B., WANG, D.-Y., JETHWA, D., TSANG, R., MEILER-RODRIGUEZ, E., WANG, P., BATE, N., ZENT, R. & BARSUKOV, I. L. 2015. Vinculin controls talin engagement with the actomyosin machinery. *Nature communications,* 6.

BAKOLITSA, C., COHEN, D. M., BANKSTON, L. A., BOBKOV, A. A., CADWELL, G. W., JENNINGS, L., CRITCHLEY, D. R., CRAIG, S. W. & LIDDINGTON, R. C. 2004. Structural basis for vinculin activation at sites of cell adhesion. *Nature,* 430**,** 583-586.

BALABAN, N. Q., SCHWARZ, U. S., RIVELINE, D., GOICHBERG, P., TZUR, G., SABANAY, I., MAHALU, D., SAFRAN, S., BERSHADSKY, A., ADDADI, L. & GEIGER, B. 2001. Force and focal adhesion assembly: a close relationship studied using elastic micropatterned substrates. *Nat Cell Biol,* 3**,** 466-72.

BALCIOGLU H. E., HEDDE VAN HOORN, DOMINIQUE M. DONATO, THOMAS SCHMIDT & DANEN, A. E. H. J. 2015. The integrin expression profile modulates orientation and dynamics of force transmission at cell–matrix adhesions. *Journal of Cell Science,* 128**,** 1316-1326.

BARBEY, R., LAVANANT, L., PARIPOVIC, D., SCHÜWER, N., SUGNAUX, C., TUGULU, S. & KLOK, H.-A. 2009. Polymer brushes via surface-initiated controlled radical polymerization: synthesis, characterization, properties, and applications. *Chemical reviews,* 109**,** 5437-5527.

BARCZYK, M., CARRACEDO, S. & GULLBERG, D. 2010. Integrins. *Cell and tissue research,* 339**,** 269.

BATES, F. S. 1991. Polymer-polymer phase behavior. *Science,* 251**,** 898-905.

BATHAWAB, F. M., BENNETT, M. A. P., CANTINI, M., REBOUD, J., DALBY, M. J. & SALMERÓN-SÁNCHEZ, M. 2015. Lateral Chain Length in PolyAlkyl Acrylates Determines the Mobility of Fibronectin at the Cell/Material Interface. *Langmuir*.

BERGINSKI, M. E., VITRIOL, E. A., HAHN, K. M. & GOMEZ, S. M. 2011. High-resolution quantification of focal adhesion spatiotemporal dynamics in living cells. *PLoS One,* 6**,** e22025.

BERRIER, A. L. & YAMADA, K. M. 2007. Cell–matrix adhesion. *Journal of cellular physiology,* 213**,** 565-573.

BERSHADSKY, A. D., BALLESTREM, C., CARRAMUSA, L., ZILBERMAN, Y., GILQUIN, B., KHOCHBIN, S., ALEXANDROVA, A. Y., VERKHOVSKY, A. B., SHEMESH, T. & KOZLOV, M. M. 2006. Assembly and mechanosensory function of focal adhesions: experiments and models. *Eur J Cell Biol,* 85**,** 165-73.

BIGGS, M. J. P., RICHARDS, R. G., GADEGAARD, N., WILKINSON, C. D. W., OREFFO, R. O. C. & DALBY, M. J. 2009. The use of nanoscale topography to modulate the dynamics of adhesion formation in primary osteoblasts and ERK/MAPK signalling in STRO-1+enriched skeletal stem cells. *Biomaterials,* 30**,** 5094-5103.

BIRK, D. E. & TRELSTAD, R. L. 1984. Extraceilular Compartments in Matrix Morphogenesis: Collagen Fibril, Formation by Corneal Fibroblasts. *The Journal of cell biology,* 99**,** 2024-2033.

BROWN, A. A., KHAN, N. S., STEINBOCK, L. & HUCK, W. T. 2005. Synthesis of oligo (ethylene glycol) methacrylate polymer brushes. *European polymer journal,* 41**,** 1757-1765.

BRUINSMA, R. 2005. Theory of force regulation by nascent adhesion sites. *Biophys J,* 89**,** 87-94.

CARDAMONE, L., LAIO, A., TORRE, V., SHAHAPURE, R. & DESIMONE, A. 2011. Cytoskeletal actin networks in motile cells are critically self-organized systems synchronized by mechanical interactions. *Proc Natl Acad Sci U S A,* 108**,** 13978-83.

CARISEY, A., TSANG, R., GREINER, A. M., NIJENHUIS, N., HEATH, N., NAZGIEWICZ, A., KEMKEMER, R., DERBY, B., SPATZ, J. & BALLESTREM, C. 2013. Vinculin regulates the recruitment and release of core focal adhesion proteins in a force-dependent manner. *Curr Biol,* 23**,** 271-81.

CASE, L. B., BAIRD, M. A., SHTENGEL, G., CAMPBELL, S. L., HESS, H. F., DAVIDSON, M. W. & WATERMAN, C. M. 2015. Molecular mechanism of vinculin activation and nanoscale spatial organization in focal adhesions. *Nat Cell Biol,* 17**,** 880-92.

CASSIDY, J. W., ROBERTS, J. N., SMITH, C. A., ROBERTSON, M., WHITE, K., BIGGS, M. J., OREFFO, R. O. & DALBY, M. J. 2014. Osteogenic lineage restriction by osteoprogenitors cultured on nanometric grooved surfaces: the role of focal adhesion maturation. *Acta Biomater,* 10**,** 651-60.

CAVALCANTI-ADAM, E. A., MICOULET, A., BLUMMEL, J., AUERNHEIMER, J., KESSLER, H. & SPATZ, J. P. 2006. Lateral spacing of integrin ligands influences cell spreading and focal adhesion assembly. *Eur J Cell Biol,* 85**,** 219-24.

CAVALCANTI-ADAM, E. A., VOLBERG, T., MICOULET, A., KESSLER, H., GEIGER, B. & SPATZ, J. P. 2007. Cell spreading and focal adhesion dynamics are regulated by spacing of integrin ligands. *Biophysical journal,* 92**,** 2964-2974.

CHANG, C.-W. & KUMAR, S. 2013. Vinculin tension distributions of individual stress fibers within cell–matrix adhesions. *J Cell Sci,* 126**,** 3021-3030.

CHARO, I. F., NANNIZZI, L., SMITH, J. W. & CHERESH, D. A. 1990. The vitronectin receptor alpha v beta 3 binds fibronectin and acts in concert with alpha 5 beta 1 in promoting cellular attachment and spreading on fibronectin. *The Journal of cell biology,* 111**,** 2795-2800.

CHEN, C. S., MRKSICH, M., HUANG, S., WHITESIDES, G. M. & INGBER, D. E. 1997. Geometric control of cell life and death. *Science,* 276**,** 1425-8.

CHEN, C. S., MRKSICH, M., HUANG, S., WHITESIDES, G. M. & INGBER, D. E. 1998. Micropatterned surfaces for control of cell shape, position, and function. *Biotechnol Prog,* 14**,** 356-63.

CHEN, W., VILLA-DIAZ, L. G., SUN, Y., WENG, S., KIM, J. K., LAM, R. H., HAN, L., FAN, R., KREBSBACH, P. H. & FU, J. 2012. Nanotopography influences adhesion, spreading, and self-renewal of human embryonic stem cells. *ACS Nano,* 6**,** 4094-103.

CHENG, Z. A., ZOUANI, O. F., GLINEL, K., JONAS, A. M. & DURRIEU, M. C. 2013. Bioactive chemical nanopatterns impact human mesenchymal stem cell fate. *Nano Lett,* 13**,** 3923-9.

CHOI, C. K., VICENTE-MANZANARES, M., ZARENO, J., WHITMORE, L. A., MOGILNER, A. & HORWITZ, A. R. 2008. Actin and alpha-actinin orchestrate the assembly and maturation of nascent adhesions in a myosin II motor-independent manner. *Nat Cell Biol,* 10**,** 1039-50.

CHONG, E., PHAN, T., LIM, I., ZHANG, Y., BAY, B., RAMAKRISHNA, S. & LIM, C. 2007. Evaluation of electrospun PCL/gelatin nanofibrous scaffold for wound healing and layered dermal reconstitution. *Acta biomaterialia,* 3**,** 321-330.

CHRISTMAN, K. L., ENRIQUEZ-RIOS, V. D. & MAYNARD, H. D. 2006. Nanopatterning proteins and peptides. *Soft Matter,* 2**,** 928-939.

CHRISTOPHERSON, G. T., SONG, H. & MAO, H. Q. 2009. The influence of fiber diameter of electrospun substrates on neural stem cell differentiation and proliferation. *Biomaterials,* 30**,** 556-64.

CHRZANOWSKA-WODNICKA, M. & BURRIDGE, K. 1996. Rho-stimulated contractility drives the formation of stress fibers and focal adhesions. *The Journal of cell biology,* 133**,** 1403-1415.

CONNELLY, J. T., GAUTROT, J. E., TRAPPMANN, B., TAN, D. W., DONATI, G., HUCK, W. T. & WATT, F. M. 2010. Actin and serum response factor transduce physical cues from the microenvironment to regulate epidermal stem cell fate decisions. *Nat Cell Biol,* 12**,** 711-8.

COURTEMANCHE, N., LEE, J. Y., POLLARD, T. D. & GREENE, E. C. 2013. Tension modulates actin filament polymerization mediated by formin and profilin. *Proc Natl Acad Sci U S A,* 110**,** 9752-7.

COYER, S. R., GARCIA, A. J. & DELAMARCHE, E. 2007. Facile preparation of complex protein architectures with sub-100-nm resolution on surfaces. *Angew Chem Int Ed Engl,* 46**,** 6837-40.

COYER, S. R., SINGH, A., DUMBAULD, D. W., CALDERWOOD, D. A., CRAIG, S. W., DELAMARCHE, E. & GARCIA, A. J. 2012. Nanopatterning reveals an ECM area threshold for focal adhesion assembly and force transmission that is regulated by integrin activation and cytoskeleton tension. *J Cell Sci,* 125**,** 5110-23.

CRAMER, L. P., SIEBERT, M. & MITCHISON, T. J. 1997. Identification of novel graded polarity actin filament bundles in locomoting heart fibroblasts: implications for the generation of motile force. *The Journal of cell biology,* 136**,** 1287-1305.

CURTIS, A. S., CASEY, B., GALLAGHER, J. O., PASQUI, D., WOOD, M. A. & WILKINSON, C. D. 2001. Substratum nanotopography and the adhesion of biological cells. Are symmetry or regularity of nanotopography important? *Biophys Chem,* 94**,** 275-83.

DALBY, M. J., GADEGAARD, N., RIEHLE, M. O., WILKINSON, C. D. & CURTIS, A. S. 2004. Investigating filopodia sensing using arrays of defined nano-pits down to 35 nm diameter in size. *Int J Biochem Cell Biol,* 36**,** 2005-15.

DALBY, M. J., GADEGAARD, N., TARE, R., ANDAR, A., RIEHLE, M. O., HERZYK, P., WILKINSON, C. D. & OREFFO, R. O. 2007. The control of human mesenchymal cell differentiation using nanoscale symmetry and disorder. *Nat Mater,* 6**,** 997-1003.

DANEN, E. H., SONNEVELD, P., BRAKEBUSCH, C., FÄSSLER, R. & SONNENBERG, A. 2002. The fibronectin-binding integrins α5β1 and αvβ3 differentially modulate RhoA–GTP loading, organization of cell matrix adhesions, and fibronectin fibrillogenesis. *The Journal of cell biology,* 159**,** 1071-1086.

DANEN, E. H., VAN RHEENEN, J., FRANKEN, W., HUVENEERS, S., SONNEVELD, P., JALINK, K. & SONNENBERG, A. 2005. Integrins control motile strategy through a Rho–cofilin pathway. *The Journal of cell biology,* 169**,** 515-526.

DARLING, S. B. 2007. Directing the self-assembly of block copolymers. *Progress in Polymer Science,* 32**,** 1152-1204.

DAS, R. K., ZOUANI, O. F., LABRUGERE, C., ODA, R. & DURRIEU, M. C. 2013. Influence of nanohelical shape and periodicity on stem cell fate. *ACS Nano,* 7**,** 3351-61.

DE VRIEZE, S., VAN CAMP, T., NELVIG, A., HAGSTRÖM, B., WESTBROEK, P. & DE CLERCK, K. 2009. The effect of temperature and humidity on electrospinning. *Journal of materials science,* 44**,** 1357.

DEEG, J. A., LOUBAN, I., AYDIN, D., SELHUBER-UNKEL, C., KESSLER, H. & SPATZ, J. P. 2011. Impact of local versus global ligand density on cellular adhesion. *Nano Lett,* 11**,** 1469-76.

DEFRANCO, J. A., SCHMIDT, B. S., LIPSON, M. & MALLIARAS, G. G. 2006. Photolithographic patterning of organic electronic materials. *Organic Electronics,* 7**,** 22-28.

DEITZEL, J. M., KLEINMEYER, J., HARRIS, D. & TAN, N. C. B. 2001. The effect of processing variables on the morphology of electrospun nanofibers and textiles. *Polymer,* 42**,** 261-272.

DEL CAMPO, A. & ARZT, E. 2008. Fabrication approaches for generating complex micro- and nanopatterns on polymeric surfaces. *Chem Rev,* 108**,** 911-45.

DEL RIO, A., PEREZ-JIMENEZ, R., LIU, R., ROCA-CUSACHS, P., FERNANDEZ, J. M. & SHEETZ, M. P. 2009. Stretching single talin rod molecules activates vinculin binding. *Science,* 323**,** 638-41.

DI CIO, S., BOGGILD, T. M., CONNELLY, J., SUTHERLAND, D. S. & GAUTROT, J. E. 2016. Differential Integrin Expression Regulates Cell Sensing of the Matrix Nanoscale Geometry. *Acta Biomaterialia*.

DI CIO, S. & GAUTROT, J. E. 2016. Cell sensing of physical properties at the nanoscale: Mechanisms and control of cell adhesion and phenotype. *Acta biomaterialia,* 30**,** 26-48.

DIKE, L. E., CHEN, C. S., MRKSICH, M., TIEN, J., WHITESIDES, G. M. & INGBER, D. E. 1999. Geometric control of switching between growth, apoptosis, and differentiation during angiogenesis using micropatterned substrates. *In Vitro Cellular & Developmental Biology-Animal,* 35**,** 441-448.

DUMBAULD D.W., TED T. LEEA, ANKUR SINGHA, JAN SCRIMGEOURB, CHARLES A. GERSBACHA, EVAN A. ZAMIR, JIANPING FUD, CHRISTOPHER S. CHENE, JENNIFER E. CURTISB, SUSAN W. CRAIGF & GARCÍA, A. A. J. 2013. How vinculin regulates force transmission. *PNAS,* 110**,** 9788–9793.

EDLUND, M., LOTANO, M. A. & OTEY, C. A. 2001. Dynamics of α-actinin in focal adhesions and stress fibers visualized with α-actinin-green fluorescent protein. *Cell motility and the cytoskeleton,* 48**,** 190-200.

EDMONDSON, S., OSBORNE, V. L. & HUCK, W. T. 2004. Polymer brushes via surface-initiated polymerizations. *Chemical society reviews,* 33**,** 14-22.

EGELMAN, E. H. 1985. The structure of F-actin. *J Muscle Res Cell Motil,* 6**,** 129-51.

EHRLICHER, A. J., NAKAMURA, F., HARTWIG, J. H., WEITZ, D. A. & STOSSEL, T. P. 2011. Mechanical strain in actin networks regulates FilGAP and integrin binding to filamin A. *Nature,* 478**,** 260-3.

EIMER, W., NIERMANN, M., EPPE, M. & JOCKUSCH, B. 1993. Molecular shape of vinculin in aqueous solution. *Journal of molecular biology,* 229**,** 146-152.

ELKHATIB, N., NEU, M. B., ZENSEN, C., SCHMOLLER, K. M., LOUVARD, D., BAUSCH, A. R., BETZ, T. & VIGNJEVIC, D. M. 2014. Fascin plays a role in stress fiber organization and focal adhesion disassembly. *Curr Biol,* 24**,** 1492-9.

ENDLICH, N., OTEY, C. A., KRIZ, W. & ENDLICH, K. 2007. Movement of stress fibers away from focal adhesions identifies focal adhesions as sites of stress fiber assembly in stationary cells. *Cytoskeleton,* 64**,** 966-976.

ENGLER, A. J., SEN, S., SWEENEY, H. L. & DISCHER, D. E. 2006. Matrix elasticity directs stem cell lineage specification. *Cell,* 126**,** 677-89.

ESUE, O., HARRIS, E. S., HIGGS, H. N. & WIRTZ, D. 2008. The filamentous actin cross-linking/bundling activity of mammalian formins. *J Mol Biol,* 384**,** 324-34.

FLETCHER, D. A. & MULLINS, R. D. 2010. Cell mechanics and the cytoskeleton. *Nature,* 463**,** 485-492.

FOOTER, M. J., KERSSEMAKERS, J. W. J., THERIOT, J. A. & DOGTEROM, M. 2007. Direct measurement of force generation by actin filament polymerization using an optical trap. *Proceedings of the National Academy of Sciences of the United States of America,* 104**,** 2181-2186.

FRALEY, S. I., FENG, Y., KRISHNAMURTHY, R., KIM, D. H., CELEDON, A., LONGMORE, G. D. & WIRTZ, D. 2010. A distinctive role for focal adhesion proteins in three-dimensional cell motility. *Nat Cell Biol,* 12**,** 598-604.

FRANK, D. E. & CARTER, W. G. 2004. Laminin 5 deposition regulates keratinocyte polarization and persistent migration. *Journal of cell science,* 117**,** 1351-1363.

FRIDRIKH, S. V., YU, J. H., BRENNER, M. P. & RUTLEDGE, G. C. 2003. Controlling the fiber diameter during electrospinning. *Phys Rev Lett,* 90**,** 144502.

FU, J., WANG, Y. K., YANG, M. T., DESAI, R. A., YU, X., LIU, Z. & CHEN, C. S. 2010. Mechanical regulation of cell function with geometrically modulated elastomeric substrates. *Nat Methods,* 7**,** 733-6.

GADEGAARD, N., THOMS, S., MACINTYRE, D. S., MCGHEE, K., GALLAGHER, J., CASEY, B. & WILKINSON, C. D. W. 2003. Arrays of nano-dots for cellular engineering. *Microelectronic Engineering,* 67-8**,** 162-168.

GALBRAITH, C. G., YAMADA, K. M. & SHEETZ, M. P. 2002. The relationship between force and focal complex development. *J Cell Biol,* 159**,** 695-705.

GALLANT, N. D., MICHAEL, K. E. & GARCIA, A. J. 2005. Cell adhesion strengthening: contributions of adhesive area, integrin binding, and focal adhesion assembly. *Mol Biol Cell,* 16**,** 4329-40.

GARDEL, M. L., SABASS, B., JI, L., DANUSER, G., SCHWARZ, U. S. & WATERMAN, C. M. 2008. Traction stress in focal adhesions correlates biphasically with actin retrograde flow speed. *J Cell Biol,* 183**,** 999-1005.

GATES, B. D., XU, Q., STEWART, M., RYAN, D., WILLSON, C. G. & WHITESIDES, G. M. 2005. New approaches to nanofabrication: molding, printing, and other techniques. *Chem Rev,* 105**,** 1171-96.

GAUTROT, J. E., MALMSTROM, J., SUNDH, M., MARGADANT, C., SONNENBERG, A. & SUTHERLAND, D. S. 2014. The nanoscale geometrical maturation of focal adhesions controls stem cell differentiation and mechanotransduction. *Nano Lett,* 14**,** 3945-52.

GAUTROT, J. E., TRAPPMANN, B., OCEGUERA-YANEZ, F., CONNELLY, J., HE, X., WATT, F. M. & HUCK, W. T. 2010. Exploiting the superior protein resistance of polymer brushes to control single cell adhesion and polarisation at the micron scale. *Biomaterials,* 31**,** 5030-41.

GAUTROT, J. E., WANG, C., LIU, X., GOLDIE, S. J., TRAPPMANN, B., HUCK, W. T. & WATT, F. M. 2012. Mimicking normal tissue architecture and perturbation in cancer with engineered micro-epidermis. *Biomaterials,* 33**,** 5221-5229.

GAVARA, N. & CHADWICK, R. S. 2016. Relationship between cell stiffness and stress fiber amount, assessed by simultaneous atomic force microscopy and live-cell fluorescence imaging. *Biomechanics and modeling in mechanobiology,* 15**,** 511-523.

GEIGER, B., SPATZ, J. P. & BERSHADSKY, A. D. 2009. Environmental sensing through focal adhesions. *Nat Rev Mol Cell Biol,* 10**,** 21-33.

GEISSLER, M. & XIA, Y. N. 2004. Patterning: Principles and some new developments. *Advanced Materials,* 16**,** 1249-1269.

GHASSEMI, S., MEACCI, G., LIU, S., GONDARENKO, A. A., MATHUR, A., ROCA-CUSACHS, P., SHEETZ, M. P. & HONE, J. 2012. Cells test substrate rigidity by local contractions on submicrometer pillars. *Proc Natl Acad Sci U S A,* 109**,** 5328-33.

GHODSSI, R. & LIN, P. 2011. *MEMS materials and processes handbook*, Springer Science & Business Media.

GIANCOTTI, F. G. & RUOSLAHTI, E. 1999. Integrin signaling. *Science,* 285**,** 1028-1033.

GIANNONE, G., DUBIN-THALER, B. J., DÖBEREINER, H.-G., KIEFFER, N., BRESNICK, A. R. & SHEETZ, M. P. 2004. Periodic lamellipodial contractions correlate with rearward actin waves. *Cell,* 116**,** 431-443.

GIMOND, C., VAN DER FLIER, A., VAN DELFT, S., BRAKEBUSCH, C., KUIKMAN, I., COLLARD, J. G., FÄSSLER, R. & SONNENBERG, A. 1999. Induction of cell scattering by expression of β1 integrins in β1-deficient epithelial cells requires activation of members of the rho family of GTPases and downregulation of cadherin and catenin function. *The Journal of cell biology,* 147**,** 1325-1340.

GINGER, D. S., ZHANG, H. & MIRKIN, C. A. 2004. The evolution of dip-pen nanolithography. *Angew Chem Int Ed Engl,* 43**,** 30-45.

GRASHOFF, C., HOFFMAN, B. D., BRENNER, M. D., ZHOU, R., PARSONS, M., YANG, M. T., MCLEAN, M. A., SLIGAR, S. G., CHEN, C. S., HA, T. & SCHWARTZ, M. A. 2010. Measuring mechanical tension across vinculin reveals regulation of focal adhesion dynamics. *Nature,* 466**,** 263-6.

GREINER, A. & WENDORFF, J. H. 2007. Electrospinning: a fascinating method for the preparation of ultrathin fibers. *Angew Chem Int Ed Engl,* 46**,** 5670-703.

GUERRA, N. B., GONZÁLEZ-GARCÍA, C., LLOPIS, V., RODRÍGUEZ-HERNÁNDEZ, J. C., MORATAL, D., RICO, P. & SALMERÓN-SÁNCHEZ, M. 2010. Subtle variations in polymer chemistry modulate substrate stiffness and fibronectin activity. *Soft Matter,* 6**,** 4748-4755.

GUGUTKOV, D., GONZALEZ-GARCIA, C., RODRIGUEZ HERNANDEZ, J. C., ALTANKOV, G. & SALMERON-SANCHEZ, M. 2009. Biological activity of the substrate-induced fibronectin network: insight into the third dimension through electrospun fibers. *Langmuir,* 25**,** 10893-900.

GUPTA, P., ELKINS, C., LONG, T. E. & WILKES, G. L. 2005. Electrospinning of linear homopolymers of poly (methyl methacrylate): exploring relationships between fiber formation, viscosity, molecular weight and concentration in a good solvent. *Polymer,* 46**,** 4799-4810.

HALL, A. 1998. Rho GTPases and the actin cytoskeleton. *Science,* 279**,** 509-514.

HAN, S. J., OAK, Y., GROISMAN, A. & DANUSER, G. 2015. Traction microscopy to identify force modulation in subresolution adhesions. *Nat Methods,* 12**,** 653-6.

HARBURGER & CALDERWOOD 2009. Integrin signalling at a glance. *Journal of Cell Science* 122**,** 159-163.

HE, L., LIAO, S., QUAN, D., MA, K., CHAN, C., RAMAKRISHNA, S. & LU, J. 2010. Synergistic effects of electrospun PLLA fiber dimension and pattern on neonatal mouse cerebellum C17.2 stem cells. *Acta Biomater,* 6**,** 2960-9.

HIGGINS, A. M., BANIK, B. L. & BROWN, J. L. 2015. Geometry sensing through POR1 regulates Rac1 activity controlling early osteoblast differentiation in response to nanofiber diameter. *Integr Biol* 7**,** 229-36.

HOTULAINEN, P. & LAPPALAINEN, P. 2006. Stress fibers are generated by two distinct actin assembly mechanisms in motile cells. *The Journal of cell biology,* 173**,** 383-394.

HU, K., JI, L., APPLEGATE, K. T., DANUSER, G. & WATERMAN-STORER, C. M. 2007. Differential transmission of actin motion within focal adhesions. *Science,* 315**,** 111-5.

HUA, F., SUN, Y. G., GAUR, A., MEITL, M. A., BILHAUT, L., ROTKINA, L., WANG, J. F., GEIL, P., SHIM, M., ROGERS, J. A. & SHIM, A. 2004. Polymer imprint lithography with molecular-scale resolution. *Nano Lett,* 4**,** 2467-2471.

HUANG, C. B., CHEN, S. L., LAI, C. L., RENEKER, D. H., QIU, H., YE, Y. & HOU, H. Q. 2006. Electrospun polymer nanofibres with small diameters. *Nanotechnology,* 17**,** 1558-1563.

HUANG, J., GRATER, S. V., CORBELLINI, F., RINCK, S., BOCK, E., KEMKEMER, R., KESSLER, H., DING, J. & SPATZ, J. P. 2009. Impact of order and disorder in RGD nanopatterns on cell adhesion. *Nano Lett,* 9**,** 1111-6.

HUANG, L., NAGAPUDI, K., P. APKARIAN, R. & CHAIKOF, E. L. 2001. Engineered collagen–PEO nanofibers and fabrics. *Journal of biomaterials science, Polymer edition,* 12**,** 979-993.

HUEBSCH, N., ARANY, P. R., MAO, A. S., SHVARTSMAN, D., ALI, O. A., BENCHERIF, S. A., RIVERA-FELICIANO, J. & MOONEY, D. J. 2010. Harnessing traction-mediated manipulation of the cell/matrix interface to control stem-cell fate. *Nat Mater,* 9**,** 518-26.

HUMPHRIES, J. D., WANG, P., STREULI, C., GEIGER, B., HUMPHRIES, M. J. & BALLESTREM, C. 2007. Vinculin controls focal adhesion formation by direct interactions with talin and actin. *J Cell Biol,* 179**,** 1043-57.

ISHIZAKI, T., UEHATA, M., TAMECHIKA, I., KEEL, J., NONOMURA, K., MAEKAWA, M. & NARUMIYA, S. 2000. Pharmacological properties of Y-27632, a specific inhibitor of rho-associated kinases. *Molecular pharmacology,* 57**,** 976-983.

JAISWAL, D. & BROWN, J. L. 2012. Nanofiber diameter-dependent MAPK activity in osteoblasts. *J Biomed Mater Res A,* 100**,** 2921-8.

JIN, G., PRABHAKARAN, M. P. & RAMAKRISHNA, S. 2011. Stem cell differentiation to epidermal lineages on electrospun nanofibrous substrates for skin tissue engineering. *Acta Biomaterialia,* 7**,** 3113-3122.

KANCHANAWONG, P., SHTENGEL, G., PASAPERA, A. M., RAMKO, E. B., DAVIDSON, M. W., HESS, H. F. & WATERMAN, C. M. 2010. Nanoscale architecture of integrin-based cell adhesions. *Nature,* 468**,** 580-4.

KERN, W. & DECKERT, C. A. 1978. Chemical etching. *Thin film processes,* 1.

KHETAN, S., GUVENDIREN, M., LEGANT, W. R., COHEN, D. M., CHEN, C. S. & BURDICK, J. A. 2013. Degradation-mediated cellular traction directs stem cell fate in covalently crosslinked three-dimensional hydrogels. *Nat Mater,* 12**,** 458-65.

KILIAN, K. A., BUGARIJA, B., LAHN, B. T. & MRKSICH, M. 2010. Geometric cues for directing the differentiation of mesenchymal stem cells. *Proc Natl Acad Sci U S A,* 107**,** 4872-7.

KIM, D. H., LIPKE, E. A., KIM, P., CHEONG, R., THOMPSON, S., DELANNOY, M., SUH, K. Y., TUNG, L. & LEVCHENKO, A. 2010. Nanoscale cues regulate the structure and function of macroscopic cardiac tissue constructs. *Proc Natl Acad Sci U S A,* 107**,** 565-70.

KLOK, H. A. & LECOMMANDOUX, S. 2001. Supramolecular materials via block copolymer self-assembly. *Advanced Materials,* 13**,** 1217-1229.

KLOTZSCH, E., SMITH, M. L., KUBOW, K. E., MUNTWYLER, S., LITTLE, W. C., BEYELER, F., GOURDON, D., NELSON, B. J. & VOGEL, V. 2009. Fibronectin forms the most extensible biological fibers displaying switchable force-exposed cryptic binding sites. *Proc Natl Acad Sci U S A,* 106**,** 18267-72.

KOLODZIEJ, C. M., KIM, S. H., BROYER, R. M., SAXER, S. S., DECKER, C. G. & MAYNARD, H. D. 2012. Combination of integrin-binding peptide and growth factor promotes cell adhesion on electron-beam-fabricated patterns. *J Am Chem Soc,* 134**,** 247-55.

KOLODZIEJ, C. M. & MAYNARD, H. D. 2012. Electron-Beam Lithography for Patterning Biomolecules at the Micron and Nanometer Scale. *Chemistry of Materials,* 24**,** 774-780.

KOVAC, B., TEO, J. L., MÄKELÄ, T. P. & VALLENIUS, T. 2013. Assembly of non-contractile dorsal stress fibers requires α-actinin-1 and Rac1 in migrating and spreading cells. *J Cell Sci,* 126**,** 263-273.

KUMAR, N. & HAHM, J. I. 2005. Nanoscale protein patterning using self-assembled diblock copolymers. *Langmuir,* 21**,** 6652-5.

KUO, C. W., CHUEH, D. Y. & CHEN, P. 2014. Investigation of size-dependent cell adhesion on nanostructured interfaces. *J Nanobiotechnology,* 12**,** 54.

LAAKSO, J. M., LEWIS, J. H., SHUMAN, H. & OSTAP, E. M. 2008. Myosin I can act as a molecular force sensor. *Science,* 321**,** 133-6.

LAI, C. Q. & CHENG, H. 2014. Versatile fabrication and applications of dense, orderly arrays of polymeric nanostructures over large areas. *Journal of Materials Chemistry B,* 2**,** 5982-5991.

LAVELIN, I., WOLFENSON, H., PATLA, I., HENIS, Y. I., MEDALIA, O., VOLBERG, T., LIVNE, A., KAM, Z. & GEIGER, B. 2013. Differential effect of actomyosin relaxation on the dynamic properties of focal adhesion proteins. *PLoS One,* 8**,** e73549.

LE DEVEDEC, S. E., GEVERTS, B., DE BONT, H., YAN, K., VERBEEK, F. J., HOUTSMULLER, A. B. & VAN DE WATER, B. 2012. The residence time of focal adhesion kinase (FAK) and paxillin at focal adhesions in renal epithelial cells is determined by adhesion size, strength and life cycle status. *Journal of Cell Science,* 125**,** 4498-4506.

LEE, C. Y., LOU, J., WEN, K. K., MCKANE, M., ESKIN, S. G., ONO, S., CHIEN, S., RUBENSTEIN, P. A., ZHU, C. & MCINTIRE, L. V. 2013a. Actin depolymerization under force is governed by lysine 113:glutamic acid 195-mediated catch-slip bonds. *Proc Natl Acad Sci U S A,* 110**,** 5022-7.

LEE, H. S., ANEKAL, P., LIM, C. J., LIU, C. C. & GINSBERG, M. H. 2013b. Two modes of integrin activation form a binary molecular switch in adhesion maturation. *Mol Biol Cell,* 24**,** 1354-62.

LEE, K. B., PARK, S. J., MIRKIN, C. A., SMITH, J. C. & MRKSICH, M. 2002a. Protein nanoarrays generated by dip-pen nanolithography. *Science,* 295**,** 1702-5.

LEE, K. H., KIM, H. Y., LA, Y. M., LEE, D. R. & SUNG, N. H. 2002b. Influence of a mixing solvent with tetrahydrofuran and N, N-dimethylformamide on electrospun poly (vinyl chloride) nonwoven mats. *Journal of polymer science part B: polymer physics,* 40**,** 2259-2268.

LEE, M. R., KWON, K. W., JUNG, H., KIM, H. N., SUH, K. Y., KIM, K. & KIM, K.-S. 2010. Direct differentiation of human embryonic stem cells into selective neurons on nanoscale ridge/groove pattern arrays. *Biomaterials,* 31**,** 4360-4366.

LIU, J., WANG, Y., GOH, W. I., GOH, H., BAIRD, M. A., RUEHLAND, S., TEO, S., BATE, N., CRITCHLEY, D. R. & DAVIDSON, M. W. 2015. Talin determines the nanoscale architecture of focal adhesions. *Proceedings of the National Academy of Sciences,* 112**,** E4864-E4873.

LIU, Y., JI, Y., GHOSH, K., CLARK, R. A., HUANG, L. & RAFAILOVICH, M. H. 2009. Effects of fiber orientation and diameter on the behavior of human dermal fibroblasts on electrospun PMMA scaffolds. *Journal of Biomedical Materials Research Part A,* 90**,** 1092-1106.

LIU, Y., MEDDA, R., LIU, Z., GALIOR, K., YEHL, K., SPATZ, J. P., CAVALCANTI-ADAM, E. A. & SALAITA, K. 2014. Nanoparticle tension probes patterned at the nanoscale: impact of integrin clustering on force transmission. *Nano Lett,* 14**,** 5539-46.

LIVNE, A. & GEIGER, B. 2016. The inner workings of stress fibers− from contractile machinery to focal adhesions and back. *J Cell Sci,* 129**,** 1293-1304.

LOESBERG, W., TE RIET, J., VAN DELFT, F., SCHÖN, P., FIGDOR, C., SPELLER, S., VAN LOON, J., WALBOOMERS, X. & JANSEN, J. 2007. The threshold at which substrate nanogroove dimensions may influence fibroblast alignment and adhesion. *Biomaterials,* 28**,** 3944-3951.

LOOSLI, Y., LABOUESSE, C., LUGINBUEHL, R., MEISTER, J. J., SNEDEKER, J. G. & VIANAY, B. 2013. An actin length threshold regulates adhesion maturation at the lamellipodium/lamellum interface. *Integr Biol,* 5**,** 865-76.

LOOSLI, Y., LUGINBUEHL, R. & SNEDEKER, J. G. 2010. Cytoskeleton reorganization of spreading cells on micro-patterned islands: a functional model. *Philos Trans A Math Phys Eng Sci,* 368**,** 2629-52.

LOOSLI, Y., VIANAY, B., LUGINBUEHL, R. & SNEDEKER, J. G. 2012. Numerically bridging lamellipodial and filopodial activity during cell spreading reveals a potentially novel trigger of focal adhesion maturation. *Integr Biol* 4**,** 508-21.

LOVE, J. C., PAUL, K. E. & WHITESIDES, G. M. 2001. Fabrication of Nanometer-Scale Features by Controlled Isotropic Wet Chemical Etching. *Advanced Materials,* 13**,** 604-607.

LOWERY, J. L., DATTA, N. & RUTLEDGE, G. C. 2010. Effect of fiber diameter, pore size and seeding method on growth of human dermal fibroblasts in electrospun poly(epsilon-caprolactone) fibrous mats. *Biomaterials,* 31**,** 491-504.

LUO, B.-H., CARMAN, C. V. & SPRINGER, T. A. 2007. Structural basis of integrin regulation and signaling. *Annu. Rev. Immunol.,* 25**,** 619-647.

LUTOLF, M. P. & HUBBELL, J. A. 2005. Synthetic biomaterials as instructive extracellular microenvironments for morphogenesis in tissue engineering. *Nat Biotechnol,* 23**,** 47-55.

MAI, Y. & EISENBERG, A. 2012. Self-assembly of block copolymers. *Chem Soc Rev,* 41**,** 5969-85.

MAIURI, P., RUPPRECHT, J. F., WIESER, S., RUPRECHT, V., BENICHOU, O., CARPI, N., COPPEY, M., DE BECO, S., GOV, N., HEISENBERG, C. P., CRESPO, C. L., LAUTENSCHLAEGER, F., LE BERRE, M., LENNON-DUMENIL, A. M., RAAB, M., THIAM, H. R., PIEL, M., SIXT, M. & VOITURIEZ, R. 2015. Actin Flows Mediate a Universal Coupling between Cell Speed and Cell Persistence. *Cell,* 161**,** 374-386.

MALMSTROM, J., CHRISTENSEN, B., JAKOBSEN, H. P., LOVMAND, J., FOLDBJERG, R., SORENSEN, E. S. & SUTHERLAND, D. S. 2010. Large area protein patterning reveals nanoscale control of focal adhesion development. *Nano Lett,* 10**,** 686-94.

MALMSTRÖM, J., LOVMAND, J., KRISTENSEN, S., SUNDH, M., DUCH, M. & SUTHERLAND, D. S. 2011. Focal Complex Maturation and Bridging on 200 nm Vitronectin but Not Fibronectin Patches Reveal Different Mechanisms of Focal Adhesion Formation. *Nano Lett,* 11**,** 2264–2271.

MATYJASZEWSKI, K. 2012. Atom transfer radical polymerization (ATRP): current status and future perspectives. *Macromolecules,* 45**,** 4015-4039.

MATYJASZEWSKI, K. & XIA, J. 2001. Atom transfer radical polymerization. *Chemical reviews,* 101**,** 2921-2990.

MCBEATH, R., PIRONE, D. M., NELSON, C. M., BHADRIRAJU, K. & CHEN, C. S. 2004. Cell shape, cytoskeletal tension, and RhoA regulate stem cell lineage commitment. *Dev Cell,* 6**,** 483-95.

MCCULLOUGH, B. R., BLANCHOIN, L., MARTIEL, J. L. & DE LA CRUZ, E. M. 2008. Cofilin increases the bending flexibility of actin filaments: implications for severing and cell mechanics. *J Mol Biol,* 381**,** 550-8.

MCMURRAY, R. J., GADEGAARD, N., TSIMBOURI, P. M., BURGESS, K. V., MCNAMARA, L. E., TARE, R., MURAWSKI, K., KINGHAM, E., OREFFO, R. O. & DALBY, M. J. 2011. Nanoscale surfaces for the long-term maintenance of mesenchymal stem cell phenotype and multipotency. *Nat Mater,* 10**,** 637-44.

MICHELOT, A., BERRO, J., GUERIN, C., BOUJEMAA-PATERSKI, R., STAIGER, C. J., MARTIEL, J. L. & BLANCHOIN, L. 2007. Actin-filament stochastic dynamics mediated by ADF/cofilin. *Curr Biol,* 17**,** 825-33.

MIRON-MENDOZA, M., SEEMANN, J. & GRINNELL, F. 2010. The differential regulation of cell motile activity through matrix stiffness and porosity in three dimensional collagen matrices. *Biomaterials,* 31**,** 6425-35.

MOORE, S. W., ROCA-CUSACHS, P. & SHEETZ, M. P. 2010. Stretchy proteins on stretchy substrates: the important elements of integrin-mediated rigidity sensing. *Dev Cell,* 19**,** 194-206.

MORIMATSU, M., MEKHDJIAN, A. H., ADHIKARI, A. S. & DUNN, A. R. 2013. Molecular tension sensors report forces generated by single integrin molecules in living cells. *Nano Lett,* 13**,** 3985-9.

MORIMATSU, M., MEKHDJIAN, A. H., CHANG, A. C., TAN, S. J. & DUNN, A. R. 2015. Visualizing the interior architecture of focal adhesions with high-resolution traction maps. *Nano Lett,* 15**,** 2220-8.

MOSTAFAVI-POUR, Z., ASKARI, J. A., PARKINSON, S. J., PARKER, P. J., NG, T. T. & HUMPHRIES, M. J. 2003. Integrin-specific signaling pathways controlling focal adhesion formation and cell migration. *The Journal of cell biology,* 161**,** 155-167.

MUTSAERS, S. E., BISHOP, J. E., MCGROUTHER, G. & LAURENT, G. J. 1997. Mechanisms of tissue repair: from wound healing to fibrosis. *The international journal of biochemistry & cell biology,* 29**,** 5-17.

NAGAI, T., IBATA, K., PARK, E. S., KUBOTA, M., MIKOSHIBA, K. & MIYAWAKI, A. 2002. A variant of yellow fluorescent protein with fast and efficient maturation for cell-biological applications. *Nature biotechnology,* 20**,** 87-90.

NAUMANEN, P., LAPPALAINEN, P. & HOTULAINEN, P. 2008. Mechanisms of actin stress fibre assembly. *Journal of microscopy,* 231**,** 446-454.

NIE, Z. & KUMACHEVA, E. 2008. Patterning surfaces with functional polymers. *Nat Mater,* 7**,** 277-90.

NOBES, C. D. & HALL, A. 1995. Rho, rac, and cdc42 GTPases regulate the assembly of multimolecular focal complexes associated with actin stress fibers, lamellipodia, and filopodia. *Cell,* 81**,** 53-62.

OZDEMIR, T., XU, L. C., SIEDLECKI, C. & BROWN, J. L. 2013. Substrate curvature sensing through Myosin IIa upregulates early osteogenesis. *Integr Biol* 5**,** 1407-16.

PAREKH, S. H., CHAUDHURI, O., THERIOT, J. A. & FLETCHER, D. A. 2005. Loading history determines the velocity of actin-network growth. *Nat Cell Biol,* 7**,** 1219-23.

PARSONS, J. T., HORWITZ, A. R. & SCHWARTZ, M. A. 2010. Cell adhesion: integrating cytoskeletal dynamics and cellular tension. *Nature reviews Molecular cell biology,* 11**,** 633-643.

PASAPERA, A. M., PLOTNIKOV, S. V., FISCHER, R. S., CASE, L. B., EGELHOFF, T. T. & WATERMAN, C. M. 2015. Rac1-dependent phosphorylation and focal adhesion recruitment of myosin IIA regulates migration and mechanosensing. *Curr Biol,* 25**,** 175-86.

PASAPERA, A. M., SCHNEIDER, I. C., RERICHA, E., SCHLAEPFER, D. D. & WATERMAN, C. M. 2010. Myosin II activity regulates vinculin recruitment to focal adhesions through FAK-mediated paxillin phosphorylation. *J Cell Biol,* 188**,** 877-90.

PATLA, I., VOLBERG, T., ELAD, N., HIRSCHFELD-WARNEKEN, V., GRASHOFF, C., FASSLER, R., SPATZ, J. P., GEIGER, B. & MEDALIA, O. 2010. Dissecting the molecular architecture of integrin adhesion sites by cryo-electron tomography. *Nat Cell Biol,* 12**,** 909-15.

PEARTON, S., SHUL, R. & REN, F. 2000. A review of dry etching of GaN and related materials. *MRS Internet Journal of Nitride Semiconductor Research,* 5**,** e11.

PELLEGRIN, S. & MELLOR, H. 2007. Actin stress fibres. *Journal of cell science,* 120**,** 3491-3499.

PEREZA D.G., ESTHER PUNZÓN QUIJORNAA, RUY SANZD, VICENTE TORRES-COSTA, JOSEFA P. GARCÍA RUIZE & SILVÁN, M. M. 2015. Nanotopography enhanced mobility determines mesenchymal stem cell distribution on micropatterned semiconductors bearing nanorough areas *Colloids and Surfaces B: Biointerfaces,* 126**,** 146–153.

PETIT, V. & THIERY, J. P. 2000. Focal adhesions: structure and dynamics. *Biol Cell,* 92**,** 477-94.

PHAM, Q. P., SHARMA, U. & MIKOS, A. G. 2006. Electrospinning of polymeric nanofibers for tissue engineering applications: a review. *Tissue engineering,* 12**,** 1197-1211.

PIRES, D., HEDRICK, J. L., DE SILVA, A., FROMMER, J., GOTSMANN, B., WOLF, H., DESPONT, M., DUERIG, U. & KNOLL, A. W. 2010. Nanoscale three-dimensional patterning of molecular resists by scanning probes. *Science,* 328**,** 732-735.

POLLARD, T. D., BLANCHOIN, L. & MULLINS, R. D. 2000. Molecular mechanisms controlling actin filament dynamics in nonmuscle cells. *Annu Rev Biophys Biomol Struct,* 29**,** 545-76.

PONTI, A., MACHACEK, M., GUPTON, S. L., WATERMAN-STORER, C. M. & DANUSER, G. 2004. Two distinct actin networks drive the protrusion of migrating cells. *Science,* 305**,** 1782-6.

PRAGER-KHOUTORSKY, M., LICHTENSTEIN, A., KRISHNAN, R., RAJENDRAN, K., MAYO, A., KAM, Z., GEIGER, B. & BERSHADSKY, A. D. 2011. Fibroblast polarization is a matrix-rigidity-dependent process controlled by focal adhesion mechanosensing. *Nat Cell Biol,* 13**,** 1457-65.

PRASS, M., JACOBSON, K., MOGILNER, A. & RADMACHER, M. 2006. Direct measurement of the lamellipodial protrusive force in a migrating cell. *J Cell Biol,* 174**,** 767-72.

RAHMOUNI, S., LINDNER, A., RECHENMACHER, F., NEUBAUER, S., SOBAHI, T. R. A., KESSLER, H., CAVALCANTI-ADAM, E. A. & SPATZ, J. P. 2013. Hydrogel Micropillars with Integrin Selective Peptidomimetic Functionalized Nanopatterned Tops: A New Tool for the Measurement of Cell Traction Forces Transmitted through αvβ3 - or α5β1 -Integrins. *Adv. Mater.,* 25**,** 5869–5874.

REYMANN A. C., RAJAA BOUJEMAA-PATERSKI, JEAN-LOUIS MARTIEL, CHRISTOPHE GUÉRIN, WENXIANG CAO, HARVEY F. CHIN, ENRIQUE M. DE LA CRUZ, MANUEL THÉRY & BLANCHOIN, L. 2012. Actin Network Architecture Can Determine Myosin Motor Activity. *Science,* 336.

REYMANN, A. C., MARTIEL, J. L., CAMBIER, T., BLANCHOIN, L., BOUJEMAA-PATERSKI, R. & THERY, M. 2010. Nucleation geometry governs ordered actin networks structures. *Nat Mater,* 9**,** 827-32.

RICO, P., RODRIGUEZ HERNANDEZ, J. C., MORATAL, D., ALTANKOV, G., MONLEON PRADAS, M. & SALMERON-SANCHEZ, M. 2009. Substrate-induced assembly of fibronectin into networks: influence of surface chemistry and effect on osteoblast adhesion. *Tissue Eng Part A,* 15**,** 3271-81.

ROCA-CUSACHS, P., DEL RIO, A., PUKLIN-FAUCHER, E., GAUTHIER, N. C., BIAIS, N. & SHEETZ, M. P. 2013. Integrin-dependent force transmission to the extracellular matrix by alpha-actinin triggers adhesion maturation. *Proc Natl Acad Sci U S A,* 110**,** E1361-70.

ROCA-CUSACHS, P., GAUTHIER, N. C., DEL RIO, A. & SHEETZ, M. P. 2009. Clustering of α5β1 integrins determines adhesion strength whereas αvβ3 and talin enable mechanotransduction. *Proceedings of the National Academy of Sciences of the United States of America* 106**,** 16245–16250.

ROGNONI, L., STIGLER, J., PELZ, B., YLANNE, J. & RIEF, M. 2012. Dynamic force sensing of filamin revealed in single-molecule experiments. *Proc Natl Acad Sci U S A,* 109**,** 19679-84.

ROSLER, A., VANDERMEULEN, G. W. M. & KLOK, H. A. 2012. Advanced drug delivery devices via self-assembly of amphiphilic block copolymers. *Advanced Drug Delivery Reviews,* 64**,** 270-279.

ROSSIER, O., OCTEAU, V., SIBARITA, J. B., LEDUC, C., TESSIER, B., NAIR, D., GATTERDAM, V., DESTAING, O., ALBIGES-RIZO, C., TAMPE, R., COGNET, L., CHOQUET, D., LOUNIS, B. & GIANNONE, G. 2012. Integrins beta1 and beta3 exhibit distinct dynamic nanoscale organizations inside focal adhesions. *Nat Cell Biol,* 14**,** 1057-67.

RUOSLAHTI, E. 1996. RGD and other recognition sequences for integrins. *Annual review of cell and developmental biology,* 12**,** 697-715.

SALMERON-SANCHEZ, M., RICO, P., MORATAL, D., LEE, T. T., SCHWARZBAUER, J. E. & GARCIA, A. J. 2011. Role of material-driven fibronectin fibrillogenesis in cell differentiation. *Biomaterials,* 32**,** 2099-105.

SAUNDERS, R. M., HOLT, M. R., JENNINGS, L., SUTTON, D. H., BARSUKOV, I. L., BOBKOV, A., LIDDINGTON, R. C., ADAMSON, E. A., DUNN, G. A. & CRITCHLEY, D. R. 2006. Role of vinculin in regulating focal adhesion turnover. *European journal of cell biology,* 85**,** 487-500.

SCHAUFLER, V., CZICHOS-MEDDA, H., HIRSCHFELD-WARNECKEN, V., NEUBAUER, S., RECHENMACHER, F., MEDDA, R., KESSLER, H., GEIGER, B., SPATZ, J. P. & CAVALCANTI-ADAM, E. A. 2016. Selective binding and lateral clustering of α 5 β 1 and α v β 3 integrins: Unraveling the spatial requirements for cell spreading and focal adhesion assembly. *Cell adhesion & migration,* 10**,** 505-515.

SCHILLER, H. B., HERMANN, M.-R., POLLEUX, J., VIGNAUD, T., ZANIVAN, S., FRIEDEL, C. C., SUN, Z., RADUCANU, A., GOTTSCHALK, K.-E., THÉRY, M., MANN, M. & FÄSSLER, R. 2013. β1- and αv-class integrins cooperate to regulate myosin II during rigidity sensing of fibronectin-based microenvironments *Nat Cell Biol* 15**,** 625-636.

SCHVARTZMAN, M., PALMA, M., SABLE, J., ABRAMSON, J., HU, X., SHEETZ, M. P. & WIND, S. J. 2011. Nanolithographic control of the spatial organization of cellular adhesion receptors at the single-molecule level. *Nano Lett,* 11**,** 1306-12.

SCHWINGEL, M. & BASTMEYER, M. 2013. Force mapping during the formation and maturation of cell adhesion sites with multiple optical tweezers. *PLoS One,* 8**,** e54850.

SENCADAS, V., CORREIA, D. M., AREIAS, A., BOTELHO, G., FONSECA, A. M., NEVES, I. C., RIBELLES, J. L. G. & MENDEZ, S. L. 2012. Determination of the parameters affecting electrospun chitosan fiber size distribution and morphology. *Carbohydrate Polymers,* 87**,** 1295-1301.

SHAHAPURE, R., DIFATO, F., LAIO, A., BISSON, G., ERCOLINI, E., AMIN, L., FERRARI, E. & TORRE, V. 2010. Force generation in lamellipodia is a probabilistic process with fast growth and retraction events. *Biophys J,* 98**,** 979-88.

SHATTIL, S. J., KIM, C. & GINSBERG, M. H. 2010. The final steps of integrin activation: the end game. *Nat Rev Mol Cell Biol,* 11**,** 288-300.

SHIN, Y. M., HOHMAN, M. M., BRENNER, M. P. & RUTLEDGE, G. C. 2001. Electrospinning: A whipping fluid jet generates submicron polymer fibers. *Applied Physics Letters,* 78**,** 1149-1151.

SHROFF, H., GALBRAITH, C. G., GALBRAITH, J. A. & BETZIG, E. 2008. Live-cell photoactivated localization microscopy of nanoscale adhesion dynamics. *Nat Methods,* 5**,** 417-23.

SHROFF, H., GALBRAITH, C. G., GALBRAITH, J. A., WHITE, H., GILLETTE, J., OLENYCH, S., DAVIDSON, M. W. & BETZIG, E. 2007. Dual-color superresolution imaging of genetically expressed probes within individual adhesion complexes. *Proc Natl Acad Sci U S A,* 104**,** 20308-13.

SJOSTROM, T., DALBY, M. J., HART, A., TARE, R., OREFFO, R. O. & SU, B. 2009. Fabrication of pillar-like titania nanostructures on titanium and their interactions with human skeletal stem cells. *Acta Biomater,* 5**,** 1433-41.

SLATER, J. H., BOYCE, P. J., JANCAITIS, M. P., GAUBERT, H. E., CHANG, A. L., MARKEY, M. K. & FREY, W. 2015. Modulation of endothelial cell migration via manipulation of adhesion site growth using nanopatterned surfaces. *ACS Appl Mater Interfaces,* 7**,** 4390-400.

SMALL, J. V., ROTTNER, K., KAVERINA, I. & ANDERSON, K. 1998. Assembling an actin cytoskeleton for cell attachment and movement. *Biochimica Et Biophysica Acta (BBA)-Molecular Cell Research,* 1404**,** 271-281.

SMART, T., LOMAS, H., MASSIGNANI, M., FLORES-MERINO, M. V., PEREZ, L. R. & BATTAGLIA, G. 2008. Block copolymer nanostructures. *Nano Today,* 3**,** 38-46.

SMITH, P. G., GARCIA, R. & KOGERMAN, L. 1997. Strain reorganizes focal adhesions and cytoskeleton in cultured airway smooth muscle cells. *Exp Cell Res,* 232**,** 127-36.

SONNENBERG, A., CALAFAT, J., JANSSEN, H., DAAMS, H., VANDERRAAIJHELMER, L. M. H., FALCIONI, R., KENNEL, S. J., APLIN, J. D., BAKER, J., LOIZIDOU, M. & GARROD, D. 1991. Integrin-Alpha-6-Beta-4 Complex Is Located in Hemidesmosomes, Suggesting a Major Role in Epidermal-Cell Basement-Membrane Adhesion. *Journal of Cell Biology,* 113**,** 907-917.

STEINER, U., KLEIN, J. & FETTERS, L. J. 1994. Surface phase inversion in finite-sized binary mixtures. *Phys Rev Lett,* 72**,** 1498-1501.

STEVENS, M. M. & GEORGE, J. H. 2005. Exploring and engineering the cell surface interface. *Science,* 310**,** 1135-1138.

STOCKER, D., SCHUBERT, E. & REDWING, J. 1998. Crystallographic wet chemical etching of GaN. *Applied Physics Letters,* 73**,** 2654-2656.

STREICHFUSS, M., ERBS, F., UHRIG, K., KURRE, R., CLEMEN, A. E., BOHM, C. H., HARASZTI, T. & SPATZ, J. P. 2011. Measuring forces between two single actin filaments during bundle formation. *Nano Lett,* 11**,** 3676-80.

SUAREZ C., ROLAND, RAJAA BOUJEMAA-PATERSKI, HYERAN KANG, BRANNON R. MCCULLOUGH, ANNE-CÉCILE REYMANN, CHRISTOPHE GUÉRIN, JEAN-LOUIS MARTIEL, ENRIQUE M. DE LA CRUZ & BLANCHOIN, A. L. 2011. Cofilin Tunes the Nucleotide State of Actin Filaments and Severs at Bare and Decorated Segment Boundaries. *Current Bilogy,* 21**,** 862–868.

SWITKES, M. & ROTHSCHILD, M. 2001. Immersion Lithography at 157 nm. *Journal of Vacuum Science & Technology B: Microelectronics and Nanometer Structures Processing, Measurement, and Phenomena,* 19**,** 2353-2356.

TAKAGI, J. 2004. Structural basis for ligand recognition by RGD (Arg-Gly-Asp)-dependent integrins. Portland Press Limited.

TAN, K. Y., LIN, H., RAMSTEDT, M., WATT, F. M., HUCK, W. T. & GAUTROT, J. E. 2013. Decoupling geometrical and chemical cues directing epidermal stem cell fate on polymer brush-based cell micro-patterns. *Integr Biol* 5**,** 899-910.

TAPON, N. & HALL, A. 1997. Rho, Rac and Cdc42 GTPases regulate the organization of the actin cytoskeleton. *Current opinion in cell biology,* 9**,** 86-92.

TEE, Y. H., SHEMESH, T., THIAGARAJAN, V., HARIADI, R. F., ANDERSON, K. L., PAGE, C., VOLKMANN, N., HANEIN, D., SIVARAMAKRISHNAN, S. & KOZLOV, M. M. 2015. Cellular chirality arising from the self-organization of the actin cytoskeleton. *Nature cell biology,* 17**,** 445-457.

TEIXEIRA, A. I., ABRAMS, G. A., BERTICS, P. J., MURPHY, C. J. & NEALEY, P. F. 2003. Epithelial contact guidance on well-defined micro-and nanostructured substrates. *Journal of cell science,* 116**,** 1881-1892.

TEIXEIRA, A. I., MCKIE, G. A., FOLEY, J. D., BERTICS, P. J., NEALEY, P. F. & MURPHY, C. J. 2006. The effect of environmental factors on the response of human corneal epithelial cells to nanoscale substrate topography. *Biomaterials,* 27**,** 3945-3954.

TEO, W. E. & RAMAKRISHNA, S. 2006. A review on electrospinning design and nanofibre assemblies. *Nanotechnology,* 17**,** R89.

THÉRY, M., PÉPIN, A., DRESSAIRE, E., CHEN, Y. & BORNENS, M. 2006. Cell Distribution of Stress Fibres in Responseto the Geometry of the Adhesive Environment. *Cell Motility and the Cytoskeleton,* 63**,** 341-355.

THERY, M., RACINE, V., PEPIN, A., PIEL, M., CHEN, Y., SIBARITA, J. B. & BORNENS, M. 2005. The extracellular matrix guides the orientation of the cell division axis. *Nat Cell Biol,* 7**,** 947-53.

THERY, M., RACINE, V., PIEL, M., PEPIN, A., DIMITROV, A., CHEN, Y., SIBARITA, J. B. & BORNENS, M. 2006. Anisotropy of cell adhesive microenvironment governs cell internal organization and orientation of polarity. *Proc Natl Acad Sci U S A,* 103**,** 19771-6.

THIEVESSEN, I., THOMPSON, P. M., BERLEMONT, S., PLEVOCK, K. M., PLOTNIKOV, S. V., ZEMLJIC-HARPF, A., ROSS, R. S., DAVIDSON, M. W., DANUSER, G., CAMPBELL, S. L. & WATERMAN, C. M. 2013. Vinculin-actin interaction couples actin retrograde flow to focal adhesions, but is dispensable for focal adhesion growth. *The Journal of cell biology,* 202**,** 163-177.

TOJKANDER, S., GATEVA, G. & LAPPALAINEN, P. 2012. Actin stress fibers–assembly, dynamics and biological roles. *J Cell Sci,* 125**,** 1855-1864.

TOJKANDER, S., GATEVA, G., SCHEVZOV, G., HOTULAINEN, P., NAUMANEN, P., MARTIN, C., GUNNING, P. W. & LAPPALAINEN, P. 2011. A molecular pathway for myosin II recruitment to stress fibers. *Current Biology,* 21**,** 539-550.

TRAPPMANN, B., GAUTROT, J. E., CONNELLY, J. T., STRANGE, D. G., LI, Y., OYEN, M. L., COHEN STUART, M. A., BOEHM, H., LI, B., VOGEL, V., SPATZ, J. P., WATT, F. M. & HUCK, W. T. 2012. Extracellular-matrix tethering regulates stem-cell fate. *Nat Mater,* 11**,** 642-9.

TRICHET, L., LE DIGABEL, J., HAWKINS, R. J., VEDULA, S. R., GUPTA, M., RIBRAULT, C., HERSEN, P., VOITURIEZ, R. & LADOUX, B. 2012. Evidence of a large-scale mechanosensing mechanism for cellular adaptation to substrate stiffness. *Proc Natl Acad Sci U S A,* 109**,** 6933-8.

TRUONG, H. & DANEN, E. H. 2009. Integrin switching modulates adhesion dynamics and cell migration. *Cell adhesion & migration,* 3**,** 179-181.

TSENG, Y., KOLE, T. P., LEE, J. S., FEDOROV, E., ALMO, S. C., SCHAFER, B. W. & WIRTZ, D. 2005. How actin crosslinking and bundling proteins cooperate to generate an enhanced cell mechanical response. *Biochem Biophys Res Commun,* 334**,** 183-92.

TSIMBOURI, P., GADEGAARD, N., BURGESS, K., WHITE, K., REYNOLDS, P., HERZYK, P., OREFFO, R. & DALBY, M. J. 2014. Nanotopographical effects on mesenchymal stem cell morphology and phenotype. *J Cell Biochem,* 115**,** 380-90.

TUGULU, S., SILACCI, P., STERGIOPULOS, N. & KLOK, H.-A. 2007. RGD—Functionalized polymer brushes as substrates for the integrin specific adhesion of human umbilical vein endothelial cells. *Biomaterials,* 28**,** 2536-2546.

VAN HOORN, H., HARKES, R., SPIESZ, E. M., STORM, C., VAN NOORT, D., LADOUX, B. & SCHMIDT, T. 2014. The nanoscale architecture of force-bearing focal adhesions. *Nano Lett,* 14**,** 4257-62.

VANTERPOOL, F. A., CANTINI, M., SEIB, F. P. & SALMERON-SANCHEZ, M. 2014. A material-based platform to modulate fibronectin activity and focal adhesion assembly. *Biores Open Access,* 3**,** 286-96.

VOGEL, V. & SHEETZ, M. 2006. Local force and geometry sensing regulate cell functions. *Nat Rev Mol Cell Biol,* 7**,** 265-75.

WAYNER, E. A., ORLANDO, R. A. & CHERESH, D. A. 1991. Integrins alpha v beta 3 and alpha v beta 5 contribute to cell attachment to vitronectin but differentially distribute on the cell surface. *The Journal of cell biology,* 113**,** 919-929.

WEN, J. H., VINCENT, L. G., FUHRMANN, A., CHOI, Y. S., HRIBAR, K. C., TAYLOR-WEINER, H., CHEN, S. & ENGLER, A. J. 2014. Interplay of matrix stiffness and protein tethering in stem cell differentiation. *Nat Mater,* 13**,** 979-87.

WILSON, D. L., MARTIN, R., HONG, S., CRONIN-GOLOMB, M., MIRKIN, C. A. & KAPLAN, D. L. 2001. Surface organization and nanopatterning of collagen by dip-pen nanolithography. *Proc Natl Acad Sci U S A,* 98**,** 13660-4.

WISEMAN, P. W., BROWN, C. M., WEBB, D. J., HEBERT, B., JOHNSON, N. L., SQUIER, J. A., ELLISMAN, M. H. & HORWITZ, A. F. 2004. Spatial mapping of integrin interactions and dynamics during cell migration by image correlation microscopy. *J Cell Sci,* 117**,** 5521-34.

WNEK, G. E., CARR, M. E., SIMPSON, D. G. & BOWLIN, G. L. 2003. Electrospinning of nanofiber fibrinogen structures. *Nano Letters,* 3**,** 213-216.

WOLFENSON, H., BERSHADSKY, A., HENIS, Y. I. & GEIGER, B. 2011. Actomyosin-generated tension controls the molecular kinetics of focal adhesions. *J Cell Sci,* 124**,** 1425-1432.

WOLFENSON H., ALEXANDER BERSHADSKY, HENIS, Y. I. & GEIGER, A. B. 2010. Actomyosin-generated tension controls the molecular kinetics of focal adhesions. *Journal of Cell Science,* 124**,** 1425-1432.

WOO, K. M., CHEN, V. J. & MA, P. X. 2003. Nano-fibrous scaffolding architecture selectively enhances protein adsorption contributing to cell attachment. *Journal of biomedical materials research Part A,* 67**,** 531-537.

WOOD, M. A. 2007. Colloidal lithography and current fabrication techniques producing in-plane nanotopography for biological applications. *J R Soc Interface,* 4**,** 1-17.

WORTH, D. C. & PARSONS, M. 2008. Adhesion dynamics: mechanisms and measurements. *Int J Biochem Cell Biol,* 40**,** 2397-409.

XU, K., BABCOCK, H. P. & ZHUANG, X. 2012. Dual-objective STORM reveals three-dimensional filament organization in the actin cytoskeleton. *Nat Methods,* 9**,** 185-8.

YANG, K., JUNG, K., KO, E., KIM, J., PARK, K. I., KIM, J. & CHO, S.-W. 2013. Nanotopographical manipulation of focal adhesion formation for enhanced differentiation of human neural stem cells. *ACS applied materials & interfaces,* 5**,** 10529-10540.

YANG, M. T., FU, J., WANG, Y. K., DESAI, R. A. & CHEN, C. S. 2011. Assaying stem cell mechanobiology on microfabricated elastomeric substrates with geometrically modulated rigidity. *Nat Protoc,* 6**,** 187-213.

YANG, S. M., JANG, S. G., CHOI, D. G., KIM, S. & YU, H. K. 2006. Nanomachining by colloidal lithography. *Small,* 2**,** 458-75.

YIM, E. K., DARLING, E. M., KULANGARA, K., GUILAK, F. & LEONG, K. W. 2010. Nanotopography-induced changes in focal adhesions, cytoskeletal organization, and mechanical properties of human mesenchymal stem cells. *Biomaterials,* 31**,** 1299-306.

ZAIDEL-BAR, R., BALLESTREM, C., KAM, Z. & GEIGER, B. 2003. Early molecular events in the assembly of matrix adhesions at the leading edge of migrating cells. *J Cell Sci,* 116**,** 4605-13.

ZAIDEL-BAR, R., ITZKOVITZ, S., MA'AYAN, A., IYENGAR, R. & GEIGER, B. 2007a. Functional atlas of the integrin adhesome. *Nature cell biology,* 9**,** 858-867.

ZAIDEL-BAR, R., MILO, R., KAM, Z. & GEIGER, B. 2007b. A paxillin tyrosine phosphorylation switch regulates the assembly and form of cell-matrix adhesions. *Journal of cell science,* 120**,** 137-148.

ZENT, M. B. S. A. R. 2010. Integrin Structure and Function. *Cell-Extracellular Matrix Interactions in Cancer.*

ZHANG, S. 2003. Fabrication of novel biomaterials through molecular self-assembly. *Nat Biotechnol,* 21**,** 1171-8.

ZHANG, X. 2013. Fabrication of micro/nanofiber patterns and polymer brush for cell behaviour study. Queen Mary University of London.

ZHANG, X., JIANG, G., CAI, Y., MONKLEY, S. J., CRITCHLEY, D. R. & SHEETZ, M. P. 2008. Talin depletion reveals independence of initial cell spreading from integrin activation and traction. *Nat Cell Biol,* 10**,** 1062-8.

ZIABARI, M., MOTTAGHITALAB, V. & HAGHI, A. 2009. Application of direct tracking method for measuring electrospun nanofiber diameter. *Brazilian Journal of Chemical Engineering,* 26**,** 53-62.

Appendix 1

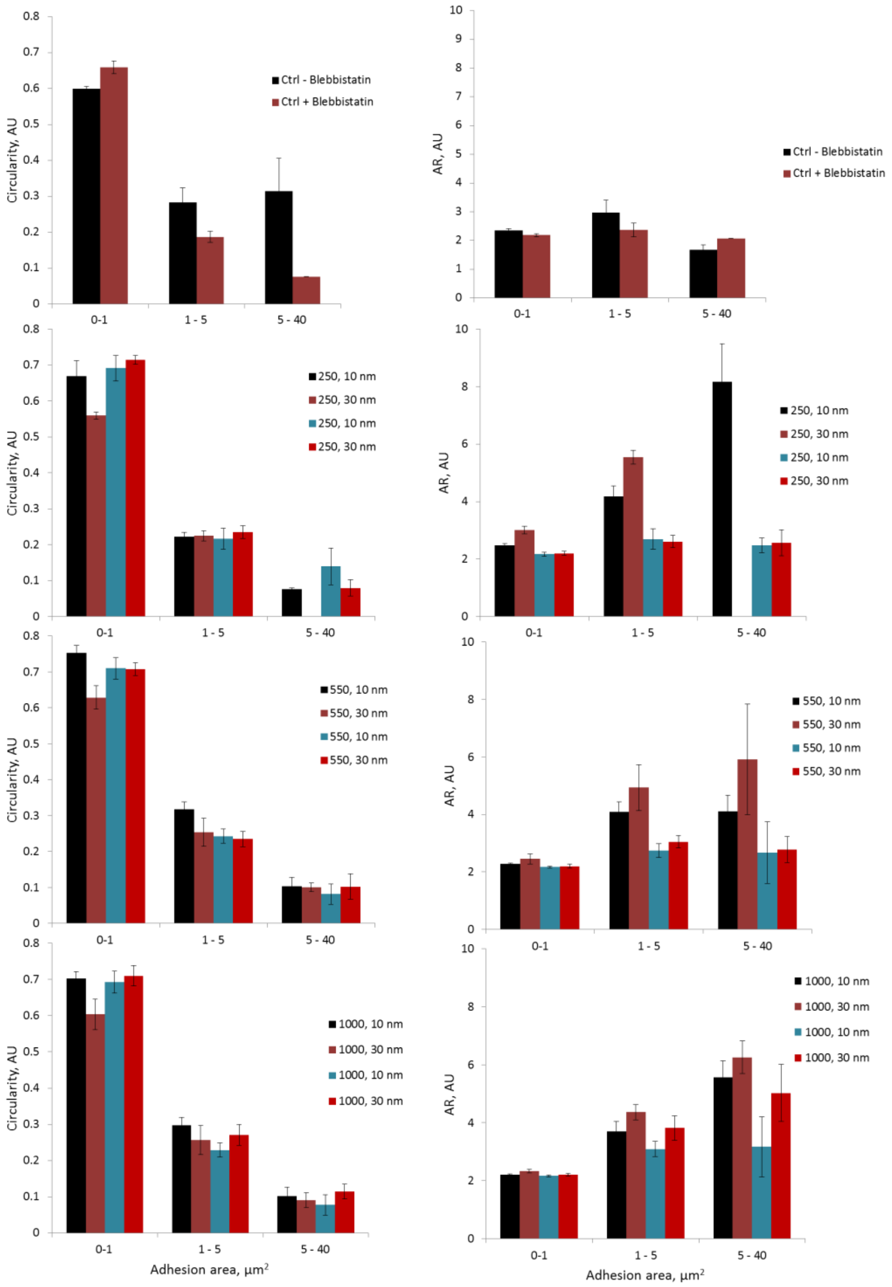

Figure A1.1 Focal adhesion shape descriptors distribution of the GEβ3 cells on the different nanofibres diameters (250, 550 and 1000 nm) and brushes height and treated with blebbistatin: circularity (left) and aspect ratio (right). Ctrl is the homogenous control surface. Error bars are SE, n = 3, with n representing the number of experiments. For statistical test: *, P < 0.05; **, P < 0.01; ***, P < 0.001; ****, P < 0.0001. For Chapter 5.

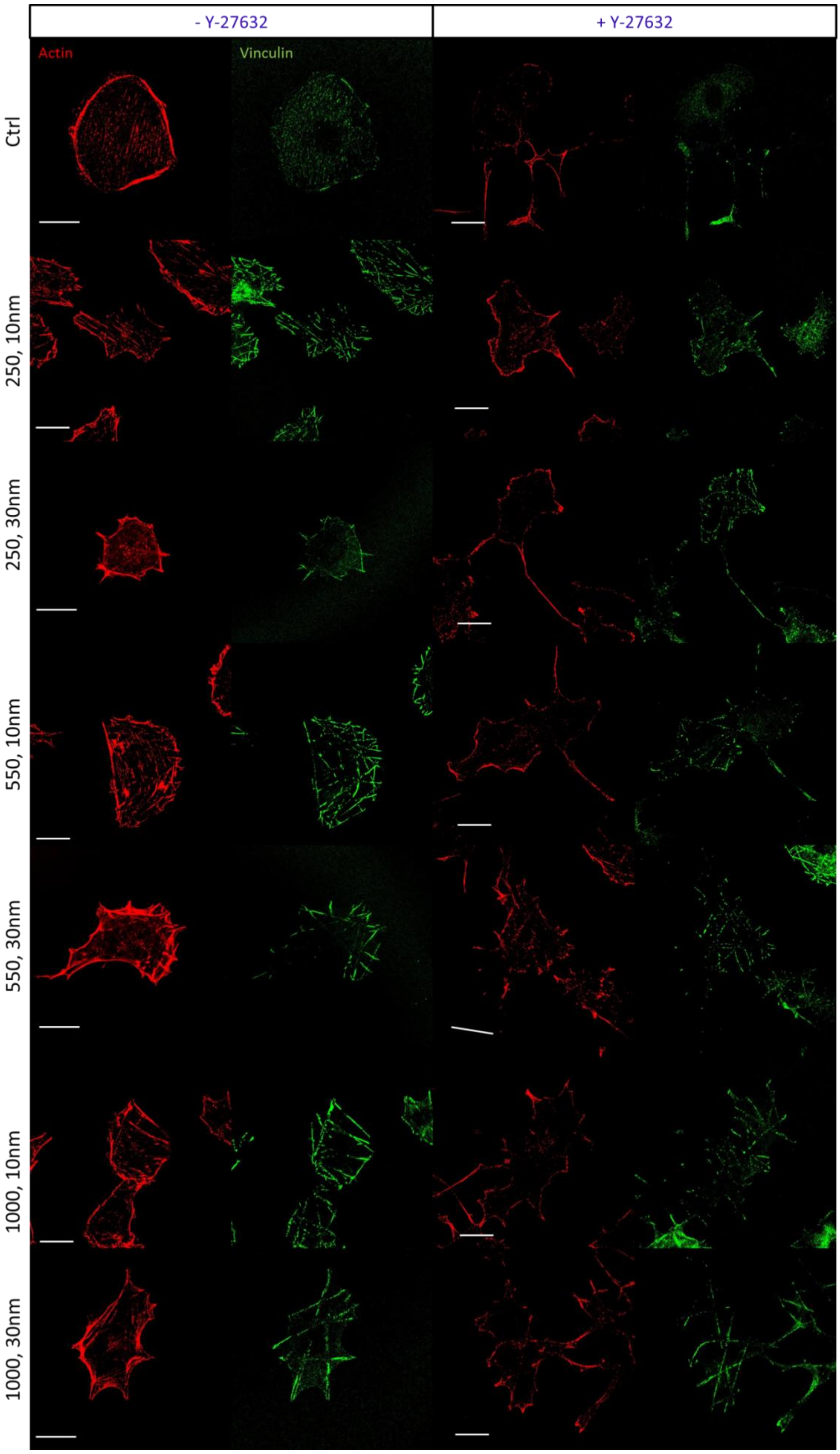

Figure A1.2 Confocal images of Geβ3 cells seeded on different nanofibres diamaters (250, 550 and 1000 nm) and brush heights (10 and 30 nm) and treated or not with the cytoskeleton inhibitor Y-27632. Red is actin cytoskeleton and green is vinculin. Scale bar is 20 µm. For Chapter 5.

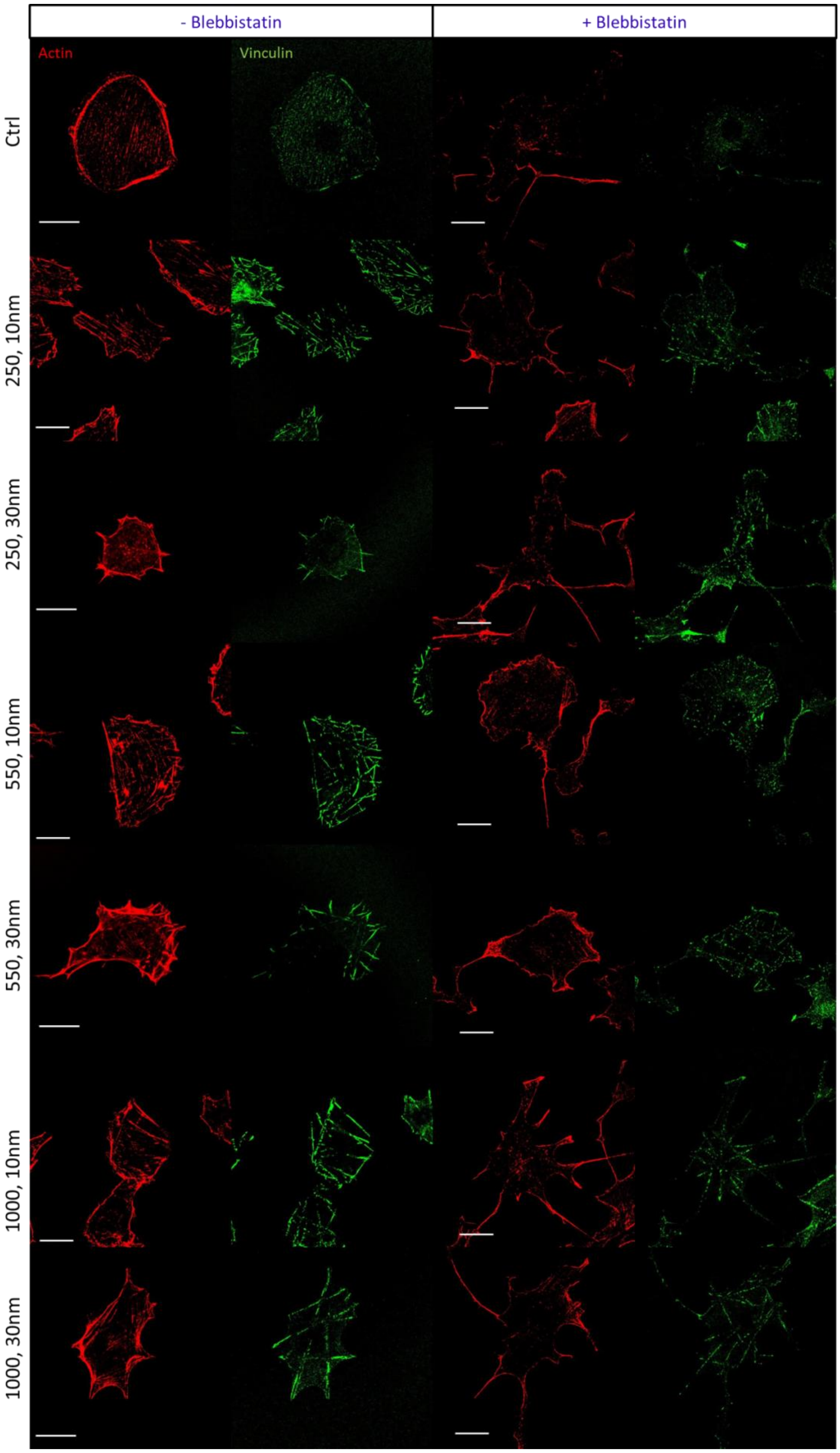

Figure A1.3 Confocal images of Geβ3 cells seeded on different nanofibres diameters (250, 550 and 1000 nm) and brush heights (10 and 30 nm) and treated or not with the cytoskeleton inhibitor blebbistatin. Red is actin cytoskeleton and green is vinculin. Scale bar is 20 µm. For Chapter 5.

Appendix 2

Table A2.1 Statistical analysis for as spun fibre dimension starting from different PMMA concentration. For statistical test: *P < 0.05, **P < 0.01, ***P < 0.001, ****P < 0.0001 (corresponding to Fig. 2.7).

PMMA concentration, w/w%	Probability
4 - 3.5	0.7727
5 - 3.5	0.0004765
5 - 4	0.00941
7 w salt - 3.5	5.24E-04
7 w salt - 4	0.01195
7 w/o salt - 5	0.0000696
7 w/o salt - 7 w salt	0.0000238
10 w salt - 3.5	0.0000000
10 w salt - 4	0.0000001
10 w salt - 7 w salt	0.0000005
10 w/o salt - 5	0.0000000
10 w/o salt - 7 w/o salt	0.0000080
10 w/o salt - 10 w salt	0.0002408
10 w salt - 7 w/o salt	0.33856

Table A2.2 Statistical analysis for gap area on 250, 550 and 800 nm nanofibres at low density. For statistical test: *P < 0.05, **P < 0.01, ***P < 0.001, ****P < 0.0001 (corresponding to Fig. 2.24).

Gap area on different nanofibres size (nm)	Probability
550 – 800	0.7727
550 - 250	0.0004765
800 - 250	0.00941

Table A2.3 Statistical analysis for patterns roughness data before and after fibronectin deposition (Figure S6). For statistical test: *P < 0.05, **P < 0.01, ***P < 0.001, ****P < 0.0001. No differences can be noticed for this analysis (corresponding to Fig. 2.27).

Nanofibres	Fibre wFN/	Brush wFN/	Fibre wFN/	Fibre woFN/	brush wFN/	brush woFN/

size (nm)	woFN	woFN	wFN	woFN	wFN	woFN
250	0.87329	0.51383				
800 – 250			0.8809	1	0.99422	0.92132
800	0.23096	1				

Table A2.4 Statistical analysis for HaCaT cell area and relative ratio on low, medium and high density nanofibres. Ctrl is the homogenous surface. For statistical test: *P < 0.05, **P < 0.01, ***P < 0.001, ****P < 0.0001 (corresponding to Fig. 3.3).

Pattern type	Ratio_ Low	Area_ low	Ratio_ Medium	Area_ Medium	Ratio_ High	Area_ high
250 – Ctrl	2.71E-04	7.68E-06	0.13404	0.00165	0.38051	1.81E-04
550 - Ctrl	0.00609	0.00294	0.90595	0.47033	0.33279	1.35E-04
550 - 250	0.01759	0.16418	0.1543	0.75838	0.99919	0.99952
800 – Ctrl	0.00312	0.00342	0.85658	0.01978	0.61892	0.94554
800 - 250	0.05888	0.14453	0.05008	0.94013	0.99366	0.22813
800 - 550	0.8612	0.99987	0.99999	0.97446	0.97876	0.18324
1000 – Ctrl			0.33314	0.0010	0.9897	0.75489
1000 - 250			0.83751	0.99676	0.15499	0.26809
1000 - 550			0.54836	0.61204	0.11744	0.21303
1000 - 800			0.37258	0.81689	0.59037	0.99897

Table A2.5 Statistical analysis for HaCaT cell shape descriptor (circularity and aspect ratio, AR) on low, medium and high density nanofibres. Ctrl is the homogenous surface. For statistical test: *P < 0.05, **P < 0.01, ***P < 0.001, ****P < 0.0001 (corresponding to Fig. 3.3).

Pattern type	Low density		Medium density		High density	
	Circularity	AR	Circularity	AR	Circularity	AR
250 – Ctrl	0.99771	1.06E-05	0.99973	0.00289	1.00E+00	2.80E-04
550 - Ctrl	0.03471	5.20E-05	0.96152	0.76712	9.56E-01	3.07E-04
550 - 250	0.11067	0.96744	0.98812	0.56806	0.96625	0.99998
800 – Ctrl	0.08591	0.00525	0.1711	0.04268	4.81E-02	0.64679
800 - 250	0.21497	0.6945	0.41427	0.91045	0.06246	0.60642
800 - 550	0.9878	0.51645	0.90476	0.91699	0.16584	0.57467
1000– Ctrl			0.42756	0.02003	0.71404	0.12088
1000- 250			0.68063	0.99287	0.74602	0.94359
1000- 550			0.97943	0.78921	0.9517	0.92557
1000- 800			0.99597	0.99446	0.61405	0.96462

Table A2.6 Statistical analysis for HaCaT cell density on different pattern type (circular or fibrous), size (250, 550 800 and 100 nm for fibrous, 300, 500 and 800 nm for circular) and density (low, medium and high). Ctrl is the homogenous surface. For statistical test: *P < 0.05, **P < 0.01, ***P < 0.001, ****P < 0.0001. No significant differences can be noticed for this analysis (corresponding to Fig. 3.4 and 3.7 C).

Fibrous patterns		**Circular patterns/ Circular-fibrous patterns**	
250 low – Ctrl	0.99607	**300 - 250 low**	1
250 high - Ctrl	0.99939	**300 - 250 high**	0.99987
250 high - 250 low	1	**300 – 250 medium**	1
550 low – Ctrl	1	**300 - Ctrl**	0.99952
550 low - 250 low	0.99786	**500 - 550 low**	0.99666
550 high – Ctrl	0.99449	**500 - 550 high**	0.87032
550 high - 250 high	0.74915	**500 - 550 medium**	1
550 high - 550 low	1	**500 - Ctrl**	1
800 low - C	1	**500 - 300**	1
800 low - 250 low	1	**800 - 800 low**	1
800 low - 550 low	0.99999	**800 - 800 high**	1
800 high – Ctrl	0.99999	**800 - 800 medium**	0.99801
800 high - 250 high	1	**800 - Ctrl**	1
800 high - 550 high	0.97635	**800 - 300**	1
800 high - 800 low	1	**800 - 500**	1
1000 high – Ctrl	0.99882		
1000 high - 250 high	1		
1000 high - 550 high	0.85383		
1000 high - 800 high	1		
250 medium – Ctrl	0.99964		
250 medium - 250 low	1		
250 medium - 250 high	1		
250 medium – 300	1		
550 medium – Ctrl	1		
550 medium - 550 low	0.99999		
550 medium - 550 high	0.98971		
550 medium - 500	1		
550 medium - 250 m	1		
800 medium – Ctrl	1		
800 medium - 800 low	0.99997		
800 medium - 800 high	0.99983		
800 medium - 800	0.99801		
800 medium - 250 medium	0.99816		
800 medium - 550 medium	0.99997		
1000 medium – Ctrl	0.99978		
1000 medium - 1000 high	1		
1000 medium - 250 medium	1		
1000 medium - 550 medium	1		
1000 medium - 800 medium	0.99864		

Table A2.7 Statistical analysis for HaCaT cell area and relative ratio on circular patterns. For statistical test: *P < 0.05, **P < 0.01, ***P < 0.001, ****P < 0.0001 (corresponding to Fig. 3.7 A).

Pattern size	Ratio	Area
300 – Ctrl	3.34E-05	1.68E-04
500 - Ctrl	1.11E-04	5.22E-04
500 - 300	0.47577	0.63075
800 – Ctrl	0.00103	0.00467
800 - 300	0.01887	0.04905
800 - 500	0.15464	0.26646

Table A2.8 Statistical analysis for HaCaT cells shape descriptor seeded on circular patches (300, 500 and 800 nm diameter): circularity and aspect ratio. For statistical test: *P < 0.05, **P < 0.01, ***P < 0.001, ****P < 0.0001 (corresponding to Fig. 3.7 B).

Circular patterns	Circularity	Circular patterns	Aspect Ratio
300 – Ctrl	0.0328	**300 – Ctrl**	0.83405
500 - Ctrl	0.3791	**500 - Ctrl**	0.24337
500 - 300	0.34171	**500 - 300**	0.63129
800 - Ctrl	0.07927	**800 - Ctrl**	0.52158
800 - 300	9.67E-04	**800 - 300**	9.35E-01
800 - 500	0.00776	**800 - 500**	0.91556

Table A2.9 Statistical analysis for GE, GEβ1 and GEβ3 cell area and relative ratio on fibrous patterns with 250, 550 and 1000 nm diameters and control surfaces (Ctrl). For statistical test: *P < 0.05, **P < 0.01, ***P < 0.001, ****P < 0.0001 (corresponding to Fig. 3.9).

Nanofibres / Ctrl	GE		GEβ1		GEβ3	
	Ratio	**Area**	**Ratio**	**Area**	**Ratio**	**Area**
250 – Ctrl	9.18E-06	0	0.00777	9.07E-06	0.00135	7.67E-08
550 - Ctrl	1.88E-05	0	0.15005	0.00176	0.05908	1.14E-04
550 - 250	0.46925	0.57061	0.04634	0.01287	0.01252	0.0015
1000 – Ctrl	6.28E-04	1.58E-06	0.68143	0.15336	0.09324	2.61E-04
1000 - 250	4.34E-04	5.59E-04	0.00275	1.83E-04	0.00379	2.20E-04
1000 - 550	0.005	0.00784	0.26326	0.09124	0.93789	0.84573

Table A2.10 Statistical analysis for GE cells shape descriptor (circularity and aspect ratio, AR) seeded on different nanofibres sizes (250, 550 and 1000nm fibre diameter) and control surfaces (Ctrl). For statistical test: *P < 0.05, **P < 0.01, ***P < 0.001, ****P < 0.0001 (corresponding to Fig. 3.9).

Pattern type	**GE**		**GEβ1**		**GEβ3**	
	Circularity	**AR**	**Circularity**	**AR**	**Circularity**	**AR**
250 – Ctrl	0.93312	0.0202	0.00004	0.01138	0.94027	0.00001
550 - Ctrl	0.0353	0.00326	0.53267	0.02184	0.9584	0.01946
550 - 250	0.14734	0.92811	0.00109	0.98079	0.99956	0.02222
1000 – Ctrl	0.00139	0.00991	0.99999	0.12207	0.07775	0.00302
1000 - 250	0.00796	0.97927	0.00006	0.72548	0.34858	0.069
1000 - 550	0.46874	0.99766	0.58092	0.89706	0.23132	0.92167

Table A2.11 . Statistical analysis for GE, GE β1 and GE β3 cells density on different fibrous pattern size (250, 550 and 1000 nm fibre diameter) and control surfaces (Ctrl). For statistical test: *P < 0.05, **P < 0.01, ***P < 0.001, ****P < 0.0001 (corresponding to Fig. 3.9 G).

Nanofibres size/control	**GE**	**GE β1**	**GE β3**
250 – Ctrl	0.000245	0.000822	0.03958
550 - Ctrl	0.00104	0.0304	0.46821
550 - 250	0.88188	0.20027	0.4837
1000 – Ctrl	0.82465	0.51865	0.99394
1000 - 250	0.00134	0.00866	0.06146
1000 - 550	0.00593	0.29944	0.60667

Table A2.12 Statistical analysis for GE, GE β1 and GE β3 focal adhesion size distribution (for adhesion sizes between 1 to 5 μm^2) on fibrous patterns (250, 550 and 1000 nm) and homogenous surfaces (Ctrl). For statistical test: *P < 0.05, **P < 0.01, ***P < 0.001, ****P < 0.0001 (corresponding to Fig. 4.1).

Nanofibres size/ control	**FA size 1 -5 μm^2**		
	GE	**GEβ1**	**GEβ3**
Ctrl – 250	6.90E-04	0.48602	0.99609
Ctrl – 550	0	0.16687	1.53E-06
550 - 250	0.04529	0.00998	1.77E-06
1000 - Ctrl	0	7.66E-07	1.10E-06
1000 – 250	0.05083	3.80E-08	1.29E-06

1000 – 550	0.99978	0.0037	0.99985

Table A2.13 Statistical analysis for GE, GEβ1 and GEβ3 focal adhesion shape factors (circularity and aspect ratio, AR) distributions on fibrous patterns (250, 550 and 1000 nm) and homogenous surfaces (Ctrl) for adhesion sizes between 1 to 5 µm^2. For statistical test: *P < 0.05, **P < 0.01, ***P < 0.001, ****P < 0.0001 (corresponding to Fig. 4.2).

Nanofibres size/ control	**Circularity, FA size 1 -5 µm^2**		
	GE	**GEβ1**	**GEβ3**
Ctrl – 250	0.99962	0.93441	0.59412
Ctrl – 550	0.97623	0.1542	0.81121
550 - 250	0.99503	0.78536	0.92118
1000 - Ctrl	0.69321	0.99249	0.84932
1000 – 250	0.8477	0.97883	0.90155
1000 – 550	0.89564	0.25319	0.99983
	AR, FA size 1 -5 µm^2		
	GE	**GEβ1**	**GEβ3**
Ctrl – 250	0.93925	0.75796	0.00222
Ctrl – 550	0.21441	6.51E-04	9.08E-04
550 - 250	0.71009	0.16167	0.79427
1000 - Ctrl	0.99972	0.18774	0.02561
1000 – 250	0.9571	0.96116	0.29418
1000 – 550	0.23352	0.11049	0.61135

Table A2.14 Statistical analysis for GE, GEβ1 and GEβ3 focal adhesion mean grey value (binned depending on adhesion size, µm2) on fibrous patterns (250, 550 and 1000 nm) and homogenous surfaces (Ctrl). For statistical test: *P < 0.05, **P < 0.01, ***P < 0.001, ****P < 0.0001 (corresponding to Fig. 4.3).

Nanofibres size/ control	**Mean grey value, FA size 1 -5 µm^2**		
	GE	**GEβ1**	**GEβ3**
Ctrl – 250	0.36499	0.00426	0.99773
Ctrl – 550	0.99783	0.2622	0.20168
550 - 250	0.43536	0.10692	0.38652
1000 - Ctrl	0.45829	0.96107	0.8344
1000 – 250	0.02965	0.00162	0.86321
1000 – 550	0.33757	0.10543	0.64743

Table A2.15 Statistical analysis for FRAP experiments on GEβ3 cells. Comparison of recovery rates (*k*, s^{-1}) and immobile fraction of cells seeded on 550 and 1000 nm nanofibres and homogenous surfaces

(Ctrl). For statistical test: *P < 0.05, **P < 0.01, ***P < 0.001, ****P < 0.0001 (corresponding to Fig. 4.4).

Nanofibres size/ Ctrl	*k*	Immobile fraction
Ctrl- 1000	0.0243	0.84304
Ctrl- 550	0.1074	0.95566
550 - 1000	0.7601	0.95892

Table A2.16 Statistical analysis for MEFvin^{-}/$^{-}$ cells spreading on homogenous surfaces (Ctrl) or different nanofibres size (300, 550 and 1000 nm) and being transfected (T) or not. Cell were transfected with vinculin venus, T12 and 880. For statistical test: *P < 0.05, **P < 0.01, ***P < 0.001, ****P < 0.0001 (corresponding to Fig. 4.5 A).

Nanofibres size/ Ctrl	Vnc venus	Vnc T12	Vnc 880
Ctrl – Ctrl T	1	0.99468	0.00155
300T – Ctrl T	3.29E-07	7.12E-07	3.10E-07
300 – Ctrl	4.30E-07	6.18E-08	0
300 - 300 T	1	0.99999	0.90801
500T - Ctrl T	0.0019	3.61E-04	0.00617
500T - 300 T	0.03836	0.43482	0.01784
500 - Ctrl	0.00678	9.38E-05	3.48E-06
500 - 300	0.01761	0.01178	0.02473
500 - 500T	1	0.93831	0.94619
1000T - Ctrl T	0.1917	0.11183	0.07622
1000T - 300 T	8.27E-04	5.40E-04	0.00116
1000T - 500T	0.70166	0.16861	0.96808
1000 - Ctrl	0.1554	0.19571	5.74E-04
1000 - 3300	0.00168	9.39E-06	1.89E-04
1000 - 500	0.94899	0.09584	0.629
1000 - 1000T	0.99998	0.96542	0.01135

Nanofibres size/ type of vinculin transfected	
300 T12 - 300 venus	0.89237
300 880 - 300 venus	0.97825
300 880 - 300 T12	0.95669
500 880 - 500 T12	0.77008
500 venus - 500 T12	0.14249
500 venus - 500 880	0.28876
1000 T12 - 1000 venus	0.64459
1000 880 - 1000 venus	0.09153
1000 880 - 1000 T12	0.32131
Ctrl T12 - Ctrl venus	0.48251
Ctrl 880 - Ctrl venus	0.06294
Ctrl 880 - Ctrl T12	0.34719

Table A2.17 Statistical analysis for MEFvin^{-}/$^{-}$ cells shape descriptor (circularity and aspect ratio – AR) on homogenous surfaces (Ctrl) or different nanofibres size (300, 550 and 1000 nm) and being transfected (T) or not. Cell were transfected with vinculin venus, T12 and 880. For statistical test: *P < 0.05, **P < 0.01, ***P < 0.001, ****P < 0.0001 (corresponding to Fig. 4.5 B).

Nanofibres size/ Ctrl	**Vnc venus**		**Vnc T12**		**Vnc 880**	
	Circ	**AR**	**Circ**	**AR**	**Circ**	**AR**
Ctrl – Ctrl T	0.99741	0.99999	0.99998	0.92605	0.6418	0.75022
300T – Ctrl T	0.9996	0.3314	0.71934	0.6864	0.01986	1
300 – Ctrl	0.80239	0.8631	0.46558	0.99931	0.00711	1
300 - 300 T	0.99997	0.92141	0.99939	0.34363	0.97775	0.84786
500T - Ctrl T	0.99999	0.96803	0.99875	0.23859	0.92051	0.35619
500T - 300 T	0.99407	0.90178	0.97775	0.99586	5.54E-04	0.40687
500 - Ctrl	1	0.96447	0.99775	0.25497	1	0.05721
500 - 300	0.90968	0.99997	0.21525	0.52926	0.00263	0.08268
500 - 500T	1	0.99999	0.98562	0.91897	0.98011	0.99787
1000T - Ctrl T	0.99999	0.98947	1	0.71328	0.99996	0.99188
1000T - 300 T	0.99503	0.88245	0.74303	0.99999	0.02799	0.99237
1000T - 500T	1	1	0.99922	0.95913	0.71532	0.82952
1000 - Ctrl	1	0.99705	0.996	0.9883	0.96122	0.45545
1000 - 3300	0.89257	0.99837	0.10771	0.99998	0.04575	0.51863
1000 - 500	1	0.99999	1	0.71154	0.87022	0.94615
1000 - 1000T	1	0.99988	0.99969	0.49697	0.91507	0.99998

Nanofibres size/ type of vinculin transfected	Circularity	AR
300 T12 - 300 venus	0.94684	0.94514
300 880 - 300 venus	0.82405	0.63362
300 880 - 300 T12	0.97273	0.86668
500 880 - 500 T12	0.11864	0.45045
500 venus - 500 T12	0.78748	0.11811
500 venus - 500 880	0.2679	0.53546
1000 T12 - 1000 venus	0.90409	0.50278
1000 880 - 1000 venus	0.99891	0.99727
1000 880 - 1000 T12	0.87139	0.42457
Ctrl T12 - Ctrl venus	0.83592	0.47669
Ctrl 880 - Ctrl venus	0.91545	0.48056
Ctrl 880 - Ctrl T12	0.98924	0.99997

Table A2.18 Statistical analysis for GE, GEβ1 and GEβ3 cells (and cross analysis between the different cell type) cytoskeleton parameters after immunostaining (apparent thickness and length, chirality and convexity). Cells were seeded on different nanofibres sizes and homogenous surfaces (Ctrl). For statistical test: *P < 0.05, **P < 0.01, ***P < 0.001, ****P < 0.0001 (corresponding to Fig. 5.3).

Nanofibres size (nm)/	**GE**			
	Thickness	*Chirality*	*Convexity*	*Length*
250 - 1000	2.52E-04	6.31E-04	0.77197	7.90E-04
550 - 1000	1.35E-05	0.8594	0.92178	0.13167
550 - 250	0.78377	0.00508	0.37516	0.20146
Ctrl - 1000	0.10302	0.97363	0.49989	0.0086
Ctrl - 250	0.18579	2.29E-04	0.95796	0.9143
Ctrl - 550	0.02593	0.62818	0.18544	0.59096
	GEβ1			
	Thickness	*Chirality*	*Convexity*	*Length*
250 - 1000	4.48E-05	0.47681	0.03796	0.03932
550 - 1000	9.63E-05	0.04048	0.17264	0.00175
550 - 250	0.94168	0.62549	0.80344	0.82555
Ctrl - 1000	0.99822	0.8849	0.29166	4.26E-05
Ctrl - 250	2.68E-07	0.76825	0.50396	0.31602
Ctrl - 550	2.69E-07	0.06321	0.96253	0.80495
	GEβ3			
	Thickness	*Chirality*	*Convexity*	*Length*
250 - 1000	1.86E-06	0.0013	0.76085	0.99364
550 - 1000	0.92763	0.54844	0.99993	0.0863
550 - 250	8.51E-06	0.04813	0.69454	0.12051
Ctrl - 1000	0.0034	0.04683	0.02626	0.98738
Ctrl - 250	0.26184	0	7.22E-04	0.92774
Ctrl - 550	0.0136	4.68E-04	0.02095	0.03404
	Thickness			
	Ctrl	*250*	*550*	*1000*
GEβ3 – GEβ1	0.04005	1.38E-06	0	1.01E-05
GE- GEβ1	0.72267	0.05881	0.88165	0.027
GE- GEβ3	0.61899	0.08744	0	0.24992
	Chirality			
	Ctrl	*250*	*550*	*1000*
GEβ3 – GEβ1	0	0.03674	0	1.39E-05
GE- GEβ1	0	0.09482	0	1.86E-06
GE- GEβ3	0.97222	0.99088	0.05021	0.27582
	Convexity			
	Ctrl	*250*	*550*	*1000*
GEβ3 – GEβ1	0	0.00313	2.74E-08	0
GE- GEβ1	2.64E-06	0.00265	9.68E-08	0
GE- GEβ3	0.1404	0.7012	0.40994	0.60506
	Length			

	Ctrl	*250*	*550*	*1000*
GEβ3 – GEβ1	0.9462	0.87732	0.01868	0.02233
GE- GEβ1	0.87105	0.05193	0.95017	0.98586
GE- GEβ3	0.77975	0.10869	0.18986	0.09485

Table A2.19 Statistical analysis for GEβ1 and GEβ3 cells velocity on different nanofibres sizes (250, 500 and 1000 nm) and homogenous surfaces (Ctrl). For statistical test: *P < 0.05, **P < 0.01, ***P < 0.001, ****P < 0.0001 (corresponding to Fig. 5.6).

Nanofibres size/ Ctrl	β1	β3
500 - 250	0.99989	0.3049
250 - 1000	0.46687	0.00176
500 - 1000	0.50816	0.14059
Ctrl- 250	0.87686	2.23275E-4
Ctrl- 500	0.92753	0.02974
Ctrl- 1000	0.13957	0.89395

Table A2.20 Statistical analysis for GEβ3 cells spreading, density and shape descriptors (circularity and aspect ratio) on different nanofibres size (250, 550 and 1000 nm) and with brush height of either 10 or 30 nm. For statistical test: *P < 0.05, **P < 0.01, ***P < 0.001, ****P < 0.0001 (corresponding to Fig. 5.14).

Nanofibres size (nm)/ brush height (nm)	Area	Density	Circularity	Aspect ratio
250, 30 – 250, 10	0.00109	0.99998	0.9999	6.64E-05
550, 10 - 250, 10	1	0.99899	1	1
550, 30 - 550, 10	0.99238	0.99999	0.99998	1
1000, 10 – 250, 10	1	1	0.7447	1
1000, 10 – 550, 10	1	0.99995	0.73295	1
1000,30 – 250, 10	1	1	0.64676	0.99386
1000,30 – 550, 10	0.99705	0.99964	0.6406	0.99982
1000,30 – 1000, 10	1	1	1	0.99993

Table A2.21 Statistical analysis for Geβ3 cells spreading on different nanofibres size (250, 550 or 1000 nm) and with brush height of either 10 or 30 nm and treated (+) or not (-) with either Y-27632 or Blebbistatin. For statistical test: *P < 0.05, **P < 0.01, ***P < 0.001, ****P < 0.0001 (corresponding to Fig. 5.15).

Pattern type, +/- inhibitor	Y-27632 (cell area)	Blebbistatin (cell area)
250, 30 + – 250, 10 +	0.37319	0.99955
550, 10 + - 250, 10 +	1	1
550, 10 + - 250, 30 +	0.70684	0.96294
550, 30 + - 250, 10 +	1	1
550, 30 + - 250, 30 +	0.61848	1
550, 30 + - 550, 10 +	1	0.99869
1000, 10 + – 250, 10 +	1	0.773
1000, 10 + – 250, 30 +	0.72655	0.99785
1000, 10 + – 550, 10 +	1	0.41663
1000, 10 + – 550, 30 +	1	0.95222
1000, 30 + – 250, 10 +	0.70556	0.90041
1000, 30 + – 250, 30 +	1	0.99996
1000, 30 + – 550, 10 +	0.94412	0.56319
1000, 30 + – 550, 30 +	0.90197	0.99182
1000,30 + – 1000, 10 +	0.95176	1
Ctrl + - 250, 10 +	0.06971	0.32463
Ctrl + - 250, 30 +	1.60E-04	0.05156
Ctrl + - 550, 10 +	0.01925	0.67454
Ctrl + - 550, 30 +	0.02735	0.14313
Ctrl + - 1000, 10 +	0.01771	0.0034
Ctrl + - 1000, 30 +	6.67E-04	0.00427
250, 10 - - 250, 10 +	0.37582	0.99675
250, 30 - - 250, 30 +	0.04242	4.66E-05
550, 10 - - 550, 10 +	1	0.99877
550, 30 - - 550, 30 +	0.13507	0.96782
1000, 10 - - 1000, 10 +	1	0.96611
1000, 30 - - 1000, 30 +	1	1
Ctrl - - Ctrl +	0.99964	1
Ctrl - - 250, 10 -	0.04896	0.00925
Ctrl - - 550, 10 -	0.17035	0.0494
Ctrl - - 1000, 10 -	0.14972	0.04126

Table A2.22 Statistical analysis for Geβ3 cells density and shape descriptors (circularity and aspect ratio – AR) on different nanofibres size (250, 550 or 1000 nm) and with brush height of either 10 or 30 nm and treated (+) or not (-) with either Y-27632 or Blebbistatin. For statistical test: *P < 0.05, **P < 0.01, ***P < 0.001, ****P < 0.0001 (corresponding to Fig. 5.15).

Pattern type, +/- inhibitor	**Y-27632**		
	Density	**Circularity**	**AR**
250, 30 + – 250, 10 +	1	1	1
550, 10 + - 250, 10 +	0.97399	0.99988	1
550, 10 + - 250, 30 +	0.99608	1	0.99908
550, 30 + - 250, 10 +	1	1	0.99998
550, 30 + - 250, 30 +	1	1	1
550, 30 + - 550, 10 +	0.99935	1	0.99522
1000, 10 + – 250, 10 +	0.98039	0.99109	1
1000, 10 + – 250, 30 +	0.99735	0.99978	0.99635
1000, 10 + – 550, 10 +	1	1	1
1000, 10 + – 550, 30 +	0.99961	0.99997	0.9862
1000, 30 + – 250, 10 +	1	0.99743	0.99998
1000, 30 + – 250, 30 +	1	0.99998	1
1000, 30 + – 550, 10 +	0.99885	1	0.99536
1000, 30 + – 550, 30 +	1	1	1
1000,30 + – 1000, 10 +	0.99929	1	0.98652
Ctrl + - 250, 10 +	1	0.99843	0.99953
Ctrl + - 250, 30 +	1	0.99999	0.9699
Ctrl + - 550, 10 +	0.99795	1	1
Ctrl + - 550, 30 +	1	1	0.93262
Ctrl + - 1000, 10 +	0.99867	1	1
Ctrl + - 1000, 30 +	1	1	0.93358
250, 10 - - 250, 10 +	1	1.51E-05	0.92624
250, 30 - - 250, 30 +	1	1.22E-04	0.044
550, 10 - - 550, 10 +	1	3.95E-06	0.99953
550, 30 - - 550, 30 +	1	1.41E-06	0.92116
1000, 10 - - 1000, 10 +	0.99995	2.77E-04	0.99998
1000, 30 - - 1000, 30 +	1	6.26E-04	0.99701
Ctrl - - Ctrl +	0.99998	7.15E-08	0.57735
Ctrl - - 250, 10 -	0.99999	0.76283	0.8634
Ctrl - - 550, 10 -	1	0.89636	0.7828
Ctrl - - 1000, 10 -	1	0.0399	0.74636
	Blebbistatin		
	Density	**Circularity**	**AR**
250, 30 + – 250, 10 +	0.96636	0.91315	0.96118
550, 10 + - 250, 10 +	1	1	0.77333
550, 10 + - 250, 30 +	0.99649	0.9843	1
550, 30 + - 250, 10 +	1	0.99986	0.99987
550, 30 + - 250, 30 +	0.99862	0.99977	0.99998

550, 30 + - 550, 10 +	1	1	0.99469
1000, 10 + – 250, 10 +	1	1	0.99424
1000, 10 + – 250, 30 +	0.97174	0.60549	1
1000, 10 + – 550, 10 +	1	0.99944	0.99989
1000, 10 + – 550, 30 +	1	0.97559	1
1000, 30 + – 250, 10 +	1	0.99999	1
1000, 30 + – 250, 30 +	0.99571	0.58029	0.99253
1000, 30 + – 550, 10 +	1	0.99914	0.9003
1000, 30 + – 550, 30 +	1	0.96978	1
1000,30 + – 1000, 10 +	1	1	0.99956
Ctrl + - 250, 10 +	0.99998	1	0.61188
Ctrl + - 250, 30 +	0.99992	0.82652	0.99994
Ctrl + - 550, 10 +	1	1	1
Ctrl + - 550, 30 +	1	0.99849	0.97053
Ctrl + - 1000, 10 +	0.99999	1	0.99781
Ctrl + - 1000, 30 +	1	1	0.7779
250, 10 - - 250, 10 +	0.99992	1.10E-06	0.46244
250, 30 - - 250, 30 +	1	0.00212	1.67E-04
550, 10 - - 550, 10 +	1	6.53E-06	1
550, 30 - - 550, 30 +	1	3.97E-06	0.99981
1000, 10 - - 1000, 10 +	1	1.08E-04	0.99995
1000, 30 - - 1000, 30 +	1	1.43E-04	0.99995
Ctrl - - Ctrl +	1	8.39E-08	0.73481
Ctrl - - 250, 10 -	0.99999	0.79269	0.69765
Ctrl - - 550, 10 -	1	0.91274	0.57712
Ctrl - - 1000, 10 -	1	0.0504	0.52903

Table A2.23 Statistical analysis for GE β3 focal adhesion size (0.2, 0.3 0.46 and 3.46 μm^2 adhesion sizes) distribution on different nanofibres size (250, 550 or 1000 nm) and with brush height of either 10 or 30 nm and treated (+) or not (-) with either Y-27632 or Blebbistatin. For statistical test: *P < 0.05, **P < 0.01, ***P < 0.001, ****P < 0.0001 (corresponding to Fig. 5.17 and 5.18).

Pattern type	FA size 1- 5 μm^2	
	Y-27632	**Blebbistatin**
Ctrl + / Ctrl -	0.27025	0.09411
250, 30 - /250, 10 -	2.41E-07	0
250, 10 + /250,10 -	0.01105	1.90E-04
250, 30 + /250, 30 -	3.42E-04	0.00143
250, 30 + /250, 10 +	0.6153	0.72304
550, 30 - /550, 10 -	0.0436	0.0285
550, 10 + /550,10 -	0.07838	2.19E-04
550, 30 + /550, 30 -	0.91806	0.69894
550, 30 + /550, 10 +	0.99527	0.04273
1000, 30 - /1000, 10 -	5.21E-04	0.01648
1000, 10 + /1000,10 -	0.00221	0.1815
1000, 30 + /1000, 30 -	0.23638	0

1000, 30 + /1000, 10 +	0.48323	0

Table A2.24 Statistical analysis for GE β3 total number of focal adhesion per cell seeded on different nanofibres size (250, 550 or 1000 nm) and with brush height of either 10 or 30 nm and treated (+) or not (-) with either Y-27632 or Blebbistatin. For statistical test: *P < 0.05, **P < 0.01, ***P < 0.001, ****P < 0.0001 (corresponding to Fig. 5.19).

Pattern type (no inhibitor)	**Tot number of focal adhesion/ cell**	
250, 30 /250, 10	4.13E-07	
550, 10 /250,10	1	
550, 30 /550, 10	0.00552	
1000, 10 /250, 10	0.04755	
1000, 10 /550, 10	0.04841	
1000, 10 /1000, 30	9.73E-04	
Ctrl /250,10	1.75E-06	
Ctrl /550,10	1.92E-05	
Ctrl /1000,10	0.53836	
Pattern type, +/- inhibitor	**Y-27632**	**Blebbistatin**
Ctrl - / Ctrl +	0.92135	0.73836
250, 10 + / 250, 10 -	2.33E-04	0.00235
Ctrl + / 250, 10 +	0.03692	0.01278
250, 30 + / 250, 30 -	4.12E-04	1.05E-05
250, 30 + / Ctrl +	5.53E-06	9.20E-06
250, 30 + / 250, 10 +	0.00547	0.96301
550, 10 + / 550, 10 -	1.89E-07	5.34E-05
550, 10 + / Ctrl +	0.99383	0.34352
550,10 + / 250, 10 +	0.53501	0.99525
550, 30 + / 550, 30 -	0	1.29E-07
550, 30 + / Ctrl +	0.69194	0.00834
550, 30 + / 250, 30 +	0.03931	0.077
550, 30 + / 550, 10 +	0.99947	0.99173
1000, 10 + / 1000, 10 -	0.98531	1
1000, 10 + / Ctrl +	0.00889	0.00413
1000, 10 + / 250, 10 +	1	1
1000, 10 + / 550, 10 +	0.92922	0.96653
1000, 30 + / 1000, 30 -	0.0092	2.48E-07
1000, 30 + / Ctrl +	2.00E-04	3.98E-07
1000, 30 + / 250, 30 +	0.99997	1
1000, 30 + / 550, 30 +	0.00609	0.72037
1000, 30 + / 1000, 10 +	0.0123	0.8771